Helicity of the W Boson in Single-Lepton $t\bar{t}$ events

by

Maria Florencia Canelli

Submitted in Partial Fulfillment

of the

Requirements for the Degree

Doctor of Philosophy

Supervised by

Professor Thomas Ferbel

Department of Physics and Astronomy

The College

Arts and Sciences

University of Rochester

Rochester, New York

2003

To my parents and grandparents

Acknowledgements

I would like to thank those who contributed toward this analysis.

First of all, I would like to thank Tom Ferbel, my advisor, who is by far the greatest example I have had. His dedication to his students and wisdom to solve any problem is a source of inspiration for me.

I am immensely grateful to Gaston Gutierrez for teaching me the steps required to be a physicist. From hardware to the intricacies of analysis, Gaston has helped orient me with tremendous patience and generosity.

I am especially thankful to my partner in crime, Juan Estrada, for all his help and time. He is a great friend and a great collaborator.

Brian Connolly helped me create Monte Carlo events in the last VAX available at DØ and the Florida State University group allowed me to use their machines. Without their help, this analysis would not have been possible.

I would like to thank the Rochester group at DØ, especially Marek Zielinski, George Ginther, and Paul Slattery, who always had time to answer my questions.

As top group management, Cecilia Gerber, Emanuela Barberis, and Aurelio Juste were really helpful in pushing this analysis forward.

The members of the Editorial Board 142 shaped this analysis with useful questions and comments, especially Suyong Choi who read many versions of this analysis.

Conversations with Harrison Prosper and John Conway were illustrative in clarifying statistical issues. Tim Tait could always answer my theoretical questions about top.

And lastly, I am deeply grateful to Ben Kilminster (my husband!) who has been my greatest fan and critic.

Abstract

We have applied a general approach for extracting information from data to a study of top quarks produced in proton-antiproton ($p\overline{p}$) collisions in the process $p\overline{p} \rightarrow t\overline{t}$. This reaction can be calculated in the Standard Model (SM), in which the top (or antitop) quarks decay into b quarks and W bosons: $t \rightarrow W^{+}b, \overline{t} \rightarrow W^{-}\overline{b}$. We examine the decays of the W boson in these events in order to establish how the spin of the W correlates with its momentum vector. This is defined by the helicity of the W boson (projection of its spin along its line of flight), which is also predicted by the SM. The analysis is based on a direct calculation of a probability for each event as a function of the helicity of the W bosons in top-antitop events in the lepton+jets final state. These events correspond to one W decaying into a lepton and its neutrino, and the other W into a quark-antiquark pair, with the quarks from the W and the two b quarks evolving into jets of particles. The probability is calculated by convoluting the differential cross section with the resolution and acceptance of the detector. This measurement uses top quarks collected by the DØ experiment in 125 events/pb of data in $p\overline{p}$ collisions at $\sqrt{s}$=1.8 TeV during Run I of the Fermilab TeVatron. Assuming the "V–A" coupling of the SM decay, we obtain a longitudinal helicity fraction of F_0=0.56$\pm$0.31(stat)$\pm$0.07(syst) for the W, which is consistent with the prediction of the Standard Model of F_0=0.70 for a top-quark mass of 175 GeV/c^2. The method employed in this analysis offers the possibility of increasing statistical precision by using both of the decays of W bosons in these events. Also Monte Carlo studies indicate that the approach provides an unbiased result in the limit of poor statistics. Although our measurement is severely limited by the small event sample of Run I, this powerful technique will provide far greater sensitivity to any departures from the SM in the data anticipated from Run II.

Contents

List of Tables

List of Figures

Chapter 1

Introduction

The goal of high-energy physics is to learn about the nature of the universe at the most fundamental level. To achieve this, high-energy (or particle) physicists study the interactions of particles that cannot be subdivided. This means trying to identify such particles and to formulate the forces acting among them. In the past, as knowledge about the fundamental structure of nature increased, the apparatus needed to probe structure at even smaller distances, that is at higher scales of energy, became more complex and expensive, needing more scientific collaborations and time to design, construct and run the experiments. The analysis presented in this dissertation was completed at the Fermi National Accelerator Laboratory (Fermilab) in Batavia, Il. Fermilab has been at the frontier of particle energy for more than a decade, colliding beams of protons (p) and antiprotons ($\overline{p}$) counterrotating in a four mile ring of magnets. These proton and antiprotons collide at two points, where the results coming from these collisions are measured using immense detectors. This analysis is based on data from the DØ experiment, one of these collision points. The data was obtained during "Run I" (1992 to 1996), where the collision center-of-mass energy ($\sqrt{s}$) was 1.8 TeV. Another run (Run II) is currently in progress, at a collision center-of-mass energy increased to $\sqrt{s}$=1.96 TeV, with an upgraded accelerator, and improved detectors to accommodate the increase in beam intensities and collision energy.

Increasing the energy of the collisions, or their absolute number, provides the means of searching for particles that could not produced (or produced less effectively) at lower energy. This is the case of the top quark, which is the most massive fundamental particle known to date, and was discovered at Fermilab during Run I. Analyzing the

decay properties of the top quark can determine whether it behaves in a way predicted by theory. In this analysis we examine one of these properties, the W helicity, that is, the projection of the spin vector of the W boson along its momentum vector. This property follows from the theory that describes fundamental particles and their interactions, and is referred as the Standard Model (SM). Any departures from expectation would be very exciting as it would indicated the presence of new physical phenomena.

In this chapter we summarize the theoretical understandings of the Standard Model, that is our understanding of fundamental particles and their interactions. We focus on the role of the top quark in the SM and the motivation for a measurement of the helicity of the W boson in top decays. Chapter 2 describes the Fermilab TeVatron accelerator and the DØ apparatus, and also algorithms used to identify objects observed in the detector. Chapter 3 summarizes the method of analysis used in this dissertation. Chapter 4 discusses the mapping between parton and jet energies. Chapters 5 and 6 contain Monte Carlo studies performed using resolution-smeared partons, and fully simulated and reconstructed events, respectively. Chapter 7 summarizes the results obtained using Run I data. Chapter 8 contains studies of systematics. Conclusions are drawn in Chapter 9.

1.1 The Standard Model of High Energy Physics

The Standard Model of particle physics describes the physical world at high energy scales, or small distances, in terms of interacting quantum fields [1, 2, 3]. In Quantum Field Theory (QFT), excitations of these quantized fields correspond to particles, with different fields representing different type of particles. Physical processes cannot be calculated exactly in quantum field theories, and approximation techniques are therefore required to obtain predictions. One of the most powerful techniques is *perturbation theory*. This theory creates small fluctuations around the vacuum state, describing the physical process through an infinite series in increasing powers of the "coupling strength" of the interaction. The leading terms in such calculations usually agree with experiment, but when higher-order terms are needed, the calculation usually diverges. To get around these infinities, a method called *renormalization* was invented to obtain a physical result.

There are many possible quantum field theories, the issue is how to select a QFT

that best describes natural phenomena. Restrictions can be obtained by considering only those theories whose Lagrangians are invariant under a phase transformation (gauge transformation). These type of theories are named gauge theories, and it was shown by 't Hooft that they can be renormalized [4]. The Standard Model, formulated more than twenty years ago, is the simplest of these theories, and encompasses all the known interactions (aside from gravity) and all fundamental particles. To this day, it is consistent with essentially all experimental observations [5].

The Standard Model is based on the gauge quantum-field symmetry groups SU(3) $\times$ SU(2) $\times$ U(1). Each of these groups corresponds to one interaction, and each to a distinct quantum theory. U(1) corresponds to the electromagnetic force of Quantum Electrodynamics (QED) [6], SU(2) corresponds to the weak force and the V–A theory of weak interactions [7], and SU(3) to the strong force Quantum Chromodynamics (QCD) [8]. Since gravitation is so much weaker than the other three interactions, it is no likely to influence subatomic processes, and has been ignored in the past [9]. Moreover, unlike the other interactions, gravitation cannot as yet be described by a quantum field theory [10].

Table 1.1 shows the properties of the fundamental particles, with their "flavors", masses, electric charges (in units of the electron charge), and interactions in which they participate [11]. The SM requires each particle to have its own antiparticle, with the same mass and lifetime, but opposite charge flavors. We denote antiparticles by placing bars above the particle symbols. Particles are divided in three groups: quarks, leptons, and gauge bosons. Quarks and leptons are spin-1/2 particles, and therefore obey the Pauli exclusion principle. Matter is usually defined as comprised of quarks and leptons, which are grouped in three "generations", each containing doublets that share similar properties. Besides the mysterious "dark-matter" and "dark-energy" of the Universe [12], all "normal" matter is composed of objects from the first generation. (In fact, normal nuclear matter contains tightly bound quarks and gluons.) To produce objects of higher generations, requires high-energy accelerators, either in collapsing stars (producing cosmic rays) or man-made particle accelerators. The particles from higher generations are unstable, and eventually decay into particles of the first generation or into photons.

Each generation of leptons has one charged particle (the electron e, muon μ, and tau τ) and one neutral particle (the associated neutrinos). In the Standard Model, the masses

Table 1.1: Particles contained in the Standard Model.

	Particle Name	Charge	Mass (GeV/c^2)	Interaction
Leptons	Electron (e)	-1	0.000511	EM, Weak
(spin = 1/2)	Electron neutrino (ν_e)	0	$<3 \times 10^{-6}$	Weak
	Muon (μ)	-1	0.1057	EM, Weak
	Muon neutrino (ν_μ)	0	$<0.19 \times 10^{-3}$	Weak
	Tau (τ)	-1	1.777	EM, Weak
	Tau neutrino (ν_τ)	0	$<18.2 \times 10^{-3}$	Weak
Quarks	Up (u)	+2/3	1.5 to 4.5 $\times 10^{-3}$	EM, Weak, Strong
(spin = 1/2)	Down (d)	-1/3	5 to 8.5 $\times 10^{-3}$	EM, Weak, Strong
	Strange (s)	-1/3	80 to 155 $\times 10^{-3}$	EM, Weak, Strong
	Charm (c)	+2/3	1 to 1.4	EM, Weak, Strong
	Bottom (b)	-1/3	4 to 4.5	EM, Weak, Strong
	Top (t)	+2/3	175	EM, Weak, Strong
Gauge Bosons	Photon (γ)	0	0	EM
(spin = 1)	W boson (W)	1.	80.4	Weak
	Z boson (Z)	0	91.2	Weak
	Gluon (g)	0	0	Strong

of the neutrinos are assumed to be zero. Recent data constrain the neutrino masses to be small but finite in value [13]. Neutrinos interact only via the weak interaction, which means that they have small collision probabilities, and cannot be detected easily. In experiments of the kind we will discuss, they are detected through an imbalance observed in the measured vector momentum in a collision.

The difference between quarks and leptons is that the quarks have fractional electric charge, and that they interact through the strong "color" force. The electric charge of the quarks is 1/3 or 2/3 the charge of an electron. The remnant effects of the strong force are also responsible for holding nuclei together.

The third group of particles, the gauge bosons, are quanta of the gauge fields and responsible for interactions between particles. The interaction between any two particles can be visualized as a process in which two particles exchange a virtual gauge boson. The electromagnetic interaction involves all particles that have electric charge. It is mediated by the photon, and its coupling strength increases logarithmically with the energy of the interaction [1].

The weak interaction is mediated by the W and Z bosons. These particles are very massive, and the fact that they have masses close to 100 GeV/c^2, means that their

interactions are characterized by small distances. One of the most important steps in the development of the SM was the unification of electromagnetism and the weak interaction into the electroweak theory [14]. This unification follows from the idea that there is a scalar field, known as the Higgs field, whose presence breaks the symmetry of SU(2) $\times$ U(1). The process of symmetry breaking suggests the existence of the W bosons, the Z boson, and the photon, and allows the W and Z to acquire mass [15, 16]. The predictions made on the basis of electroweak theory have been verified by experiments to high levels of precision [17].

The strong force Quantum Chromodynamics (QCD) describes the color interaction [18]. This interaction provides the binding of protons and neutrons and other hadrons, as well as atomic nuclei. QCD is mediated by color-carrying gluons, which couple to any objects possessing "color charge", that is, quarks and other gluons. Color charge has three possible values, conventionally called red, green, and blue for quarks (antiquarks come in anti-red, anti-green, and anti-blue). The strength of the strong coupling gets smaller as the energy of the interaction increases [18]. As a consequence, quarks behave as almost free particles at high energies and their interactions can be calculated using perturbative methods. When energies are low, these methods cannot be used anymore because the coupling becomes strong. A technique called *resummation* has been developed to minimize the effects of singularities, to avoid divergent terms by re-ordering of the perturbative series [18]. Another consequence of the increasing strength of color coupling with decreasing energy is that quarks can appear only in bound states. Thus far, no free quarks have been observed, and it seems that nature provides only combinations of quarks that are color-neutral. This can be done in two ways: one being three quarks with different colors, red+blue+green (baryons), and the second being of color-anticolor (mesons). When quarks or gluons are produced in collisions, they are not observed as such, but transformed to hadrons in a complex evolution from objects with color to colorless hadrons. This kind of process is called *fragmentation*. In effect, instead of observing a single quark or gluon, we detect color-neutral combinations of quarks and gluons that form the physical particles (hadrons) that move in the same direction as the original quark or gluon. This fragmented parton (quark or gluon) is referred to as a "jet". The masses of the quarks, especially the light ones, are not well defined since they are not free particles.

1.2 The Top Quark

The Standard Model accommodates the properties of all fundamental particles, but does not account for the values of their masses. Because the top quark is so much more massive than the other fermions, it has been speculated that it may play a unique role within the SM. It is therefore very important to understand the properties of the top quark, their degree of consistency with the Standard Model, and to check whether or not the top quark is truly exceptional. Yet, because of its relatively large mass, and only recent discovery, the properties of the top quark are not well known.

Studying top quarks is interesting for several reasons. Because it is so massive ($\approx$ 174 GeV/c^2) [11], it probes physics at a much higher energy scale than other fermions. This might provide non-SM contributions in its decay. An important consequence of a heavy top quark is that, to good approximation, it decays as a free quark. Its expected lifetime is $\approx 0.5 \times 10^{-24}$ s [19], and it therefore does not have time to bind with other quarks before it decays. In fact, the momentum and spin information carried by top quarks is expected to be passed on directly to their decay products, and the production and decay of top quarks can therefore provide a probe of the basic dynamics, with little impact from gluon radiation or other strong interactions [20].

The top quark was first observed in Run I of the Fermilab TeVatron, in $\approx$100 events/pb of integrated luminosity collected at the CDF and DØ experiments [21]. The top quark is detected indirectly via its decay products, which are a W boson and a b quark ($t \to Wb$). In the limit of a massless b quark, the standard V–A coupling at the tbW vertex requires that the b quark in top decays is produced left handed, restricting the helicity of the W^+ to values of 0 and -1. Observation of a significant "wrong" ± 1 helicity component in $W^\pm$ decays would clearly indicate the presence of physics (e.g., V+A coupling) beyond the SM [22].

In this analysis, we examine the nature of tbW vertex in $t\bar{t}$ events observed at the DØ experiment [24], and produced in $p\bar{p}$ collisions at a center-of-mass energy $\sqrt{s}$=1.8 TeV. Making use of information contained in these events, we will extract the fraction of the longitudinal W production in the data, F_0. In particular, we will rely on a direct comparison of data to the matrix element for the production and decay of $t\bar{t}$ states.

1.2.1 Production

In p-$\bar{p}$ collisions, the energies of the proton and antiproton are divided among partons, and the energy available in a partonic collision to create top quarks is only a fraction of the center-of-mass energy of the $p\bar{p}$ system.

There are two ways to produce pairs of top quarks: either via $q\overline{q}$ or gluon fusion. Fig. 1.1 shows the leading-order diagrams for $t\overline{t}$ production. At the TeVatron, the main contribution to the $t\overline{t}$ yield is from $q\overline{q}$ annihilation. This is purely the result of the fact that the *parton distribution functions* (PDFs) favor this channel at $\sqrt{s}$=1.8 TeV. In fact, about 90% of the top quarks are produced through the quark interaction. This rate changes with the energy of the collision, developing more gluon fusion with higher energy. Single top quarks can also be produced at the TeVatron through an electroweak process, which has yet to be confirmed. (The single-top final state is very difficult to distinguish from background.)

The $t\overline{t}$ cross section can be calculated using perturbative methods, and it depends on the mass of the top quark (M_t). A measurement of both parameters can check the validity of the QCD calculation. The current values of the top mass and cross section are:

$$M_t = 174.1 \pm 5.1 \text{ GeV/c}^2 \quad \text{TeV combined (DØ and CDF) [25]}$$
$$\sigma_{t\bar{t}} \ (M_t = 172 \text{ GeV/c}^2) = 5.9 \pm 1.7 \text{ pb DØ [26]}$$
$$\sigma_{t\bar{t}} \ (M_t = 175 \text{ GeV/c}^2) = 7.1 \pm 1.7 \text{ pb CDF [27]}$$

The $p\overline{p}$ total interaction cross section at this $\sqrt{s}$ is about 50 mb, and therefore experiments that collect $\approx 10^{12}$ interactions contain very small samples of $t\overline{t}$ data.

1.2.2 Decay

The top quark decays via the weak interaction, which does not conserve flavor. According to the SM, the top quark is almost always expected to decay to a b quark and a W boson. Although it has not been measured directly, the coupling of W to tb can be inferred to be close to unity ($V_{tb} \approx 0.999$) [11]. Therefore, the produced top (antitop) quarks decay rapidly into W^+b ($W^-\overline{b}$). This is followed by the W^+ (W^-) decay into the "hadronic" $u\overline{d}, c\overline{s}$ ($\overline{u}d, \overline{c}s$) or leptonic ($l$) $l^+\nu$ ($l^-\overline{\nu}$) channels. The final state of the $t\overline{t}$ system has different topological classifications that depend on the decay of the W:

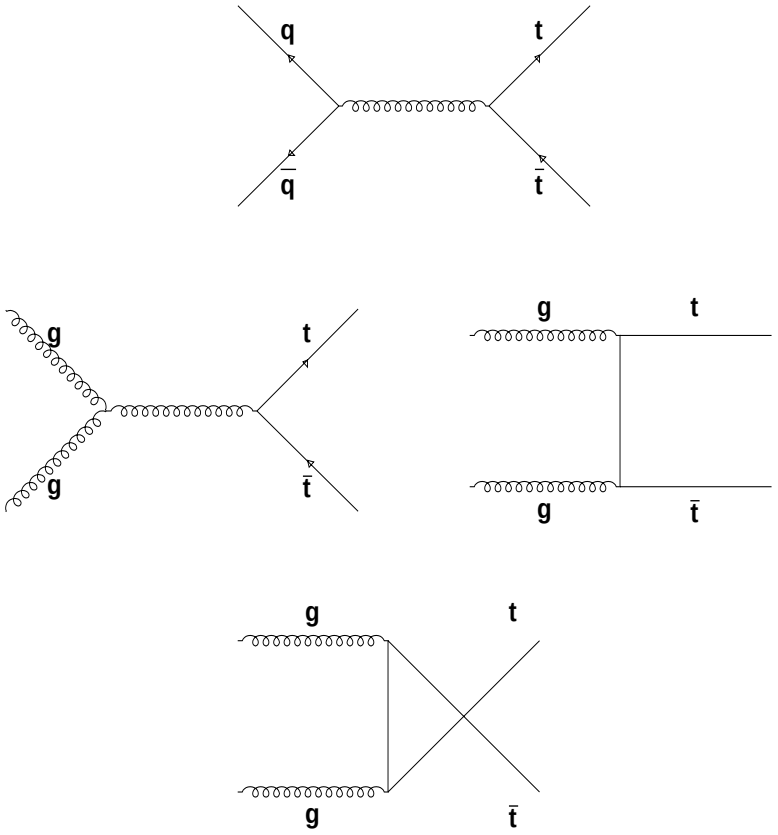

Figure 1.1: Top-antitop production mechanisms.

- "Dileptons": both W bosons decay leptonically. Since τ leptons are difficult to identify, this channel refers only to the ee, $e\mu$, and $\mu\mu$ combinations. This channel has the smallest branching ratio (4/81), as well the smallest background rate. Although there are two neutrinos in the final state, given the six kinematic constraints (two M_t, two M_W and conservation of transverse momentum), it is possible to fully reconstruct the three momenta of the two neutrinos and the entire $t\overline{t}$ system.

- "Lepton+jets": one W decays leptonically, while the other W decays hadronically. The initial system is overconstrained, and can be fully reconstructed with only one neutrino in the final state. This channel has a branching fraction of 8/27 (without having into account τs), but the amount of background is substantially larger than in the dilepton channel. Our analysis will rely on this channel.

Table 1.2: $t\bar{t}$ decay branching ratios for different channels. The factor of 2/3 for $q\overline{q}$ reflects the two hadronic channels and three colors for all quarks: 2×3×1/9=2/3.

	$W \to e\nu_e$ (1/9)	$W \to \mu\nu_\mu$ (1/9)	$W \to \tau\nu_\tau$ (1/9)	$W \to q\overline{q}$ (2/3)
$W \to e\nu_e$ (1/9)	1/81	1/81	1/81	2/27
$W \to \mu\nu_\mu$ (1/9)	1/81	1/81	1/81	2/27
$W \to \tau\nu_\tau$ (1/9)	1/81	1/81	1/81	2/27
$W \to q\overline{q}$ (2/3)	2/27	2/27	2/27	4/9

- "All jets": both W bosons decay hadronically. The branching fraction is largest for this channel (36/81). The major problem is that the amount of background from multijet production makes it exceedingly challenging to analyze.

Table 1.2 lists all the $t\bar{t}$ final states and their respective branching ratios.

1.2.3 Weak Interaction of the Top Quark

The standard top quark has a V–A charged-current weak interaction (see Fig. 1.2). To conserve angular momentum, the spin of the emitted b quark (essentially massless when compared to the top mass, with its helicity dominantly negative, i.e., spin pointing opposite to its line of flight in the rest frame of the top quark) can point either along the top spin, with the spin projection of the W vanishing (i.e., longitudinally polarized), or in the direction opposite to the top spin, in which case the W must be left-hand polarized (negative helicity). Hence, for massless b quarks [28, 29], a top quark can decay to a left-handed W (negative helicity W_-) or a longitudinal W (zero helicity W_0). Figure 1.3 illustrates these cases. In the SM, top quarks decay to longitudinal W bosons with a branching ratio [22, 23]:

$$B(t \to W_0 b) = \frac{M_t^2}{M_t^2 + 2M_W^2} \approx 0.7 \tag{1.1}$$

where we take $M_t = 174.3$ GeV/c^2 and $M_W = 80.4$ GeV/c^2 [11]. CDF has measured this branching ratio [30]:

$$B(t \to W_0 b) = 0.91 \pm 0.37 \pm 0.13, \tag{1.2}$$

which, within its large uncertainly, is consistent with SM expectations.

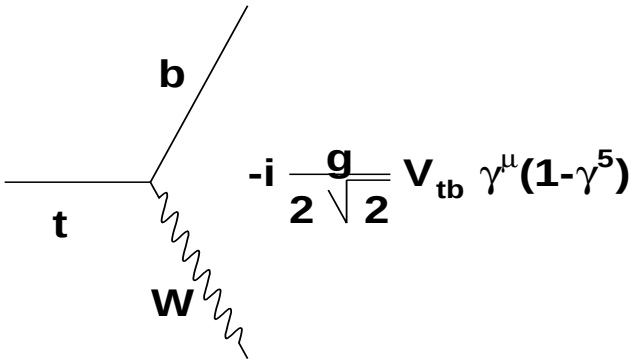

Figure 1.2: V-A coupling in top-quark decay.

Assuming the branching fraction $B(t \to W_0 b) = 0.70$, the CDF experiment has also extracted a branching rate for top-quark decay to a W boson of positive helicity [30]:

$$B(t \to W_+ b) = 0.11 \pm 0.15, \tag{1.3}$$

which is consistent with zero, as expected in the Standard Model.

The anticipated accuracy of the measurement of $B(t \to W_0 b)$ in the initial stage of Run II of the TeVatron (integrated luminosity of 2 events/fb) is 5.5%, with an ultimate uncertainty (for 30 events/fb) of less than 2% [31].

1.2.4 The Leading-Order Matrix Element

When only one W decays leptonically (lepton+jets events), the signature is one lepton, imbalance in transverse momentum (missing E_T or $\not\!\!E_T$), and at least four jets. This signal is not as clean as that for dileptons, but has better statistics, and the background is far smaller than for the case when both W^+ and W^- decay into jets. DØ has 91 events in Run I that are candidates for $t\bar{t}$ in the lepton + jets process [32], in which more than 60% are expected to be background events. We will restrict our analysis to this sample. Ignoring a contribution of $\approx 10\%$ from $gg \to t\bar{t}$, we study only the

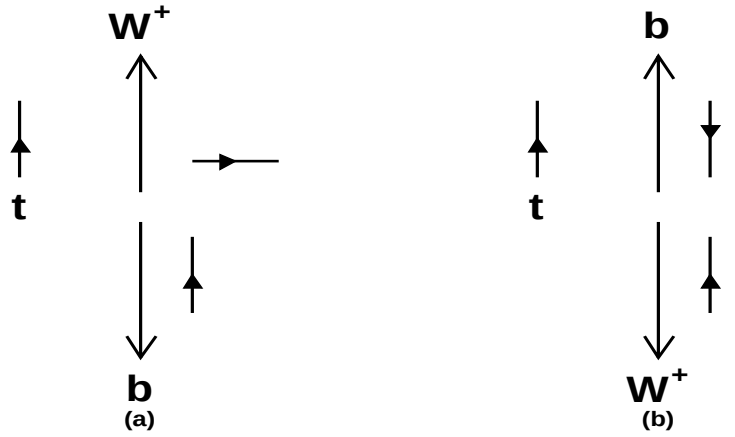

Figure 1.3: Angular momentum conservation in the decay of the top quark. Filled arrows indicate the spin direction of the particle and large arrows the momentum direction in the rest frame of the top quark. Since the b quark can be considered massless, it is almost completely left-handed. (a) Longitudinal W^+, emitted along the spin direction of the top quark. (b) Left-handed W^+, emitted opposite to the spin direction of the top quark.

square of the matrix element for $q\overline{q} \to t\overline{t}$. The production and decay process $q\overline{q} \to t\overline{t}$ $\to (W^+b)(W^-\overline{b}) \to (\overline{e}\nu b)(d\overline{u}\overline{b})$, (and similarly for $W^+ \to \overline{\mu}\nu$ and $W^- \to c\overline{s}$), averaged over the initial quark colors and spins, and summed over the final colors and spins, is given by [33]:

$$|M|^2 = \frac{g_s^4}{9} F\overline{F}\left((2-\beta^2 s_{qt}^2) - \frac{(1-c_{\overline{e}q}c_{d\overline{q}}) - \beta(c_{\overline{e}t}+c_{d\overline{t}}) + \beta c_{qt}(c_{\overline{e}q}+c_{d\overline{q}}) + \frac{1}{2}\beta^2 s_{qt}^2(1-c_{\overline{e}d})}{\gamma^2(1-\beta c_{\overline{e}t})(1-\beta c_{d\overline{t}})} \right) \quad , \tag{1.4}$$

where s_{ij} and c_{ij} are the sines and cosines of the angle between particles i and j, calculated in the $q\overline{q}$ center of mass (CM), g_s is the strong coupling constant, β is the top quark's velocity (v/c) in the $q\overline{q}$ CM, and $\gamma = (1-\beta^2)^{-1/2}$. F reflects the production and leptonic decay of the top quark $t \to W^+b \to \overline{e}\nu_e b$:

$$F = \frac{g_w^4}{4}\left[\frac{m_t^2 - m_{\overline{e}\nu}^2}{(m_t^2 - M_t^2)^2 + (M_t,\ _t)^2}\right]\left[\frac{w(\cos\hat{\phi}_{\overline{e}b})}{(m_{\overline{e}\nu}^2 - M_W^2)^2 + (M_W,\ _W)^2}\right] \quad , \tag{1.5}$$

where $\hat{\phi}_{\overline{e}b}$ is the polar angle between the e^+ and b in the W^+ rest frame, $m_{\overline{e}\nu}^2$ is the invariant mass of the positron-neutrino system, $(M_t,,\ _t)$ and $(M_W,,\ _W)$ are the masses

and widths of the top quark and W boson, and g_w is the weak coupling constant. (M_t refers to the pole mass, and m_t to the mass of top in any event. The measured mass of the top quark of 174.3 GeV/c^2 would correspond to M_t.) There is a similar expression for F for the $W \to \overline{\mu}\nu$ decay. The term $w(\cos\hat{\phi}_{\overline{e}b})$ will be discussed in more detail in the next section. The top width , $_t$ is a function of the top mass, and, in the narrow–width approximation, is given by

$$\begin{aligned} , _t &= \frac{g_w^4 M_t^3 \overline{\pi}}{2^7 (2\pi)^3 3} \; \frac{1 - 3(M_W/M_t)^2 + 2(M_W/M_t)^3}{M_W, _W} \\ \overline{\pi} &= arctg[\frac{(M_t - M_b)^2 - M_W^2}{M_W, _W}] - arctg[\frac{(M_{\overline{e}} + M_{\nu_e})^2 - M_W^2}{M_W, _W}] \end{aligned} \tag{1.6}$$

Similarly, $\overline{F}$ corresponds to the decay $\overline{t} \to W^- \overline{b} \to d\overline{u}\overline{b}$:

$$\overline{F} = \frac{g_w^4}{4} \left[\frac{m_t^2 - m_{d\overline{u}}^2}{(m_t^2 - M_t^2)^2 + (M_t, _t)^2} \right] \left[\frac{w(\cos\hat{\phi}_{d\overline{b}})}{(m_{d\overline{u}}^2 - M_W^2)^2 + (M_W, _W)^2} \right] \quad , \tag{1.7}$$

where $\hat{\phi}_{d\overline{b}}$ is the angle between d and $\overline{b}$ in the W^- rest frame, $m_{d\overline{u}}^2$ is the invariant mass of the $d - \overline{u}$ system, and, as before, $(M_t,, _t)$ and $(M_W,, _W)$ are the masses and widths of the top quark and W boson, and g_w is the weak coupling constant. (There is an analogous term for $W \to c\overline{s}$ decay.)

Although version 6.4 of the HERWIG Monte Carlo (MC) generators includes $t\overline{t}$ spin correlations, we deal only with MC events generated with a previous version. Therefore, the correlation term in Eq. 1.4 will be ignored, and Eq. 1.4 will simplify to:

$$|M|^2 = \frac{g_s^4}{9} F\overline{F}(2 - \beta^2 s_{qt}^2) \quad . \tag{1.8}$$

It will be assumed that the parton q originates from the proton, and $\overline{q}$ from the antiproton. The electron charge was not measured in DØ's Run I, and it is therefore not possible to distinguish between t and $\overline{t}$. However, since $s_{qt}^2 = s_{q\overline{t}}^2$, Eq. 1.8 is invariant with respect to the exchange $t \leftrightarrow \overline{t}$.

1.2.5 Angular Dependence of the Standard $t\bar{t}$ Matrix Element

The angular part of the matrix element for top decay is contained in $w(\cos\hat{\phi}_{\overline{e}b})$ for the leptonic branch and in $w(\cos\hat{\phi}_{d\bar{b}})$ for the hadronic branch. The decay angles of interest are shown in Fig. 1.4.

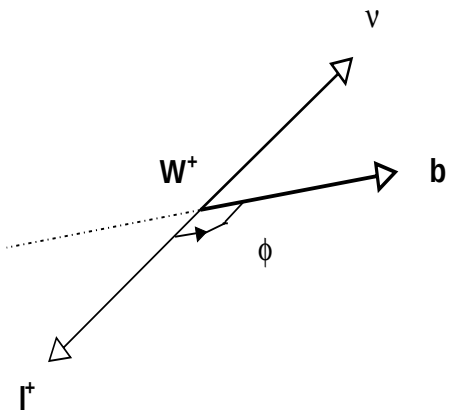

Figure 1.4: Definition of decay angles for top–quark decay in the W rest frame. The dotted line represents the spin direction of the top–quark. $\hat{\phi}$ is the angle between the lepton (or d or s quark) and this axis.

Our definition of the $\hat{\phi}$ angle follows the convention of Mahlon and Parke [34]. Usually, the angle is defined with respect to the W line of flight ("helicity" frame) instead of the b direction, as we have done here. The general form of the angular distribution of the charged lepton (or d or s quark) in the W frame is given by [29]:

$$w(\cos\hat{\phi}) = \frac{4}{3}\big(M_t^2 w_0(\cos\hat{\phi}) + 2M_W^2 w_-(\cos\hat{\phi}) + M_b^2 w_+(\cos\hat{\phi})\big) \tag{1.9}$$

where $\hat{\phi}$ refers to the leptonic ($\overline{e}b$ or $\overline{\mu}b$) or hadronic ($d\bar{b}$ or $s\bar{b}$) decay angle in the W rest frame. The normalized functions $w(\cos\hat{\phi})$ have the following form:

$$w_+(\cos\hat{\phi}) = \frac{3}{8}(1-\cos\hat{\phi})^2 \tag{1.10}$$

$$w_0(\cos\hat{\phi}) = \frac{3}{4}(1-\cos^2\hat{\phi}) \tag{1.11}$$

$$w_-(\cos\hat{\phi}) = \frac{3}{8}(1+\cos\hat{\phi})^2 \tag{1.12}$$

where these functions (all normalized to unity) reflect the angular dependence of the matrix element for the three helicity states of the W, and are given by the distributions sketched in Fig. 1.5.

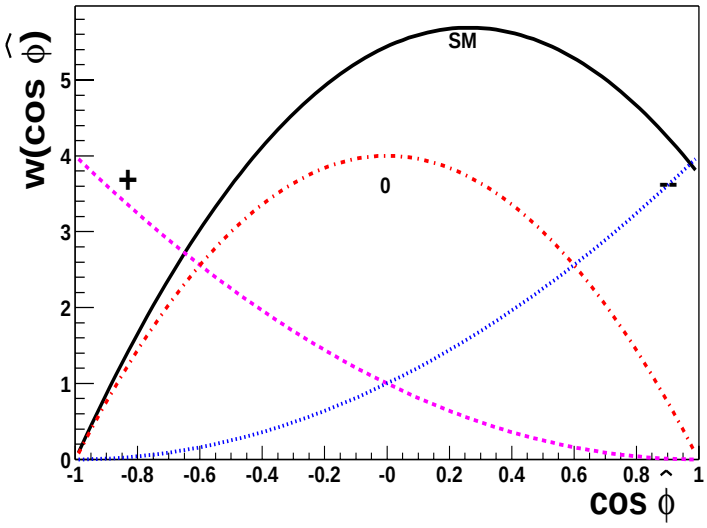

Figure 1.5: The decay functions $w(\cos\hat{\phi})$ for W_+, W_- and W_0, and the expectation for W^+ decay in the SM. (W^- decays would be just mirror-image relative to cosϕ=0.)

We can rewrite Eq. 1.9 in the general form:

$$w(\cos\hat{\phi}) = \frac{w(\cos\hat{\phi})}{\frac{4}{3}(M_t^2 + 2M_W^2 + M_b^2)} = F_- w_-(\cos\hat{\phi}) + F_0 w_0(\cos\hat{\phi}) + F_+ w_+(\cos\hat{\phi}) \tag{1.13}$$

where the three components of this equation refer to an arbitrary mixture of the three helicity states of the W: left-handed, longitudinal, and right-handed. The helicity fractions F_-, F_0, F_+ depend on M_t, M_W and M_b, and correspond to the branching fractions of top into a b and a W in left-handed, longitudinal, and right-handed helicity states, respectively. The three quantities (F_-, F_0, F_+) are probabilities, and therefore all are $\geq$0, and $F_- + F_0 + F_+ = 1$. Since $M_b << M_W$ and $M_b << M_t$, the b-quark mass can, to good approximation, be set to zero [28]. Hence, in the SM (neglecting M_b), for W^+, we

obtain:

$$F_- = \frac{2\gamma}{1+2\gamma} \tag{1.14}$$

$$F_0 = \frac{1}{1+2\gamma} \tag{1.15}$$

$$F_+ = 0 \tag{1.16}$$

where

$$\gamma = \frac{M_W^2}{M_t^2} \tag{1.17}$$

In conclusion, the angular term of the $t\bar{t}$ matrix element when the W decays leptonically is given by,

$$w(\cos\hat{\phi}_{\overline{e}b}) = F_0\frac{3}{4}(1-\cos^2\hat{\phi}_{\overline{e}b}) + F_-\frac{3}{8}(1+\cos\hat{\phi}_{\overline{e}b})^2 \tag{1.18}$$

Since it is essentially impossible to differentiate between the two jets in the hadronic decay of the W, the two combinations are related by $\cos\hat{\phi}_{\overline{u}\overline{b}}$=$-\cos\hat{\phi}_{d\overline{b}}$, which therefore symmetrizes Eq. 1.7. Therefore, the angular term of the $t\bar{t}$ matrix element when the W decays hadronically is,

$$w(\cos\hat{\phi}_{d\overline{b}}) = F_0\frac{3}{4}(1-\cos^2\hat{\phi}_{d\overline{b}}) + F_-\frac{3}{8}(1+\cos\hat{\phi}^2_{d\overline{b}}) \tag{1.19}$$

Also, in this study, we use exclusively only the lepton+4 jets events, and therefore have only twelve unique assignments of jets to quarks, because the combination that interchanges the jets assigned to any W is already considered in the symmetrization of Eq. 1.19.

1.2.6 Angular Dependence for a Non-Standard $t\bar{t}$ Matrix Element

The presence of any non-standard couplings in top decays requires a general angular analysis of the helicities of the W. A V+A coupling will introduce a component of right-handed W helicity (see Fig. 1.6), but, the addition of a right-handed decay will not affect

the branching fraction to longitudinal W. It will rather decrease the branching to left-handed W. In Figure 1.6, we show how adding a right-handed contribution (w_+) affects the decay distributions for W^+ decaying leptonically and hadronically. The longitudinal contribution remains fixed to 0.70 , and as the sum of the left and right distributions is 0.30. As mentioned in the previous section, the hadronic distribution is symmetrized with respect to two decay quarks.

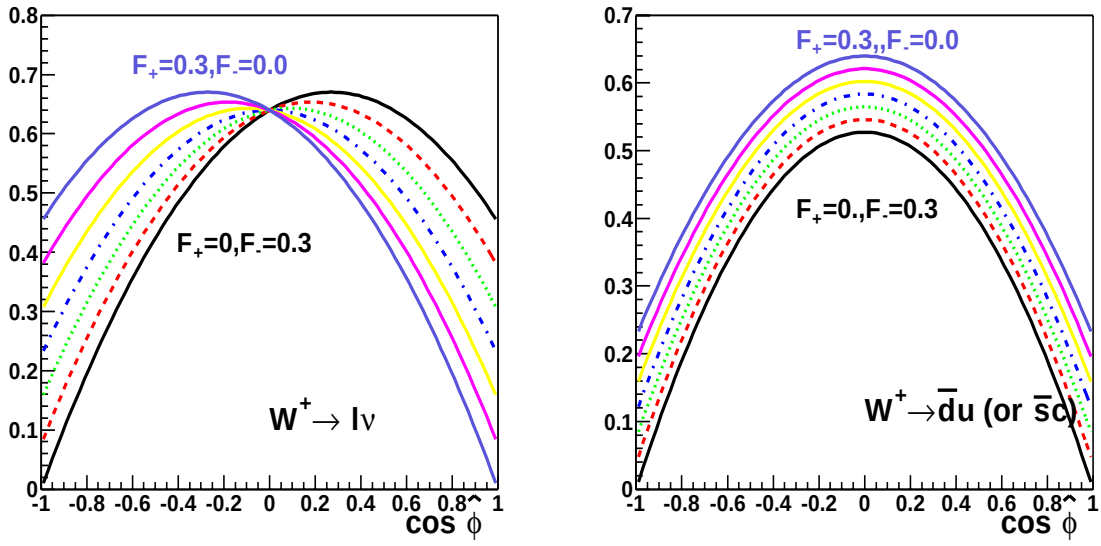

Figure 1.6: Arbitrarily normalized angular distributions $w(\cos\hat{\phi}_l)$ for different contributions from F_+. The contribution from the longitudinal angular distribution is fixed to F_0=0.70, as well as $F_- + F_+$=0.30.

Chapter 2

The Experiment

Due to its large mass, direct $t\bar{t}$ production requires collisions of high-energy particles. The TeVatron located at Fermilab has sufficient energy to produce top quarks in $p\overline{p}$ interactions. There are two collision points in the TeVatron ring where data can be collected, one is used by DØ and the other by the CDF experiment [24, 35]. This analysis is based on data from the DØ experiment, obtained during "Run I" (1992 to 1996), where the collision center-of-mass energy was 1.8 TeV. Another run (Run II) is currently in progress, where the collision center-of-mass energy is 1.96 TeV, with an upgraded accelerator and improved detectors. In this chapter, we describe the configuration of the accelerator and the DØ detector during Run I, and provide a summary of the reconstruction and particle-identification codes used during Run I at DØ.

2.1 The Accelerator and the Beam

The acceleration of protons and antiprotons to a final energy of 0.9 TeV is done in seven stages. The final configuration consists of six bunches of protons and six bunches of antiprotons colliding with a maximum beam energy of 0.9 TeV each. Figure 2.1 shows an overview of the Fermilab accelerator complex. The elements of which are [36]:

- *Cockroft-Walton.* This is an electrostatic generator that accelerates H^- ions through successive potential differences to a final energy of 750 keV.

- *Linac.* This is a 150 m long linear accelerator that uses RF cavities to provide an alternating electric field, where the H^- ions are timed with the accelerating part of the field, to bring the H^- ions up to an energy of 400 MeV. At the end of the

acceleration, the electrons are stripped off the H^- ions by passing the H^- through a carbon foil, thereby leaving bare protons.

- *Booster.* This is a standard synchrotron, where the protons circulate through a circular vacuum chamber in a tunnel filled with bending magnets. The acceleration is achieved using RF cavities located in the tunnel. The frequency of the accelerating potential and the strength of the magnetic field are increased as the proton energy increases to a final energy of 8 GeV.

- *Main Ring.* This is also a synchrotron with a radius of $\approx$1 km, and it shares the accelerator tunnel with the TeVatron. Protons are accelerated up to 120 GeV to produce antiprotons, by colliding protons with a nickel target. The original ring was modified to accommodate the collision points for DØ and CDF, when the Main Ring became the pre-accelerator for the TeVatron.

- *Debuncher.* The effective yield of antiprotons is about 10^{-5} per incident proton. After their production, the antiprotons must be "cooled", that is their transverse momentum decreased to keep the $\overline{p}$ beam from flying apart. The Debuncher changes the RF-bunched antiprotons to a continuous band that has a small spread in momentum. After this stage, follows the process of stochastic cooling. This lowers the momentum spread of the beam by measuring and then correcting the trajectory of the beam to the desired orbit. The antiprotons are kept in the Debuncher until the next bunch of antiprotons arrives, that is for $\approx$ 2.4 s.

- *Accumulator.* The antiprotons are kept in this storage ring for several hours, that is, until there are about 10^{12} accumulated antiprotons. This storage ring also uses stochastic cooling to produce a dense core of antiprotons near the inner radius of the Accumulator. This 8 GeV beam is subsequently injected backwards to the Main Ring, accelerated to 150 GeV, and injected into the TeVatron.

- *TeVatron.* This is also a synchrotron, but uses superconducting magnets in order to reach high energy. It receives protons and antiprotons in bunches. Protons and antiprotons circulate in opposite directions, and are accelerated from 150 to 900 GeV, providing a 1.8 TeV center-of-mass energy at the interaction points of DØ and CDF. For most of the circumference, the protons and antiprotons

Table 2.1: Run I TeVatron parameters.

Accelerator radius	1000 m
Maximum beam energy	900 GeV
Injection energy	150 GeV
Peak luminosity	10^{31} cm^{-2}s^{-}1
Number of bunches	$6p$,$6\overline{p}$
Intensity per bunch	$\approx$100 $\times 10^9 p$, $\approx$50 $\times$ $10^9 \overline{p}$
Crossing angle	0
Bunch length	50 cm
Traverse beam radius	43 μm
Energy spread	0.15×10^{-3}
RF frequency	53 MHz
$\overline{p}$ stacking rate	$\approx 3.5 \times 10^{10}$/hour
Beam crossing frequency	290 kHz
Period between crossings	3.5 μsec

are kept apart with special electrostatic separators. At the collision points, the TeVatron contains special focusing magnets to reduce the beam sizes to about 50 μm. Table 2.1 shows several important TeVatron parameters. The number of bunches determine the collision frequency of 3.5 μsec. The setup of a $p\overline{p}$ "store" takes about 2-3 hours, and the stores last for about 15 hours, after which the beams are aborted on a special beam dump, and the cycle repeated. Because of the low yield of antiprotons, the Main Ring is used to produce $\overline{p}$ during most of the time that collisions are taking place within the TeVatron.

2.2 The DØ detector

DØ is a multi-purpose detector that was designed to identify electrons, muons, jets and neutrinos [24]. It was optimized for physics at large transverse momenta (p_T) and high-mass states. The detector weighs approximately 5,500 tons, and has dimensions of about $13 \times 11 \times 17$ m^3. The original detector was used between 1992 and 1996, with data in this analysis accumulated in 1994-1996 (Run IB and Run IC). Run II of the TeVatron started on March, 2001, with an upgraded DØ detector. Some of the systems described in these chapter are no longer in use, and have been replaced with newer technology [37].

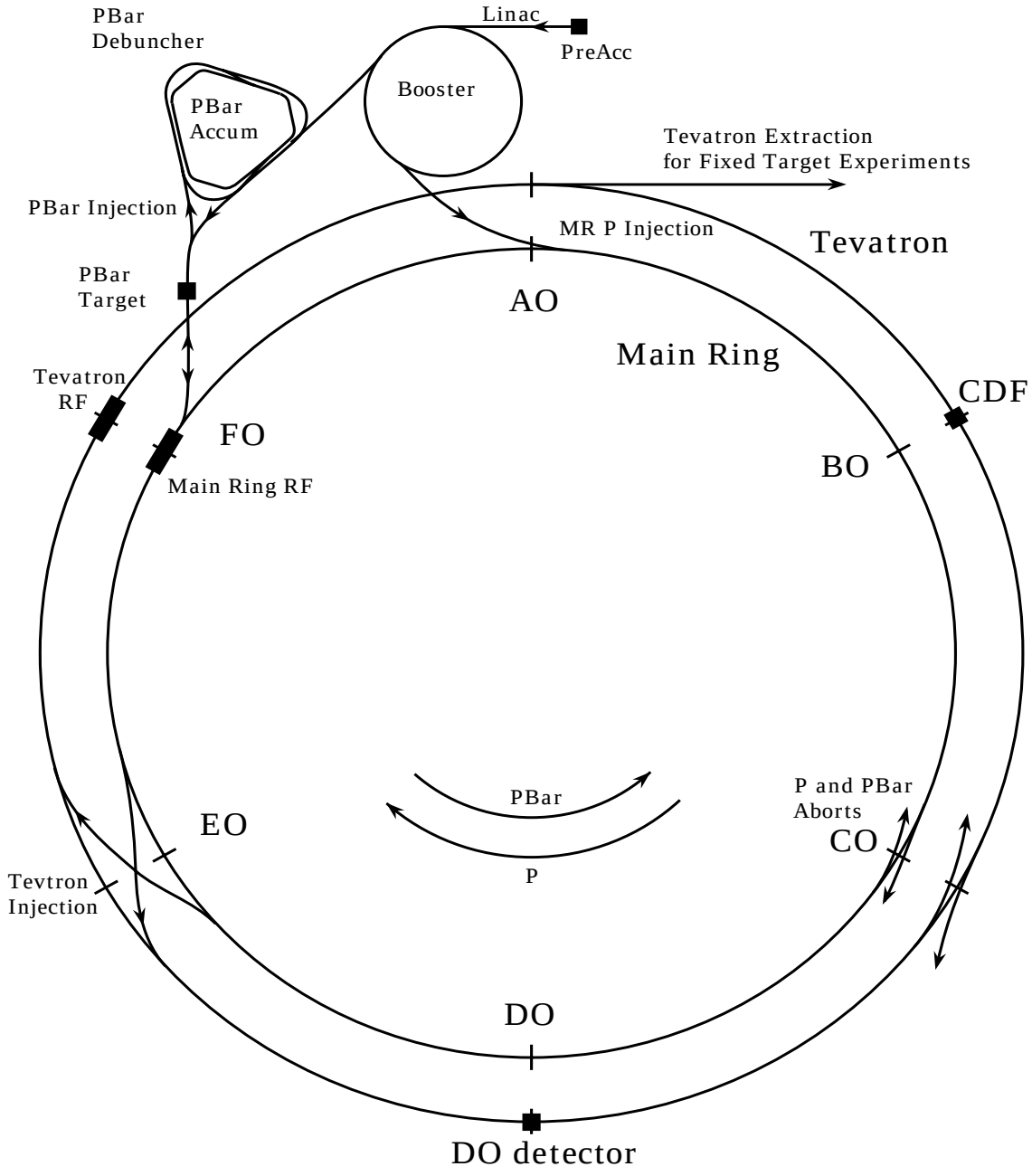

Figure 2.1: An overview of the Fermilab accelerator complex.

The Run I detector contained three major systems: tracking chambers, calorimeter, and a muon system, all concentric with the beam line. This configuration reflects the interactions of particles with matter. The tracking detectors are designed to measure the trajectories of charged particles. These detectors contain as little material as possible so as to minimize multiple scattering and energy loss before the calorimeter. In contrast, the calorimeter contains sufficient material required to absorb the energy of any incident particle. Muons, unlike electrons and jets, do not interact substantially in the detector, and because of their long lifetime can be identified using tracking chambers outside of the calorimeter. Neutrinos are not detected, and their presence is inferred from an imbalance in momentum perpendicular to the beam axis. Figure 2.2 shows an overview of the DØ detector. The beam pipe of the Main Ring is seen to pass through the upper part of the calorimeter. The detector stands on a support platform that is mounted on rollers, to allow the detector be rolled from the assembly building to the collision hall. The platform also houses some minimal detector electronics. Most of the electronic analog signals are routed from the platform in the collision hall to the Moving Counting House (MCH), a structure that contains all the digitization electronics, the Level-1 high-voltage supplies for the trigger, and other services. This structure moves with the detector. In this way, the cables are kept short to maximize signal relative to noise. The data is taken from the MCH to the Fixed Counting House (FCH) that is located on the second floor of the assembly building. For defining positions of objects inside the detector, the DØ collaboration uses a standard right-handed coordinate system, the origin is at the center of the detector, the positive z-axis along the proton direction, and the y-axis upward. Cylindrical coordinates are also used frequently, where r is the distance from the beam line, ϕ the azimuthal angle with respect to the positive x-axis, and θ the polar angle with respect of the z-axis. The polar direction is sometimes replaced by the pseudorapidity (η), defined as η=–ln tan(θ/2). It is convenient to use (η,ϕ) coordinates because for massless particles, η is the same as the Lorentz invariant rapidity $y = \frac{1}{2}\ln((E + p_z)/(E - p_z))$.

2.2.1 Central Tracker

The central detectors are designed to measure the trajectories of charged particles, determine position of interaction vertexes, and to distinguish between ionization for a singly charged particle and two electrons from photon conversion ($\gamma \rightarrow e^+e^-$) in the detector.

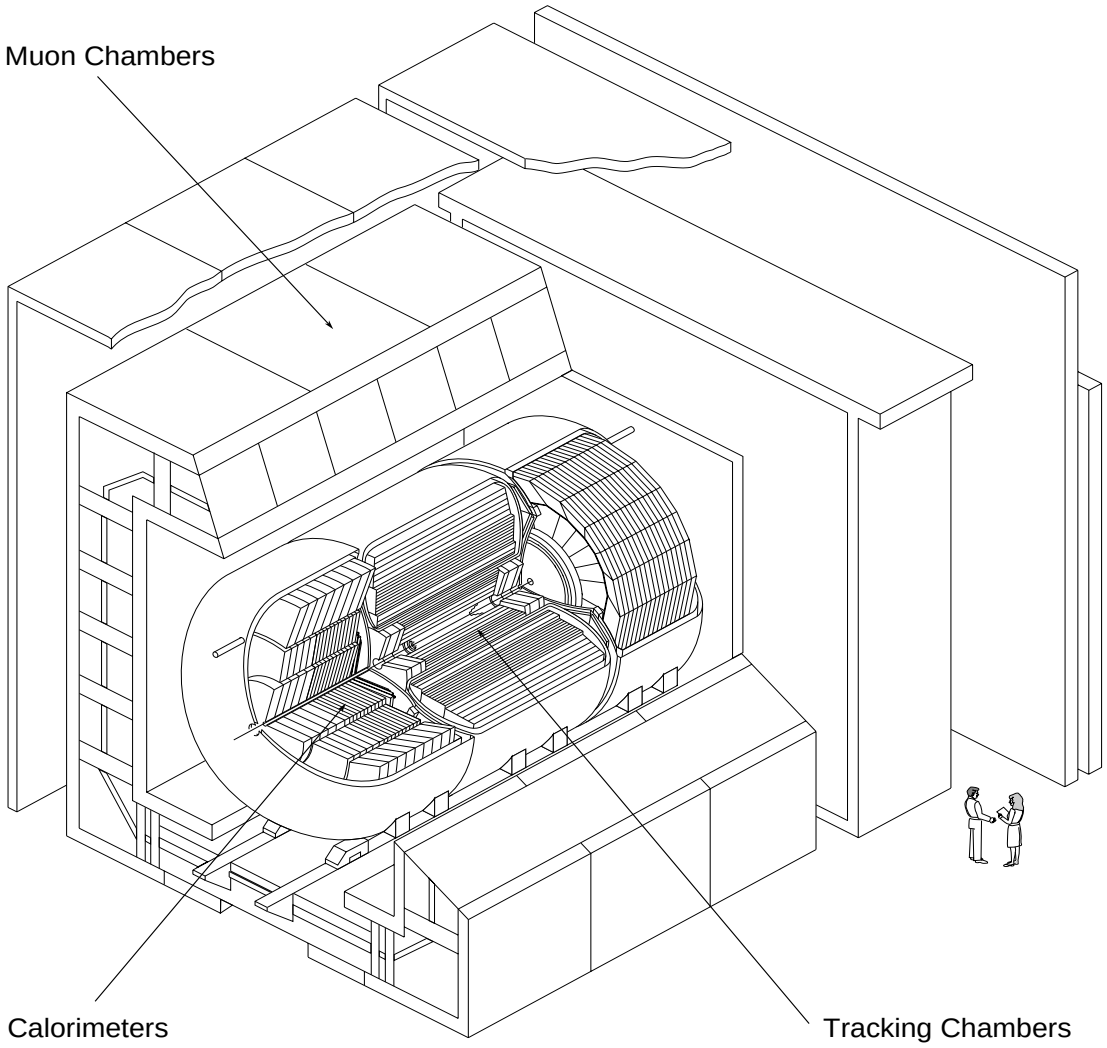

Figure 2.2: An overview of the DØ detector.

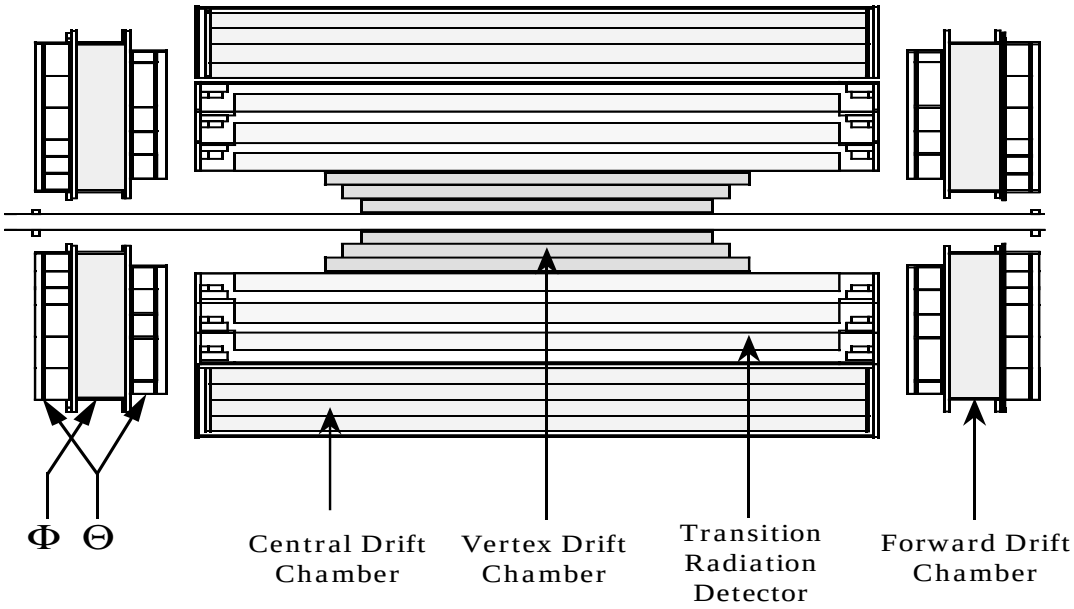

Figure 2.3: Side view of the DØ central tracking detector.

Precise position measurements are also used to cross-check measurement of position in the calorimeter and the momentum in the muon system. The central detector contains no magnetic field, hence there is no momentum information at this stage. The central tracker is composed of a set of drift chambers and a transition-radiation detector [24].

Vertex Drift Chamber (VTX)

The VTX drift chamber is the innermost of the tracking chambers [38]. It is designed to measure the interaction vertex along the z direction. The VTX consists of three layers of sense wires. It occupies the region $3.7 < r < 16.2$ cm. The chamber is filled with a mixture of carbon dioxide (CO_2, 94.5%), ethone (C_2H_6, 5%), and 0.5% of water (H_2O). The sense wires are parallel to the beam line and operate at an electric potential of 2.5 keV. The first layer has 16 cells of sense wires and an active length of 97 cm. The successive layers contain 32 cells, with active lengths of about 10 cm more than previous layers. Each of these cells contains 8 wires along the radial direction to determine the ϕ coordinate of each hit. Adjacent wires are staggered by 100 μm to avoid dead regions and also to help resolve left-right ambiguities.

The $r\phi$ position of a charged particle is determined by drift time, or the time difference between the $p\overline{p}$ collision and the arrival of the ionization electrons at the wire. A

charge division technique is used to find the position along z. The spatial resolution of the VTX is about 60 μm in $r\delta\phi$ and 1.5 cm in z. For further details on drift chamber principles and implementation, see [39, 40]

Transition Radiation Detector (TRD)

The TRD is located between the VTX and the CDC (17.5 $< r <$40.9 cm) [41]. The purpose of the TRD is to provide electron identification, in addition to that from the calorimeter. The TRD operates on the principle that when highly relativistic charged particles of large γ ($\gamma > 10^3$, where $\gamma = E/(mc^2)$) cross boundaries between two materials of different dielectric constant (foil and gas for the TRD), they radiate X-rays in the forward direction. The intensity of the radiation is proportional to γ and is concentrated on a cone with a half opening angle of $\approx 1/\gamma$ about the particle's trajectory. Electrons and positrons are the lightest charged particles, and since the amount of transition radiation depends inversely on a particle's mass, electrons emit far more radiation than pions of same energy. Transition radiation can therefore be used to distinguish electrons from heavier particles. In fact, the TRD provides an additional factor of 50 rejection for isolated charged pions relative to what can be obtained from calorimetry, and this at a loss of only $\approx$ 10 % of the isolated electrons [42].

The TRD consists of three 10.5 cm thick cylinders. Each cylinder contains 393 layers of 18 μm thick polypropylene foils used as radiator. These layers have a mean separation of 150 μm and they produce a transition radiation spectrum that peaks at 8 keV (X-rays). The gaps are filled with dry nitrogen (N_2). The radiators and the nitrogen are sealed by a Mylar window. A drift-wire chamber, filled with a mixture of Xenon (Xe), methane (CH_4), and ethane gas (91%:7%:2%), is located downstream of each set of foils. Each drift chamber is approximately 8 mm $\times$ 8 mm, with wires oriented parallel to the z axis, providing a radial drift field. X rays ionize the Xe atoms, and the resultant charge provides a measure of the X-ray energy.

Central Drift Chamber (CDC)

The central drift chamber (CDC) is the outermost tracker in the central region [43], and is located between the TRD and the calorimeter. It covers the pseudorapidity range of $|\eta| <$1.2. The CDC consists of four layers of cells in the region 49.5$< r <$74.5 cm, and has a length of 184 cm. It is constructed from 32 identical azimuthal modules, contained

within an aluminum tube, with a carbon fiber sealing the inner radius. Each cell has 7 sense wires, staggered by 200 μm relative to each other in order to resolve left-right ambiguities. There are two field-shaping wires between each pair of sense wires. The active medium in the CDC is a gas mixture of argon (Ar), methane, carbon dioxide, and water (92.5%:4%:3%:0.5%). As for the VTX, the $r\phi$ position of a hit is determined via the drift time and the hit wire. The z position is measured by comparing the arrival times of the pulse at the two ends of the wire.

The z position of the vertex in the CDC is reconstructed by pointing the tracks from the CDC to the beam line. Signals propagate at 2.4 μm/ns along the wires, so that reading out the delay lines at both ends provides a measurement of interaction vertex along z with a resolution of about 4 mm.

Through matching tracks to clusters of energy deposited in the calorimeter, the CDC can be utilized in the identification of photons, electrons, and hadronic jets. Similarly, the CDC helps in identifying muons observed in the outer muon detector.

Forward Drift Chamber (FDC)

The FDC extends the coverage of the outer tracker to $|\eta| \approx 3.2$ [44]. Two sets of FDC chambers are installed at each end of the CDC and VTX, oriented with their axes parallel to the beam direction. The construction and operation of these chambers are similar to those of the CDC, and the gas used is identical. Figure 2.4 is a diagram of one of the FDCs. Each set of FDCs consists of three chambers: one Θ chamber between two Φ chambers. The Φ chamber has radial sense wires to determine the azimuthal coordinate (ϕ) of each hit. The two Θ chambers are used to measure the polar angle (θ) of each hit. The Φ chamber contains 36 segments, each with 16 sense wires that are 50 cm long (in z). This chamber covers the full range of azimuth. The Θ chambers are made of four independent quadrants. Each of the quadrants contains six rectangular cells. Each of these cells contains 8 layers of sense wires as well as one delay line. To reduce ambiguities, the two Θ chambers on each side of the two Φ chambers are rotated in ϕ by $\pi/4$ relative to each other.

Central Detector Electronics

The readout electronics for the VTX, TRD, CDC, and FDC are quite similar [45]. There are three stages of signal processing. First, the signals are read out with preamplifiers

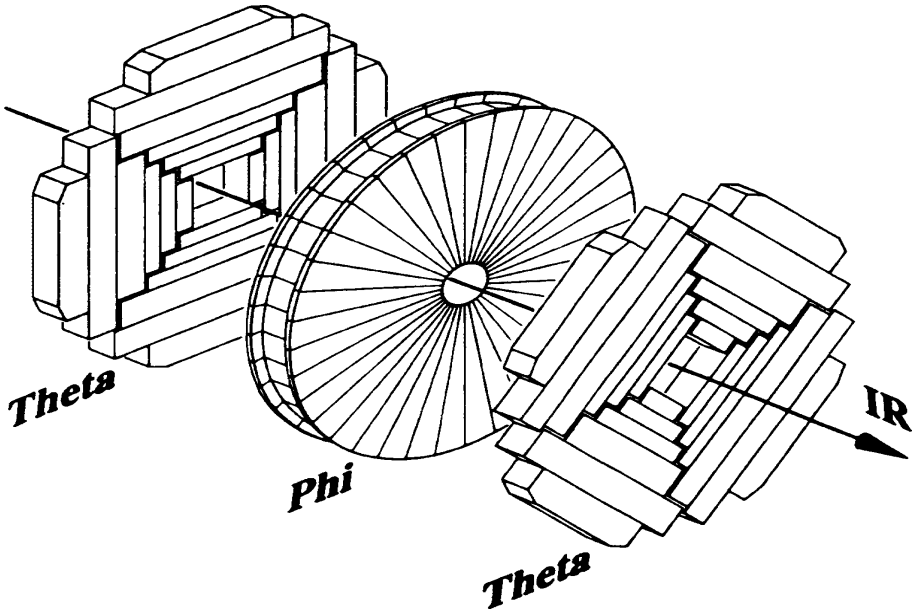

Figure 2.4: Exploded view showing the orientation of the Forward Drift Chambers.

mounted on the surfaces of the detectors. Second, these pre-amplified signals are carried about 15 m on coaxial cable to the platform beneath the detector where analog pulse-shaping cards remove the long tail of the signals. Finally, signals are digitized with Flash-Analog-To-Digital converters (FADCs). These are located in the Moving Counting House, where the signals are sampled and digitized at the rate of 106 MHz. Since there are 6,080 instrumented channels in the central tracking detector, reading out every channel in every event would saturate the data acquisition system. Thus, if an event is not accepted by Level-1 of the trigger, the data are overwritten at the next beam crossing. However, if the event is accepted by the Level-1 trigger, the data are compressed by comparing the signal to pulses adjacent in time, a process known as $zero-suppression$, and sent on to Level-2 of the trigger.

2.2.2 The Calorimeter

After passing through the central detector, all particles except for muons and neutrinos lose essentially all their energy through radiation and collisions in the calorimeter. The DØ calorimeter was designed to identify electrons, photons, and jets, and to determine the degree of balance in transverse momentum ($P_T \approx E_T = E\sin\theta$) in any event [24].

Due to the absence of a central magnetic field, it was very important to have this detector achieve good resolution.

Electrons, photons, and hadrons lose energy in material through different mechanisms. High-energy electrons (>>10 MeV) lose energy primarily through bremsstrahlung, while high-energy photons lose energy primarily through electron-positron production. The particles produced in these processes can produce new photons or electron-positron pairs, creating an *electromagnetic shower*. The rate of energy loss for electrons can be described by:

$$\frac{dE}{E} = -\frac{dx}{X_0}, \tag{2.1}$$

where X_0 is called the *radiation length* of the material, which is the thickness required for an electron to lose all but 1/e of its initial energy. After an incident photon converts to an e^-e^+ pair, the subsequent shower development can also be characterized by Eq. 2.1.

Hadronic particles also produce showers in material, but they lose energy primarily through inelastic collisions with the atomic nuclei. These collisions produce more hadrons that can interact again, etc., thereby creating a *hadronic shower*. The energy loss can be also characterized by Eq. 2.1, but with X_0 replaced by the *nuclear interaction length* (λ). Nuclear interactions lengths in high-Z material are far larger than X_0, and hadrons therefore travel greater distances in calorimeters before losing their energy.

DØ uses a "sampling" calorimeter to measure the energies of electromagnetic and hadronic showers. A sampling calorimeter alternates layers of dense, inert, absorber material, with layers of active medium that are sensitive to energy deposited in the medium. Depleted uranium (^{238}U) is the main absorbing material, and liquid argon (LAr) is the active material in DØ calorimeters. Most of the energy is absorbed in the inert material, and only a portion of the incident energy is detected. This fraction is called the *sampling fraction*.

Hadronic showers contain a large fraction of electrons and photons since hadrons can produce electrons and photons when interacting with nuclei, and because π^0 and η mesons are produced in hadronic collisions, and decay to two photons. Such photons produce local secondary electromagnetic showers. About 30% of the incident energy in

a hadronic shower is lost to the breakup of nuclei, nuclear excitation, and to producing low-energy evaporation neutrons and protons, all of which do not provide detectable signals. The calorimeter response to hadrons will therefore tend to be smaller than to electromagnetically interacting objects. This is quantified by the e/π *ratio*, the relation between the calorimeter response to electrons and pions. It is desirable to produce equal response to electron and pion, or e/π=1. If this ratio is not close to unity, then the measured shower energy will have a strong dependence on the ratio of charged to neutral pions in the shower, leading to a degradation in overall energy resolution. A calorimeter with $e/\pi \approx 1$ is called a *compensating* calorimeter. The DØ calorimeter achieved e/π ratio close to 1, and is nearly compensating. There are a large number of effects that can degrade resolution. The resolution of a calorimeter is limited by the statistical nature of the energy loss processes in matter, and scales as $\frac{1}{\sqrt{N_{ion}}}$, where N_{ion} is the number of liberated ionization electrons. Since N_{ion} is proportional to the total incident energy of the particle, one expects the resolution to scale approximately as $\frac{1}{\sqrt{E}}$. In-depth discussions of calorimetry in high-energy physics can be found in Ref. [46].

Design of the Calorimeter

The DØ calorimeter uses liquid argon as the active medium [24]. Therefore, a cryostat and a cooling system had to be used to contain the argon. The calorimeter consists of one central calorimeter (CC) covering $|\eta|$ <1.2, two End Calorimeters (EC) extending the coverage to $|\eta|$ ≈4, and the Inter-Cryostat Detector (ICD), covering the region between CC and EC modules. Figure 2.5 shows a cut-away of the calorimeter in the DØ detector.

The DØ calorimeter is segmented finely in the transverse and longitudinal directions. The CC and EC regions are subdivided into electromagnetic and hadronic zones (electromagnetic particles and hadronic particles produce showers of different size). The radiation length in uranium is $X_0 \approx 3.2$ mm. To assure containment of photons and electrons, the electromagnetic region of the calorimeter has (at η=0) a uranium thickness of 65.6 mm ($20.5X_0$). The nuclear interaction length for nucleons in uranium is ≈ 10.5 cm. At η=0, the hadronic region consists of 33.6 cm (3.2 λ) of uranium in the "Fine Hadronic" (FH) region, and 46.5 mm (3.2 λ) of copper in the "Coarse Hadronic" (CH) region.

The calorimeter is constructed from separate modules of readout cells. Each cell consists of alternating absorber plates and signal readout boards, as sketched in Fig.

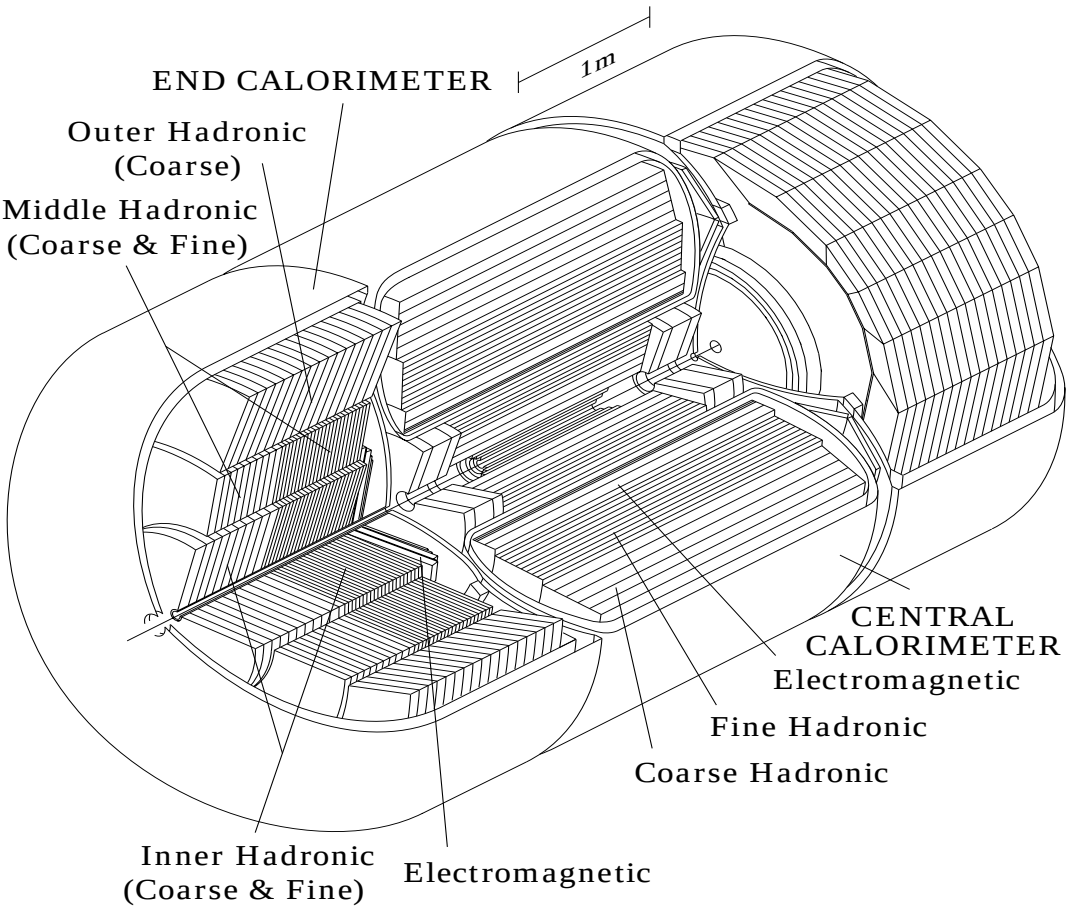

Figure 2.5: Elements of the DØ calorimetry.

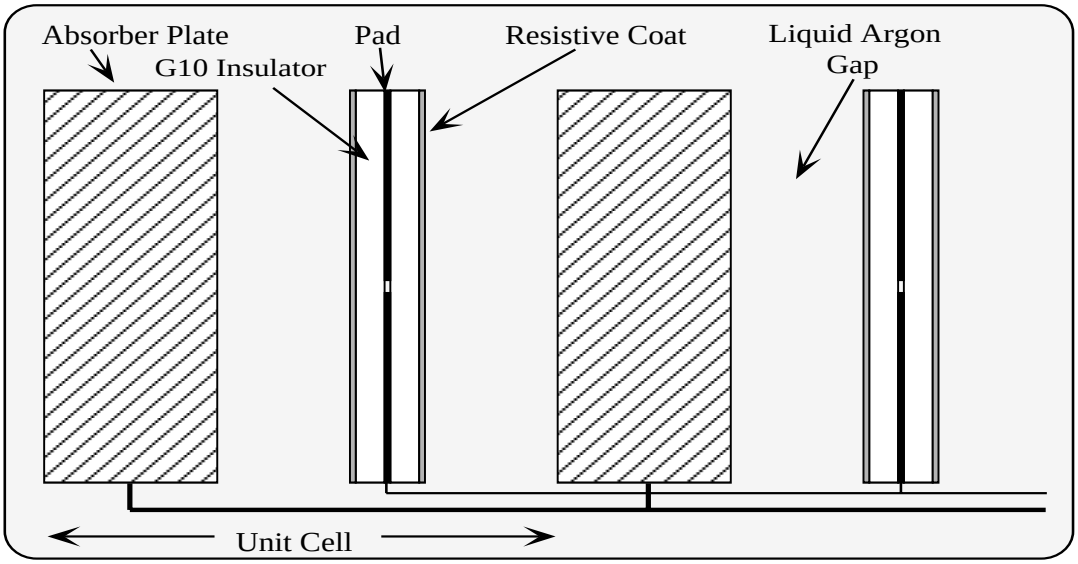

Figure 2.6: Two unit cells of the DØ calorimeter.

2.6. The absorber uranium plates are separated from signal boards by 2.3 mm gaps of liquid argon. The signal boards consist of copper pads with 0.5 mm thick G10 sheets laminated on each side, whose outer surfaces are coated with highly resistive epoxy. The outer surfaces of the pads are held at high voltage (approximatedly 2.5 keV), and act as anodes. When an incoming particle hits the absorber plate, it showers into many particles, ionizing the liquid argon. The signal boards pick up the image charge of the drifted electrons.

The DØ calorimeter contains $\approx$ 47,000 readout channels. Each signal from a cell has a pulse widths of 450 ns, reflecting the electron drift time. There are three steps to the readout. First, the signals are preamplified on top of the cryostats. Then the preamplified signals are transported to baseline-substractor (BLS) modules located on the platform underneath the detector. The BLS modules perform analog signal shaping, then split the signal into two. After summing the signals into 0.2×0.2 $\eta\phi$ trigger towers (or "large tiles"), one part of the signal is used as input to the Level-1 trigger. The other part of the signal is used for readout: it is sampled just before the beam crossing and 2.2 μs later. The difference between the two samples is a dc voltage proportional to the collected charge. Finally, if the event is accepted by the Level-1 trigger, this difference is sent to ADCs that digitize, then zero-suppress the information, before sending it on

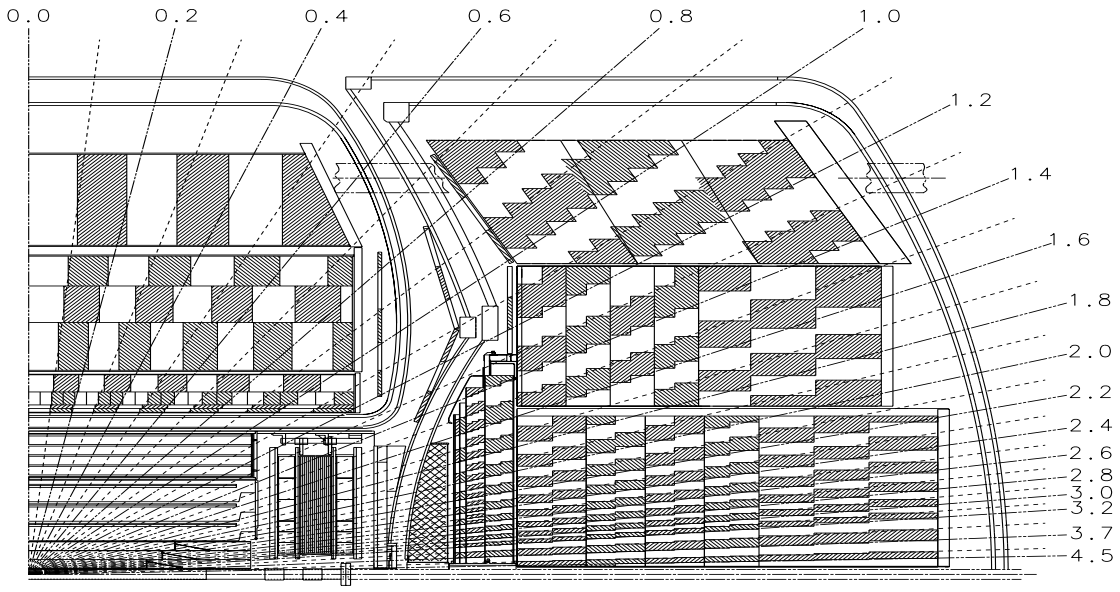

Figure 2.7: A side view of one quarter of the DØ calorimeters and the central tracking detectors. The numbers refer to values of η relative to the center of the collision region.

to the Level-2 trigger.

The ICD is used to compensate for the energy loss in the region between CC and EC. The ICD consists of two arrays of 384 scintillation counter tiles mounted on the front surface of each EC cryostat.

The structure of the readout layers is pseudoprojective, as can be seen in Fig 2.7. The centers of calorimeter cells lie on lines of constant pseudorapidity, while module boundaries are perpendicular to the absorber plates.

Calorimeter Readout and Performance

The energy resolutions of electrons and pions were measured in test beams [47]. They are:

$$\frac{\delta E}{E}|_e = \frac{15\%}{\sqrt{E(GeV)}} + 0.003 \tag{2.2}$$

$$\frac{\delta E}{E}|_{\pi^+} = \frac{41\%}{\sqrt{E(GeV)}} + 0.03 \tag{2.3}$$

where the symbol + means addition in quadrature.

The energy resolution for hadronic jets was determined from studies based on balancing jet energies in dijet events [47]. The result is:

$$\frac{\delta E}{E}|_{jet} \approx \frac{80\%}{\sqrt{E(GeV)}} \tag{2.4}$$

2.2.3 Muon System

Muons have mean lives of 2.2 μs. And since they do not interact strongly, and have relatively large mass ($\approx$200m$_e$), they do not radiate. High-energy muons deposit only a small amount of energy in material (mainly via ionization), and tend to pass through the calorimeter without being absorbed. Muons are therefore detected and measured in the outermost part of the DØ detector, the muon system [48]. This system consists of five magnetized iron toroids, with a field strength of approximately 2 Tesla, interspersed with several layers of proportional drift tubes (PDTs). These PDTs are used to measure the momentum of the muons by measuring their trajectories before and after they pass through the magnetized iron. The toroids and associated PDT layers are shown in Fig. 2.8.

The muon system is divided into two spectrometers: the wide angle muon spectrometer (WAMUS) and the small angle muon spectrometer (SAMUS). The WAMUS chambers are formed from three layers of PDTs, the A layer mounted between the calorimeter and the toroid, and the B and C layers after the toroid. Each plane in the A layer contains four PDTs. These determine the incident direction of a muon to 0.6 $m$rad, and its position to 100 μm. The B and C chambers consists of three PDTs each. They determine an outgoing muon direction to 0.2 $m$rad, and its position to 170 μm.

The WAMUS has three subsections: the Central Iron (CF), covering range $|\eta|$ <1, and the two End Irons (EF), covering the range 1< $|\eta|$ <2.5. Except for two gaps underneath the detector, required for supporting structures of the calorimeter, the CF has nearly full coverage in ϕ. The SAMUS relies on two magnets, but the high background rates in this forward region prevented its use in this analysis.

The observed muon momentum resolution for WAMUS can be parameterized as:

$$\delta(1/p) = 0.18(p - 2.0)/p^2 + 0.003, \tag{2.5}$$

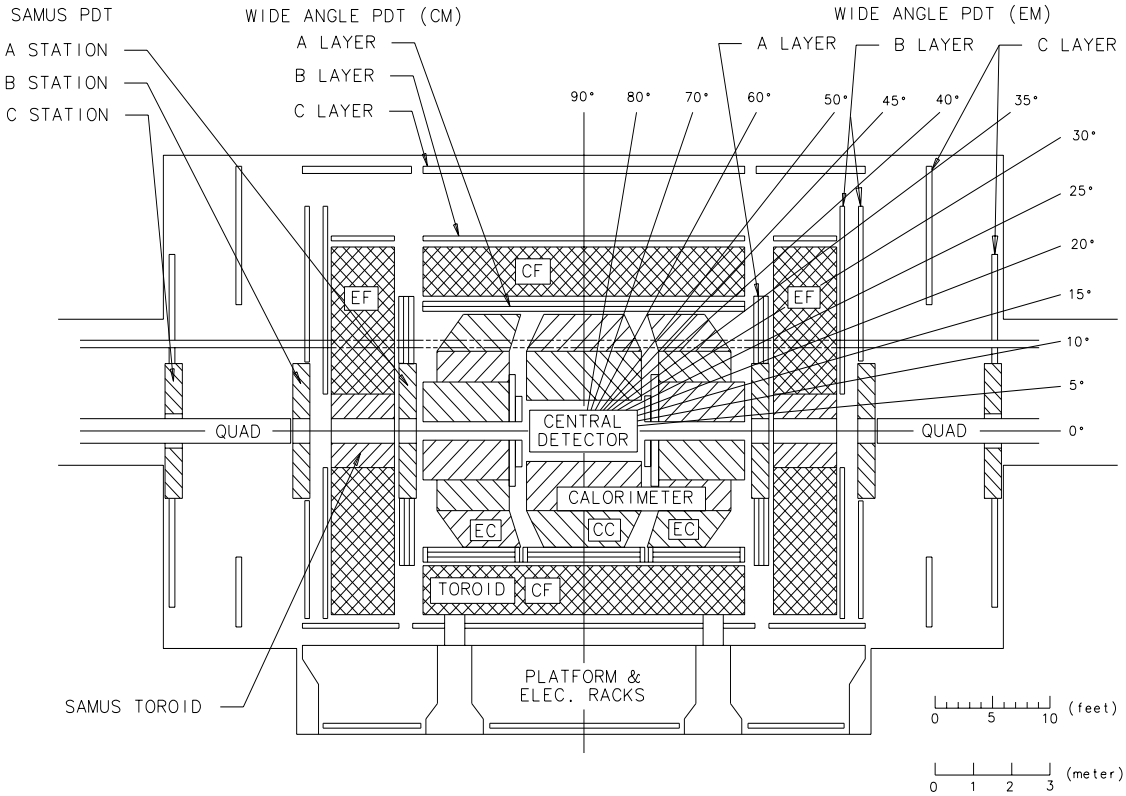

Figure 2.8: Muon system.

for muons with momentum p >4.0 GeV/c. (Muons with p <4.0 GeV/c cannot penetrate beyond the material of the calorimeter even near $|\eta| \approx 0$.)

2.2.4 Trigger

During Run I, the TeVatron operated with 3.5 μs interval between bunch crossings, that is, at a data rate of about 286 kHz ($\approx$ 1/3.5 μs). For a typical luminosity of 5×10^{30} events/cm^2-s, nearly all of these crossings produce at least one $p\overline{p}$ collision. Because most of the processes of interest have rather small cross sections compared to the total inelastic $p\overline{p}$ cross section of 50 mb at $\sqrt{s}$=1.8 TeV, it is impractical, nor of any interest, to save all the information about each crossing. A real-time event-processing system is therefore needed to decide which events are sufficiently interesting to be preserved for

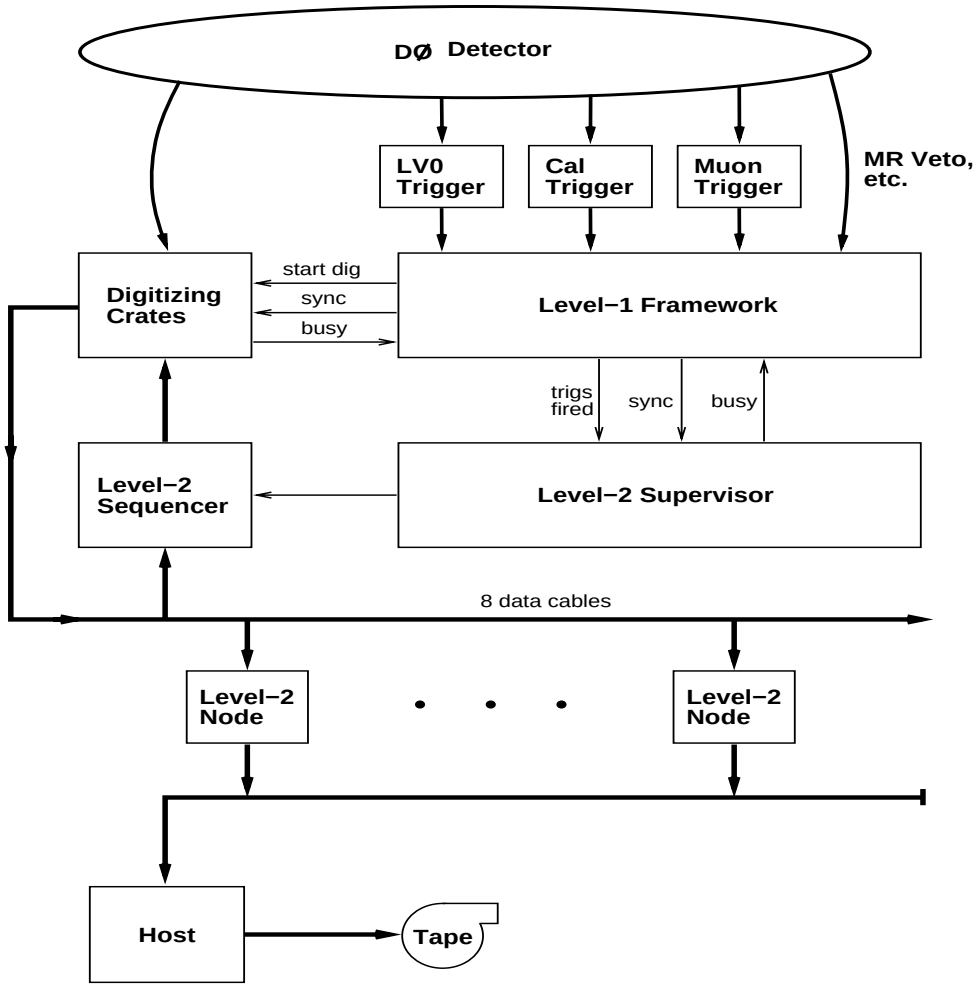

Figure 2.9: The DØ data acquisition system.

offline analysis.

A schematic overview of the DØ trigger system is shown in Fig 2.9. It involves three levels of decision-making. Each level provides more precise characterization of the nature of any event.

Level 0

The Level-0 trigger uses a set of scintillator counters, located in front of each EC, to indicate the presence of an inelastic collision [49]. Using the two sets of counters in coincidence, it distinguishes between accepted inelastic beam-beam ($p\overline{p}$) and rejected elastic or singly-difractive, or beam-gas, collisions. It reduces the initial 286 kHz rate

down to about 150-200 kHz.

Level 1

The Level-1 triggering system uses information from the calorimeter and muon system to determine in less than 3.5 μs if an event meets certain criteria on energy deposition and topological requirements, before the event is passed for further scrutiny in the next trigger stage (Level 2). The system consists of fast and programmable digital signal processors (DSPs), with decisions based on calorimeter trigger towers of $\Delta\eta \times \Delta\phi$=0.2×0.2. Depending on the kind of physical object, Level-1 sets certain criteria that an event must pass to be accepted. Electrons must have a transverse energy in the EM sections of a trigger tower above some programmable thresholds. Jets must have the sum of transverse energy in the EM and FH sections of a trigger tower also above a programmed thresholds. The rate out of Level 1 is roughly 800 Hz. For more details see Ref. [50].

Level 1.5

The Level 1.5 triggering system is also based on DSPs. It improves the measurement of E_T by performing a fast clustering of electromagnetic calorimeter-tower energies. It also selects purer electron candidates by using variables such as the EM fraction in a cluster, and EM isolation. The rate out of Level 1.5 is 200 Hz.

Level 2

Unlike the other levels, the Level-2 trigger is software based [51]. It reconstructs events using a simplified and fast version of the reconstruction program. If an event passes the Level-2 trigger, it is then written to magnetic tape for offline reconstruction. The rate out of Level-2 is approximately 2 Hz. The limiting factor of this rate is the speed of recording. The Level-2 trigger system reconstructs and identifies specific objects such as electrons, photons, jets, muons, and $\not\!\!E_T$(imbalance in transverse momentum or "missing-E_T"). The system uses a large farm of DEC VAX nodes that runs software filters. These software filters usually require an event to have a certain number of objects above some given E_T thresholds, contained within specific regions of the detector.

2.3 Event Reconstruction

The data written to tape consist of pulse heights, temporal widths, and arrival times of signals that must be translated into physical events. This translation involves the reconstruction program. The software package that is responsible for converting the detector data into physical objects is called DØRECO. The offline reconstruction is performed on a farm of up to 96 SCI and IBM nodes. Data is stored in ZEBRA format. The output of DØRECO consists of energies and directions of electrons, muons, photons, jets, and $\not\!\!E_T$. In the following sections we described the DØRECO program along with the techniques used for classifying physical objects.

2.3.1 The DØRECO Program

The reconstruction process can be divided into three major phases:

- *Hit finding*, where the collider data is unpacked and converted into "hits". In this step, signals from sense wires of the tracking chambers are converted into spatial location of hits, and signals from each calorimeter cell are converted into energy depositions.

- *Tracking and clustering*, during which the tracking chamber hits are joined together to produce tracks, while the calorimeter cells are grouped into clusters of energy.

- *Particle identification*, where the information coming from the tracking and calorimeter is combined to produce objects that are candidates for being jets, electrons, and muons.

The criteria used by the reconstruction program to identify physical objects are quite generous, and substantial rejection of spurious electrons and muons is gained by further off-line processing.

2.3.2 Particle Identification

Electrons

The first step in the reconstruction of electrons and photons is to form clusters of energy using electromagnetic towers. These clusters are defined using a "nearest neighbor algorithm" [52]. That is, starting with the highest-E_T tower, all neighboring towers with E_T above 50 MeV are added to the cluster, and the process repeats until no towers neighboring the cluster satisfy the energy requirement. The process is repeated with the highest-E_T tower not previously assigned to a cluster.

Any cluster in the calorimeter is required to have more than 90% of its energy in the electromagnetic layers (and more than 40% in a single tower). A cluster that passes these requirements is identified by the reconstruction program as an electron or photon candidate. This alone removes most hadronic clusters, while retaining more than 99% of true electrons and photons. Since photons do not leave tracks, electron candidates are distinguished from the photon candidates by the presence of CDC or FDC tracks within a road size of $\delta\eta \times \delta\phi$=0.1×0.1 pointing from the primary vertex to the cluster.

There are two primary background processes that can mimic an electron: one is π^0 decay to two photons, producing an electromagnetic cluster, with a track provided by the random overlap of a low-energy charged hadron. The other is photon conversion to e^+e^- pairs early in the tracking system. Since there is no magnetic field in the tracking region, the electron and positron continue on nearly the same trajectory and may be misidentified as a single track. In order to suppress these backgrounds, while retaining high efficiency for identifying true electrons, information from the calorimeter and the tracking system is combined. The selection criteria used in forming electron candidates are quite generous, and depending on the analysis, users apply their own more austere selections. There are many variables for recognizing electrons, those used in this analysis are:

- The first quantity considered is the *isolation* of the electromagnetic cluster. This is defined by comparing the electromagnetic energy within a cone of radius $\sqrt{(\delta\phi)^2 + (\delta\eta)^2}$=0.2 centered on the cluster ($EM(0.2)$) to the total energy contained within a concentric cone of radius 0.4 ($EM(0.4)$). The isolation fraction is

defined as:

$$f_{iso} = \frac{E(0.4) - EM(0.2)}{EM(0.2)} \tag{2.6}$$

Our analysis requires F_{iso} <0.1. This retains 98% of the electrons, while significantly reducing the backgrounds from random track overlaps (and also from the semileptonic decay of b or c quarks).

- A detailed comparison between the shape of the cluster and that expected from an electromagnetic shower is characterized by a covariance matrix, $H - matrix$, derived from a sample of Monte Carlo electrons [53]:

$$M_{ij} = \frac{1}{N}\sum_{n=1}^{N}(x_i^n - \bar{x}_i)(x_j^n - \bar{x}_j) \tag{2.7}$$

where N is the total number of electrons in the sample, and the x_i are the variables that define the shape. A total of 41 variables is used. The matrix M is calculated individually for towers at different η, assuming symmetry in ϕ. In addition, reflection symmetry is assumed for positive and negative η regions of the detector, and so there are 37 distinct matrices.

Once M is calculated, the degree of agreement between an individual shower and that expected from an electron of that energy and η is defined by:

$$\chi^2 = \sum_{i,j=1}^{41}(x_i - \bar{x}_i)H_{ij}(x_j - \bar{x}_j) \tag{2.8}$$

where H is the inverse of M.

- The other variables used for electron identification are provided by the tracking system. The $track - match\ significance$ rejects random track overlaps, checking the consistency between the direction of the central track and the centroid of the shower. The significance of the track match for clusters in the CC(EC) is given by:

$$\sigma_{TRK}(CC(EC)) = \sqrt{(\frac{\Delta\phi}{\delta_{\Delta\phi}})^2 + (\frac{\Delta z(r)}{\delta_{\Delta z(r)}})^2} \tag{2.9}$$

where Δx are the differences in coordinate between the centroid of the cluster and

the point at which the trajectory extrapolates to the calorimeter, and $\delta_{\Delta x}$ is the resolution in the mismatch of the measurement. For this analysis, good electron candidates are defined as those with σ_{TRK} <5.

- Since DØ has no central magnetic field, the measured *track ionization* (dE/dx) is used to discriminate between prompt electrons and photon conversions. To reduce background from conversions, events with dE/dx >2 MIPs (minimum ionizing particle) are removed.

To further reduce background, the $t\bar{t} \rightarrow e$+jets analysis requires electrons with $E_T >$ 20 GeV and $|\eta^{det}|$ <2 (where *det* refers to η defined relative to the center of the detector). The final efficiency for identifying single acceptable isolated electrons with these selections is 72% in the CC and 43% in the EC, and is essentially independent of electron energy.

Electromagnetic Energy Calibration

The correction to absolute energy begins by correcting for the known differences between the test-beam and collider data. However, because of possible differences between the module used in the test-beam (never installed in the DØ detector) and the modules used at DØ, this calibration does not provide the correct mass of the Z boson in the $Z \rightarrow e^+e^-$ events. We therefore use the mass of the Z boson as a calibration point, since it is known very accurately from LEP experiments [11]. The measured electron energies are consequently scaled up so that the mass peak in $Z \rightarrow e^+e^-$ matches the LEP value. This correction is about 5% in the central calorimeter, and 1-2% in the end calorimeter.

Muons

In principle, muons are identified as tracks in the muon chamber that point back to the interaction vertex [54].

The algorithm used in identifying muons differs from the electron-identification algorithm because muons require a measurement of the bend-angle of the tracks. Track segments are formed separately before and after the outer magnet. These segments are then matched to determine the muon momentum from the change in the angle of the trajectory. There are two major backgrounds to consider: cosmic-ray muons and hadronic showers that extend beyond the calorimeter. The latter background is only

important in the parts of the detector where there is not much absorber material, and especially in the transition region between the cryostats, .

The momentum resolution of the muon spectrometer is improved by associating the muon trajectory with a track in the central detector and an interaction vertex. This provides a more accurate muon trajectory before the magnet. Other issues in muon identification are as follows.

- Calorimeter confirmation. As a muon traverses the calorimeter, it deposits energy through ionization (typically, between 1 and 3 GeV of energy in the sensitive regions). The mean energy loss can be estimated through Monte Carlo, and is usually added to the externally measured momentum. The amount of energy deposited in the calorimeter is also useful for rejecting background to muon candidates. An acceptable muon track is required to have at least 1 GeV of visible energy deposited along its trajectory in the calorimeter.

- Impact parameters. The muon momentum is measured after it passes the calorimeter. To reduce cosmic-ray background, it is required that the muon trajectories point to the interaction vertex. In particular, an impact parameter is defined in the non-bend view by projecting the muon track into the x-y plane, and extrapolating the trajectory formed by the B and C layers towards the center of the detector. Tracks that do not pass near the beam position are likely to be cosmic rays. A muon is accepted if it has an impact parameter of less than 25 cm. When a single cosmic-ray muon penetrates the detector, it produces a track in the opposite hemisphere of the detector. These type of events can be easily rejected in the central region (η <1).

- Track timing. Another way to reject cosmic rays is provided by the time T_0 at which a particle goes through a drift chamber relative to the time at which the beams cross. If the tracks are caused by cosmic rays, the drift time value will not be correct, since it is not synchronized with the accelerator. To use such information, a χ^2 fit to any muon track is minimized with respect to T_0, and the result compared with the nominal T_0 for the beam crossing. If the difference is larger than 100 nsec, the track is then rejected.

- Hit multiplicity. A muon track will typically have hits in 7-10 drift tubes, although

this depends on the particular region of the detector. High p_T muon trajectories in the end regions are required to have at least 5 hits (there is no explicit requirement in the central region).

- Isolation. A good muon must be separated from any jet by a minimum distance of R=0.5 in η, ϕ space.

Muons are required to be contained entirely within the WAMUS system, with $|\eta|$ <1.7. Our $t\bar{t}$ analysis also requires that muons from W decays have E_T >15 GeV. The efficiency for finding isolated muons in $t\bar{t}$ events with these set of criteria is ≈41%. A different set of requirements is used for identifying muons associated with decays of b quarks.

Missing-E_T, $\not\!\!E_T$

The presence of neutrinos is inferred from an imbalance in the transverse energy of an event as a whole, which, as we have stated, is known as "missing E_T", and denoted by $\not\!\!E_T$. The $\not\!\!E_T$ is determined by summing the transverse energy components of every calorimeter and ICD cell [55]:

$$\not\!\!E_{T\ x}^{\rm cal} = -\sum_{i=1}^{N_{cells}} E_{xi} \tag{2.10}$$

$$\not\!\!E_{T\ y}^{\rm cal} = -\sum_{i=1}^{N_{cells}} E_{yi} \tag{2.11}$$

The magnitude of $\not\!\!E_T^{\rm cal}$ is obtained by summing the x and y components in quadrature, and it represents the total transverse energy carried away by particles that do not interact in the calorimeter. The resolution in this quantity is determined largely by the quality of the calorimeter. Based on the distribution of E_T in a sample of events that were required to pass only the Level 0 trigger (this is referred to as *minimum-bias* events), the resolution can be parameterized as [55]:

$$\delta(\not\!\!E_T^{\ cal}) = 1.08GeV + 0.019 \times \sum_{Cells} E_T \tag{2.12}$$

In order to isolate the portion of $\not\!\!E_T{}^{cal}$ that corresponds to neutrinos, the contributions from any muons identified in the final state is substracted by each component:

$$\not\!\!E_{Tx} = \not\!\!E_T{}^{\rm cal}{}_x - \sum_{j=1}^{N_{muons}} p_x^{\mu i} \tag{2.13}$$

$$\not\!\!E_{Ty} = \not\!\!E_T{}^{\rm cal}{}_y - \sum_{j=1}^{N_{muons}} p_y^{\mu i} \tag{2.14}$$

and, again, the magnitude of $\not\!\!E_T$ equals the sum of the two components, in quadrature.

Jets and Jet Energy Calibration

When two partons are produced in a $p\overline{p}$ collision, the QCD hadronization and fragmentation effects produce a collection of colorless hadronic particles that are emitted in the direction of the momentum of the initial partons. These secondaries interact in the calorimeter, and as we mentioned, the final cluster of energy is called a calorimeter jet. In order to analyze these jets, DØ uses an algorithm that associates the depositions of energy in the calorimeter with jets. Our analysis uses the cone-clustering algorithm for reconstructing jets [56]. In this algorithm jets are formed using cones in η, ϕ space, defined by a radius R=$\sqrt{(\Delta\phi)^2 + (\Delta\eta)^2}$=0.5, where $\Delta\phi$ and $\Delta\eta$ correspond, respectively, to the sizes of the clusters in azimuth and pseudorapidity . This is a standard algorithm used in previous experiments, and will not be discussed any further.

To reconstruct of a $t\overline{t}$ event, it is necessary to identify the energy of a jet with the energy of its originating parton. At DØ, there are two steps in this kind of calibration. Initial energy corrections are applied before the events are selected, and this is all that is used in most DØ analyses. These corrections, applied via a software package called "CAFIX" [57], corrects for calorimeter effects so as to make the jet energy equal, on average, that of the summed energies of the final-state particles contained within the jet cone. These corrections will not be discussed any further. In a second step, corrections are applied to account gluons that maybe radiated from the original partons, causing some energy to fall outside the jet cone. We will concentrate in this level of jet energy corrections, which are needed to improve the resolution in reconstructed $t\overline{t}$ events.

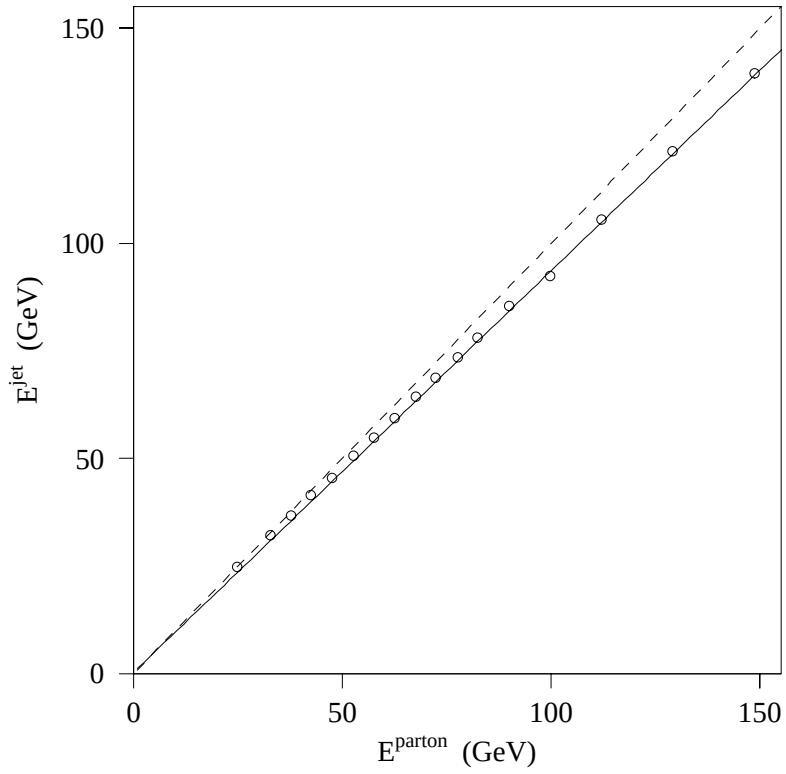

Figure 2.10: Effect of radiation outside the jet cone [32]. The reconstructed jets have on average less energy than the original parton, this is the motivation for the corrections that are based on a comparison of parton energies and energies of reconstructed jets in $t\bar{t}$ events (circles). The correction attempts to provide a 1:1 correspondence (given by the dashed line).

Figure 2.10 [32] displays a scatter plot of the energies of generated partons versus those of their reconstructed jets in lepton+jets $t\bar{t}$ Monte Carlo events [67]. As can be seen, the R=0.5 cone algorithm used in this study yields jets of smaller energy than carried by the original partons. A correction is therefore required to account for this effect when the quantity of interest is the original parton energy, as is the case in our top-quark analysis. DØ has a standard way to make such corrections, and these are described in detail in Refs. [58]. The general idea is to modify the energy of the reconstructed jet to recover, on average, the energy of the parton. Corrections are made in two steps:

- To compensate for gluon radiation outside of the cone considered in the clustering algorithm, corrections are made based on a comparison of the energy of reconstructed jets in MC simulated $t\bar{t}$ events with the energy of the corresponding

Table 2.2: Parameters for jet energy corrections to the parton level. $E_{corr} = (E_{jet} - A)/B$.

	Light quark jets		Untagged b jets	
η region	A (GeV)	B	A (GeV)	B
$0.0 < \lvert\eta_{\rm det}\rvert < 0.2$	0.322	0.933	-0.672	0.907
$0.2 < \lvert\eta_{\rm det}\rvert < 0.6$	0.635	0.930	-1.34	0.914
$0.6 < \lvert\eta_{\rm det}\rvert < 0.9$	1.86	0.883	0.002	0.868
$0.9 < \lvert\eta_{\rm det}\rvert < 1.3$	1.70	0.933	-0.548	0.904
$1.3 < \lvert\eta_{\rm det}\rvert$	4.50	0.882	2.46	0.859

partons. The correction is different for b quarks and for light quarks, and depends on η. The corrected energy E_{corr} is expressed in terms of the reconstructed jet energy E_{jet} as follows:

$$E_{corr} = \frac{E_{jet} - A}{B} \tag{2.15}$$

where A is the intercept and B is the slope (obtained from Fig. 2.10), these parameters are derived for different regions of η, and the results are shown in Table 2.2. There is a separate set of corrections for those b quarks that are tagged by soft muons, and these corrections are also described in Ref. [58], but we will concentrate only on untagged b quarks in this dissertation.

- η-dependent corrections, unlike the corrections that depend only on Monte Carlo simulated $t\bar{t}$ events, are data driven, and are used to ensure consistency of MC with observation. These are also part of the standard $t\bar{t}$ mass analysis in the single-lepton channel at DØ.

  The η-dependent corrections are obtained after applying the corrections for radiation, and are based on events with only one "photon" and one jet (γ+jet) [59]. These are not pure direct-photon events, but rather any highly electromagnetic γ-like showers produced in association with an opposing jet. Because the electromagnetic energy scale is well calibrated, the E_T is compared with that of the photon. The deviation from unity in jet energy scale can be measured by the fractional difference (ΔS) in E_T between the jet and the photon:

$$\Delta S = \frac{E_T(jet) - E_T(\gamma)}{E_T(\gamma)} \tag{2.16}$$

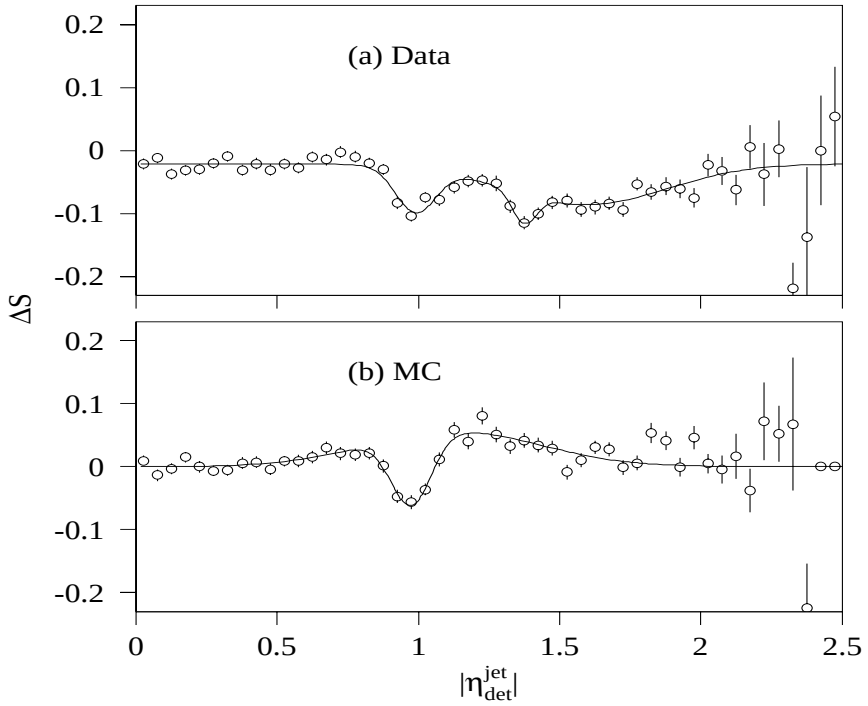

Figure 2.11: Dependence of the deviation in the jet energy scale (ΔS) for γ+jets data and MC events, as a function of $|\eta|$ [32].

The mean value of ΔS is obtained for a large sample of γ+jet events as a function of η, and the results are shown in Fig. 2.11 for data and for MC simulations of these events [58, 67]. These plots provide two functions, one to correct the data and one to correct the MC events, and define the final corrected jet energies (independent of jet type).

The η-dependent corrections are referenced to all previous levels of energy corrections, those intrinsic to the simple cone-clustering algorithm and to the radiation corrections; when those change, then the η-dependent corrections must also be re-examined.

In our analysis, we consider an alternative approach to the problem of jet energy corrections. We take account of the fact that energy losses due to hadronization and radiation are strongly asymmetric relative to the original parton energy. This is described in Chapter 4.

Chapter 3

The General Method

Our analysis is based on a comparison of data with a matrix element that was used in determining the top mass in data from Run I [61, 63]. The top mass has been measured to a precision of ≈3%. However, to measure the longitudinal fraction F_0 in W decay with some precision will require statistics of Run IIb [31]. As shown in a DØ Note 3975 [61, 62], the new formulation leads to a reduction of almost a factor of two in the statistical error on the top mass.
The most important features of the general method are that:

- It uses all possible jet combinations in the event, but each combination enters into the probability with a different weight.
- Apart from the unclustered energy, which refers to the energy deposited in the calorimeter from all sources except leptons and jets, it utilizes all measured quantities to specify every event, which provides excellent discrimination between signal and background.
- It defines a probability distribution for each event that is a function of F_0, which is based on an event-by-event mapping of energy between jets and their partons.
- It provides an internal check of the largest systematic uncertainly, namely the jet energy scale, through the dependence of the event probability on W mass.

There are, of course, approximations in the calculation of the probability, and a more complete treatment has to include the possibility of extra jets from gluon radiation, merging and/or splitting of jets, and the probability for every background process. The

higher-statistics analyses of data from Run II will require such improvements, but as a first step in the application of our method to the extraction of F_0 from the low-statistics data of Run I, our approximations should not be the limiting factor in the analysis. In this respect, restricting our study to events with exactly four jets should be beneficial, because such events should be described more correctly by the lowest-order matrix element we use in the analysis. Also, as in the extraction of the top mass, we have taken advantage of the fact that about 80% of the background is from W+jets, and have used only the W+4 jets probability in the calculation of background.

3.1 Definition of Likelihood

The likelihood function for N events is defined as (see Appendix A):

$$L(\alpha) = \mathrm{e}^{-N\int \overline{P}(x;\alpha)dx} \prod_{i=1}^{N} \overline{P}(x_i;\alpha) \tag{3.1}$$

where α is any parameter that we wish to measure. $\overline{P}(x,\alpha)$ is the probability density for observing an event characterized by a set of physical variables x, and N is the number of events in the sample. The best estimate of any given set of parameters α is obtained through a maximization of the likelihood. $L(\alpha)$ is usually a rapidly varying function of α, and it is therefore common practice to minimize –ln$L$ with respect of α,

$$-\ln(L) = -\sum_{i=1}^{N} \ln(\overline{P}(x_i;\alpha)) + N\int \overline{P}(x;\alpha)dx \tag{3.2}$$

In our case, x represents the set of variables that can be measured in the detector, that is, the momentum of the lepton and of the four jets. $\overline{P}(x_i;\alpha)$ or "measured probability" is the probability of measuring an event characterized by the quantities x observed in the detector.

In general, the probability that an event is accepted depends on the characteristics of the event, and not on the process that produced it. The measured probability density $\overline{P}(x;\alpha)$ can be related to the "produced" probability density $P(x;\alpha)$:

$$\overline{P}(x;\alpha) = Acc(x)\ P(x;\alpha) \tag{3.3}$$

where $Acc(x)$ is the detector acceptance, and includes everything that affects the acceptance or rejection of an event. For example, $Acc(x)$ usually includes the geometrical acceptance, trigger efficiencies, reconstruction efficiencies, selection criteria, etc. Of course, the detector acceptance cannot depend on any specific parameter to be estimated from data. For example, if an electron is detected with a certain momentum $\overrightarrow{p}_e$, once that momentum is specified, the detector is insensitive as to whether the electron came from W decay, Z decay, or any other process. The result of inserting Eq. 3.3 into Eq. 3.2 yields:

$$\boxed{-\ln L(\alpha) = -\sum_{i=1}^{N} \ln P(x_i;\alpha) + N \int Acc(x) P(x;\alpha) dx} \tag{3.4}$$

where the term $-\sum \ln Acc(x_i)$ has been dropped because it is independent of the parameters α, and it therefore cannot affect the minimization.

When $P(x;\alpha)$ is normalized to unity, then the integral term in Eq. 3.4 can be dropped. Very often $P(x;\alpha)$ is a nonlinear function of several parameters, and also the calculation of the normalization can depend on the acceptance. In these cases, it is very difficult to keep $P(x;\alpha)$ normalized during the minimization process. The solution to this problem is to let the normalization float, including it as another parameter in the minimization. The result of the minimization will be to keep $P(x;\alpha)$ normalized. This can be seen by replacing $P(x;\alpha) \to cP(x;\alpha)$ in Eq. 3.4, and minimizing with respect to c:

$$-\ln L = -\sum_{i=1}^{N} \ln A(x_i) - N \ln c - \sum_{i=1}^{N} \ln P(x_i;\alpha) + Nc \int A(x) P(x;\alpha) dx \tag{3.5}$$

$$\frac{\partial(-\ln L)}{\partial c} = -\frac{N}{c} + N \int Acc(x) P(x;\alpha) dx = 0 \quad \Rightarrow \quad \frac{1}{c} = \int Acc(x) P(x;\alpha) dx \tag{3.6}$$

that is, $c = \frac{1}{\int Acc(x)P(x;\alpha)dx}$, which normalizes $P(x;\alpha)$. It could happen that the normalization parameter is correlated with the rest of the parameters. In this case, the errors in the parameters α will increase. If this increase is noticeable, it could be worth going through the effort of keeping the probability normalized. Appendix B contains simple examples of the implementation of this method.

3.2 General Calculation of $P(x;\alpha)$

If the resolution of the detector is very good, and the beam energies are well known, then the probability $P(x;\alpha)$ for any signal is proportional to the differential production cross section. Following reference [11], the differential cross section can be written as

$$d\sigma = \frac{(2\pi)^4 |M|^2}{4\sqrt{(q_1 \cdot q_2)^2 - m_{q1}^2 m_{q2}^2}} \quad d\Phi_n(q_1 + q_2; p_1, ..., p_n) \quad , \tag{3.7}$$

where M is a Lorentz-invariant matrix element, q_1, q_2, m_{q1}, and m_{q2} are the four momenta and masses of the incident particles, and $d\Phi_n$ is an element of n-body phase space given by

$$d\Phi_n(P; p_1, ..., p_n) = \delta^4(P - \sum_{i=1}^{n} p_i) \prod_{i=1}^{n} \frac{d^3 p_i}{(2\pi)^3 2E_i} \quad . \tag{3.8}$$

When the reaction is initiated by partons, and the resolution of the detector cannot be ignored, then the cross section has to be folded over the parton distribution functions and detector resolution, and integrated over all the unphysical production variables. If $f(q)dq$ is the probability that a parton carries a longitudinal momentum between q and $q + dq$, then the probability density can be written as

$$P(x;\alpha) = \frac{1}{\sigma} \int d\sigma(y) dq_1 dq_2 f(q_1) f(q_2) W(y, x) \quad , \tag{3.9}$$

where $d\sigma(y)$ is the differential cross section in terms of the produced parton variables, $y = (p_1, ..., p_n)$ represents all the parton-level variables needed to specify an event, and $W(y, x)$ is the probability density for measuring a detected object x when y is produced. W equals 1.0 when the final-state object is not measured, as is the case for neutrinos, and it is assumed to be a Gaussian-like function when the resolution has to be taken into account, and a δ-function for variables that are well defined and very well measured. $W(y, x)$ satisfies the normalization condition $\int W(y, x)\, dx = 1$, which is equivalent to stating that a set of partonic variables y will always end up in some set of detector variables x. The integrated cross section σ normalizes $P(x;\alpha)$ to a probability:

$$\frac{1}{\sigma} \int P(x;\alpha)\, dx = \frac{1}{\sigma} \int d\sigma(y) dx dq_1 dq_2 f(q_1) f(q_2) W(y, x) = 1 \tag{3.10}$$

Replacing Eq. 3.7 and 3.8 into Eq. 3.9, and considering a final state with 6 particles,

the probability is now

$$P(x;\alpha) = \int \frac{(2\pi)^4 |M|^2 f(q_1) f(q_2) W(y,x)}{4\sqrt{(q_1 \cdot q_2)^2 - m_{q_1}^2 m_{q_2}^2}} d\Phi_6 dq_1 dq_2 \tag{3.11}$$

In the following sections we will constrain the calculation of the probability to $t\bar{t}$ events. First, we will make certain assumptions on the mapping between partons and measured quantities. And later we will obtain an expression for the phase space of $t\bar{t}$ events. Once these calculations are done we will come back to Eq. 3.11 to obtain a probability for $t\bar{t}$ events.

3.3 Transfer Function $W(y,x)$

As we mentioned, $W(y,x)$ is the probability of measuring the set of observable variables x that correspond to the set of production variables y. $W(y,x)$ is taken as a δ function for quantities that correspond to well measured original objects (e.g., electrons), and a Gaussian-like function when measurement errors or resolution issues cannot be ignored (e.g., jets).

The set y represents all the final-state particle momenta at the parton level. For single-lepton $t\bar{t}$ events, $y = (\overrightarrow{p}_q, \overrightarrow{p}_e, \overrightarrow{p}_\nu)$. Since the neutrino is not measured, $x =$ ($\overrightarrow{p}_e$,jet variables). Due to the excellent granularity of both the electromagnetic and hadron calorimeters, the production angles of objects will be considered as well measured. Also, since energies of electrons are measured much better than for jets, the momenta of electrons will also be considered well measured. For $W \to \mu\nu$, the muon momentum is often not well measured, so the muon momentum resolution has to be included. This effect will be taken into account integrating numerically over the resolution of the muons. The effects of muon resolution are described in Section 11.1 of Ref. [61].

For the e+jets final states, we write $W(x,y)$ in the form:

$$W(y,x) = \delta^3(\overrightarrow{p}_e^{\,y} - \overrightarrow{p}_e^{\,x}) \prod_{i=1}^{4} W_{jet}(E_i^y, E_i^x) \prod_{j=1}^{4} \delta^2(\Omega_j^y - \Omega_j^x) \tag{3.12}$$

where $\overrightarrow{p}_e^{\,y}$ and $\overrightarrow{p}_e^{\,x}$ are the produced and measured electron momenta, E_i^y and E_i^x are the parton and jet energies, and Ω_j^y and Ω_j^x are the quark and jet angles. All the variables in Eq. 3.12 are given in the $p\bar{p}$ center of mass. Section 4 will provide more detail on

$W_{jet}(E^y, E^x)$, the transfer function for jets.

3.4 The Phase Space

To calculate the probability $P_{t\bar{t}}(x;\alpha)$ in Eq. 3.9, an integration must be performed over 20 variables, corresponding to the vector momenta of the six final-state particles (four quarks, a lepton and a neutrino, giving 18 variables), and the longitudinal momenta of the incident partons (2 variables). Inside the integrals there are 15 δ-functions. Four for total energy and momentum conservation, eight for the jet angles, and three for the electron's momentum vector. The calculation of $P_{t\bar{t}}(x;\alpha)$ therefore involves a five-dimensional integral. The integrals are performed numerically, and a judicious choice of the five variables of integration is therefore very important. A possible choice that would require no transformation of variables would be the absolute values of the four quark momenta and the longitudinal momentum of the neutrino. However, this choice has the disadvantage that most of the random sampling would be done where the probability is very small. The reason for this is that the value of the matrix element $|M_{t\bar{t}}|^2$ is negligible, except near the four peaks of the Breit-Wigners (BW), corresponding to the two top and the two W masses. A better choice of integration variables would therefore appear to be the top and W masses, and the absolute value of momentum of one of the quarks. With this choice, the numerical sampling is performed only near the BW peaks, and within the limits of resolution for one of the jets. Appendix C contains a general discussion of the expression for the phase space integrals, and Appendix D contains the details of the $t\bar{t}$ phase space for lepton+jets events.

The phase space, as a function of the variables $(\overrightarrow{\Omega}_{jets}, \rho_1, M_1, m_1, M_2, m_2, \overrightarrow{p}_e)$, is given by [11]:

$$
\begin{aligned}
d\Phi_6 = & [\delta(E_{q_1} + E_{q_2} - \sum_{i=1}^{6} E_i)] \;\; [\delta(p^z_{q_1} + p^z_{q_2} - \sum_{i=1}^{6} p^z_i)] \;\; \frac{d^3\overrightarrow{p}_e}{(2\pi)^3 2E_e} \frac{d\rho_1}{(2\pi)^3 2E_\nu} \prod_{i=1}^{4} \frac{\rho_i^2 d\Omega_i}{(2\pi)^3 2E_i} \\
& \times \frac{dm_1^2}{|2E_1\frac{\rho_2}{E_2} - 2\rho_1 \cos\theta_{12}|} \frac{dM_1^2}{|2E_1\frac{\rho_3}{E_3} - 2\rho_1\cos\theta_{13} + 2E_2\frac{\rho_3}{E_3} - 2\rho_2\cos\theta_{23}|} \\
& \times \frac{dm_2^2}{|2E_e\frac{p^z_\nu}{E_\nu} - 2p^z_e|} \frac{dM_2^2}{|2E_e\frac{\rho_4}{E_4} - 2\rho_e\cos\theta_{e4} + 2E_\nu\frac{\rho_4}{E_4} - 2\rho_\nu\cos\theta_{\nu 4}|}
\end{aligned}
\tag{3.13}
$$

Therefore,

$$d\Phi_6 = \frac{4}{(2\pi)^4}\,\Phi_6\,[\delta(E_{q_1}+E_{q_2}-\sum_{i=1}^{6}E_i)]\,[\delta(p^z_{q_1}+p^z_{q_2}-\sum_{i=1}^{6}p^z_i)] \times d^3\overrightarrow{p}_e\,d\rho_1 dm_1^2 dM_1^2 dm_2^2 dM_2^2 \prod_{i=1}^{4} d\Omega_i \tag{3.14}$$

with

$$\Phi_6 = \frac{4}{(4\pi)^{14}}\frac{1}{E_e E_\nu}\prod_{i=1}^{4}\frac{\rho_i^2}{E_i} \times \frac{1}{|E_1\frac{\rho_2}{E_2}-\rho_1\cos\theta_{12}|}\frac{1}{|E_1\frac{\rho_3}{E_3}-\rho_1\cos\theta_{13}+E_2\frac{\rho_3}{E_3}-\rho_2\cos\theta_{23}|} \times \frac{1}{|E_e\frac{p^z_\nu}{E_\nu}-p^z_e|}\frac{1}{|E_e\frac{\rho_4}{E_4}-\rho_e\cos\theta_{e4}+E_\nu\frac{\rho_4}{E_4}-\rho_\nu\cos\theta_{\nu 4}|} \quad , \tag{3.15}$$

where $\rho_i = |\overrightarrow{p}^{\,i}_{quarks}|$, E_i are the quark energies, $m_1(m_2)$ is the invariant mass of the W in $W \to q\overline{q}$ ($W \to e\nu$), and $M_1(M_2)$ is the invariant mass of the top quark in the hadronic (leptonic) branch for each permutation.

3.5 Probability for Single-Lepton $t\bar{t}$ Events

Combining Eq. 3.11, Eq. 3.12, and 3.14 the probability for single-lepton $t\bar{t}$ events can be written as:

$$P_{t\bar{t}}(x;\alpha) = \int |M|^2\,\frac{f(q_1)}{|q_1|}\frac{f(q_2)}{|q_2|}\,W(y,x)\,\Phi_6\,d\rho_1 dm_1^2 dM_1^2 dm_2^2 dM_2^2 \times \delta(|q_1|+|q_2|-\sum_{i=1}^{6}E_i)\,\delta(q_1+q_2-\sum_{i=1}^{6}p^z_i)\,dq_1 dq_2 d^3\overrightarrow{p}_e\prod_{i=1}^{4}d\Omega_i \quad , \tag{3.16}$$

where the masses and transverse momenta of the initial partons are neglected, that is, $\sqrt{(q_1\cdot q_2)^2 - m_{q_1}^2 m_{q_2}^2} = 2|q_1||q_2|$. The q_i therefore stand for the longitudinal momenta of the incident partons. The integration over q_1 and q_2 eliminates the two δ-functions in Eq. 3.16. Integration over the electron momentum and the jet solid angles eliminates the δ-functions in Eq. 3.12 associated with $W(y,x)$. Therefore, the probability density

for single-lepton $t\bar{t}$ events is given by

$$\boxed{P_{t\bar{t}}(x;\alpha) = \frac{1}{12\,\sigma_{t\bar{t}}} \int d\rho_1 dm_1^2 dM_1^2 dm_2^2 dM_2^2 \sum_{comb.+\nu} |M_{t\bar{t}}|^2 \frac{f(q_1)}{|q_1|}\frac{f(q_2)}{|q_2|}\,\Phi_6 \prod_{i=1}^{4} W_{jet}(E_i^y, E_i^x)} \tag{3.17}$$

where $W_{jet}(E^x, E^y)$ is defined in Section 3.3, Φ_6 is the phase space factor given in Section 3.4, $f(q)$ is the parton distribution function, and $|M_{t\bar{t}}|^2$ is the matrix element from Section 1.2.4. Because, in general, it is not possible to distinguish jets in a $t\bar{t}$ final state, e.g., which jets are b quarks and which are remnants of $W \to q'\overline{q}$ decay, the probability must be evaluated for all possible combinations of jets that comprise the $t\bar{t}$ final state. Thus, the probability must be summed over all 12 possible assignments of jets and quarks, with their respective weights, and also over the neutrino solutions that are consistent with energy and momentum conservation. This effectively increases the $t\bar{t}$ cross section by a factor of 12, and requires the additional factor of 12 in the denominator. The integration is performed over the absolute value of the momentum of one of the quarks (ρ_1), W masses m_1 and m_2, and top masses M_1 and M_2.

For each value of the parameter α, the procedure to calculate the integral in Eq. 3.17 is as follows:

- All permutations are calculated separately and then added together

$$P_{t\bar{t}}(x;\alpha) = \frac{1}{12\sigma_{t\bar{t}}} \sum_{i=1}^{12} P_{t\bar{t}}^i(x;\alpha) \quad . \tag{3.18}$$

  (Note that there is no difference between adding $P_{t\bar{t}}^i$ inside or outside the integrals.)

- For each permutation $P_{t\bar{t}}^i(x;\alpha)$, a subroutine from the CERN mathematical library is used to perform the $d\rho_1$ integral, using an adaptive quadrature method,

$$P_{t\bar{t}}^i(x;\alpha) = \Big[\int I_1(\rho_1) d\rho_1 \Big]_\alpha \quad , \tag{3.19}$$

  where $\Big[\quad \Big]_\alpha$ means that α is fixed.

- $I_1(\rho_1)$ in Eq. 3.19 is an integral over the masses of M_1, M_2, m_1 and m_2. Since the top width is very small, the integrals over the top masses M_1 and M_2 are

performed using the narrow width approximation

$$\int \frac{F(m)dx^2}{(x^2 - M^2)^2 + (M, \ )^2} \approx \frac{\pi F(M)}{M, } \tag{3.20}$$

This simplifies the integration in dM_1^2 and dM_2^2, giving

$$I_1(\rho_1) = \Big[\int dm_1^2 \int dm_2^2 \frac{\pi B(M_1, M_t, \ )}{M_t, \ _t} \frac{\pi B(M_2, M_t, \ )}{M_t, \ _t} I_2(m_1, m_2) \Big]_{M_t, M_1 = M_2 = M_t} \ . \tag{3.21}$$

with $B(m, M, \ ) = (m^2 - M^2)^2 + (M, \ )^2$.

- The integrals in dm_1^2 and dm_2^2 in Eq. 3.21 are performed numerically. In order to sample only close to the pole of the BW, the variables m_1^2 and m_2^2 were changed to μ_1 and μ_2, with $m_1^2 = \ , \ _W M_W \tan(\mu_1) + M_W^2$ and $m_2^2 = \ , \ _W M_W \tan(\mu_2) + M_W^2$. Eq. 3.21 then transforms to

$$I_1(\rho_1) = \Big[\int_{-\pi/2}^{\pi/2} d\mu_1 \int_{-\pi/2}^{\pi/2} d\mu_2 \overline{I}_2(\mu_1, \mu_2) \Big]_{M_t, M_1 = M_2 = M_t} \ . \tag{3.22}$$

with

$$\overline{I}_2(\mu_1, \mu_2) = \frac{\pi B(M_1, M_t, \ )}{M_t, \ _t} \frac{\pi B(M_2, M_t, \ )}{M_t, \ _t} \frac{\pi B(m_1, M_t, \ )}{M_t, \ _t} \frac{\pi B(m_2, M_t, \ )}{M_t, \ _t} I_2(m_1, m_2) \tag{3.23}$$

The integrals in Eq. 3.22 are calculated using a subroutine in the CERN mathematical library for multiple-dimension Gaussian integrations, The integrand I_2 is:

$$I_2(m_1, m_2) = \sum_\nu \Big[|M|^2 \ \frac{f(q_1)}{|q_1|} \frac{f(q_2)}{|q_2|} \ \Phi_6 \ \prod_{i=1}^{4} W_{jet}(E_i^y, E_i^x) \Big]_{M_t, \rho_1, M_1 = M_2 = M_t} \ . \tag{3.24}$$

The evaluation of the right hand side of Eq. 3.24 is performed for points in the phase space that satisfy the energy and momentum constraints (Dirac δ-functions in Section 3.4), together with the constraints on $M_t, \rho_1, M_1 = M_2 = M_t, m_1, m_2$. To select the points that satisfy these requirements, we use a subroutine that solves the associated kinematic equations. Several solutions are obtained for the neutrino

momentum at each point and the solutions are added, as indicated by the sum in Eq. 3.24.

3.6 Likelihood for Signal and Background

All the processes that can contribute to the observed final state must be included in the likelihood. In general, we have

$$P(x) = \sum_{j=1}^{K} c_j P(x;j) \quad , \tag{3.25}$$

where $j = 1, 2, .., K$ represent all possible contributions to the final state under study, and $P(x;j)$ is the probability of measuring x for a particular reaction j. If the coefficients c_j are not known, then they have to be considered as additional parameters in the minimization.

It should be pointed out that when amplitudes for different processes interfere, they must be added together before squaring to obtain the probabilities. In this analysis, we consider only non-interfering processes (signal and orthogonal backgrounds), and if the individual probabilities are normalized, we can write:

$$\sum_{j=1}^{K} c_j = 1 \quad . \tag{3.26}$$

Including background, the probability for any event, can be written as:

$$P(x; c_1, c_2, \alpha) = c_1 P_{t\bar{t}}(x;\alpha) + c_2 P_{Background}(x) \quad . \tag{3.27}$$

Following Section 3.1, the measured probability is calculated as

$$\overline{P}(x; c_1, c_2, \alpha) = Acc(x)\ P(x; c_1, c_2, \alpha) \tag{3.28}$$

and –ln$L(\alpha)$ is given by

$$\boxed{\begin{aligned} -\ln L(\alpha) &= -\sum_{i=1}^{N} \ln P(x;c_1,c_2,\alpha) + N\int Acc(x)P(x;c_1,c_2,\alpha)dx \\ &= -\sum_{i=1}^{N} \ln\left[c_1 P_{t\bar{t}}(x;\alpha) + c_2 P_{Background}(x)\right] + N\left[c_1 < Acc_s(\alpha) > + c_2 < Acc_b >\right] \end{aligned}} \tag{3.29}$$

where

$$< Acc_s(\alpha) >= \int Acc(x)\, P_{t\bar{t}}(x;\alpha)\, dx \quad \text{, and} \quad < Acc_b >= \int Acc(x)\, P_{Background}(x)\, dx \tag{3.30}$$

For each value of α, we determine the most probable values of c_1 and c_2, and we then search for the most probable (or mean) value of α. The probability $\overline{P}(x;c_1,c_2,\alpha)$ is normalized automatically as a result of the minimization process. The number of observed signal events is obtained from setting

$$N_s^{obs}(\alpha) = c_1 \ < Acc_s(\alpha) > \ N \tag{3.31}$$

and the number of observed background events from:

$$N_b^{obs} = c_2 \ < Acc_b > \ N \quad . \tag{3.32}$$

3.7 Detector Acceptance for $t\bar{t}$

The effect of detector acceptance is given by the integral in Eq. 3.4. Substituting the probability given by Eq. 3.9 into Eq. 3.4 we have

$$\int Acc(x)P(x;\alpha)dx = \int Acc(x)dx\ \frac{1}{\sigma}\int d\sigma(y)dq_1dq_2 f(q_1)f(q_2)W(y,x) \tag{3.33}$$

In general, these multidimensional integrals can only be calculated using Monte Carlo techniques. In which case, the value of $Acc(x)$ is 1 if the event is accepted, and 0 otherwise. All MC programs start by generating an event at the parton level, and, after hadronization, propagating the decay products through detector simulation and reconstruction chains. It is therefore convenient to change the order of integration in

Eq. 3.33:

$$\int Acc(x)\, P(x;\alpha)\, dx = \frac{1}{\sigma} \int d\sigma(y) dq_1 dq_2\, f(q_1) f(q_2) \int dx\, Acc(x)\, W(y,x) \qquad (3.34)$$

As indicated previously, for single-lepton $t\bar{t}$ events there is also a sum over the 12 possible ways of assigning jets to partons. Since the integral is over all possible parton and all possible jet variables, all permutations will yield the same integral. The last integral is performed via Monte Carlo. Once an event with parton variables y is generated, the MC will "smear" it in the detector variables x, and accept it or reject it according to $Acc(x)$. In general, the MC and the analysis can use different forms for $d\sigma(y)$ and PDFs $f(q)$. For example, the MC may not include $t\bar{t}$ spin correlations, or it may have different W helicity parameters, or different top and W widths. The above integral is therefore calculated in terms of a ratio of cross sections and PDFs:

$$\int Acc(x)\, P_{t\bar{t}}(x,\alpha)\, dx = \frac{V}{\sigma_{t\bar{t}} N_{gen}} \sum_{i=1}^{N_{acc}} \frac{d\sigma(y)}{d\sigma_{MC}(y)} \frac{f(q_1)}{f_{MC}(q_1)} \frac{f(q_2)}{f_{MC}(q_2)} \qquad (3.35)$$

with

$$V = \int d\sigma_{MC}(y) dq_1 dq_2 f_{MC}(q_1) f_{MC}(q_2) \qquad (3.36)$$

where the unsubscripted σ and f refer to the specific choices used in the final analysis.

The sum in Eq. 3.35 is performed over the accepted subset of events N_{acc} of the N_{gen} generated in parton-level variables y. The integral in Eq. 3.35 is a function of our specific parameter $F_0 = 1/(1+2\gamma)$ that was discussed in Section 1.2.5, and there are several ways of implementing the dependence on F_0. Two equivalent methods are discussed below.

3.7.1 First Method

First, we consider the case in which sets of MC events are generated for different values of F_0. Since the probability $P_{t\bar{t}}(x, F_0)$ is properly normalized for any value of F_0, that means that $V{=}\sigma_{t\bar{t}}$ for all values of F_0. If the same PDFs and cross sections are used in both the MC generation (Eq. 3.36) as in the calculation of probability in Eq. 3.35,

then, for each value of F_0, we get:

$$\int Acc(x)\, P_{t\bar{t}}(x, F_0)\, dx = \frac{1}{N_{gen}} \sum_{i=1}^{N_{acc}} 1 \tag{3.37}$$

3.7.2 Second Method

Another way of evaluating Eq. 3.35 is to generate MC events for a fixed value of F_0, and take advantage of the fact that the probability $P_{t\bar{t}}(x, \gamma)$ can be factorized in terms of γ (see Section 1.2.4). That is,

$$\begin{aligned} \frac{V}{\sigma_{t\bar{t}}} &= \frac{\int d\sigma_{MC}(y) dq_1 dq_2 f_{MC}(q_1) f_{MC}(q_2)}{\int d\sigma(y) dq_1 dq_2 f(q_1) f(q_2)} \\ &= \frac{\int r(\gamma_{MC}) d\cos\hat{\phi} \int d\sigma'_{MC}(y) dq_1 dq_2 f_{MC}(q_1) f_{MC}(q_2)}{\int r(\gamma) d\cos\hat{\phi} \int d\sigma'(y) dq_1 dq_2 f(q_1) f(q_2)} \end{aligned} \tag{3.38}$$

where

$$r(\gamma) = [(1 - \cos^2\hat{\phi}_{\overline{e}b}) + \gamma(1 + \cos\hat{\phi}_{\overline{e}b})^2]\ [(1 - \cos^2\hat{\phi}_{d\bar{b}}) + \gamma(1 + \cos^2\hat{\phi}_{d\bar{b}})] \tag{3.39}$$

If the MC events are generated for γ_{SM}, and the same PDFs and cross sections are used in the calculation of probability, then we obtain:

$$\begin{aligned} \frac{V}{\sigma_{t\bar{t}}} &= \frac{\int r(\gamma_{MC}) d\cos\hat{\phi}}{\int r(\gamma) d\cos\hat{\phi}} \\ &= \frac{(1 + 2\,\gamma_{SM})^2}{(1 + 2\,\gamma)^2} \end{aligned} \tag{3.40}$$

Then

$$\begin{aligned} \int Acc(x)\, P_{t\bar{t}}(x, \gamma)\, dx &= \frac{V}{\sigma_{t\bar{t}} N_{gen}} \sum_{acc} \frac{r(\gamma)}{r(\gamma_{SM})} \\ &= \frac{(1 + 2\,\gamma_{SM})^2}{(1 + 2\,\gamma)^2}\ \frac{1}{N_{gen}} \sum_{i=1}^{N_{acc}} [Q_{1i} + Q_{2i}\gamma + Q_{3i}\gamma^2] \end{aligned} \tag{3.41}$$

where

$$Q_{1i} = \frac{(1 - \cos^2\hat{\phi}_{\overline{e}bi})(1 - \cos^2\hat{\phi}_{d\overline{b}i})}{r(\gamma_{SM})} \tag{3.42}$$

$$Q_{2i} = \frac{(1+\cos\hat{\phi}_{\overline{e}bi})^2(1-\cos^2\hat{\phi}_{d\overline{b}i}) + (1-\cos^2\hat{\phi}_{\overline{e}bi})(1+\cos^2\hat{\phi}_{d\overline{b}i})}{r(\gamma_{SM})} \tag{3.43}$$

$$Q_{3i} = \frac{(1+\cos\hat{\phi}_{\overline{e}bi})^2(1+\cos^2\hat{\phi}_{d\overline{b}i})}{r(\gamma_{SM})} \tag{3.44}$$

Choosing $F_0 = 1/(1+2\gamma)$, or $\gamma = (1-F_0)/(2F_0)$, Eq. 3.41 can be written as

$$\begin{aligned}\int Acc(x)\, P_{t\overline{t}}(x,F_0)\, dx &= \frac{1}{F_{0SM}^2 N_{gen}} \sum_{i=1}^{N_{acc}} \left[\frac{Q_{3i}}{4} + \frac{Q_{2i}-Q_{3i}}{2} F_0 + \frac{4Q_{1i}-2Q_{2i}+Q_{3i}}{4} F_0^2 \right] \\ &= d_1 + d_2\, F_0 + d_3\, F_0^2\end{aligned} \tag{3.45}$$

where

$$\begin{aligned}\overline{d}_1 &= \frac{1}{N_{gen}} \sum_{i=1}^{N_{acc}} d_{1i} = \frac{1}{N_{gen}} \sum_{i=1}^{N_{acc}} \frac{Q_{3i}}{4\, F_{0SM}^2} \\ \overline{d}_2 &= \frac{1}{N_{gen}} \sum_{i=1}^{N_{acc}} d_{2i} = \frac{1}{N_{gen}} \sum_{i=1}^{N_{acc}} \frac{Q_{2i}-Q_{3i}}{2\, F_{0SM}^2} \\ \overline{d}_3 &= \frac{1}{N_{gen}} \sum_{i=1}^{N_{acc}} d_{3i} = \frac{1}{N_{gen}} \sum_{i=1}^{N_{acc}} \frac{4Q_{i1}-2Q_{i2}+Q_{i3}}{4\, F_{0SM}^2}\end{aligned} \tag{3.46}$$

Hence, we can calculate the parton-level quantities, d_1, d_2, and d_3, determine the average acceptance for $t\overline{t}$ events, and substitute expression 3.45 for the integral in Eq. 3.4. The error in these parameters are calculated as following:

$$< \delta d_m \delta d_n >= \frac{1}{N_{gen}^2} \sum_{i=1}^{N_{gen}} (d_{ni} - \overline{d}_n)(d_{mi} - \overline{d}_m) \tag{3.47}$$

where d_{ni}=d_{mi}=0 for events that are not accepted and n, m=1,2,3. And the total error on the acceptance integral including all the correlations among the 3 parameters is

$$\begin{aligned}(\delta Q)^2(F_0) =& < (\delta d_1)^2 > + 2 < \delta d_1 \delta d_2 > F_0 + [2 < \delta d_1 \delta d_3 > \\ &+ < (\delta d_2)^2 >] F_0^2 + 2 < \delta d_3 \delta d_2 > F_0^3 + < (\delta d_3)^2 > F_0^4\end{aligned} \tag{3.48}$$

where $Q = \int Acc(x)\, P_{t\overline{t}}(x, F_0)\, dx$.

3.8 Calculation of $P_{VECBOS}(x)$ and $< Acc_b >$

The main background considered in this analysis is W+4 jets production. This probability was calculated by F.A. Berends, H. Kuijf, B. Tausk and W.T. Giele, and implemented in a subroutine that is part of the VECBOS code [65]. We use this subroutine to characterize the probability that any event corresponds to the W+jets hypothesis.

However, the background to the $t\bar{t}$ signal in the lepton + 4-jets final state has contributions from W+ jets and from multijets production. For the event selections used by DØ, W+jets represents 80% of the background, with the other 20% corresponding to events with multijet production where one of the jets mimics an electron. $P(x;\alpha)$ will be defined purely by a sum of the $t\bar{t}$ signal and the W+jets background. However, we will check whether the multijets background has similar character to W+jets background. Of course, an explicit treatment of the background from jet production can only improve the sensitivity to F_0, but, in any case, the presence of this background must be taken into account in the statistics and the resolution of the analysis.

VECBOS was used to simulate the W+4 jets background in the previous of DØ and CDF analyses [32, 30]. Here, the background is also considered to be well described by VECBOS, but instead of using the code to generate events, and then run them through the detector simulation, as we indicated above, we use the program to directly calculate the differential cross section. A subroutine in VECBOS returns the matrix element for the W+4 jets process. This, combined with the phase space factor, provides the differential cross section for background events.

3.8.1 Integrations Over Jet Energies

As for $t\bar{t}$ signal probability, the integrals over jet-energy resolution have also to be performed for background. All jet permutations must be considered, together with the possible values of the longitudinal momentum of the neutrino. The transfer function used for modeling the resolution is the same as given in Eq. 3.12 for $t\bar{t}$ signal.

The technique used to perform the integrals over jet energies is different from that used for the calculation of $P_{t\bar{t}}(x;\alpha)$. In the present case, the integrals are evaluated using Monte Carlo, as follows. For each measured event, a probability density for parton energy can be obtained from the observed jet energies and the transfer function. M points are selected randomly in this multidimensional space (using the transfer function), with

all probabilities calculated at the parton level (for all permutations). The measured probability density is then the average of the parton probabilities for all M points, that is,

$$P_{VECBOS}(x) = \frac{1}{M} \sum_{k=1...M} P_{VECBOS}(y_k) \quad , \tag{3.49}$$

where x represents the measured variables for an event, and y_k the parton variables for the event, as determined through a random sampling of the transfer function. The evaluation of the background probability density $P_{VECBOS}(y_k)$ requires the momentum of the neutrino (p_ν). The transverse components are determined from conservation of energy in the transverse plane, and the longitudinal component is determined by constraining the invariant mass of the electron and the neutrino ($m_{e\nu}$) to the known mass of the W boson. The finite width of the W boson is considered in performing an integration of $P_{VECBOS}(y_k)$ in $dm_{e\nu}$.

The averages described in Eq. 3.49 require choosing M sampling points. Of course, the CPU time increases linearly with M. Tests were performed using a small sample of events to study the convergence of Eq. 3.49, and $M = 100$ was found sufficient to obtain a $\approx$10% uncertainty from $P_{VECBOS}(x)$. ($M = 100$ is used in the rest of this dissertation for the evaluation of Eq. 3.49. In the final analysis of the data, we increase the number of events until the probability becomes stable.)

3.8.2 Acceptance and Total Cross Section

As discussed is Section 3.7, the part of the acceptance correction that depends on $P_{VECBOS}(x)$ is

$$\int P_{VECBOS}(x) Acc(x) dx = \mathcal{B} \quad , \tag{3.50}$$

where $\mathcal{B}$ is the average acceptance of the DØ detector for events generated using the differential cross section given by $P_{VECBOS}(x)$, with

$$P_{VECBOS}(x) = \frac{d\sigma(x)}{\sigma_{VECBOS}} \quad , \tag{3.51}$$

where $P_{VECBOS}(x)$ accounts for all branching ratios. The main difference between this and what was described in Section 3.7 for $P_{t\bar{t}}(x;\alpha)$ is that Eq. 3.50 contains no dependence on α.

3.9 Expectation Values and Errors

The probability of Eq. 3.17 is a positive definite quantity. The probability distribution for F_0 will therefore be forced to lie between 0 and 1. For poor statistics, the probability distribution can be asymmetric and not very Gaussian in character. In this Section, we will define different ways of extracting a measure and its uncertainty from these type of distributions. Appendix G has a more detailed study of such issues.

When statistics are good, the probability distribution tends to turn Gaussian, and it can be shown that

$$\ln[L(F_{0min})] - \ln[L(F_{0min} \pm \delta_{\pm 0.5})] = 0.5 \quad , \tag{3.52}$$

where $\delta_{\pm 0.5}$ is the dispersion about the true mean:

$$\delta^2_{\pm 0.5} = < (F_{0min} - F_{0true})^2 > \quad , \tag{3.53}$$

and F_{0true} stands for the true value of the parameter of interest. Hence, for the case of a Gaussian likelihood, $\delta_{\pm 0.5}$ is a good estimator of the statistical uncertainty on F_0. A common way to verify that the error is estimated correctly is to check the pull on F_0 which is defined as:

$$pull_{\pm 0.5} = \frac{F_{0min} - \overline{F_0}}{\delta_{\pm 0.5}} \quad , \tag{3.54}$$

where $\overline{F_0}$ is the mean of the distribution in F_{0min}. A correct estimation of δ will result in a pull distribution that has a standard deviation close to unity [64].

When statistics are poor, likelihoods are no longer Gaussian, and $\delta_{\pm 0.5}$ may no longer be a good estimator of uncertainty. In such cases, we can calculate the mean and RMS as follows:

$$< F_0 >= \int F_0 \; P(F_0) \; dF_0 \tag{3.55}$$

$$\delta^2 = < (F_{0min} - < F_0 >)^2 > = \int (F_0 - < F_0 >)^2 \; P(F_0) \; dF_0 \tag{3.56}$$

where $P(F_0)$ is the differential probability constructed from the likelihood function. Discretizing the integrals in Eq. 3.55 and Eq. 3.56, we can write

$$< F_0 > = \frac{\sum_i F_{0i} \; P(F_{0i})}{\sum_i P(F_{0i})} \quad , \tag{3.57}$$

and

$$\delta^2 = \frac{\sum_i (F_{0i} - < F_0 >)^2 P(F_{0i})}{\sum_i P(F_{0i})}. \tag{3.58}$$

where all intervals in F_{0i} must be identical in size. The expectation value $< F_0 >$ often does not equal the most probable value F_{0min}. This difference is most noticeable for low statistics, and especially in cases when probability distributions have cutoff boundaries. In such situations, we can refer to the most probable value F_{0min} and define its uncertainty as the interval that contains 68.27% of the probability in any given experiment. Although the region for defining this 68.27% is arbitrary we will choose the smallest 68.27% region that contains the most probable value, F_{0min}. To see whether the errors are reasonable, we check whether the interval "covers" the input value in 68.27% of the simulated experiments, that is, see whether the results of the ensemble studies are within the chosen region 68.27% of the time.

Chapter 4

Mapping Between Jet and Parton Energies

The standard jet-energy corrections used in previous top-quark analyses at DØ correct the energies of jets (rather than E_T values) in such a way that, for a given η-region and a given parton energy range, the means for the corrected jet energies (E_{corr}) and the original parton energies (E_{parton}) are equal [59], that is,

$$< \delta_E^{corr} >=< E_{parton} - E_{corr} >_{\eta, E_{parton}} = 0 \tag{4.1}$$

However, such corrections do not account for the shape of the $\delta_E = E_{parton} - E_{jet}$ distribution, which is shown for light quarks and for b quarks in Fig. 4.1. These distributions are clearly not symmetric, with a significant tail at positive values of $E_{parton} - E_{jet}$. Consequently, correcting for the mean, and assuming Gaussian resolution, can often underestimate the original parton energy. As mentioned in Section 3, the method described in this note makes use of the shape in δ_E, and is implemented through a "transfer" function $W(y, x)$. In this section, we provide details on how we obtain $W_{jet}(E_{parton}, E_{jet})$.

4.1 The Transfer Function $W_{jet}(E_{parton}, E_{jet})$

The mapping between parton energies and jet energies is determined by the transfer function $W_{jet}(E_{parton}, E_{jet})$, which we parameterize as $F(E_{parton} - E_{jet})$:

$$F(\delta) = \frac{1}{\sqrt{2\pi}(p_2 + p_3 p_5)}[\exp \frac{-(\delta - p_1)^2}{2p_2^2} + p_3 \exp \frac{-(\delta - p_4)^2}{2p_5^2}] \tag{4.2}$$

$F(\delta_E)$ is taken simply as a sum of two Gaussian distributions, one to account for the

sharp peak, and the other for the asymmetric tails. As will be shown subsequently, the parameters in Eq. 4.2 depend on parton energy. A study of the p_i as a function of E_{parton} showed that they have essentially a linear dependence on E_{parton}. We therefore use a simple linear form for the p_i:

$$p_i = a_i + b_i E_{parton} \tag{4.3}$$

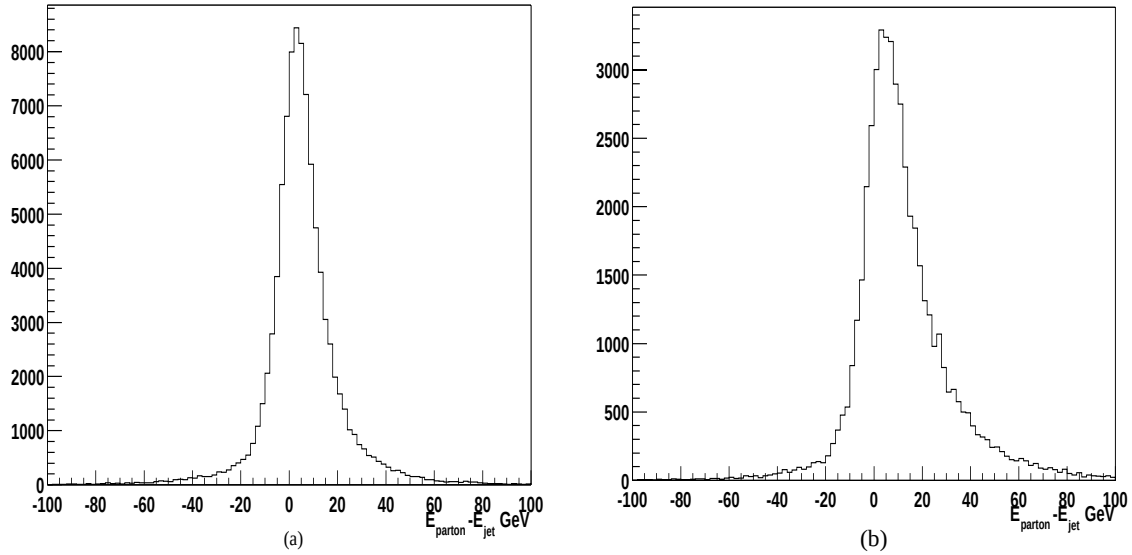

Figure 4.1: Distributions in $\delta_E = E_{parton} - E_{jet}$ for all "matched" partons for: (a) light quarks, and (b) for b quarks, in the range $|\eta| < 2$. The events were generated using HERWIG [67] $t\bar{t}$ MC (for a range of M_t) and passed through full simulation and reconstruction in the DØ detector. CAFIX energy corrections were applied to jets [57, 58]. Event selection is the same as in the mass analysis of Run I data, but the jets used in this figure are only those that could be matched to generate partons. The distributions have extended tails for $\delta_E > 0$, which can be attributed to effects from hadronization and gluon radiation.

Also, the p_i appear to be essentially independent of η, but they do depend on the type of quark. Consequently, a total of 10 parameters $(a_1, b_1, ..., a_5, b_5)$ for light quarks (u, d, c, s), and another set of 10 parameters for the b quark, will be used to define W_{jet}.

4.2 Determination of Parameters for W_{jet}

If $n(E_{jet}, E_{parton})dE_{jet}dE_{parton}$ is the number of events with jet energy between E_{jet} and $E_{jet} + dE_{jet}$ and parton energy between E_{parton} and $E_{parton} + dE_{parton}$, then

$$n(E_{jet}, E_{parton})dE_{jet}dE_{parton} = n(E_{parton})dE_{parton}W_{jet}(E_{parton}, E_{jet})dE_{jet} \tag{4.4}$$

where $n(E_{parton})dE_{parton}$ is the number of partons with an energy between $E_{parton} + dE_{parton}$. The parameters of $W_{jet}(E_{parton}, E_{jet})$ are chosen so as to maximize the agreement in Eq. 4.4. This is done using an un-binned maximum likelihood fit to the objects in $t\bar{t}$ MC events. In principle, the parameters should not depend on the parameter that we would like to measure, α, nor, for that matter, on the final state chosen for correlating parton-level to detector-level objects. Defining a likelihood by the double-density function in Eq. 4.4, we can write:

$$\begin{aligned} -lnL &= -\sum_{i=1}^{N} \ln n(E_{jet}^{(i)}, E_{parton}^{(i)}) \\ &= -\sum_{i=1}^{N} \ln n(E_{parton}^{(i)}) - \sum_{i=1}^{N} \ln W_{jet}(E_{parton}^{(i)}, E_{jet}^{(i)}) \quad . \end{aligned} \tag{4.5}$$

The sum over $\ln n(E_{parton}^{(i)})$ does not depend on the (a_i, b_i), and can therefore be ignored, and the parameters are therefore determined by minimizing:

$$-lnL = -\sum_{i=1}^{N} \ln W_{jet}(E_{parton}^{(i)}, E_{jet}^{(i)}) \quad . \tag{4.6}$$

The specific MC events used in this calculation were the same $t\bar{t}$ events used in the Run I top-mass analysis [32]. They were generated with HERWIG [67], for M_t = 140, 160, 175, 190 and 200 GeV/c^2, and then passed through the DØ simulation and reconstruction package (see Section 6). Because good statistics are required to obtain precise parameters, and W_{jet} should not depend on M_t, we combined all events into a single sample. First, standard jet corrections were applied to account for the underlying event, out-of-cone calorimeter corrections, and calorimeter response (CAFIX) [57]. Then, only the jets that could be matched to partons in the range $|\eta| < 2$ and $p_T > 15$ GeV/c were used to parameterize $W_{jet}(E_{parton}, E_{jet})$.

The fits were done separately for light quarks and for b quarks, and the results are

given in Table 4.1. The events used in the fits are shown in Figs. 4.2 and 4.3, with the crosses (and dots) in Fig. 4.2 being for light-quark jets, and in Fig. 4.3 for b-quark jets. Since events in the tails can easily bias Gaussian distributions, another set of parameters was obtained by removing events in the tails of the δ_E distributions. The more restrictive requirements were $-30 < \delta_E < f(E_{parton})$, where, for light jets, $f(E_{parton})$ is defined as:

$$f(E_{parton}) = \begin{cases} -3.53 + 0.793E_{parton} - 0.00237E_{parton}^2 & \text{, if } E_{parton} < 135 \text{ GeV} \\ 60.0 & \text{, if } E_{parton} > 135 \text{ GeV} \end{cases} \quad (4.7)$$

and for b jets:

$$f(E_{parton}) = \begin{cases} 4.28 + 0.847E_{parton} - 0.00267E_{parton}^2 & \text{, if } E_{parton} < 135 \text{ GeV} \\ 4.75 + 0.167E_{parton} & \text{, if } E_{parton} > 135 \text{ GeV} \end{cases} \quad (4.8)$$

The parameters for this second set of fits are given in Table 4.2. The events that survived these restrictions are shown as dots in Fig. 4.2 for light-quark jets, and in Fig. 4.3 for b-quark jets.

Table 4.1: Parameters for $W(E_{parton}, E_{jet})$ for jets from HERWIG $t\bar{t}$ events that were matched to partons.

	Light quark jets		b jets	
$p_i = a_i + b_i \times E_{parton}$	a_i	b_i	a_i	b_i
p_1 (GeV)	-1.65	-0.038	-3.41	-0.0333
p_2 (GeV)	2.84	0.067	3.98	0.0673
p_3 (dimensionless)	0.00	0.001	0.00	0.002
p_4 (GeV)	11.56	-0.302	3.36	-0.227
p_5 (GeV)	10.73	0.173	15.17	0.138

Table 4.2: Parameters for $W(E_{parton}, E_{jet})$ cutting out tails in δ_E.

	Light quark jets		b jets	
$p_i = a_i + b_i \times E_{parton}$	a_i	b_i	a_i	b_i
p_1 (GeV)	-2.07	-0.021	-3.67	-0.005
p_2 (GeV)	2.65	0.055	2.38	0.059
p_3 (dimensionless)	0.00	0.006	0.72	0.000
p_4 (GeV)	2.30	-0.130	-1.27	-0.192
p_5 (GeV)	8.39	0.077	4.97	0.128

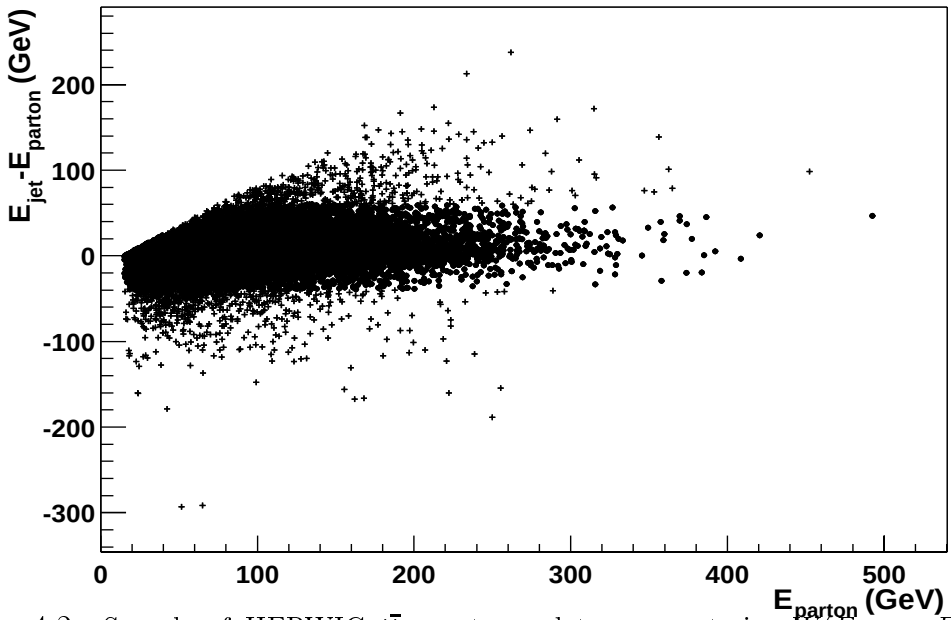

Figure 4.2: Sample of HERWIG $t\bar{t}$ events used to parameterize $W(E_{parton}, E_{jet})$ in Table 4.1 (dots and crosses), and in Table 4.2 (just dots). All events correspond to light-quark jets matched to partons generated in the range $|\eta| < 2$.

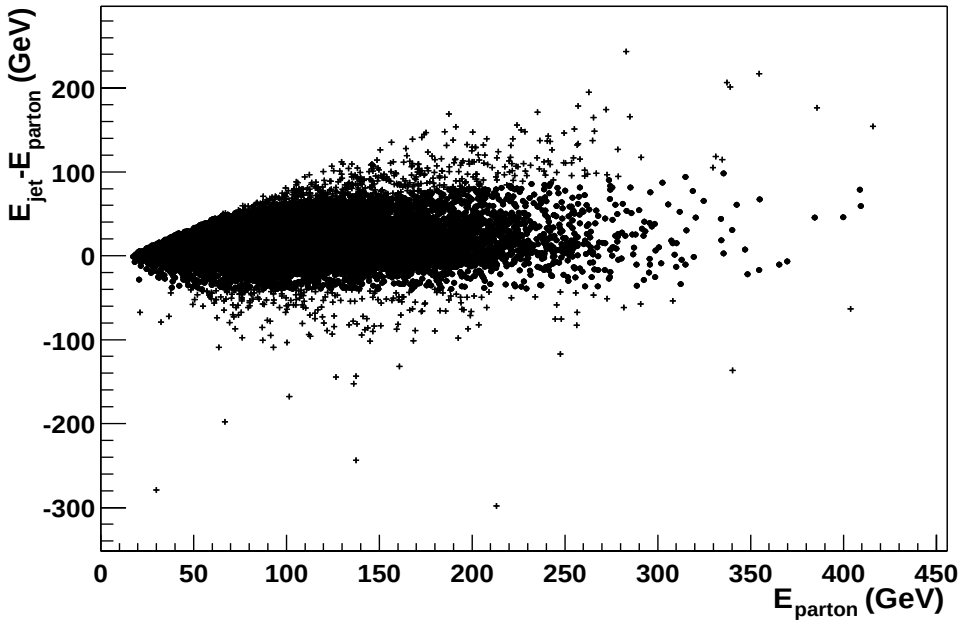

Figure 4.3: Same as Fig. 4.2, but for b-quark jets, for b quarks produced at $|\eta| < 2$.

Table 4.3: Parameters for the parton density for light quarks $n(E_{parton})$.

$\|\eta\|$ range	p_1	p_2	p_3	p_4	p_5	p_6
0.0 to 2.0	3045	55.1	26.1	1499	77.8	56.5
0.0 to 0.2	13891	-170.7	91.6	-3460	-27.4	35.2
0.2 to 0.6	33010	-210.2	102.8	-11791	-54.9	42.2
0.6 to 0.9	332	54.0	21.1	167	89.0	45.2
0.9 to 1.3	479	-2.9	78.7	-440	22.2	8.1
1.3 to 2.0	747	-114.9	123.1	-386	22.5	19.2

The quality of the parameterization can be checked by comparing the original two-dimensional distributions in (E_{parton}, E_{jet}) with the prediction using the transfer functions and $n(E_{parton})$. This is displayed in the lego contour plots of Fig. 4.4. Because it is hard to compare quantitatively such two-dimensional densities, we make one-dimensional projections of Fig. 4.4 in terms of $\delta_E = E_{parton} - E_{jet}$, for slices on parton energy. These can be calculated by integrating Eq. 4.4:

$$H(\delta_E) = \int_{E^1_{parton}}^{E^2_{parton}} dE_{parton} n(E_{parton}) W_{jet}(E_{parton}, E_{parton} - \delta_E) \quad . \tag{4.9}$$

The distribution $n(E_{parton})$ from the parton-level of the MC was parameterized for $E_{parton} > 25$ GeV, as follows:

$$n(E_{parton}) = p_1 \exp \frac{-(E_{parton} - p_2)^2}{2p_3^2} + p_4 \exp \frac{-(E_{parton} - p_5)^2}{2p_6^2} \quad . \tag{4.10}$$

The parameters $(p_1, ..., p_6)$, for different η ranges, are given in Table 4.3 for light quarks, and in Table 4.4 for b quarks. Figures 4.5a and 4.5b show the $n(E_{parton})$ distribution from the $t\bar{t}$ MC in the range $|\eta| < 2$, for light quarks and b quarks, respectively. The solid lines display results of Eq. 4.10, using the corresponding parameters given in Tables 4.3 and 4.4. The fit to b quarks is excellent, but to light quarks only moderately good. (Improving the latter would provide better agreement between the histograms and the predictions in Fig. 4.6, but, as Eqs. 4.5-4.6 show, that would not affect the determination of the transfer functions.)

Figure 4.6 shows the δ_E distributions in slices of parton energy for light quarks in the range $|\eta| < 2$. The parton energy slices ($E^{(1)}_{parton} < E_{parton} < E^{(2)}_{parton}$) are shown at the bottom of every plot. The histograms display the results for HERWIG $t\bar{t}$ MC jets

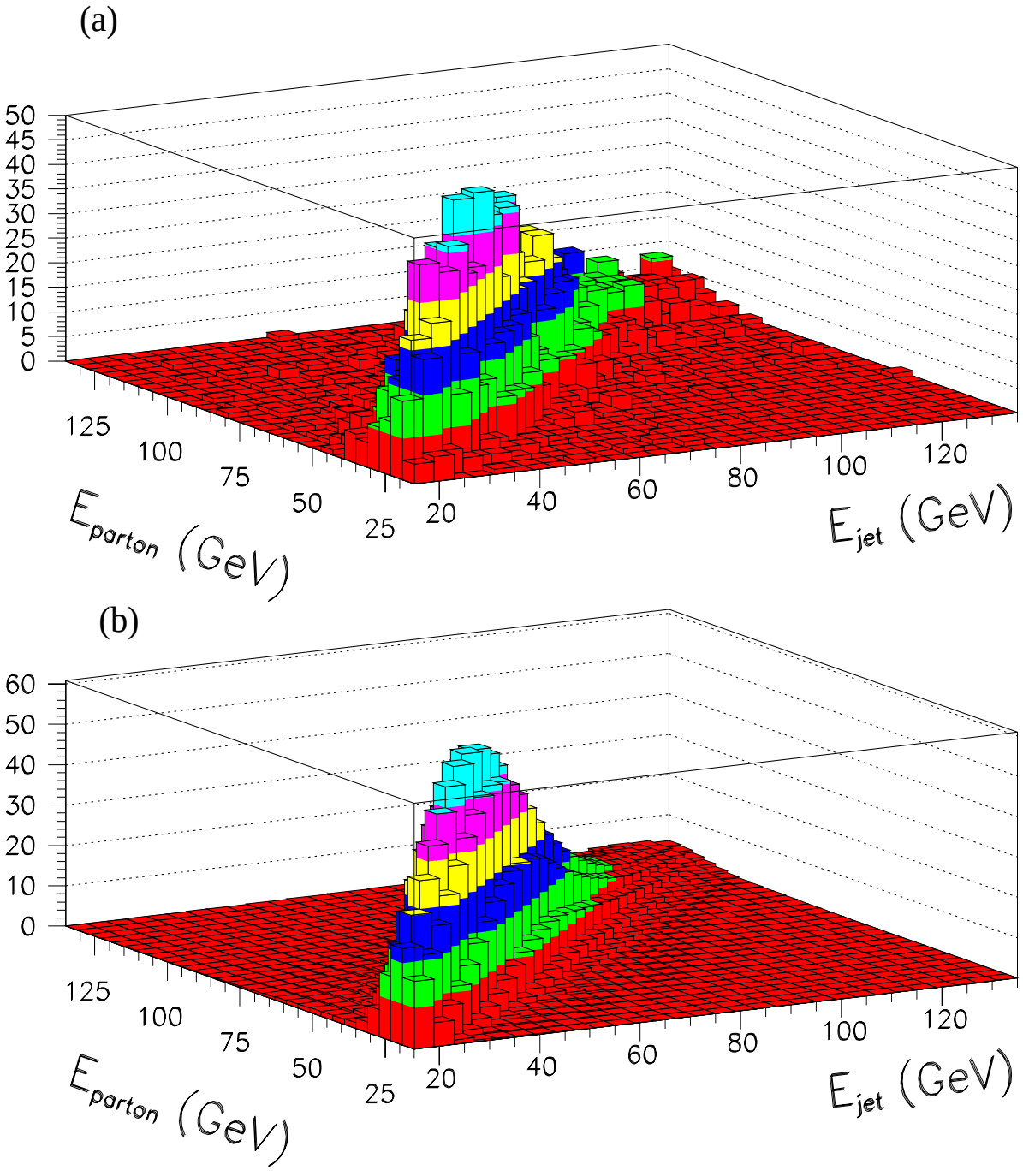

Figure 4.4: (a) Lego plot of E_{parton} vs E_{jet} for a sample of jets associated with partons in HERWIG $t\bar{t}$ Monte Carlo events, where the jets were passed through DØ detector simulation (CAFIX corrections included). (b) Lego plot of E_{parton} vs E_{jet}, where E_{jet} is predicted using $n(E_{parton})$ and the transfer function of Table 4.1.

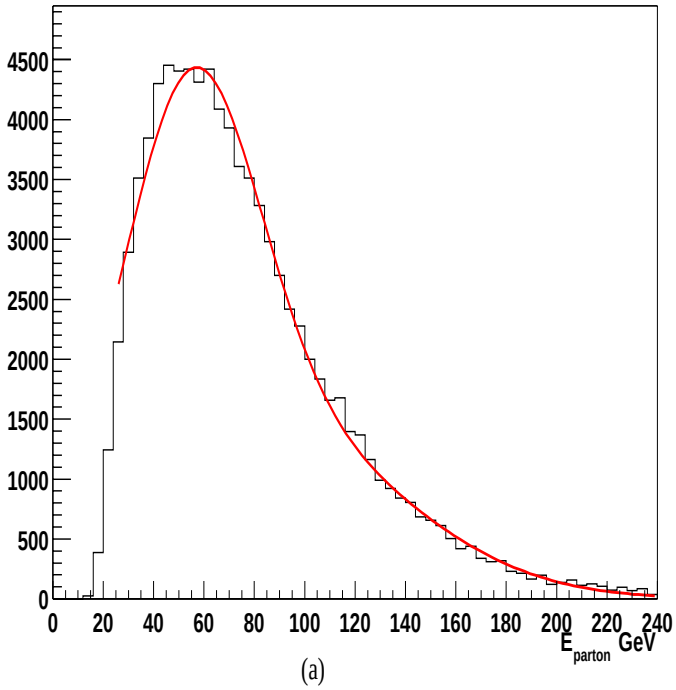

(a)

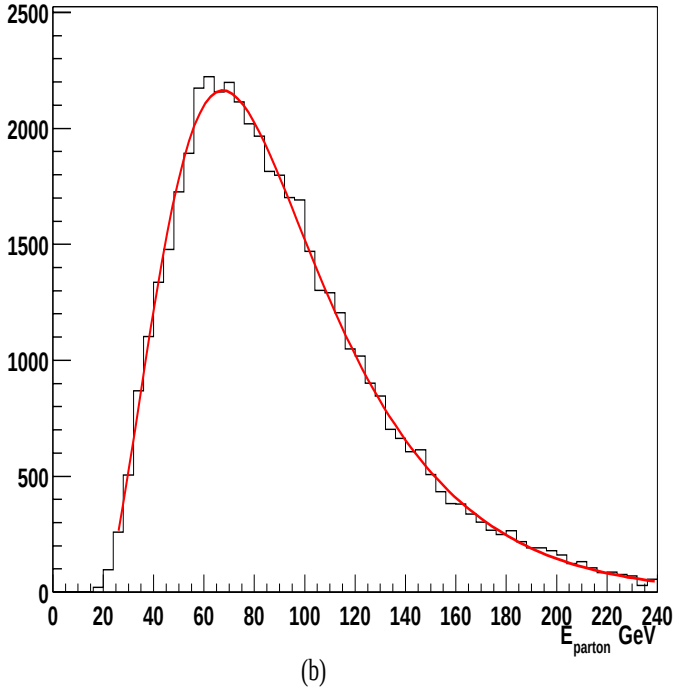

(b)

Figure 4.5: Distributions in $n(E_{parton})$ for light-quark jets (a) and b jets (b) (with $|\eta| < 2$) in $t\bar{t}$ events. The line corresponds to the fit given by Eq. 4.10 (for $E_{parton} > 25$ GeV) using the corresponding set of parameters from Table 4.3 and Table 4.4, respectively.

Table 4.4: Parameters for the b-parton density $n_b(E_{parton})$.

$\|\eta\|$ range	p_1	p_2	p_3	p_4	p_5	p_6
0.0 to 2.0	30987	-192.8	119.9	-7931	-0.169	31.3
0.0 to 0.2	1472	-93.8	86.7	-675	8.87	24.3
0.2 to 0.6	320	62.8	19.7	163	102.1	38.6
0.6 to 0.9	347	30.6	63.0	-21443	-305.4	113.9
0.9 to 1.3	157	78.9	24.6	55.1	133.9	44.8
1.3 to 2.0	89.4	86.2	23.5	54.1	146.9	45.1

(after CAFIX corrections). The dashed-dotted lines correspond to the function $H(\delta_E)$ calculated using the Table 4.1 parameters, and the solid line to $H(\delta_E)$ calculated using Table 4.2. Figure 4.7 shows the analogous δ_E distributions for b quarks.

Similar comparisons of distributions in δ_E, but for smaller ranges of η, are given in Appendix A of DØ Note 3975 [61]. In general, the functions based on Table 4.1 agree better in the tails of the MC, while functions based on Table 4.2 represent the peak regions more accurately.

It is, of course, also possible to generate projections of E_{jet} for slices on E_{parton}, and vice versa:

$$H(E_{jet}) = \int_{E^{(1)}_{parton}}^{E^{(2)}_{parton}} dE_{parton} n(E_{parton}) W_{jet}(E_{parton}, E_{jet}) \quad , \tag{4.11}$$

$$H(E_{parton}) = \int_{E^{(1)}_{jet}}^{E^{(2)}_{jet}} dE_{jet} n(E_{parton}) W_{jet}(E_{parton}, E_{jet}) \quad . \tag{4.12}$$

Comparison plots of $H(E_{jet})$ and of $H(E_{parton})$ are given in Appendix 2 of DØ Note 3975 [61].

4.3 Further Checks of W_{jet}: Invariant Masses and cos$\hat{\phi}$

The transfer function models the smearing in jet energies produced by the combined effects of radiation, hadronization, measurement resolution, and jet reconstruction algorithm. In the previous section, we compared energy distributions of jets matched to partons with those calculated by applying the transfer function to partons. In this section, we will compare two-jet (W) and three-jet (top) invariant masses calculated

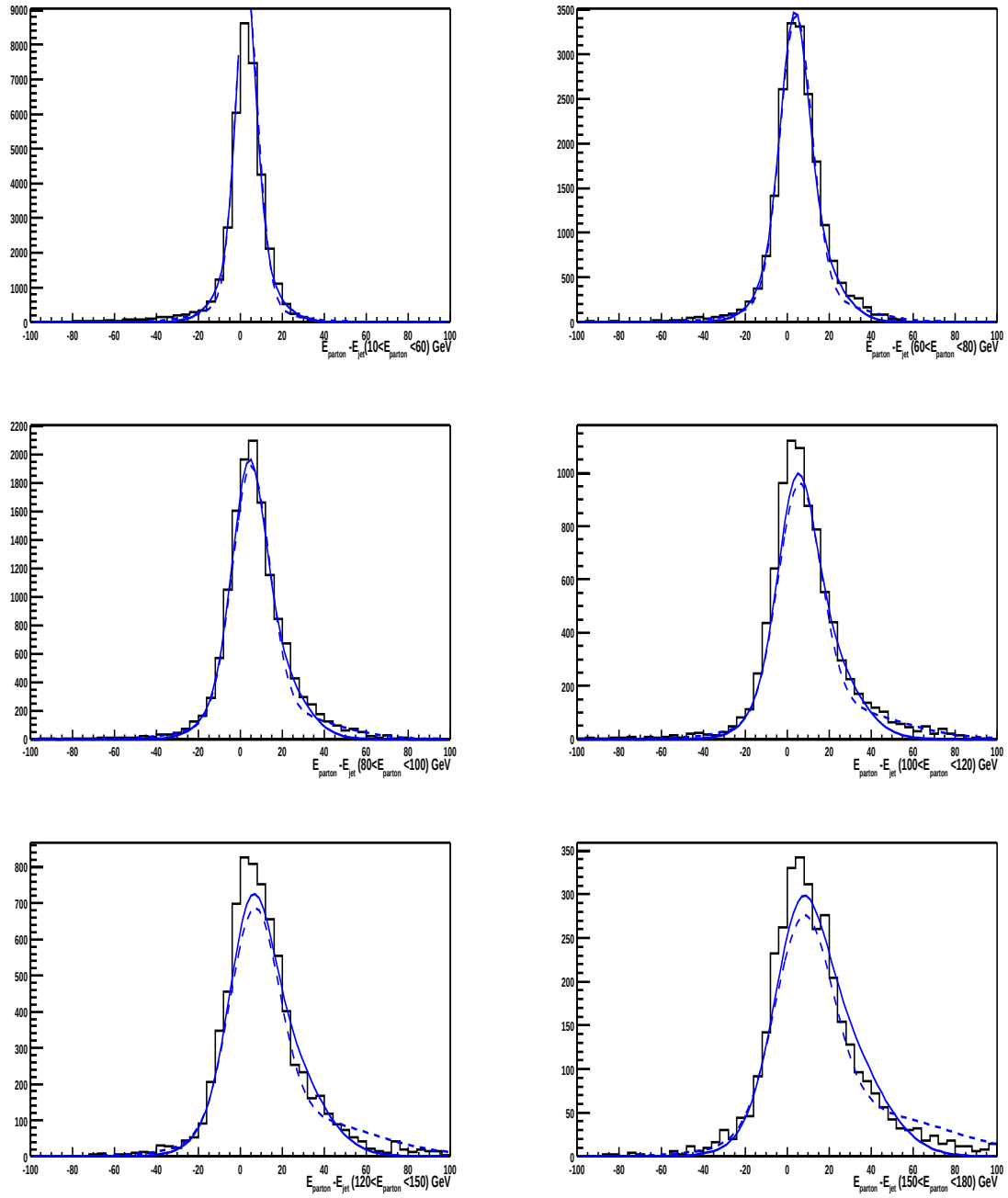

Figure 4.6: Distributions in $\delta_E = E_{parton} - E_{jet}$ for different ranges of parton energy for matched light-quark jets in the range $|\eta| < 2$. The histograms are for HERWIG $t\bar{t}$ MC events after full DØ simulation and CAFIX energy corrections. The selections are the same as used in the Run I mass analysis, but the jets are only those that match to partons. The dashed-dotted line corresponds to $H(\delta_E)$ using the Table 4.1 parameters, and the solid line is $H(\delta_E)$ calculated with the parameters of Table 4.2.

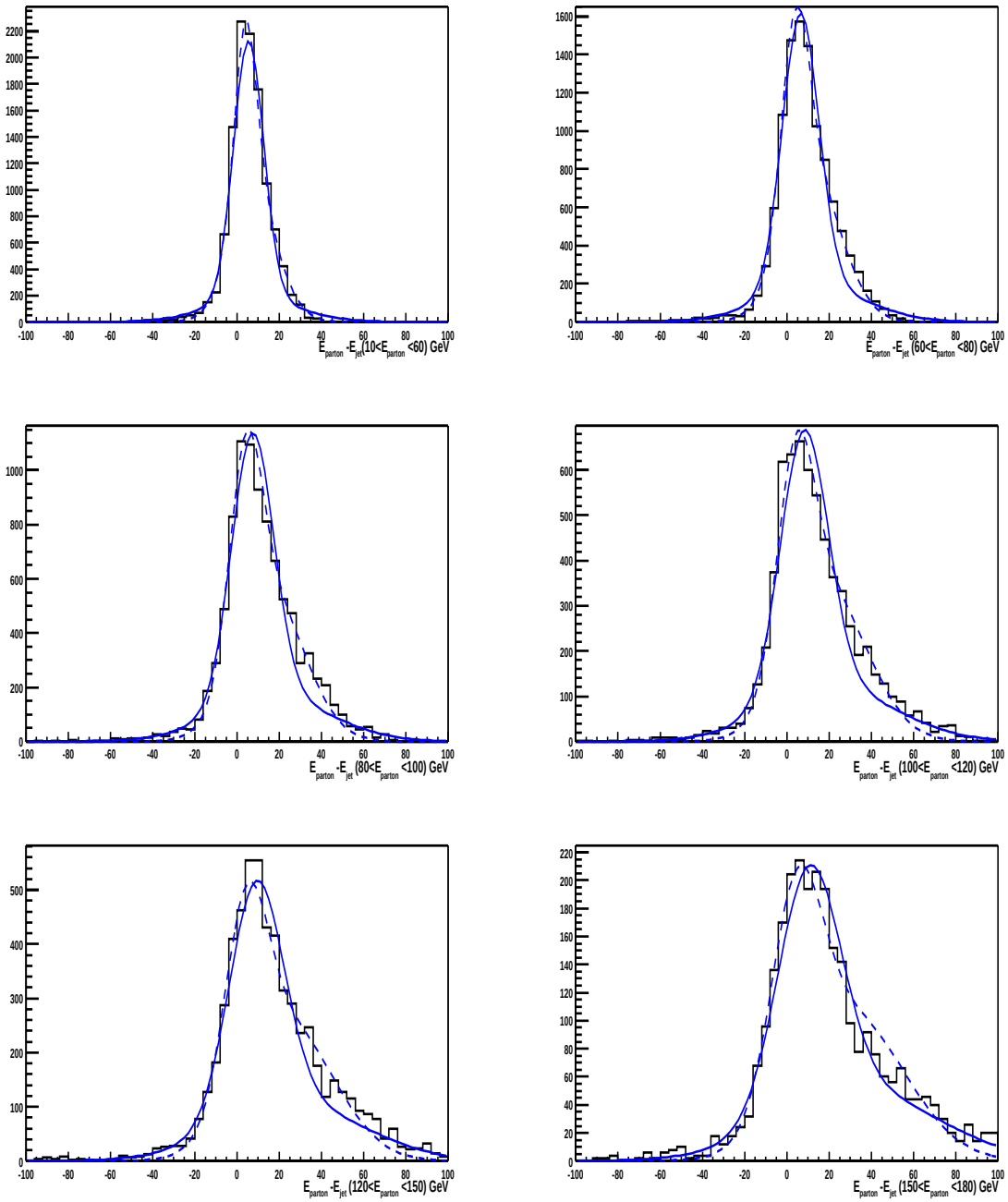

Figure 4.7: Same as in Fig. 4.6, but for matched b jets.

directly using MC jets, with predictions based on the transfer functions. We will do a similar comparison for $\cos\hat{\phi}$ (Section 1.2.5). We use masses to check the transfer functions because they correspond to more intuitive variables that are also sensitive to jet resolution. To assure that the mapping is acceptable, it is important to check that all possible jet combinations used in the mass calculation are reproduced by the transfer function, independent of whether the jets match to partons.

As shown in Appendix F, the transfer function $W_{jet}(E_{parton}, E_{jet})$ can be used to calculate any one-dimensional distribution through integration over appropriate Jacobians:

$$\frac{dN}{dm_x} = \frac{V}{N_{gen}} \sum_{acc} \sum_{perm.} \int dE_{jet}^{(2)} ... dE_{jet}^{4} J(\frac{E_{jet}^{(1)} E_{jet}^{(2)} ... E_{jet}^{(4)}}{m_x E_{jet}^{(2)} ... E_{jet}^{(4)}}) \prod_{i=1}^{4} Acc(E_{jet}^{(i)}) W_{jet}(E_{parton}^{(i)}, E_{jet}^{(i)}) \tag{4.13}$$

Since we will be normalizing the distributions to MC events, the volume V can be treated as a normalization constant, and does not have to be evaluated. The sum $\sum_{acc}$ extends over all the MC events that pass reconstruction and any other imposed criteria. Once an event is accepted, only the quark energies $E_{parton}^{(i)}$ enter into the calculation of the integral.

For example, for the two-jet invariant mass, defined as $m^2 = 2E_{jet}^{(1)} E_{jet}^{(2)} (1 - \cos\theta_{12})$, where we ignore the individual jet masses, the Jacobian becomes

$$J(\frac{E_{jet}^{(1)} E_{jet}^{(2)}}{m\ E_{jet}^{(2)}}) = \frac{m}{E_{jet}^{(2)}(1 - \cos\theta_{12})} \tag{4.14}$$

and therefore

$$\begin{aligned} \frac{dN}{dm} = \frac{V}{N_{gen}} \sum_{perm.} & \int_{E_{min}}^{E_{max}} dE_{jet}^{(4)} W_{jet}(E_{parton}^{(4)}, E_{jet}^{(4)}) \\ & \times \int_{E_{min}}^{E_{max}} dE_{jet}^{(3)} W_{jet}(E_{parton}^{(3)}, E_{jet}^{(3)}) \\ & \times \int_{E_{min}}^{E_{max}} \frac{dE_{jet}^{(2)}}{E_{jet}^{(2)}} \frac{m}{1 - \cos\theta_{12}} W_{jet}(E_{parton}^{(1)}, E_{jet}^{(1)}) W_{jet}(E_{parton}^{(2)}, E_{jet}^{(2)}) \quad , \end{aligned} \tag{4.15}$$

where E_{min} is the minimum jet energy, and E_{max} is large enough to include all jets. A similar calculation applies for the three-jet invariant mass.

The integrals in Eq. 4.15, and the analogous ones for the three-jet invariant mass,

were calculated using 1000 (generator-level) PYTHIA events with all quarks in $|\eta| < 2$, and leptons with $|\eta| < 2$, and $|p_T| > 15$ GeV/c, $E_{min} = 15$ GeV, and $E_{max} = 400$ GeV. The resulting distributions were compared with invariant masses calculated directly from $t\bar{t}$ MC events, generated for the original Run I top-mass analysis. (These were obtained using HERWIG for M_t =175 GeV/c^2, passed through the DØ simulation and reconstruction package, with jets subjected to the standard DØ CAFIX corrections.) Figures 4.8-4.21 display the comparisons between the direct and the calculated quantities.

Figures 4.8 and 4.9 show the three-jet invariant mass for four-jet events, when all four jets are matched to partons. The correct combinations of jets that yield the top quark appear in Fig. 4.8, and all combinations of 3-jets are given in Fig. 4.9. The 3-jet mass for all combinations of jets in events with four jets, but without imposition any matching requirement, is shown in Fig. 4.10. The analogous distributions in the two-jet invariant mass are shown in the same order in Figs. 4.11, 4.12, and 4.13. In all figures, the error bars correspond to HERWIG MC events. The dashed-dotted lines correspond to distributions in invariant mass dN/dm calculated using Eq. 4.15 (or the equivalent for three jets) and the parameters of Table 4.1; the solid lines are based on Table 4.2. The inner graphs show the χ^2 per degree of freedom calculated as the distribution with error bars is shifted with respect to the curves. The horizontal lines in the inner plot mark a χ^2 change of one unit (one standard deviation).

Several conclusions can be drawn from an examination of the above plots: 1) The shifts of the calculations for the two choices of parameters relative to the MC events are not statistically significant. 2) The agreement for the right combination is excellent, with a χ^2 very close to unity. 3) The χ^2 becomes worse when all combinations are included, but, nevertheless, the shapes of all distributions are quite similar. (In our analysis, each combination is weighted with the matrix element, and rarely do more than two combinations contribute in a significant way.) 4) There is not much change in overall agreement when jets that are not matched to partons are also included in the comparisons.

Finally, similar studies were performed for the W+4 jets background. The integrals in Eq. 4.15, and the equivalent for the three-jet invariant mass, were evaluated using 1000 VECBOS events (parton-level, with $W \to l\nu$), with similar conditions as used for $t\bar{t}$: $|\eta_{quarks}| < 2$, E_{min}=15 GeV, and $E_{max} = 400$ GeV. The results were compared with the invariant masses calculated using jets from the VECBOS/ISAJET W+jets MC events

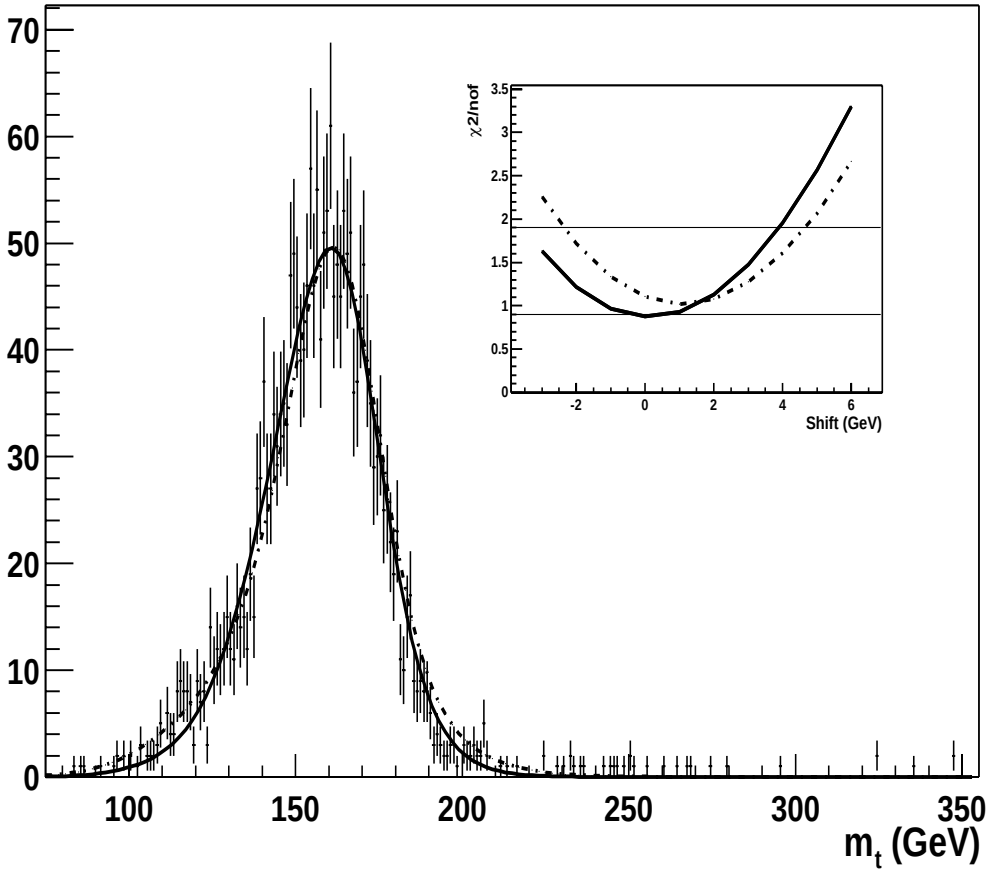

Figure 4.8: Invariant mass distribution of the three jets from the decay of the top quark. The error bars correspond to HERWIG $t\overline{t}$ MC events generated with $M_t = 175$ GeV/c^2, using full DØ simulation and CAFIX energy corrections. The selections are the same as used in the Run I mass analysis, but also require that the four jets be matched to their corresponding quarks. The dashed-dotted line corresponds to the three-jet invariant mass distribution dN/dm_t calculated using the parameters of Table 4.1, and the solid line uses those of Table 4.2. The inner graph shows the χ^2 per degree of freedom (calculated between 100 and 205 GeV/c^2) as the plot with error bars is shifted relative to the curves. The horizontal lines in the inner plot mark a χ^2 change of one unit (one standard deviation in m_t relative to the minimum value).

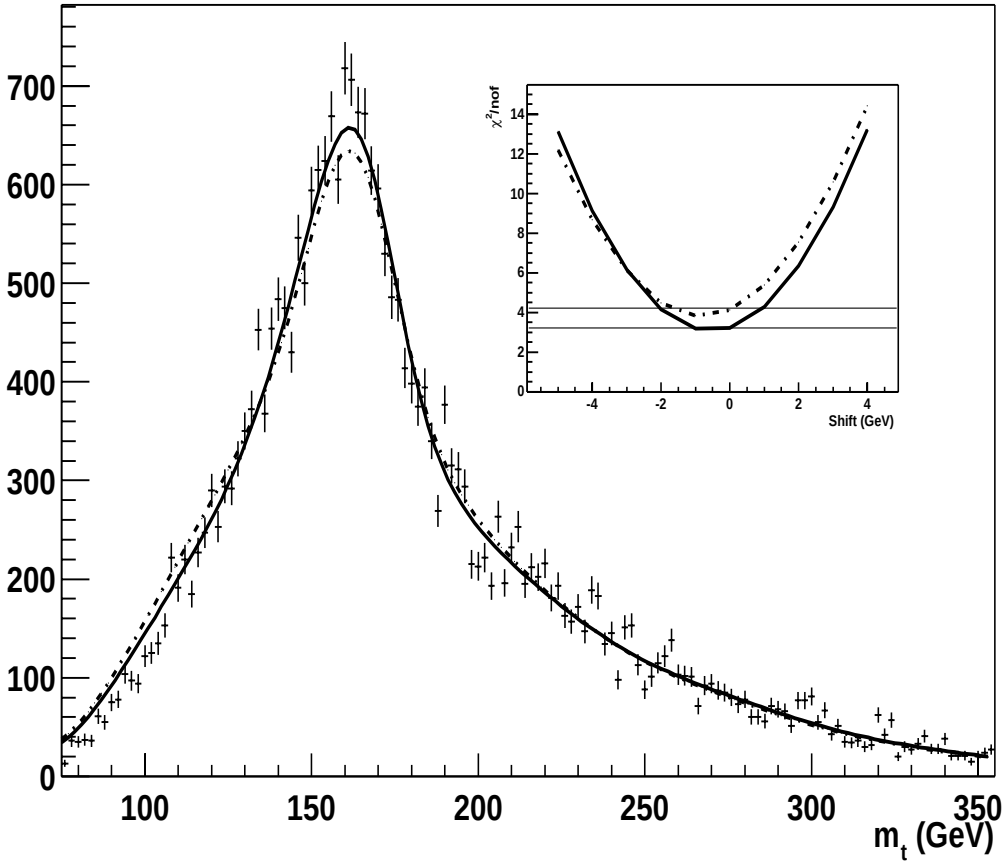

Figure 4.9: Same plot as in Fig. 4.8, but using all possible combinations of the three-jet invariant mass in four-jet events. The χ^2 was calculated between 90 and 335 GeV/c^2.

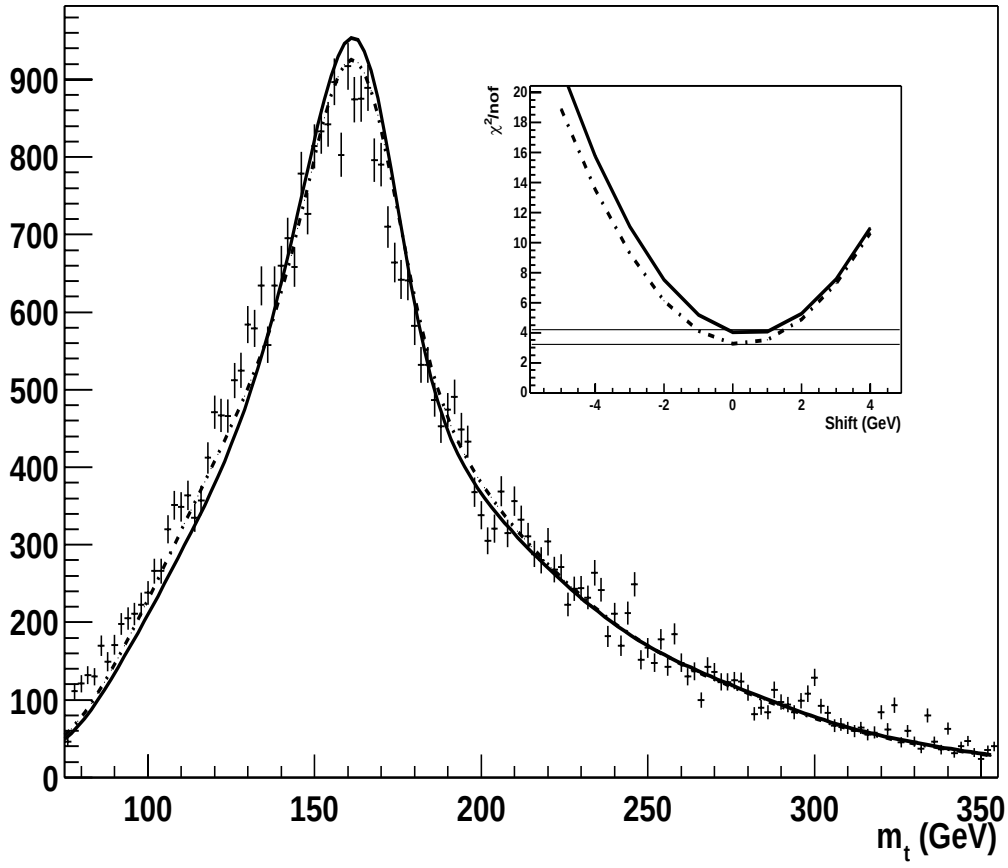

Figure 4.10: Same plot as in Fig. 4.9, but without the requirement of matching between jets and partons. All events have exactly four jets, and all possible jet combinations are used in the three-jet invariant mass. The χ^2 was calculated between 90 and 335 GeV/c^2.

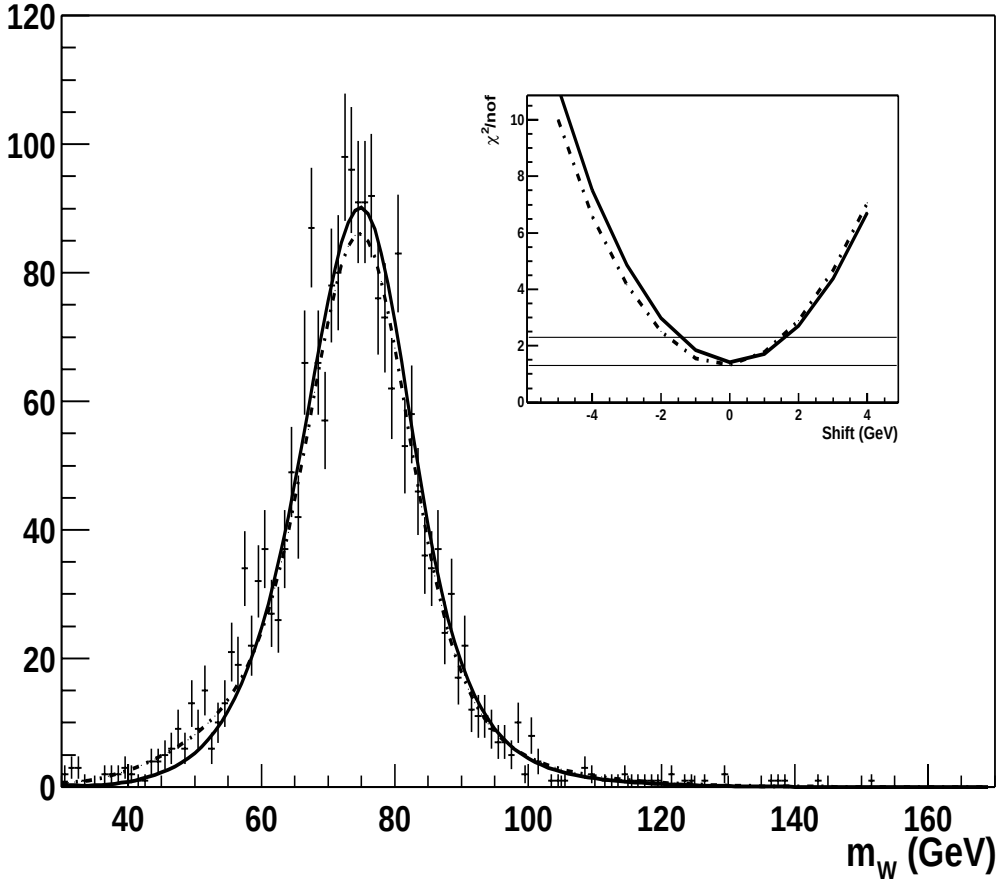

Figure 4.11: Invariant mass distribution of the two jets from the decay of the W. The error bars correspond to HERWIG $t\bar{t}$ MC events generated with M_t=175 GeV/c^2 (and M_W=80.4 GeV/c^2), using full DØ simulation and CAFIX energy corrections. The selections are the same as used in the Run I mass analysis, but also require that all four jets be matched to their corresponding quarks. The dashed-dotted line corresponds to the two-jet invariant mass distribution dN/dm_W calculated using Eq. 4.15 and the parameters of Table 4.1; the solid line uses the parameters of Table 4.2. The inner graph shows the χ^2 per degree of freedom (calculated between 40 and 110 GeV/c^2) as the plot with error bars is shifted relative to the curves. The horizontal lines in the inner plot mark a χ^2 change of one unit relative to the minimum in m_W.

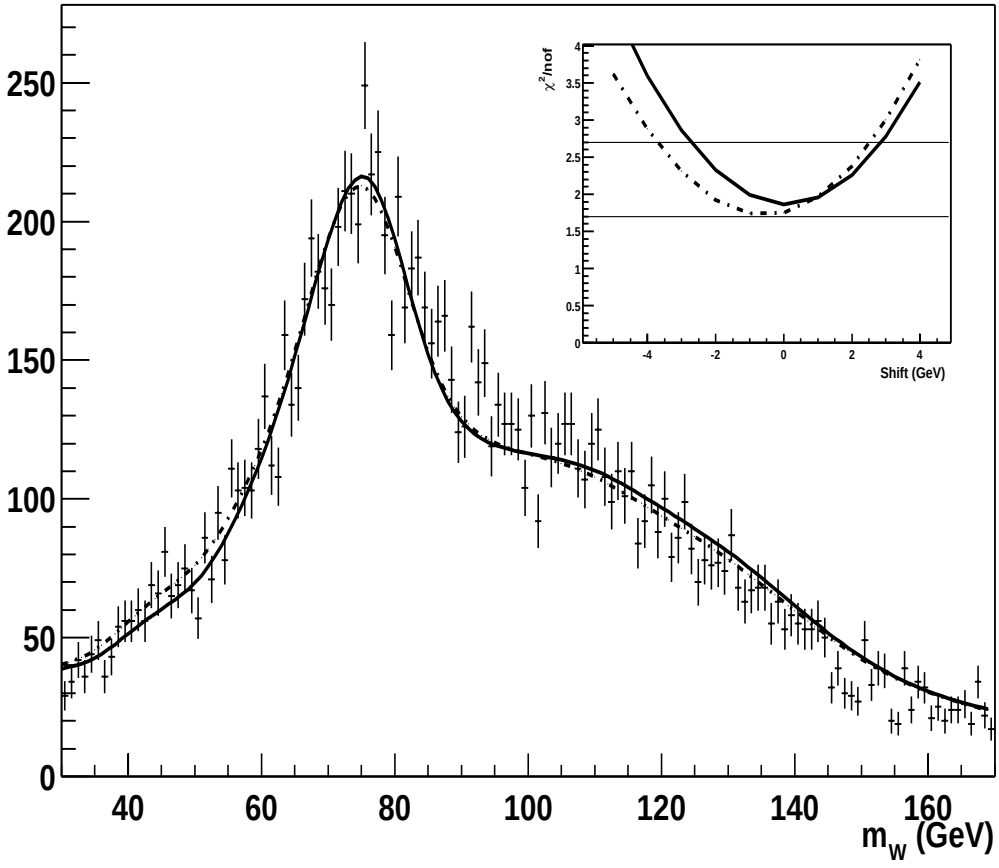

Figure 4.12: Same plot as in Fig. 4.11, but using all possible combinations of two-jet invariant mass in four-jet events. The χ^2 was calculated between 40 and 160 GeV/c^2.

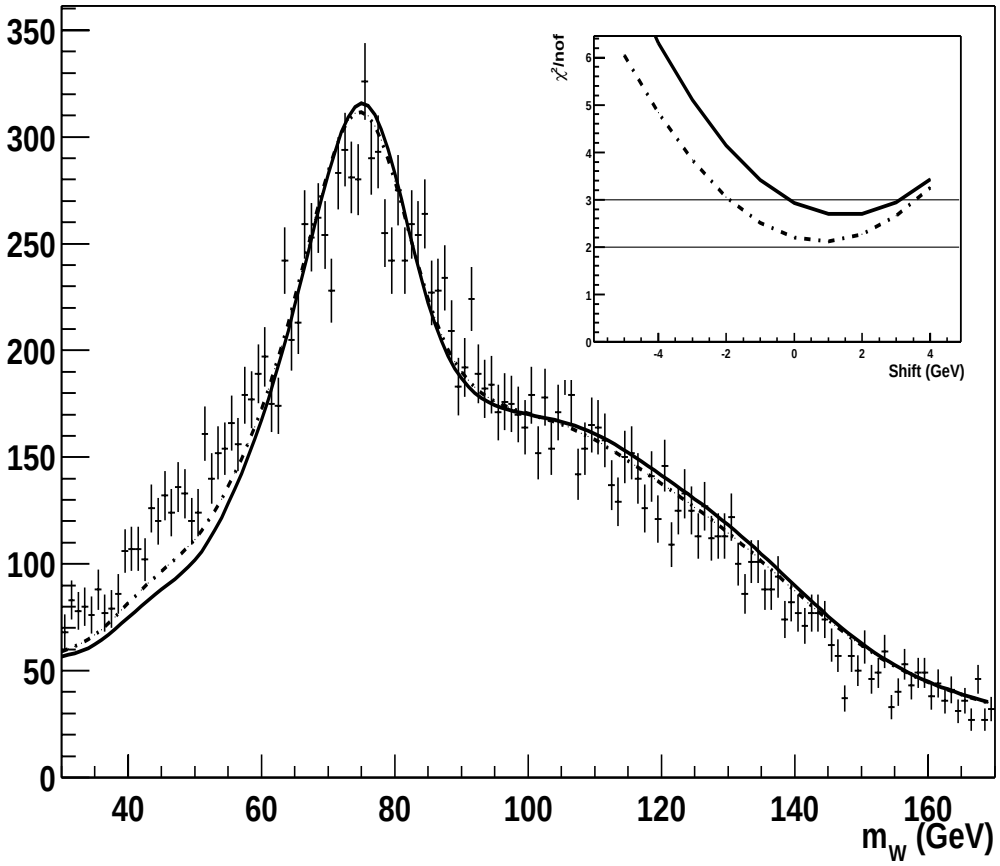

Figure 4.13: Same plot as in Fig. 4.12, but without the requirement of matching between jets and partons. All events have four jets, and all possible jet combinations are used in the two-jet invariant mass. The χ^2 was calculated between 40 and 160 GeV/c^2.

used in the previous Run I analysis. (These events were generated using VECBOS, "hadronized" with ISAJET [68], and passed through the DØ simulation and reconstruction package. Again, standard jet corrections (CAFIX) were applied to account for calorimeter effects and for the underlying event.)

Figures 4.14, 4.16 and 4.15, 4.17 provide, respectively, the distributions analogous to Figs. 4.9, 4.10 and 4.12, 4.13, for the W+4 jets events, using the parameters of Table 4.2. The agreement in Figs. 4.14–4.17 is still quite good, but not as good as observed for top events. This could be due to the fact that the transfer function was obtained using HERWIG, and the hadronization for the W+4 jets sample used ISAJET. In addition, the transfer function was obtained for light-quark jets and b jets, and the jets in W+jets are primarily gluon jets, which we have not as yet parameterized. To study this discrepancy further, we generated a transfer function using jets from VECBOS/ISAJET events (including standard DØ reconstruction and corrections). The parameters for this transfer function are given in Table 4.5. Figures 4.18 to 4.21 show the same plots as given in Fig. 4.14-4.17, but with the invariant masses predicted using the parameters of Table 4.5. We can see that, although the χ^2 does not improve very much, the agreement in shape is better using Table 4.5.

Table 4.5: Parameters for $W(E_{parton}, E_{jet})$ based on VECBOS/ISAJET events.

	All jets	
$p_i = a_i + b_i \times E_{parton}$	a_i	b_i
p_1 (GeV)	-1.434	0.018
p_2 (GeV)	3.728	0.068
p_3 (dimensionless)	0.000	0.002
p_4 (GeV)	2.770	-0.106
p_5 (GeV)	8.220	0.114

We also smeared PYTHIA $t\bar{t}$ events using Table 4.2 (see Section 5). In Fig. 4.22, we compare the p_T of the lepton and the $\cos\hat{\phi}_{ub}$ distribution between the smeared events and fully reconstructed HERWIG $t\bar{t}$ events (see Section 6). To identify the jets and leptons in the sample we matched the reconstructed objects to partons. We required a δR<0.15 for matched jets, and δR<0.1 for matched leptons ($\delta R = \sqrt{(\Delta\eta)^2 + (\Delta\phi)^2}$). Although these distributions are not as sensitive to discrepancies as the calculated top and W masses, there is good agreement between the transformed parton-level distributions and those obtained directly from reconstructed events. We make the same comparison in

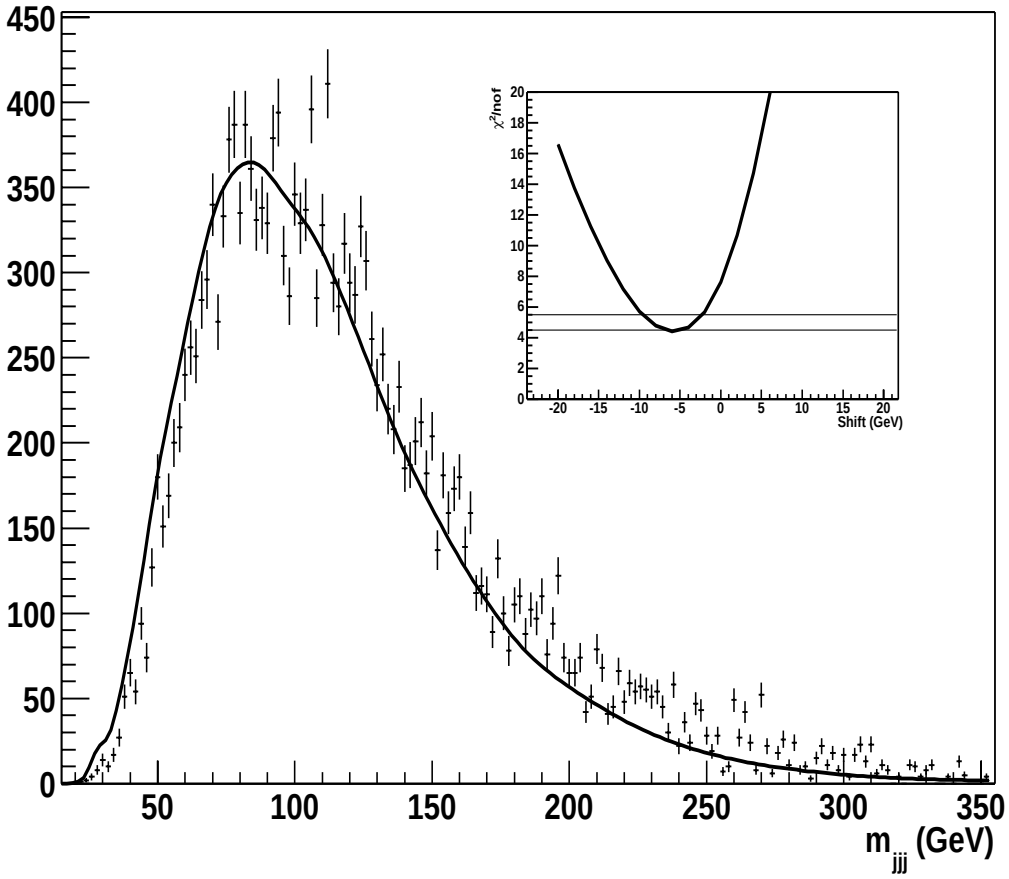

Figure 4.14: Three-jet invariant mass distribution for MC W+4 jets events. The points with error bars correspond to events generated with VECBOS/ISAJET with full DØ simulation/reconstruction and CAFIX energy corrections. The selections are the same as used in the Run I mass analysis, but require exactly four jets and a match of all four jets to their corresponding quarks. All jet combinations are used in the calculation of the three-jet invariant mass. The solid line corresponds to the three-jet invariant mass distribution dN/dm calculated using the parameters of Table 4.1. The inner graph shows the χ^2 per degree of freedom (calculated between 40 and 335 GeV/c^2) when the plot with error bars is shifted with respect to the curve. The horizontal lines in the inner plot mark a χ^2 change of one unit.

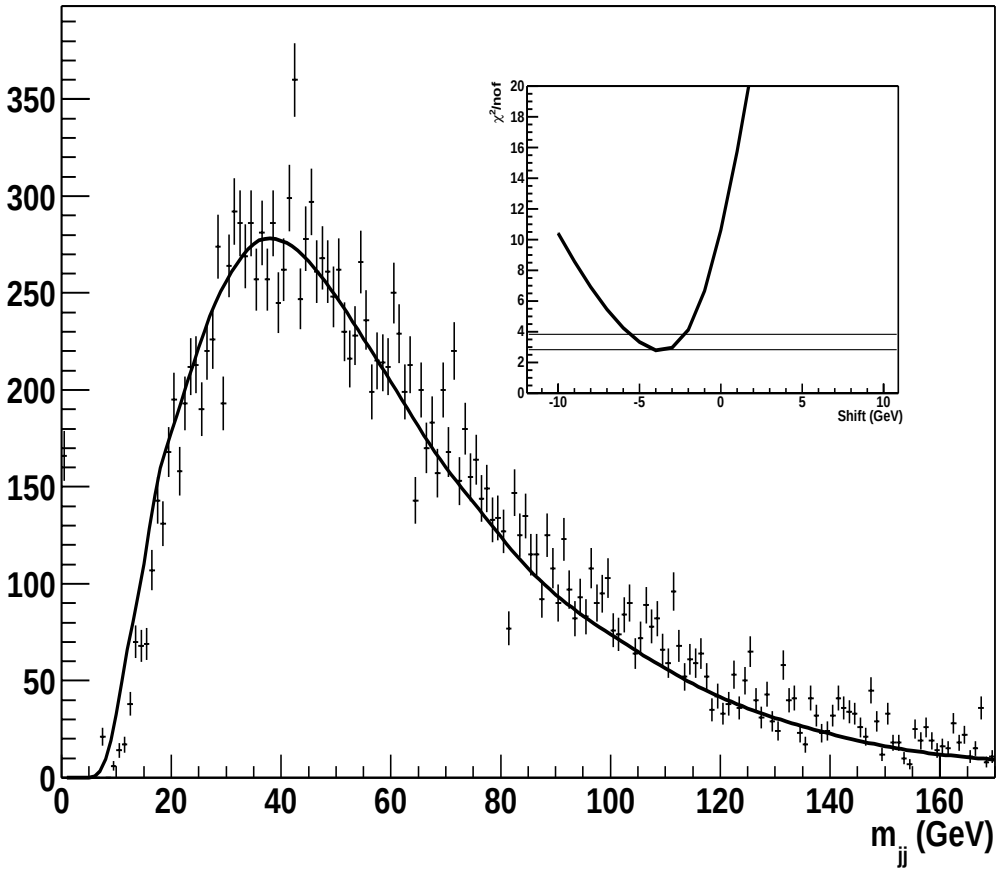

Figure 4.15: Two-jet invariant mass distribution for MC W+4 jets events. The points with error bars correspond to events generated with VECBOS/ISAJET with full DØ simulation/reconstruction and CAFIX energy corrections. The selections are the same as used in the Run I mass analysis, but require exactly four jets and a match of all four jets to their corresponding quarks. All jet combinations are used in the calculation of the two-jet invariant mass. The solid line corresponds to the two-jet invariant mass distribution dN/dm calculated using the parameters of Table 4.1. The inner graph shows the χ^2 per degree of freedom (calculated between 10 and 160 GeV/c^2) when the plot with error bars is shifted with respect to the curve. The horizontal lines in the inner plot mark a χ^2 change of one unit.

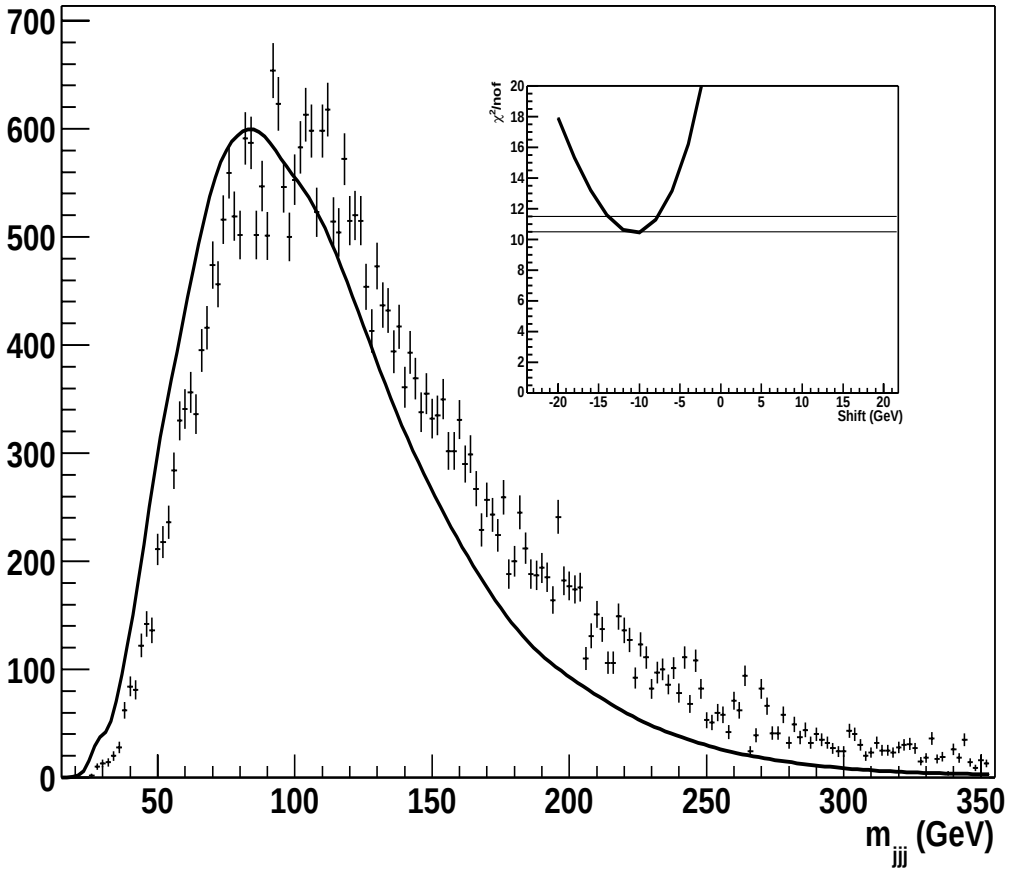

Figure 4.16: Same plot as in Fig. 4.14, but without the requirement of matching between jets and partons. All events have exactly four jets, and all possible combinations are used. The χ^2 is calculated between 40 and 335 GeV/c^2.

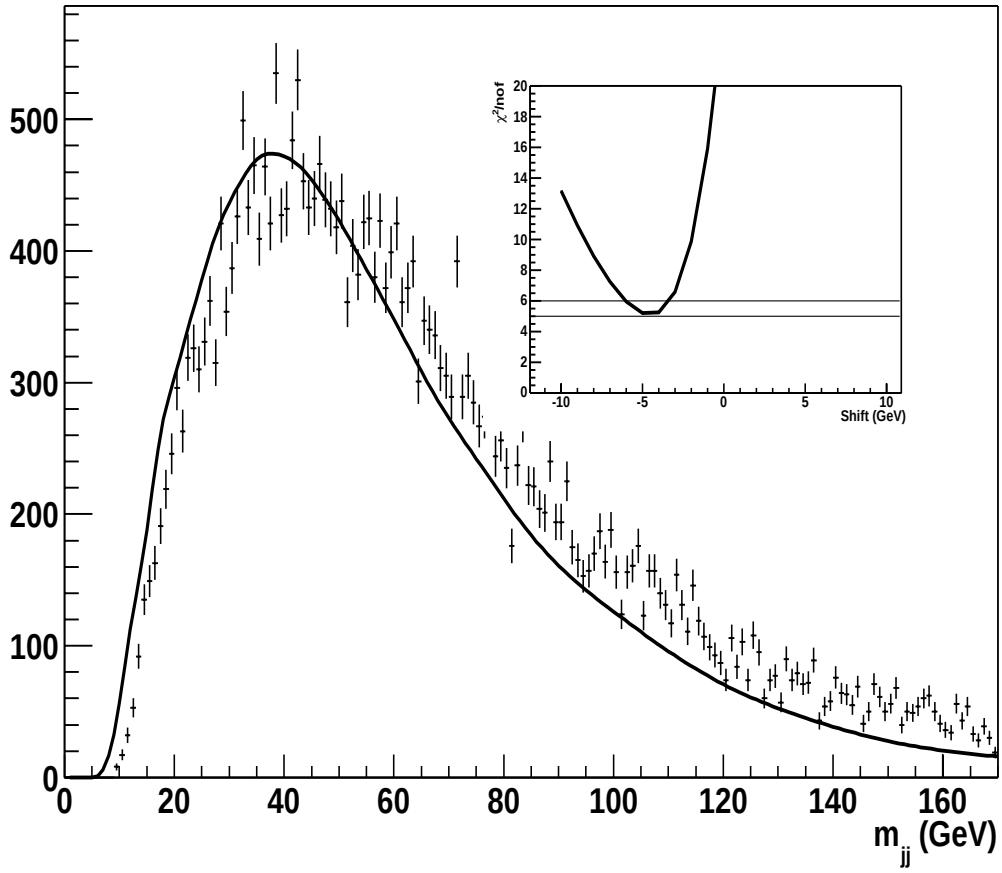

Figure 4.17: Same plot as in Fig. 4.15, but without the requirement of matching between jets and partons. All events have exactly four jets, and all possible jet combinations are used in the two-jet invariant mass. The χ^2 is calculated between 10 and 160 GeV/c^2.

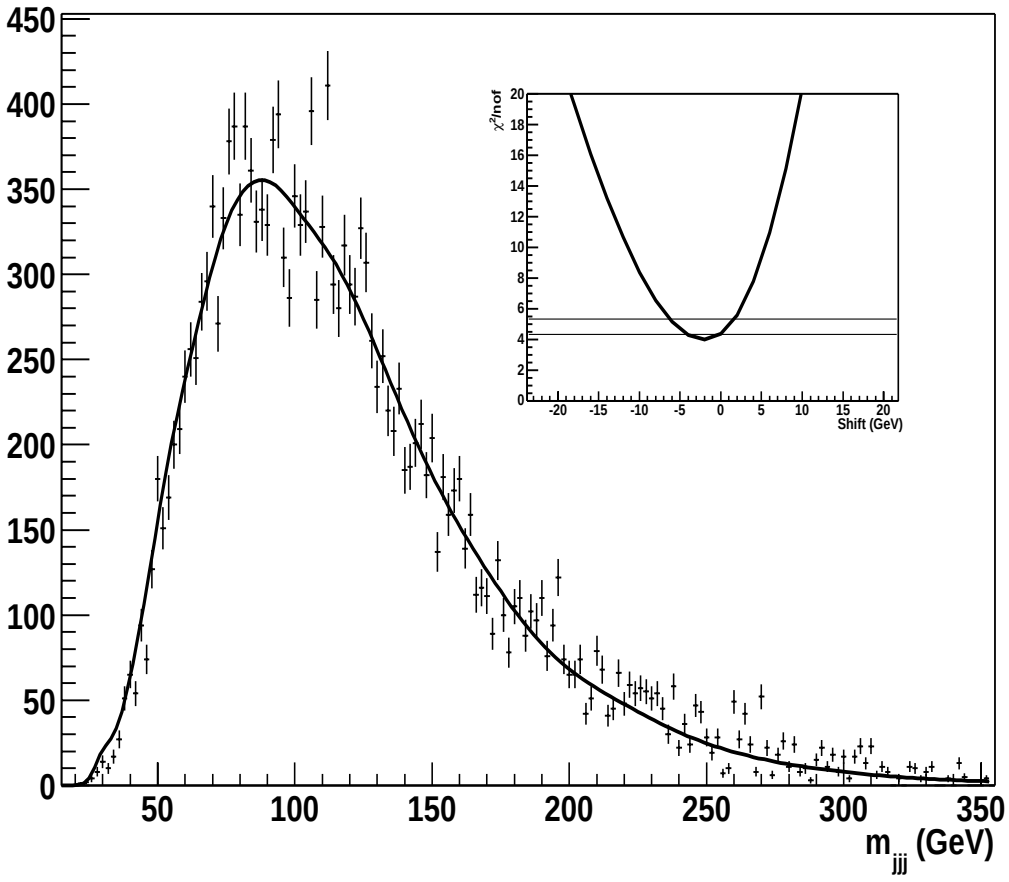

Figure 4.18: Same plot as in Fig. 4.14, but with the solid line calculated using Table 4.5. The χ^2 is evaluated between 40 and 335 GeV/c^2.

Fig. 4.23 between reconstructed VECBOS/ISAJET and transformed VECBOS events (using Table 4.5) events. We observe a small discrepancy at large $|\cos\hat{\phi}_{ub}|$, which could be indicative of additional effects from gluon radiation, not accounted for in the transfer function.

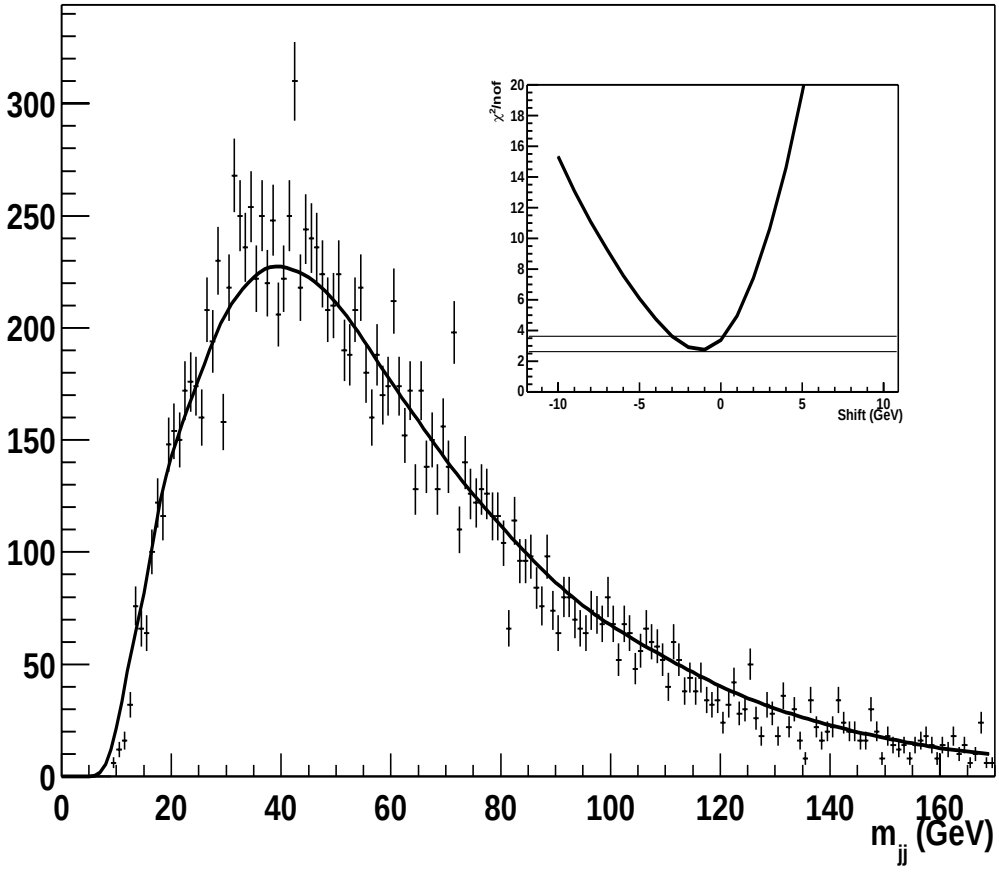

Figure 4.19: Same plot as in Fig. 4.15, but with the solid line calculated using Table 4.5. The χ^2 is evaluated between 10 and 160 GeV/c^2.

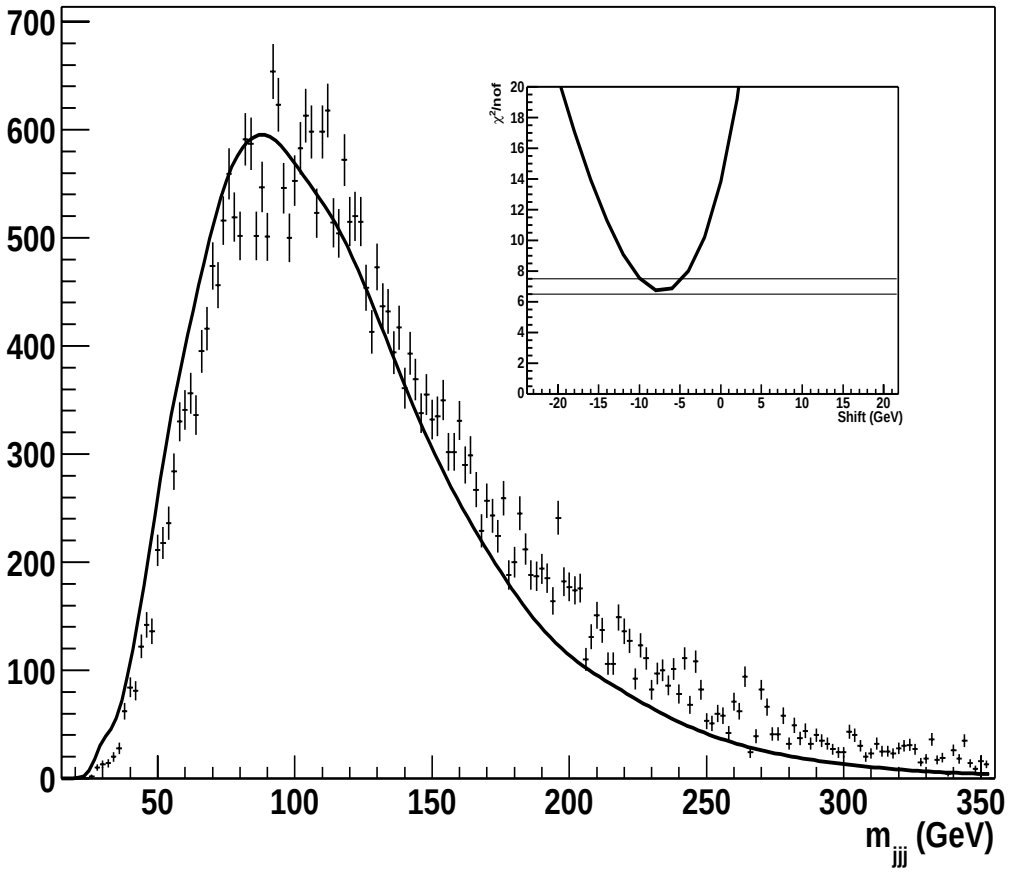

Figure 4.20: Same plot as in Fig. 4.16, but with the solid line calculated using Table 4.5. The χ^2 is evaluated between 40 and 335 GeV/c^2.

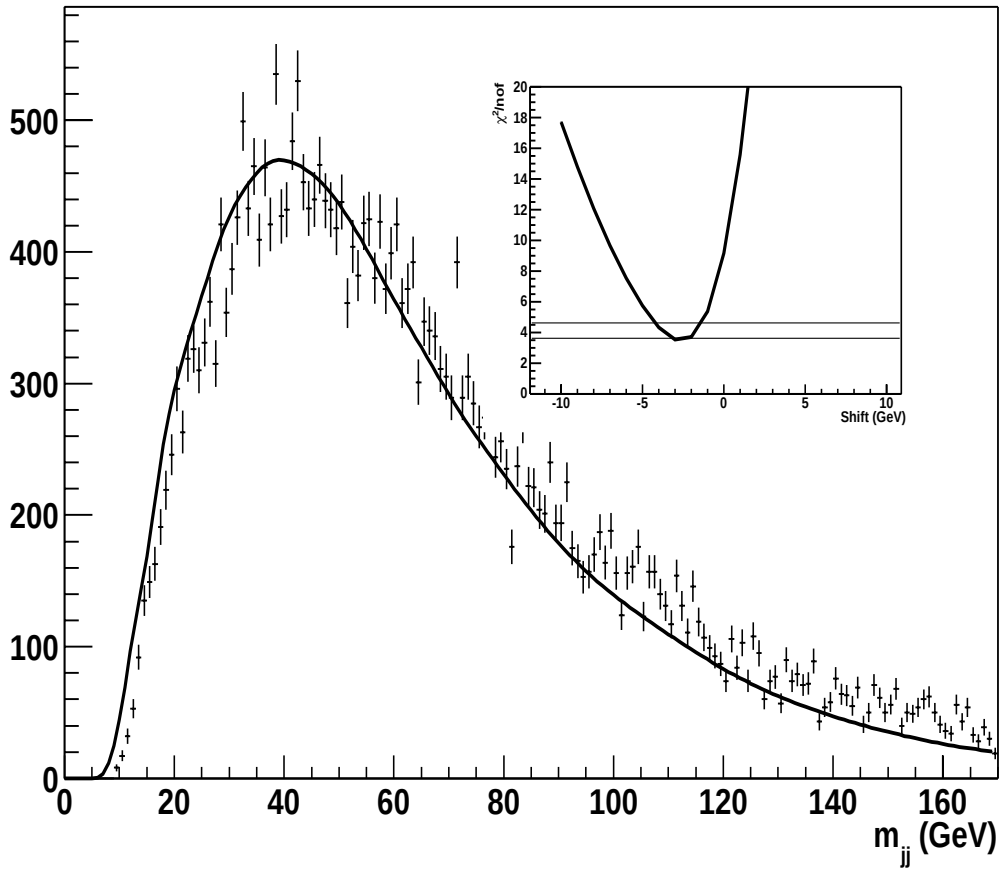

Figure 4.21: Same plot as in Fig. 4.17, but with the solid line calculated using Table 4.5. The χ^2 is evaluated between 10 and 160 GeV/c^2.

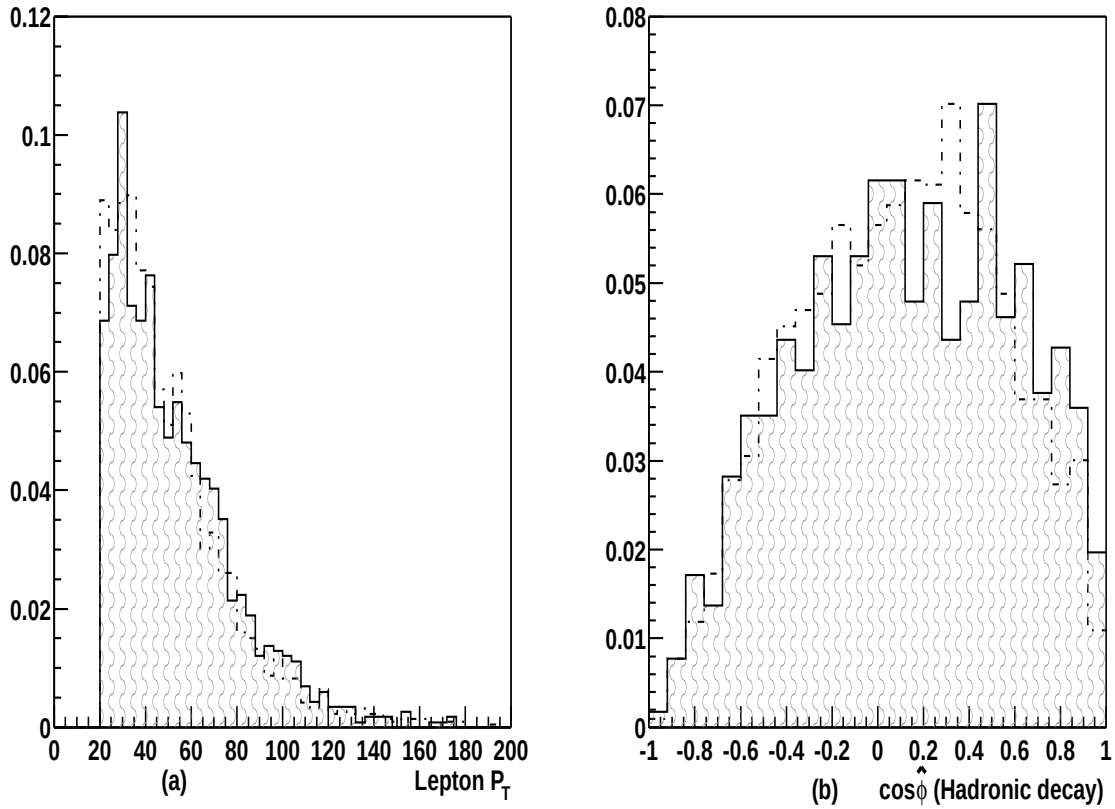

Figure 4.22: (a) Lepton p_T. (b) Angular distributions in cos$\hat{\phi}_{ub}$, where $\hat{\phi}_{ub}$ is the angle between the u and b quark in the W rest frame (not folded). Shadowed regions correspond to the transformed PYTHIA $t\bar{t}$ events (using Table 4.2), and white histogram correspond to fully simulated and reconstructed HERWIG $t\bar{t}$ events.

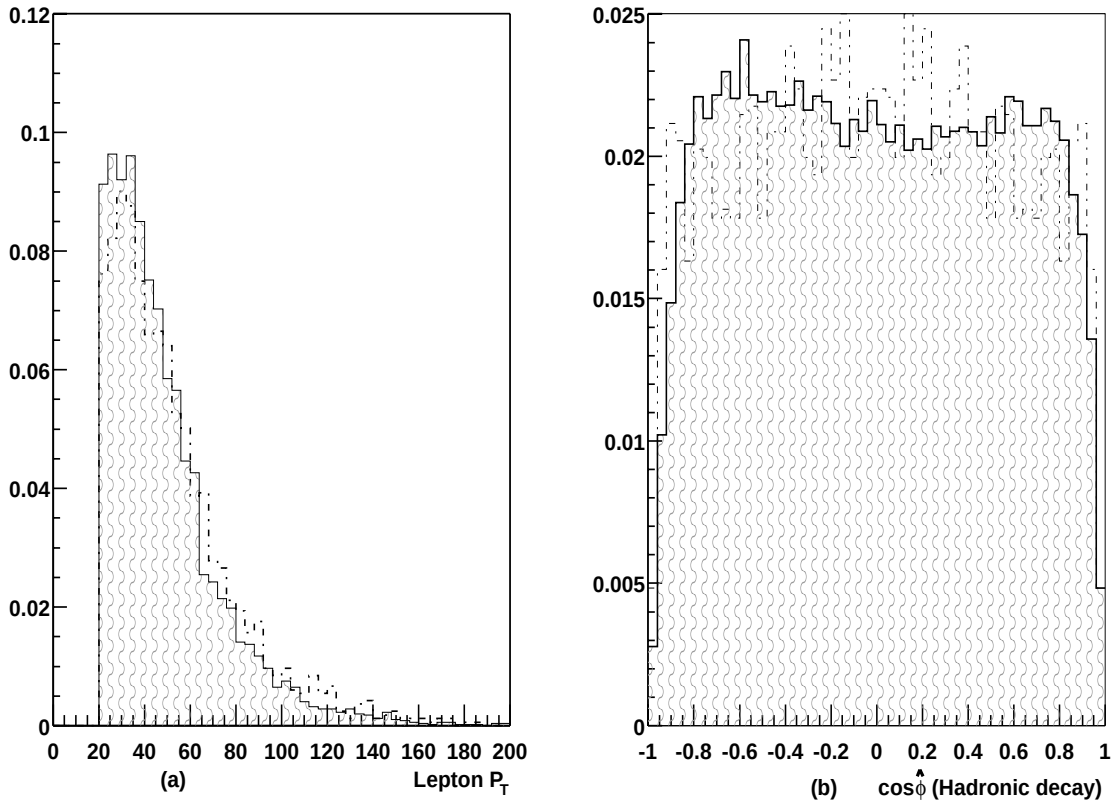

Figure 4.23: (a) Lepton p_T. (b) Angular distributions cos$\hat{\phi}_{ub}$, where $\hat{\phi}_{ub}$ is the angle between the u and b quark in the W rest frame (not folded). Shadowed regions correspond to the transformed VECBOS W+4 jets events (using Table 4.5), and white histogram correspond to fully simulated and reconstructed VECBOS/ISAJET W+4 jets events.

Chapter 5

Studies with Smeared MC Events

In this section, we study the extraction of F_0 using "smeared" generator-level samples. This is an important test for reproducing the basic analysis, without handling additional complications such as reconstruction and consideration of initial and final-state radiation. Also, without full simulation, it is easier to generate large event samples for studies of systematic effects.

5.1 Sample for $t\bar{t}$ Signal and W+jets Background

We generated a total of 80,000 SM $t\bar{t} \rightarrow$ electron+jets events with the PYTHIA MC [66], using all three possible decay forms for the W (Eqs. 1.10-1.12), for a top mass of 175 GeV/c^2, W mass of 80.4 GeV/c^2, and $\sqrt{s}$ =1.8 TeV. Initial and final-state gluon radiation and multiple-parton interactions were switched off in PYTHIA, so that only the hard process was considered. By selecting different sample fractions of W_+, W_0 and W_- contributions, the same events are used below to define subsamples with F_0 = 0.833, 0.703 (SM value), 0.625, 0.55 and 0.50. The energies of the partons in the events were transformed (or smeared) using the transfer functions from Section 4. After this smearing, the requirements for the objects in this sample were chosen to be similar to the ones used in previous Run I analyses:

$$|\eta| < 2$$

$$p_T(\nu) > 20 \text{ GeV/c}$$

$$p_T(\text{smeared parton}) > 15 \text{ GeV/c}$$

$$p_T(\mathrm{e}) > 20 \text{ GeV/c}$$

$$\cos(\mathrm{parton_i}, \mathrm{parton_j}) < 0.96, \text{ and } \cos(\mathrm{parton_i}, \mathrm{e}) < 0.98$$

The cosine requirement reflects an inefficiency of the reconstruction algorithm for events that have any overlapping objects. The angular distribution in $\cos\hat{\phi}$, where $\hat{\phi}$ is the angle between the b quark and the lepton (or one of the quarks from the W decay) in the W frame, is affected by these requirements (see Fig. 5.1). The p_T requirement has the largest impact on the angular distribution, specially for large F_0 (Fig. 5.1 has F_0=0.7). Figure 5.2 and 5.3 show $\cos\hat{\phi}$ for different F_0 values, before and after all these criteria are applied.

We also impose a selection on the probability P_{VECBOS} that any given event corresponds to background. This selection was used previously in the measurement of the top mass [61] to improve the purity of $t\bar{t}$ signal relative to background from W+jets. In Fig. 5.4, we show the values of P_{VECBOS} for equal samples of both $t\bar{t}$ signal (solid) and W+jets background (cross hatched) MC events. (Both the $t\bar{t}$ and W+jets are interpreted as W+jets in Fig. 5.4). We introduce a requirement on this probability of P_{VECBOS} <e^{-24} (vertical line) which reduces the signal by only $\approx 15\%$, and the background by a factor of ≈ 3. This is done prior to examining the data, with the intent of minimizing the impact of background on the extraction of F_0.

As we have indicated, the main background considered in this analysis is from W+4 jets production. For the selections used by DØ, these events represent 80% of the observed background, with the other 20% corresponding to multijet production where one jet mimics an electron. The parton-level VECBOS sample for W+jets (see Chapter 6) was obtained by matching jets with p_T >15 GeV/c and $|\eta|$ <2 to partons, requiring $\Delta\mathrm{R}=\sqrt{(\delta\phi)^2+(\delta\eta)^2}$ <0.15 for an accepted event, where $\delta\phi$ and $\delta\eta$ are defined as the difference in η and ϕ between the jets and partons. Events with only four jets, and only using W decayed into $l\nu$, were considered for further analysis. The partons were then transformed using the transfer function from Table 4.5.

5.2 Acceptance

In this section, we calculate the acceptance for smeared $t\bar{t}$ events using the two methods outlined in Section 3.7. For the first method (see Section 3.7.1), we use generated events

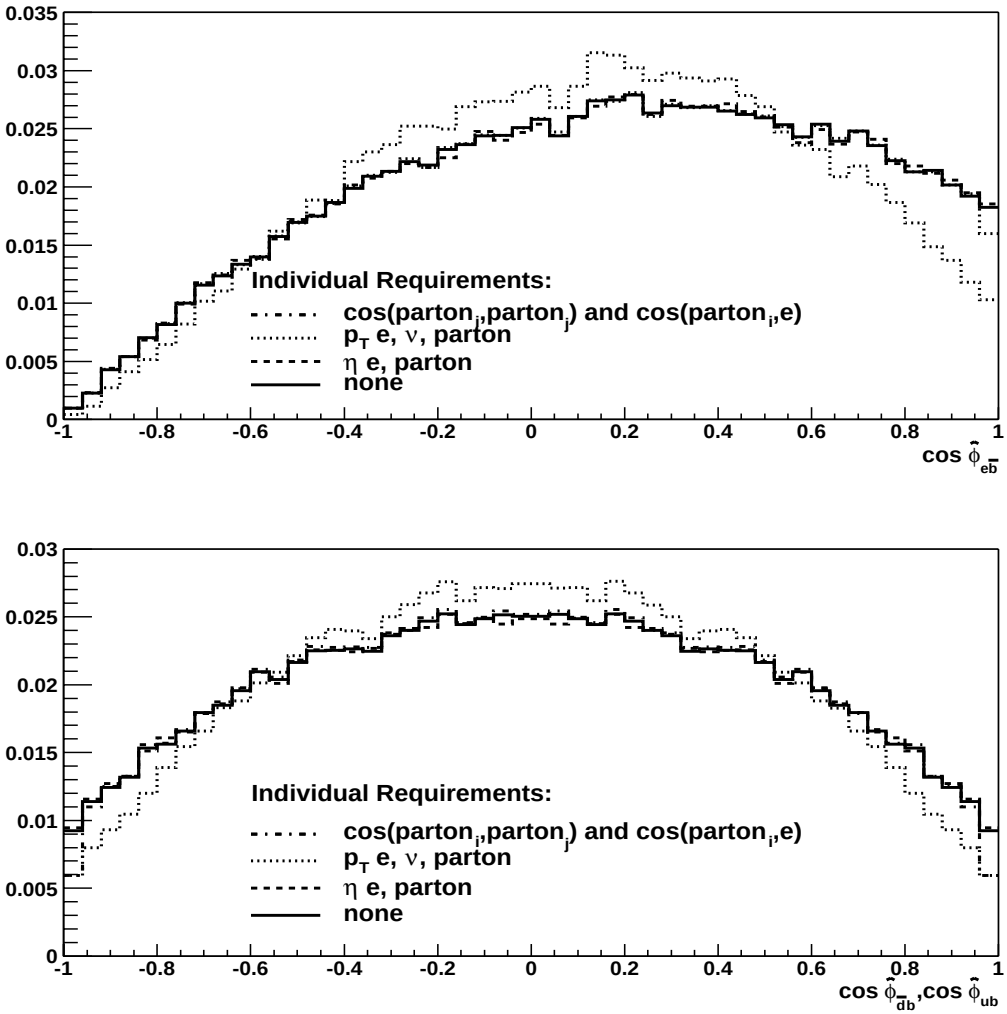

Figure 5.1: Effect of selection requirements on the shape of distributions in $\cos\hat{\phi}$ in the Standard Model. Each selection is applied separately, and the distribution renormalized to the one with no additional requirements.

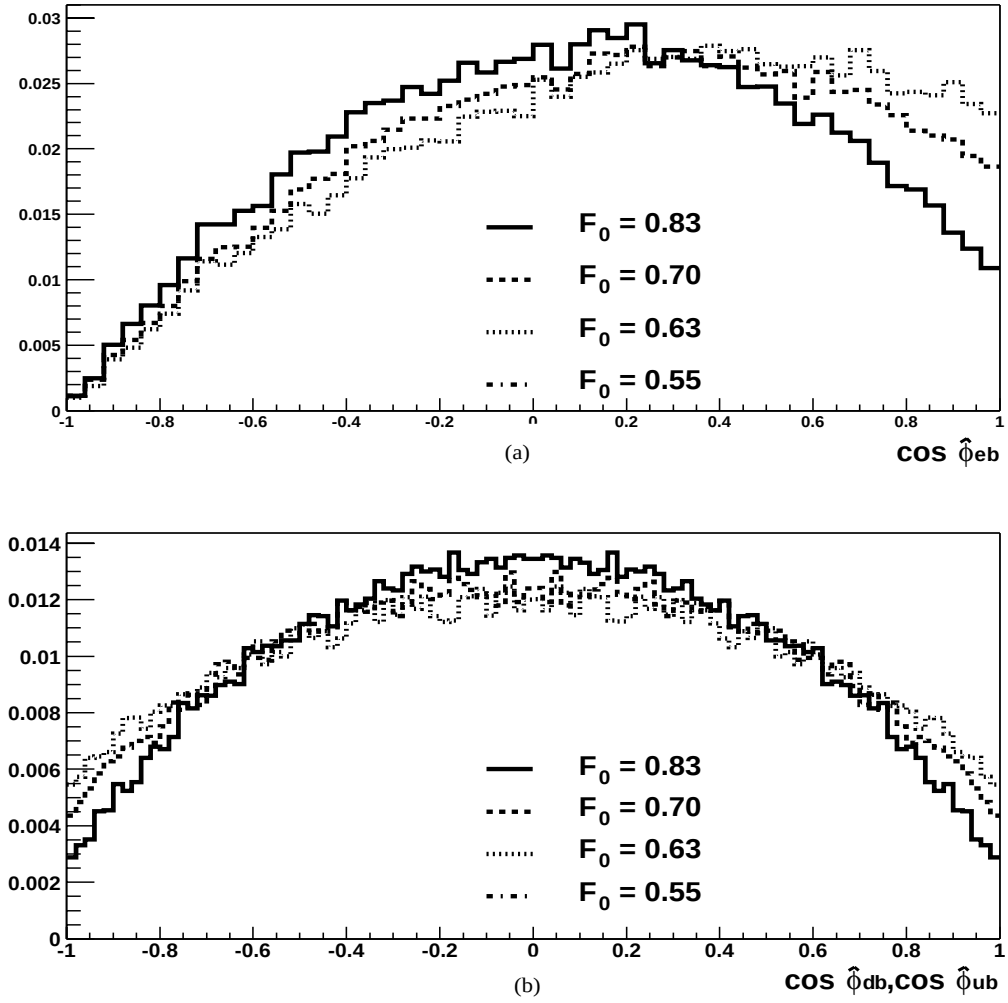

Figure 5.2: Arbitrarily normalized angular distributions in $\cos\hat{\phi}$ for samples with $F_0 = 0.833$, 0.703 (SM value), 0.625, and 0.55, after smearing of the $t\bar{t}$ events: (a) Leptonic and (b) hadronic decays of the W before applying all additional requirements for leptonic and hadronic decays.

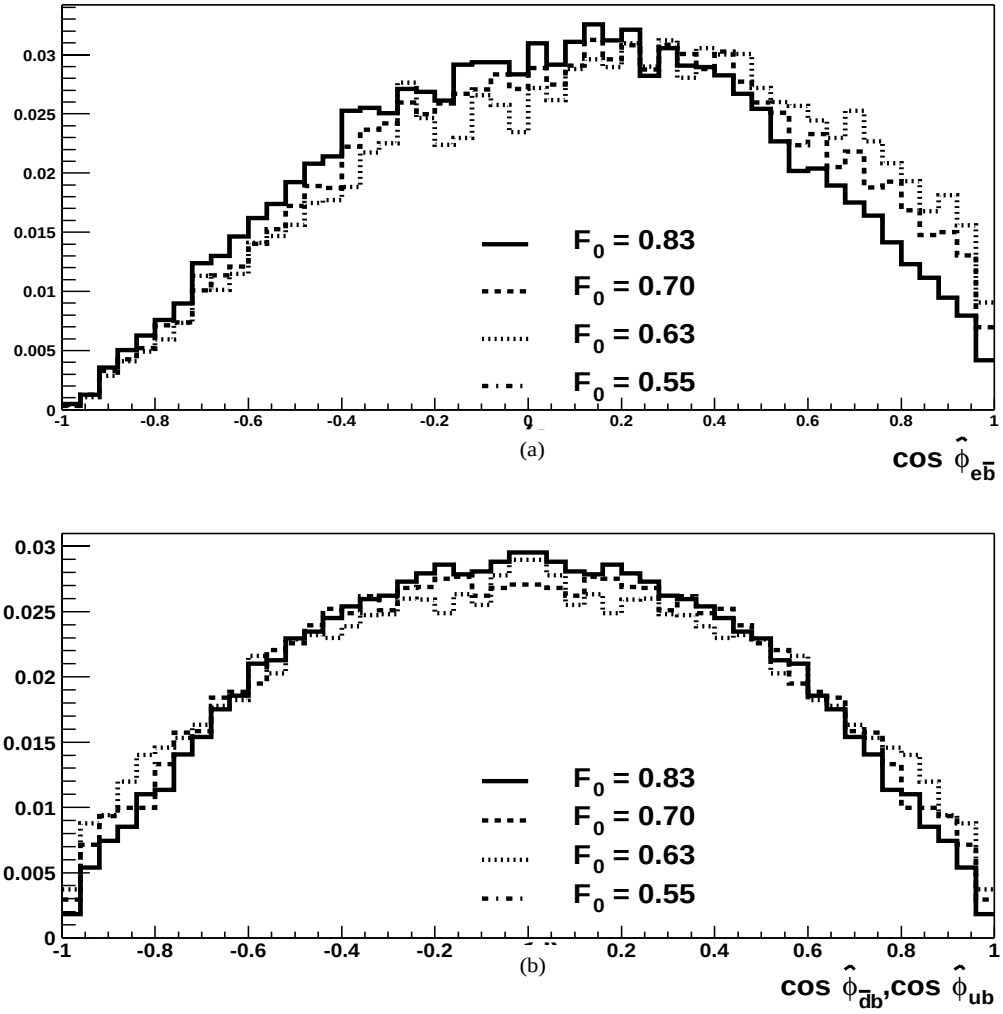

Figure 5.3: Arbitrarily normalized angular distributions in $\cos\hat{\phi}$ for samples with $F_0 = 0.833$, 0.703 (SM value), 0.625, and 0.55, after smearing of the $t\bar{t}$ events: (a) Leptonic and (b) hadronic decays of the W after applying all additional requirements for leptonic and hadronic decays.

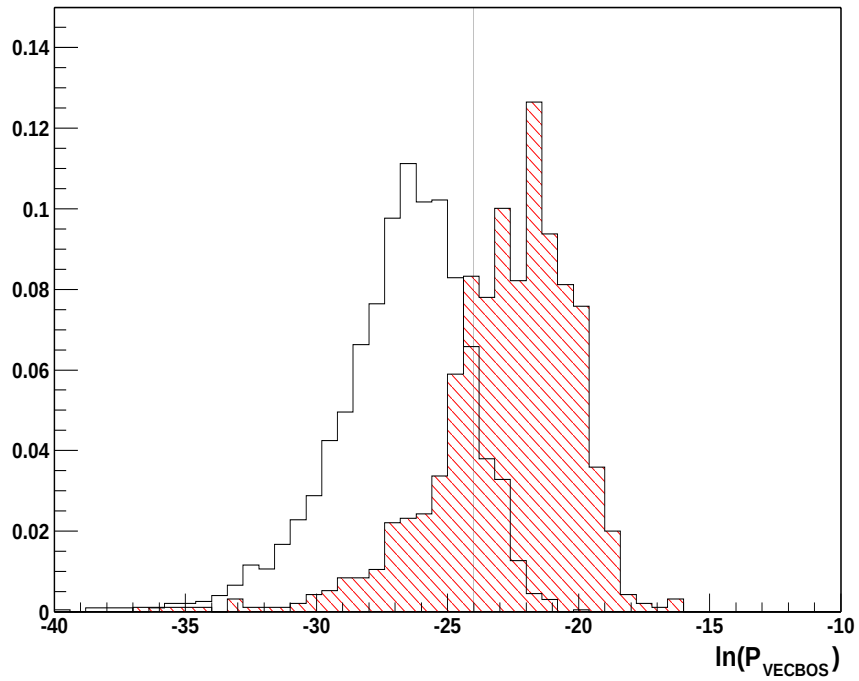

Figure 5.4: $\ln(P_{VECBOS})$ for $t\bar{t}$ signal (open) and W+jets background (hatched) events. The vertical line at P_{VECBOS}=e^{-24} represents the requirement designed to increase the purity of the $t\bar{t}$ signal in the data sample.

with different values of F_0, applying the selections from Section 5.1 to these samples. It should be recalled that that events in the different F_0 samples were obtained from the original 80,000 generated with PYTHIA, but were selected by using different admixture of helicities. We therefore expect to see some correlation among the samples. The results for acceptance are given in Table 5.1, and are also shown as the points with error bars in Fig. 5.5(a). Errors in acceptance were calculated using binomial statistics,

$$\delta < Acc(F_0) >= \sqrt{\frac{(1-Q)Q}{N_{gen}}} \tag{5.1}$$

where Q is the ratio of accepted to generated events, and N_{gen} is the number of events generated in each sample.

Table 5.1: Acceptance corrections calculated using the method outlined in Section 3.7.1. The subsamples were selected from a total of 80,000 generated events described in Section 5.1.

F_0	Generated events	Accepted events	Acceptance
0.500	35393	14204	0.401 ± 0.003
0.550	36437	14832	0.407 ± 0.003
0.625	40763	16890	0.414 ± 0.002
0.703	51820	21877	0.422 ± 0.002
0.830	56874	24630	0.433 ± 0.002

Table 5.2: Parameters defining the acceptance calculated using the method outlined in Section 3.7.2. The selections are those of Section 5.1, but without regard to background probability.

F_0	d_1	d_2	d_3	δd_1	δd_2	δd_3
0.500	0.3553	0.0892	0.0058	0.0030	0.0040	0.0020
0.550	0.3582	0.0856	0.0041	0.0031	0.0040	0.0020
0.625	0.3566	0.0887	0.0058	0.0031	0.0040	0.0020
0.703	0.3561	0.0893	0.0063	0.0030	0.0038	0.0018
0.830	0.3592	0.0834	0.0062	0.0034	0.0045	0.0021

For the second method (see Section 3.7.2), we used all the events from different F_0 samples. Table 5.2 shows the values of the parameters with their errors for all the five F_0. Combining the results of Table 5.2, yields the acceptance corrections for the selections given in Section 5.1:

$$\begin{aligned} < Acc(F_0) > &= d_1 + d_2\, F_0 + d_3\, F_0^2 \\ d_1 &= 0.357 \pm 0.001 \\ d_2 &= 0.087 \pm 0.002 \\ d_3 &= 0.006 \pm 0.001 \end{aligned} \tag{5.2}$$

The line in Fig. 5.5(a) shows this acceptance, with the band representing the uncertainty calculated taking into account all correlations among uncertainties in the parameters (see Eq. 3.48):

$$\delta < Acc(F_0 = 0.703) >= 0.001 \tag{5.3}$$

The acceptance also had to be calculated including the additional requirement on P_{VECBOS} <e^{-24}. Because of the large amount of CPU needed to obtain the P_{VECBOS} probability, only 2000 events were used at each value of F_0. Table 5.3 shows the number of events generated and the acceptance obtained using independent MC samples and the method outlined in Section 3.7.1. These results are also shown in Fig. 5.5(b) as the points with error bars. Once again, all results from the different F_0 samples were used

Table 5.3: Acceptance corrections calculated using the method outlined in Section 3.7.1. The selections are those of Section 5.1, but for background probability P_{VECBOS} <e^{-24}.

F_0	Acceptance from Table 5.1	Subsample size	P_{VECBOS} <e^{-24}	Acceptance
0.500	0.401 ± 0.003	2000	1771	0.355 ± 0.007
0.550	0.407 ± 0.003	2000	1767	0.360 ± 0.007
0.625	0.414 ± 0.002	2000	1790	0.371 ± 0.007
0.703	0.422 ± 0.002	2000	1761	0.372 ± 0.007
0.830	0.433 ± 0.002	2000	1799	0.390 ± 0.007

in a combined acceptance calculation based on the second method outlined in Section 3.7.2. Table 5.4 shows these values with their errors for all five F_0. Combining the results of Table 5.4, yields the acceptance corrections after application of the selection

Table 5.4: Parameters for the acceptance calculated using the method outlined in Section 3.7.2. The selections are those of Section 5.1, but require the background probability P_{VECBOS} <e^{-24}.

F_0	d_1	d_2	d_3	δd_1	δd_2	δd_3
0.500	0.3099	0.0866	0.0080	0.0075	0.0097	0.0050
0.550	0.3011	0.1020	0.0058	0.0076	0.0095	0.0050
0.625	0.3110	0.0888	0.0110	0.0085	0.0110	0.0055
0.703	0.3042	0.0916	0.0056	0.0090	0.0112	0.0055
0.830	0.3055	0.1024	-0.0019	0.0110	0.0128	0.0063

on background probability (P_{VECBOS} <e^{-24}):

$$\begin{aligned} < Acc(F_0) > &= d_1 + d_2\, F_0 + d_3\, F_0^2 \\ d_1 &= 0.304 \pm 0.005 \\ d_2 &= 0.094 \pm 0.007 \\ d_3 &= 0.006 \pm 0.003 \end{aligned} \tag{5.4}$$

The line in Fig. 5.5(b) gives the acceptance using Eq. 5.4, with the band showing the errors calculated from Eq. 3.48, which gives

$$\delta < Acc(F_0 = 0.703) >= 0.003 \tag{5.5}$$

In summary, the two methods used to extract the acceptance agree with each other.

For successfully matched W+4 jet events, 20% pass all the requirements stated in Section 5.1. The P_{VECBOS} selection accepts only 40±3% of these, leading to an overall acceptance of 0.08 for background. (Only 100 events were used to study the acceptance for W+jets.)

5.3 Measurement of F_0, the Longitudinal Fraction of W Decays in $t\bar{t}$

The sensitivity of the method to F_0 will be checked by studying the response in Monte Carlo to different input value of F_0 in high-statistics samples. In this way, any bias from low statistics, as such, can be decoupled from the analysis. That is, this study can determine if there is any inherent bias introduced by our specific method, or from presence of background, in the extraction of F_0. For any event, we calculate the likelihood

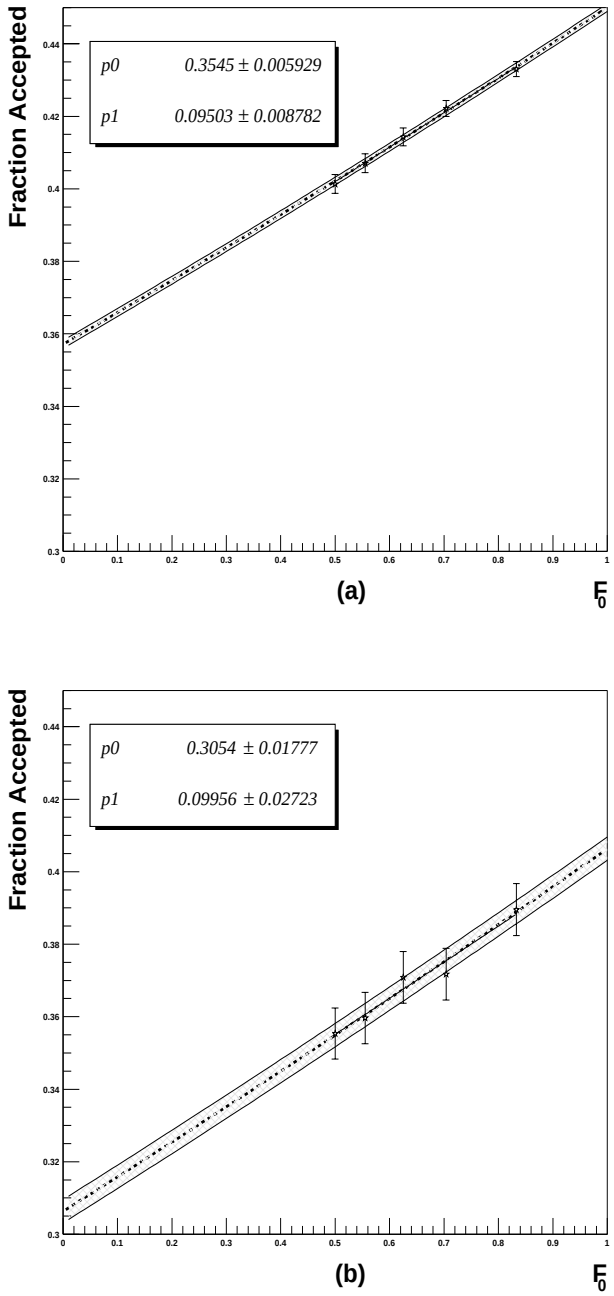

Figure 5.5: (a) Acceptance vs F_0 for events selected according to Section 5.1, and (b) after applying the extra selection $P_{VECBOS} < e^{-24}$. Points with error bars were obtained by counting events that pass all the requirements (first method in Section 3.7.1). The lines and error bands were calculated using the second method in Section 3.7.2. Because the MC samples were chosen from one initial 80,000 $t\bar{t}$ sample, the results are correlated, as are the errors bars. For more information see text.

in steps of 0.01 from F_0=0.01 to 0.99. At each point, we minimize the likelihood relative to the number of signal events c_1. We fit a fifth-order polynomial to the likelihood, which we convert to a probability distribution. The uncertainty on the most likely extracted value is obtained from the 68.27% interval in area about this value of the probability function.

5.3.1 Studies using Signal

The first test consists of using only signal events, and extracting F_0, without considering any contribution from background. We determine F_0 from experiments of about 1700 $t\bar{t}$ events for each input value, with our requirement on P_{VECBOS}. The fourth column of Table 5.3 shows the number of events used from each F_0 sample. Figure 5.6(a) shows –ln$L$ as a function of F_0 for the SM sample, and the most probable extracted F_0 is 0.72, with an uncertainty of δF_0=0.02. The response as a function of F_0 is also shown in Fig. 5.6(b). The response has a slope consistent with unity, and no offset. Figure 5.7 shows the response and its uncertainty for 200 experiments of 10 $t\bar{t}$ events, also with the requirement of P_{VECBOS} <e^{-24}, as a function of input F_0. We observe a slope smaller than unity, due to the fact that the extracted value of F_0 is restricted to lie inside the physical region. That is, in MC or true experiments, the most probable value of F_0 can be only between 0 and 1. Consequently, for low statistics, it is expected that the mean values of ensembles will shift down for large input values of F_0. This can effectively increase the slope (Figure 5.7). Figure 5.8 shows the result analogous to Fig. 5.6, with the possibility of having a background probability included in the analysis of the same pure $t\bar{t}$ samples. The minima are again near the input values of F_0, but the value of c_1 is about 0.85 (see Eq. 3.25). That is, the response is still consistent with a slope of unity and no offset, but there is $\approx$ 15% misinterpretation or loss in associating signal events with the $P_{t\bar{t}}$ probability. There is also a small shift of the minimum towards larger output F_0, which is consistent with the dependence in Fig. 5.6(b). We do not expect to retain the same extracted value once another parameter is added to the likelihood, which, in this case, is the fraction of signal/background events. We therefore do not regard this as a discrepancy.

The exact value of F_0 extracted from each likelihood depends somewhat on the measure chosen for specifying our result. For example, the mean of the distribution in our analysis is shifted to lower values of F_0 relative to the most probable value of F_0,

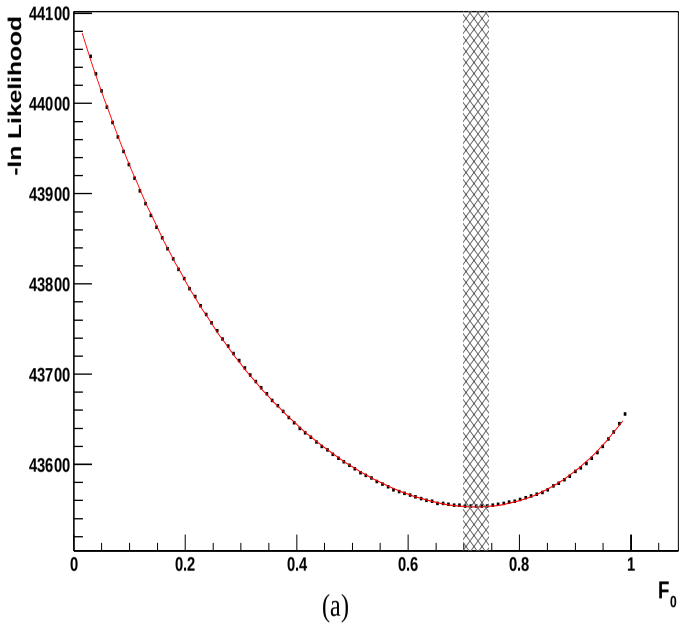

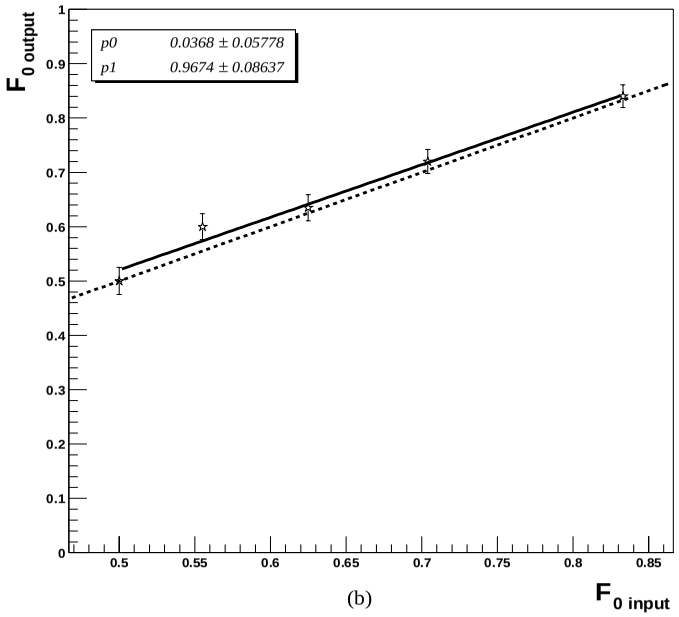

Figure 5.6: –ln(Likelihood) and response for the SM sample as a function of F_0. (a) The most probable extracted F_0 is 0.72, and its uncertainty is δF_0=0.02, for 1761 events that pass the P_{VECBOS} criteria. (b) The response for MC samples of about 1700 $t\bar{t}$ events after applying the P_{VECBOS} selection (see Table 5.3). The likelihood is based only on $P_{t\bar{t}}$, and no background probability is considered in this analysis of $t\bar{t}$ events.

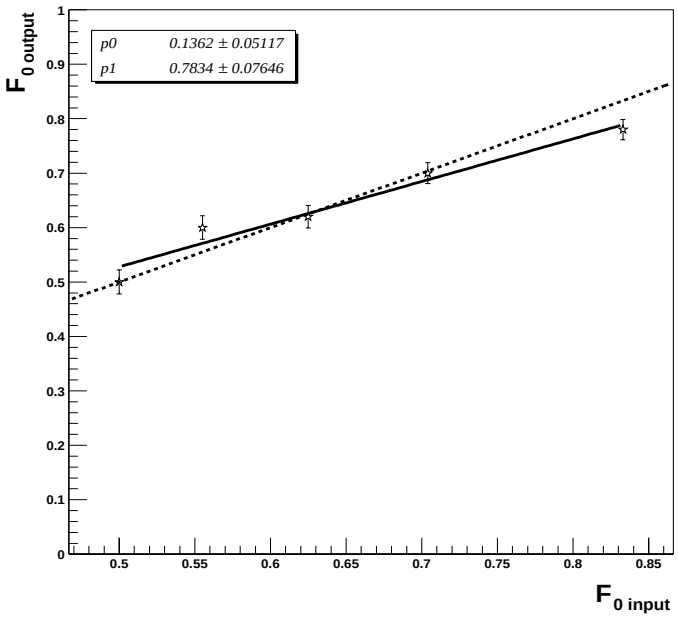

Figure 5.7: Response from 200 experiments each with 10 $t\bar{t}$ events, as a function of input F_0 value, after requiring P_{VECBOS} <e^{-24} in the analysis. The deviation at large F_0 is probably due to the fact that the extracted of F_0 is assumed to lie only inside the physical region, that is between 0 and 1.

i.e., relative the peak of the probability distribution. These two measures can become quite different for small event samples. In this analysis, we chose to quote the most probable (peak) value, and the 68.27% interval around it as its uncertainty. As a way to check whether the assigned error is realistic, we count how often an input value is within the interval defined by 68.27% of the results (see Fig. 5.9). We use 50 experiments, each containing different number of events and note that, independent of the number of events in each experiment, this interval contains the input value in about 68% of the times for the analysis using only $P_{t\bar{t}}$, which suggests that we have a reasonable definition for the uncertainty on F_0. (For more on this issue, see Appendix G.)

5.3.2 Studies using Signal and Background

We now check the analysis using samples of 1000 smeared VECBOS W+4 jets events and 1000 smeared $t\bar{t}$ lepton+4 jets PYTHIA events, before applying the selection on P_{VECBOS}. After we apply the selection on P_{VECBOS} <e^{-24}, the experiments contain ≈

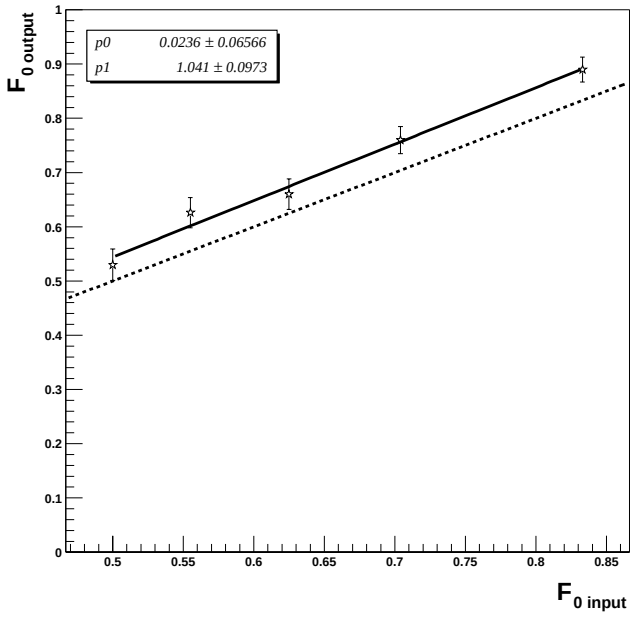

Figure 5.8: Response as a function of input F_0, obtained using about 1700 purely $t\bar{t}$ events, but a probability $P = c_1 P_{t\bar{t}} + c_2 P_{VECBOS}$. All the events in these samples passed the P_{VECBOS} <e^{-24} criterion.

0.85×1000 $t\bar{t}$ and ≈ 0.40×1000 W+4 jets events. Figure 5.10 shows the dependence of the response on input F_0. The minimization of the likelihood yields a signal fraction (c_1) of ≈ 0.62±0.03, with the response still consistent with a slope of 1 and no offset. Although a measurement of the error on c_1 requires further study, using an average retention of 85% for signal and 40% for background events after the selection on P_{VECBOS}, the expected value is 6% higher than obtained.

To look in more detail at the effect of adding background, we begin with 2000 $t\bar{t}$ events before applying the P_{VECBOS} selection, and increase the number of background events in the sample. Due to limited statistics, we in fact decrease the number of signal events once the number of background events reaches the maximum 1000. The background P_{VECBOS} selection is applied after the number of signal and background events is chosen. Figure 5.11 shows that, for both F_0=0.703 and F_0=0.50 inputs. There may be a bias toward smaller extracted values of F_0 for signal fractions below 0.4.

We now generate 100 ensembles of 12 SM $t\bar{t}$ events and 10 W+jets that pass the P_{VECBOS} selection. We chose these numbers based on the results of the previous mass

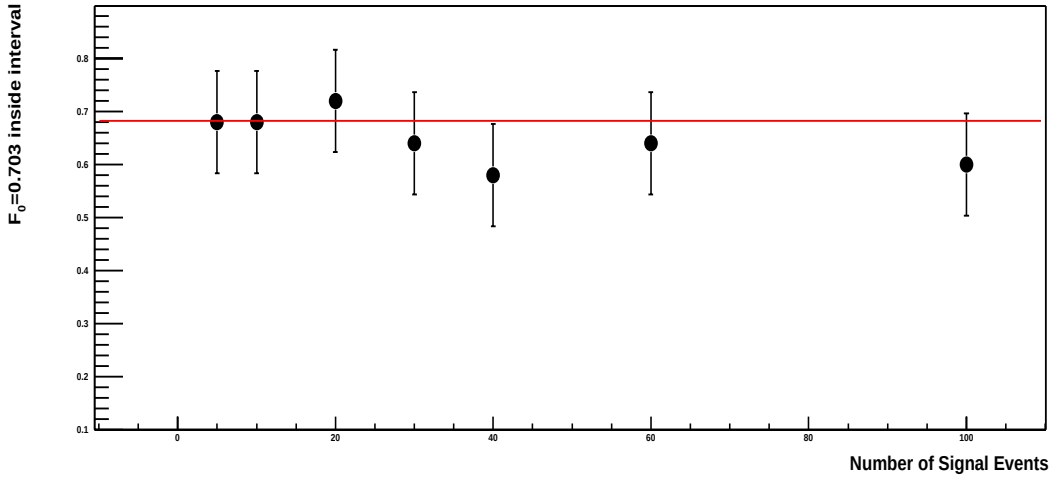

Figure 5.9: The fraction of the time that the input value F_0=0.703 lies within the 68.27% interval of probability about the extracted value, as a function of the number of $t\bar{t}$ events in a sample experiment. The error bars represent binomial uncertainties, calculated using 50 experiments.

analysis [69, 63]. We extract the most probable value and the one half of the 68.27% interval for these 100 experiments, and the results are shown in Fig 5.12. Due to the fact that we extract F_0 from a constrained region, the likelihood often has a minimum near the physical boundaries of F_0. This issue is examined further in Appendix G.

5.4 Angular Resolution

We also examined $t\bar{t}$ samples in which, in addition to energy smearing, pseudorapidities and azimuths of jets were smeared using angular resolutions obtained from fully simulated and reconstructed HERWIG $t\bar{t}$ events. These resolutions are shown in Fig. 5.13. The angles of leptons in the sample were not smeared, because their resolutions are far better than for jets (see Fig 5.14).

An analysis was performed with 2000 $t\bar{t}$ events generated according to the SM, and the extracted F_0 was 0.735±0.033. There is no significant difference between the most probable values obtained using smeared angles and energies, and those just using energy smearing (F_0=0.731±0.027). The small difference in the uncertainties is not important for the final analysis. The ≈ 20% difference in the uncertainties for these two cases is

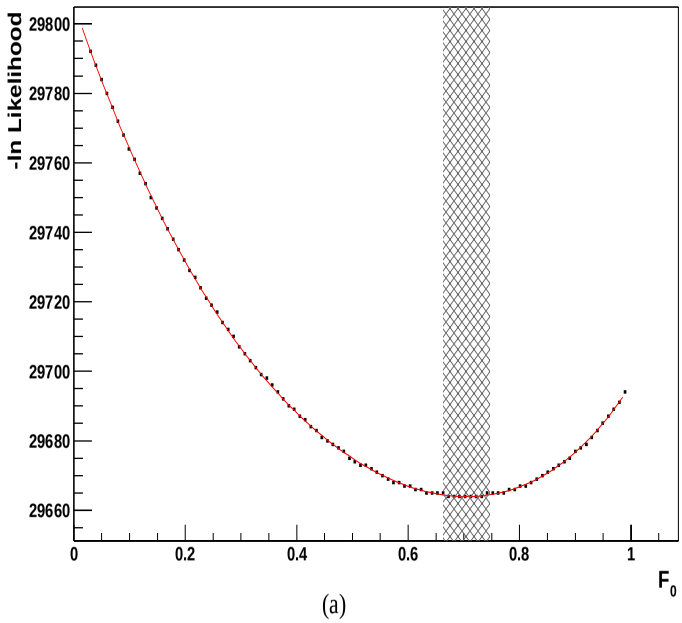

(a)

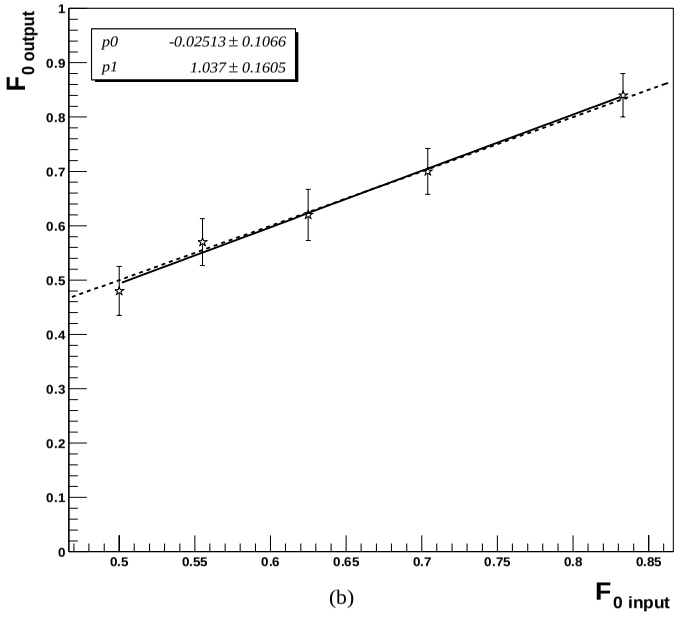

(b)

Figure 5.10: (a) –ln(Likelihood) for the SM $t\bar{t}$ sample with 845 signal and 415 background events as a function of F_0. The most probable F_0 is 0.70 and δF_0=0.02. (b) Response obtained using about 850 signal and 400 background events in each F_0 sample, fitted to $P = c_1 P_{t\bar{t}} + c_2 P_{VECBOS}$ (after selection on P_{VECBOS}), as a function of input F_0. The subsamples for different F_0 contain many of the same events (see text).

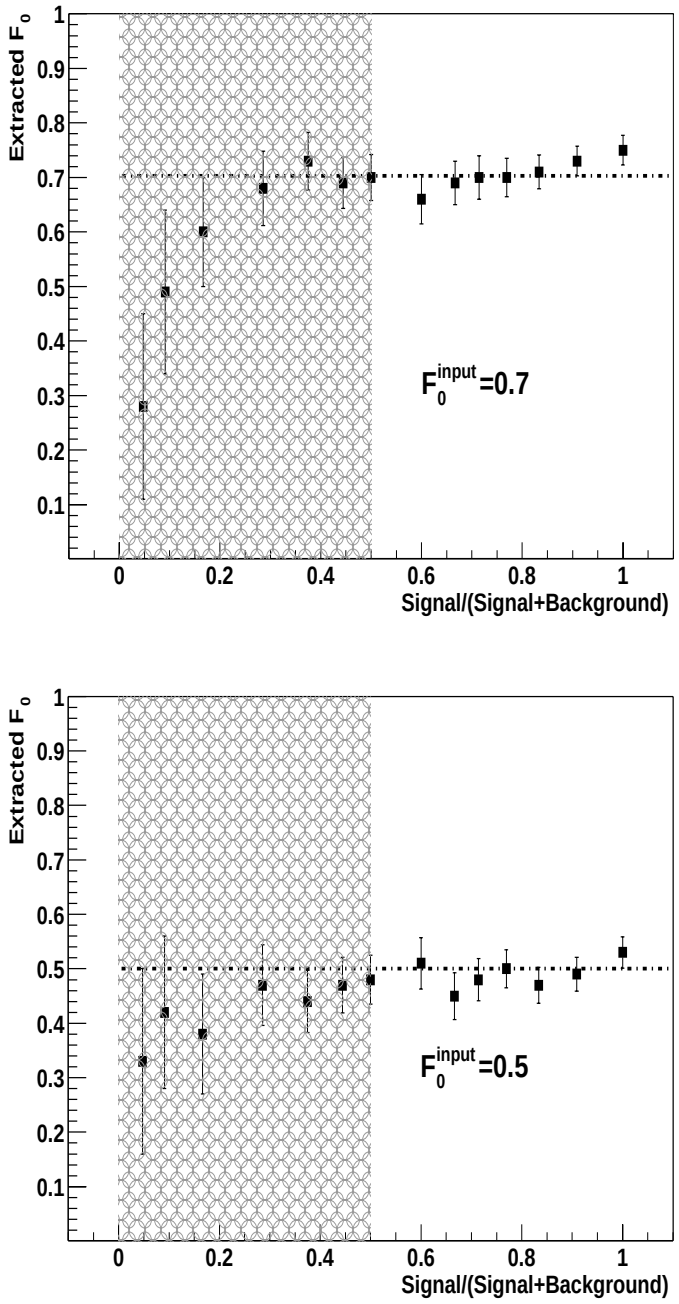

Figure 5.11: F_0 extracted using 2000 signal events before selecting on P_{VECBOS}. Due to limited statistics, the shaded region contains 1000 background events and a smaller number of signal events. The clear region contains 2000 signal events and additional background events. The background P_{VECBOS} selection is applied after the number of signal and background events is chosen at each point.

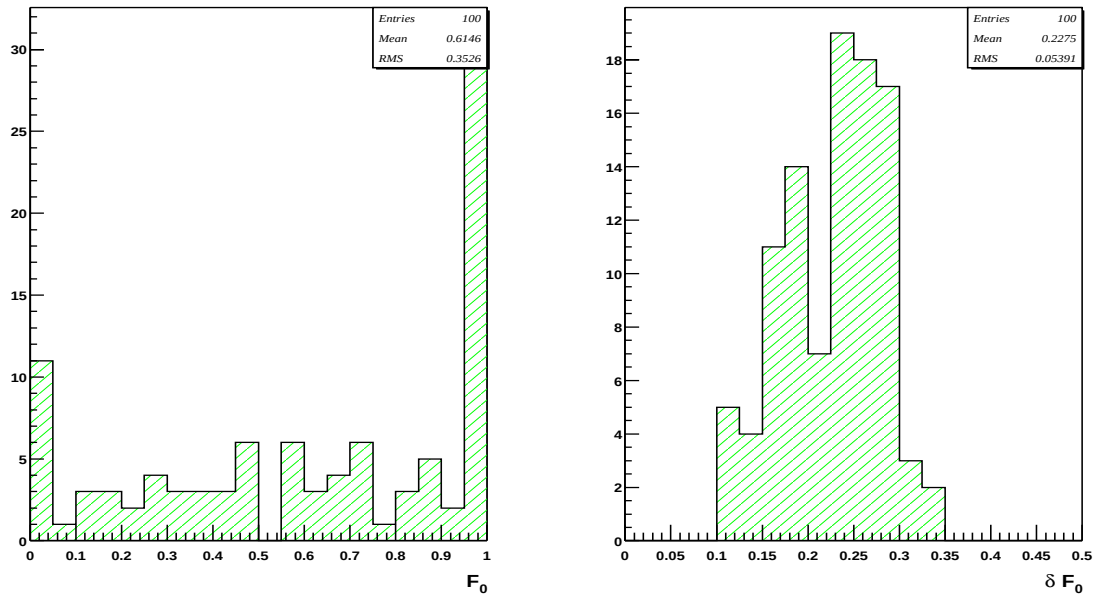

Figure 5.12: Most probable extracted value of F_0 for an input of F_0=0.703, and its half 68.27% interval (δF_0), in 100 experiments using 12 $t\bar{t}$ signal and 10 W+jets background events, after requiring a poor value for P_{VECBOS}. This interval contains the input value in $\approx$ 68% of the experiments. After the selection on P_{VECBOS}, the minimization yields the result that $< c_1 >$=0.60, which is close to what is expected (12/22=0.55).

most likely due to the fact that when angles are also smeared, signal and background become more similar, and therefore more events are lost to the background in the minimization, thereby effectively reducing statistics for signal.

5.5 Jet Energy Scale

To study how the jet energy scale affects the measurement of F_0, we change the energies of the smeared partons in the SM sample (F_0=0.703) by $\pm(2.5\% + 0.5)$ GeV. This uncertainty corresponds to that of the previous top-quark mass measurement [32, 59]. Figure 5.15 shows that this change in the energy of jets does not materially affect the angular distribution for the decay of the W. Figure 5.16 shows how the W and top masses move when this change is applied. Figure 5.17 shows the extracted values of F_0 for the same events after changing the jet energies by $\pm(2.5\% + 0.5)$ GeV. Changing the energies by +1 standard deviation yields F_0=0.682±0.033, leaving the energies unchanged yields F_0=0.705±0.042, and finally, changing the energies by −1 deviation yields F_0=0.706±0.036. The change is somewhat asymmetric, but quite small (≈ 0.02). In conclusion, we expect that the uncertainty in the jet energy scale will have only a minor effect on the systematic uncertainty in the extraction of F_0.

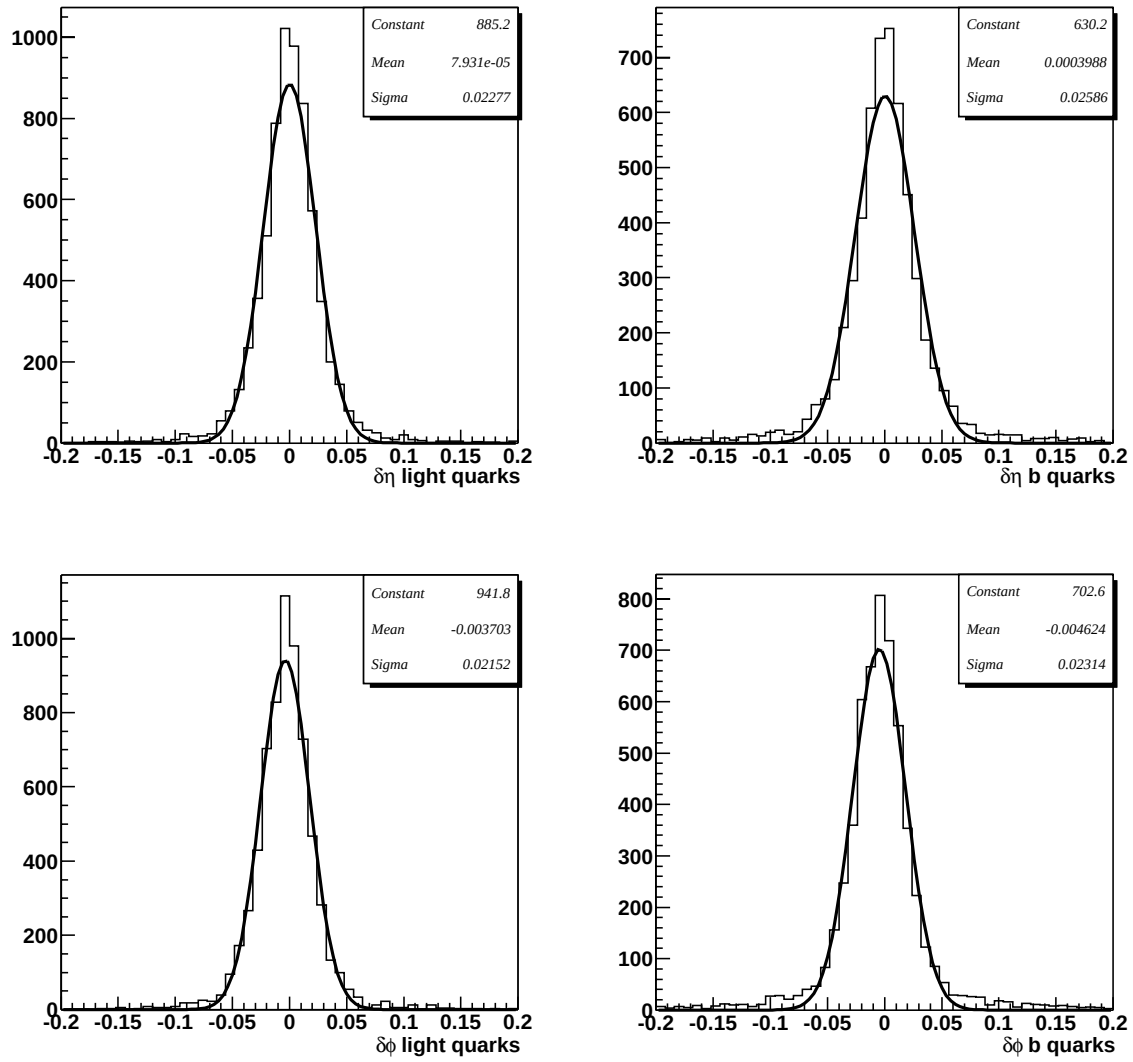

Figure 5.13: Angular resolutions $\delta\eta$ and $\delta\phi$ for b and light jets from fully simulated and reconstructed HERWIG $t\bar{t}$ events. The fits to the MC $t\bar{t}$ events were used in a test of the analysis to extract F_0.

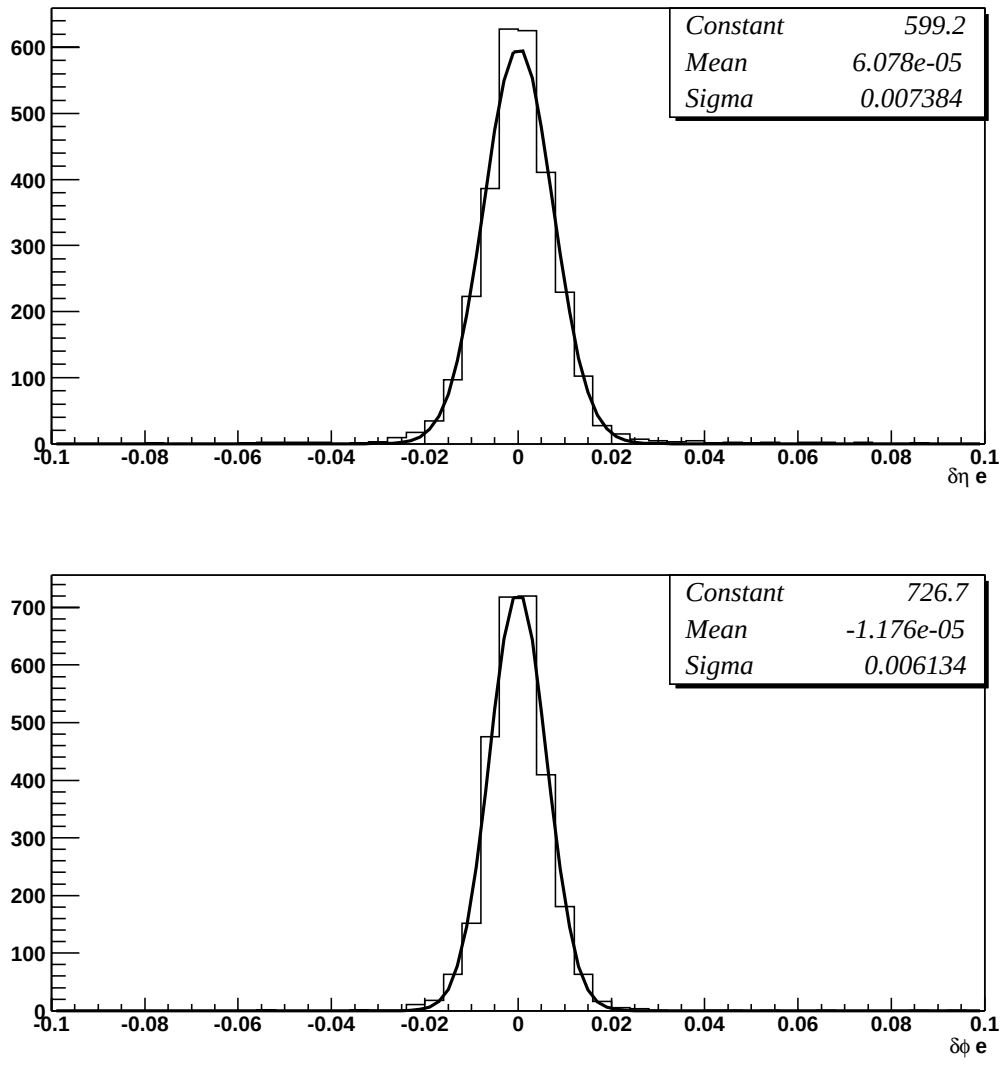

Figure 5.14: Angular resolutions $\delta\eta$ and $\delta\phi$ for electrons from fully simulated and reconstructed HERWIG $t\bar{t}$ events. These resolutions were ignored in determining the impact of angular resolutions on the extraction of F_0.

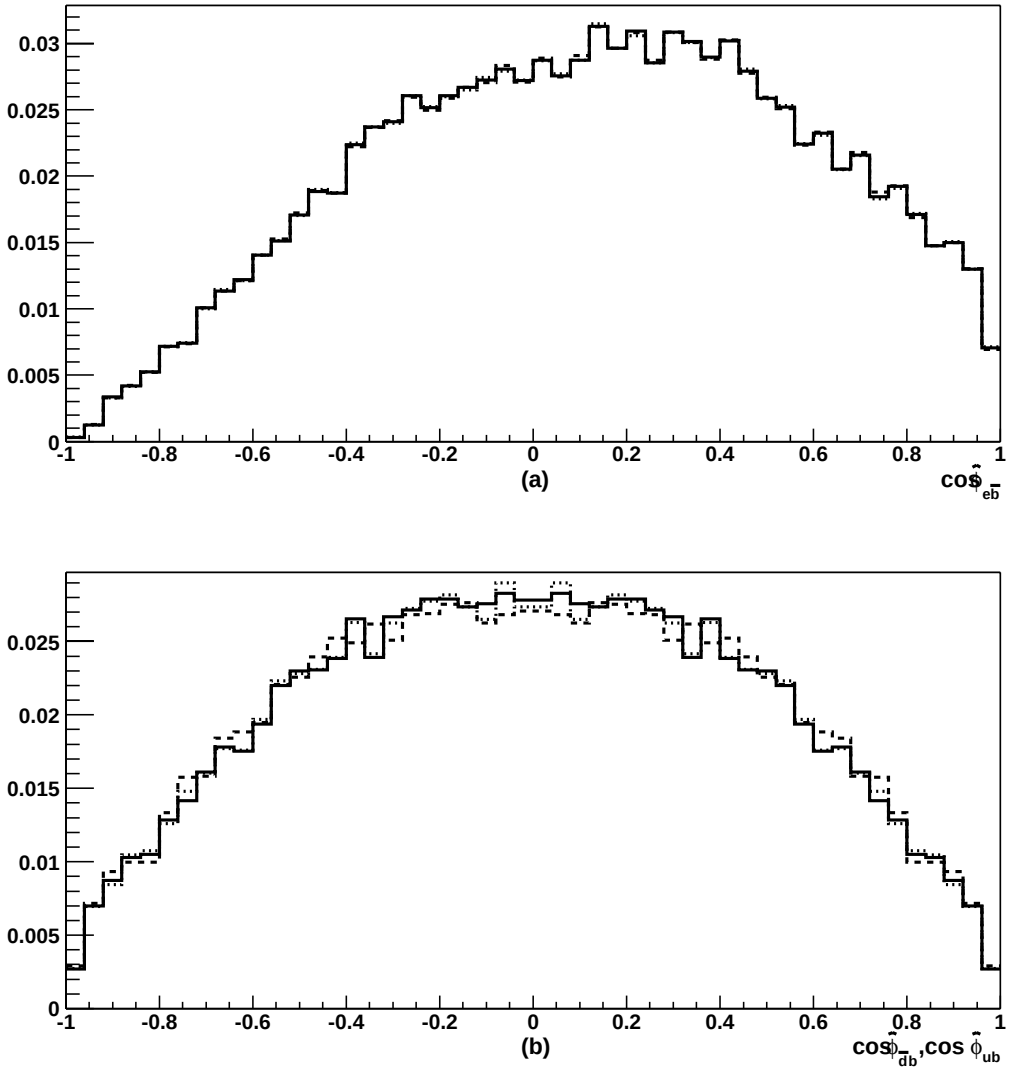

Figure 5.15: Angular distributions in $\cos\hat{\phi}$ with $F_0 = 0.703$ (SM value), after smearing the events and after applying all selection criteria. The energies of the smeared partons were changed by $\pm(2.5\% + 0.5)$ GeV. This plot shows the distributions in $\cos\hat{\phi}_{e\bar{b}}$ and $\cos\hat{\phi}_{d\bar{b}}$ and $\cos\hat{\phi}_{u\bar{b}}$, before and after the rescaling of energies.

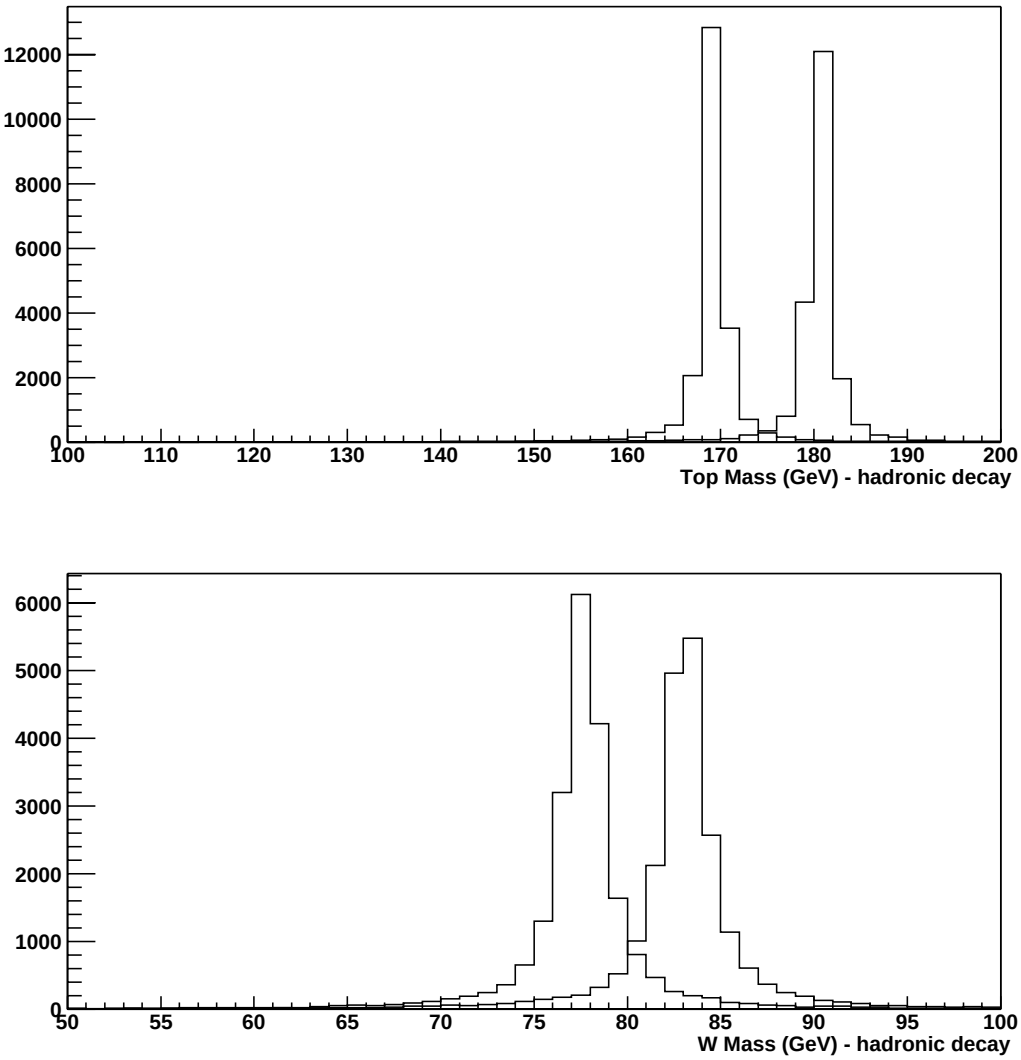

Figure 5.16: Top and W masses after smearing the events and after applying all selection criteria. The energy of the smeared partons are changed by $\pm(2.5\% + 0.5)$ GeV. In both plots, the lower (upper) masses correspond to the change that reduces (increases) the energy of the smeared partons.

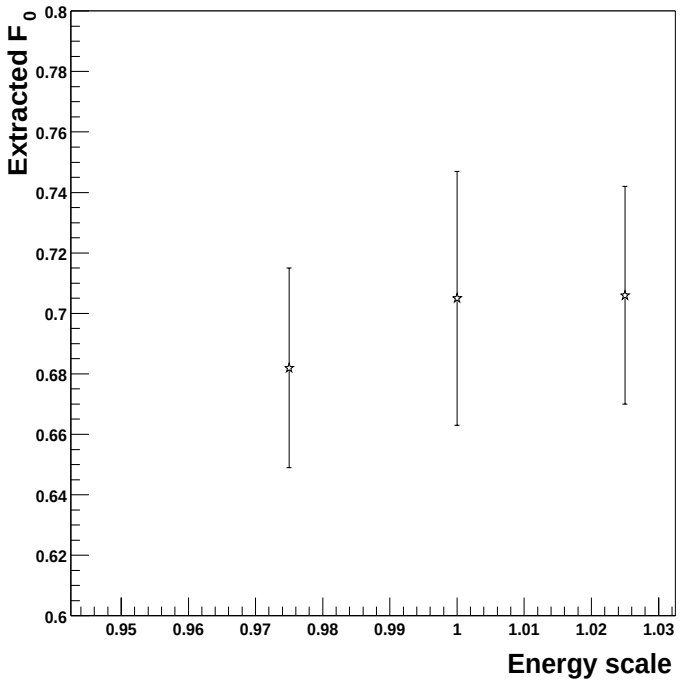

Figure 5.17: Difference in the extracted F_0 for smeared partons with their energy changed by $\pm(2.5\% + 0.5)$ GeV. Changing the energies cause little change in F_0.

Chapter 6

Full DØ Simulation and Reconstruction

We now discuss the analyses using $t\bar{t}$ events generated with HERWIG and PYTHIA, and W+jets generated with VECBOS, that were passed through full Run I simulation and reconstruction. A comparison between DØ data and these Monte Carlo events was carried out in previous DØ analyses [69, 32], in which trigger and selection criteria were also studied.

6.1 $t\bar{t}$ Samples

6.1.1 HERWIG Events

These $t\bar{t} \rightarrow$ lepton+jets events were generated and hadronized using HERWIG Version 5.7 [67]. CTEQ3M was used as the parton distribution function [72] and the CAFIX 5.0 package [58] was used to correct the energy of jets. One of the W bosons from the $t\bar{t}$ final state was forced to decay leptonically (e,μ), and the other one through any allowed mode. A total of 30,799 events was generated with a top mass of 175 GeV/c^2, W mass of 80.4 GeV/c^2, for a $p\overline{p}$ center of mass energy of $\sqrt{s}$= 1.8 TeV. Initial and final-state radiation was switched on in HERWIG. Since this sample was already well tested and studied, we will use it to obtain all the SM results, and use it also to study systematics that require Monte Carlo $t\bar{t}$ events. These 30,799 events were passed through an "ntuple-maker" code, and all the information was stored in HBOOK format [71]. We converted these ntuples to ROOT [70] format for convenience of analysis.

6.1.2 PYTHIA Events

We also generated $t\bar{t}$ samples with different values of F_0, using the PYTHIA generator Version 6.1 [66] followed by JETSET Version 7.4 to simulate fragmentation. We maintained all the specifications used in Run I: CTEQ3M parton distribution functions, a top mass of 175 GeV/c^2, a W mass of 80.4 GeV/c^2, initial and final-state radiation switched on, and multiple interactions off. One W was forced to decay to leptons (e, μ) and the other to hadrons. Events were selected at the generator level, with longitudinal fractions for the W of F_0=0.90, 0.83, 0.70, 0.62, 0.55, 0.50, 0.42, and 0.36. Each of these samples was generated using different seeds in PYTHIA to assure no correlation between them, and the events were processed through the DØGEANT detector-simulation package [73]. This package does not provide an accurate representation of efficiencies for the WAMUS muon-detection chambers. To correct for this, we apply the standard "Mu-smear"corrections to the output of DØGEANT. We used the Version Run 1b "postzap" package, which modifies the original hits according to the measured WAMUS chamber efficiency. Details about the muon-chamber efficiencies are given in [54]. The Mu-smeared events were finally reconstructed using the DØ event reconstruction program, with standard CAFIX 5.0 corrections applied to jet energies. We used the same "ntuple-maker" package as for the HERWIG sample. Although the output ntuple does not contain all the generator information, we maintained all this information with the event number in a separate ASCII file. In this way, parton-level information is available when needed.

Table 6.1: PYTHIA fully reconstructed $t\bar{t}$ samples.

F_{0input}	Number of events
0.36	10000
0.42	20000
0.50	22956
0.55	34255
0.71	29453
0.83	24908
0.91	31272

6.2 W+jets Samples

For W+jets background events, we used the Monte Carlo samples that were generated for the previous top-mass analysis. Details can be found in Ref. [69].

The VECBOS program [65] was used to model the production of a W boson with multiple jets. Once again, CTEQ3M parton distribution functions were used in the generation. The dynamical QCD scale was set to the average jet-p_T in an event. Radiation and hadronization were simulated by passing the output of VECBOS through HERWIG or ISAJET [68] for QCD evolution and fragmentation. The energies of jets were also corrected using the standard DØ package CAFIX 5.0, and the events filtered using the selections described in the following section.

A total of 28,216 events were "hadronized" using HERWIG, and 74,537 events using ISAJET. For most of the analysis we use the ISAJET sample.

6.3 Event Selection

The $t\bar{t}$ selection criteria were determined in the previous top analysis. A set of selections was introduced to improve acceptance for lepton+jets events from $t\bar{t}$ relative to background. In this analysis, we use the same selections as in previous Run I top-mass analyses [69, 32]. This is the "precut" sample defined in the published DØ measurement of the mass of the top in the single-lepton $t\bar{t}$ events [32].

The standard requirements are:

- An isolated electron with E_T >20 GeV and $|\eta|$ <2.0, or an isolated μ with p_T >20 GeV/c within $|\eta|$ <1.7. (A μ is isolated if its distance ΔR(μj)>0.5 from every jet in the event. An isolated electron is defined through calorimeter-based criteria described in Section 2.)

- $\not\!\!E_T$>20 GeV/c. The missing transverse energy determined only from the calorimeter (E_T^{cal}) is > 25 GeV/c for e+jets, and > 20 GeV/c for μ+jets events.

- At least 4 jets with E_T >15 GeV, all within $|\eta|$ <2.0.

- To reduce background from multijets, the W boson reconstructed from the lepton and the missing transverse energy must be in the $|\eta^W|$ <2.0 region, and the scalar

sum of the lepton transverse momentum and the missing transverse energy must be > 60 GeV ("E_T^W"$=|p_T^{lep}|+\not\!\!E_T > 60$ GeV).

We first use the samples with only one electron and no muons, and we require exactly 4 jets with the above criteria. The latter requirement reduces the $t\bar{t}$ sample by an additional 30%. This is true for both signal and background, and means that after this selection the ratio of signal over background remains approximately constant. The precut sample in the DØ data has 91 events, and yields 71 events with only 4 jets.

In the published mass analysis [32], events in the precut sample were processed through kinematic fits to $t\bar{t}$ hypotheses. Events that did not provide a good fit ($\chi^2 > 10$) were removed, and this reduced the sample from 91 to 77 events. Because we do not use kinematic fitting, we do not implement this selection criterion in the present analysis. Using a Neural Networks (NN) analysis, DØ found 29 $t\bar{t}$ events in the sample of 77 events. The rest was supposedly background. Before the "W"selection the background is composed of 80% W+jets, and 20% multijet production. According to this breakdown, we define the size of our equivalent sample as follows:

$$\frac{91}{77} \times 0.70 \times [29(S) + 48(B)] \approx 24(S) + 40(B) \tag{6.1}$$

where 0.70 is the expected ratio of events with 4 jets (taken from Monte Carlo). Following the new top-mass analysis based on the matrix-element approach [62], we use the identical criterion on background probability to improve the purity of the $t\bar{t}$ signal, and require a poor background probability ($P_{VECBOS} < \mathrm{e}^{-25.3}$ or $P_{VECBOS} < 10^{-11}$) for accepted events. (See our previous discussion in Section 5 for the analysis using smeared events.) Figure 6.1 shows the normalized distribution of P_{VECBOS} probability for an event being background for both $t\bar{t}$ and W+jets events. The vertical line is the boundary where we will apply the selection. This selection reduces W+jets events by $\approx$ 70% and $t\bar{t}$ signal by $\approx$ 30%, similar to the effect found on smeared events (Section 5). We therefore obtain:

$$0.70 \times 24(S) + 0.30 \times 40(B) = 17(S) + 12(B) \tag{6.2}$$

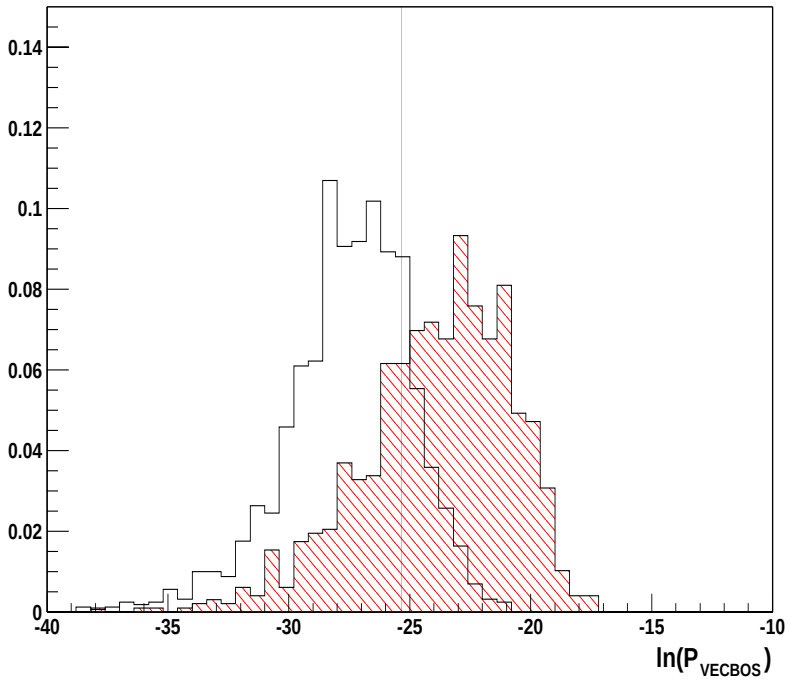

Figure 6.1: lnP_{VECBOS} probability for equal MC samples of $t\bar{t}$ e+jets (for M_t=175 GeV/c^2, and F_0=0.7) and for W+jets events (cross-hatched). The vertical line indicates where we apply the cutoff to remove $\approx$ 70% of the background, and only 30% of the signal.

where 12(B) = 9(W+jets)+3(multijets or "QCD"). This is the number of events expected on average. From the top-mass analysis [61], which uses the same selection criteria as this analysis, we obtained 12 signal and 10 background events from DØ Run I data. We have only $\approx$ 250 multijet (QCD) events before applying the cutoff on P_{VECBOS}, and we therefore do not include this background probability in our calculations. (Only 22% of these events are retained after applying the P_{VECBOS} cuttoff.) The difference between an analysis using these events and W+jets will be treated as a systematic uncertainty on the measurement. Figure 6.2 shows the normalized distribution of the probability that an event is background (based on P_{VECBOS}) for $t\bar{t}$ and multijet events.

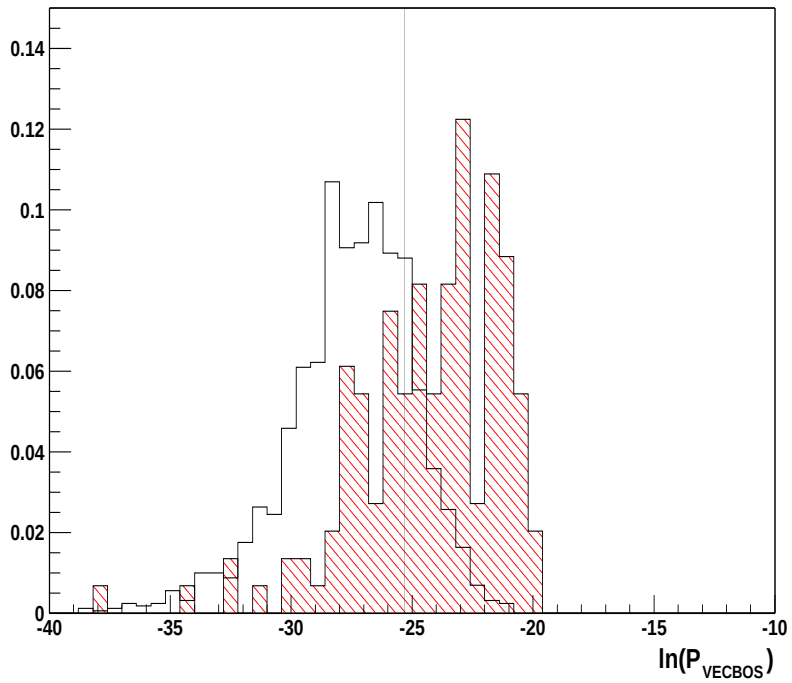

Figure 6.2: $\ln P_{VECBOS}$ probability for equal MC samples of $t\bar{t}$ e+jets (for M_t=175 GeV/c^2, and F_0=0.7) and data for multijet events (cross-hatched). The vertical line indicates where we apply the cutoff to remove $\approx$ 78% of the background, and only 30% of the signal.

6.4 Angular Distribution and p_T Spectra

In Figures 6.3-6.8 we examine variables pertinent to the decay of the W in different $t\bar{t}$ event samples. In particular, we display the p_T of the electron, and the angular distribution for the hadronic decay of the W (see Section 1.1). In Fig. 6.3 we compare HERWIG $t\bar{t}$ events at the generator and reconstructed level, and note not much difference between the two samples. Figure 6.4 shows the difference between a sample with only four jets, each matched to decay products of $t\bar{t}$, and another sample with more than 4-jets, and, again, with four of the jets matched to partons. In general, there is very little difference in the p_T spectra, but somewhat more difference in $\cos\hat{\phi}$, especially at largest $|\cos\hat{\phi}|$, which can be attributed to reconstruction inefficiencies when jets are emitted close to each other. Signal from HERWIG $t\bar{t}$ events and background from VECBOS/ISAJET for W+jets is compared in Fig. 6.5. Both of these samples have only 4 jets and, because of the permutation of jets, each event is entered 12 times in the histogram. Clearly, there is substantial difference between signal and background distributions. VECBOS events, hadronized with either ISAJET or HERWIG are compared in Fig. 6.6. There is no noticeable difference between these two evolution/hadronization procedures. Figure 6.7 shows the leptonic and hadronic angular distributions for PYTHIA samples for different F_0, after full simulation and reconstruction and after application of all selection criteria, including that on P_{VECBOS}. Not surprisingly, the samples with larger F_0 tend to be more symmetric relative to $\cos\hat{\phi}$=0 than those with smaller F_0.

6.5 Acceptance

In this section, we calculate the acceptance for the PYTHIA MC events stipulated in Table 6.1 using the two methods outlined in Section 3.7. The event selections will be those of Section 6.3, but, for comparison, we calculate the acceptance with and without the selection on the background probability ($P_{VECBOS} < 10^{-11}$). The reason for using PYTHIA instead of HERWIG $t\bar{t}$ events is that, while for HERWIG we only have events generated at F_0=0.703, for PYTHIA we have events generated at several values of F_0.

Table 6.2 shows the acceptance calculated by counting events (see Section 3.7.1) without imposing the selection on background probability. Table 6.3 shows the same results, but now with the selection on background probability. The results are plotted as points in Figs. 6.9 and 6.10, respectively.

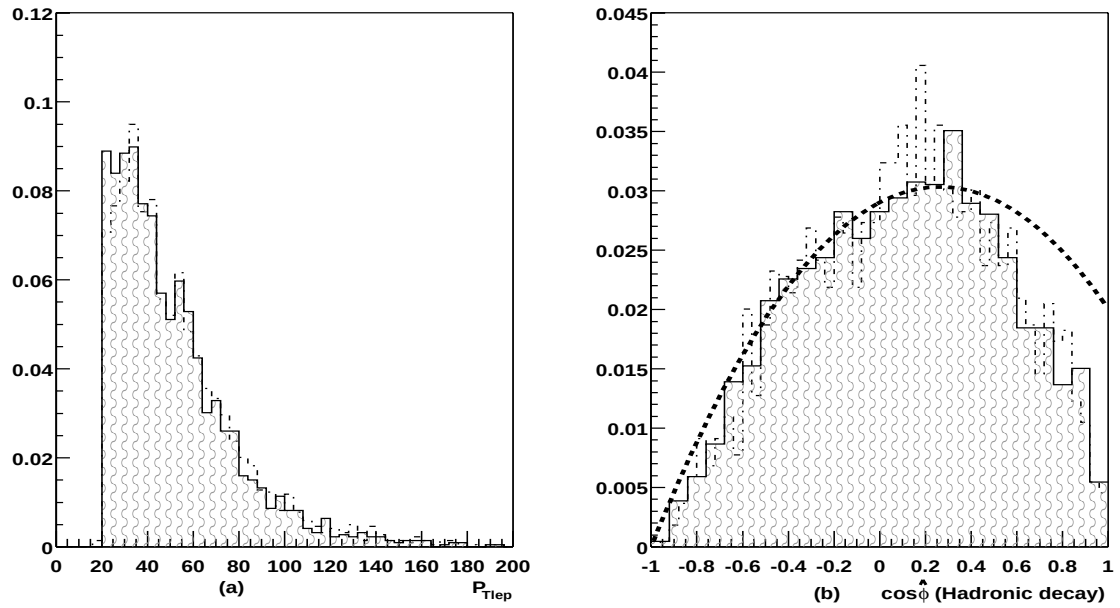

Figure 6.3: Comparison between reconstructed (shaded-histogram) and generated (dot-dashed histogram) variables for HERWIG $t\bar{t}$ e+jets events (M_t=175 GeV/c^2, F_0=0.7). (a) Electron p_T. (b) Angular distribution for the hadronic decay of the W, cos$\hat{\phi}$, where $\hat{\phi}$ is the angle between the d quark and the b quark in the W rest frame. All events passed the selections in Section 6.3, and the requirement of only four jets and that the jets be matched to partons. The matching required ΔR<0.15. The chopped line for cos$\hat{\phi}$ represents the uncorrected decay of the W in the $t\bar{t}$ matrix element.

We also calculated the acceptance using the second method outlined in Section 3.7.2. The coefficients needed to calculate the acceptance using Eq. 3.45 are shown in Table 6.4, without the selection in background probability, and in Table 6.5 for the case in which the selection in background probability was applied.

Combining all the coefficients from Table 6.4 with their errors, we obtain the following acceptance for the case in which the background probability was not applied

$$\begin{aligned} < Acc(F_0) > &= d_1 + d_2\, F_0 + d_3\, F_0^2 \\ d_1 &= 0.0780 \pm 0.0009 \\ d_2 &= 0.0220 \pm 0.0010 \\ d_3 &= -0.0007 \pm 0.0005 \end{aligned} \tag{6.3}$$

As in Section 5, the line given by Eq. 6.3 is shown as a dotted line in Fig. 6.9. The band showing the uncertainty was calculated using Eq. 3.48. And at the SM F_0 it corresponds

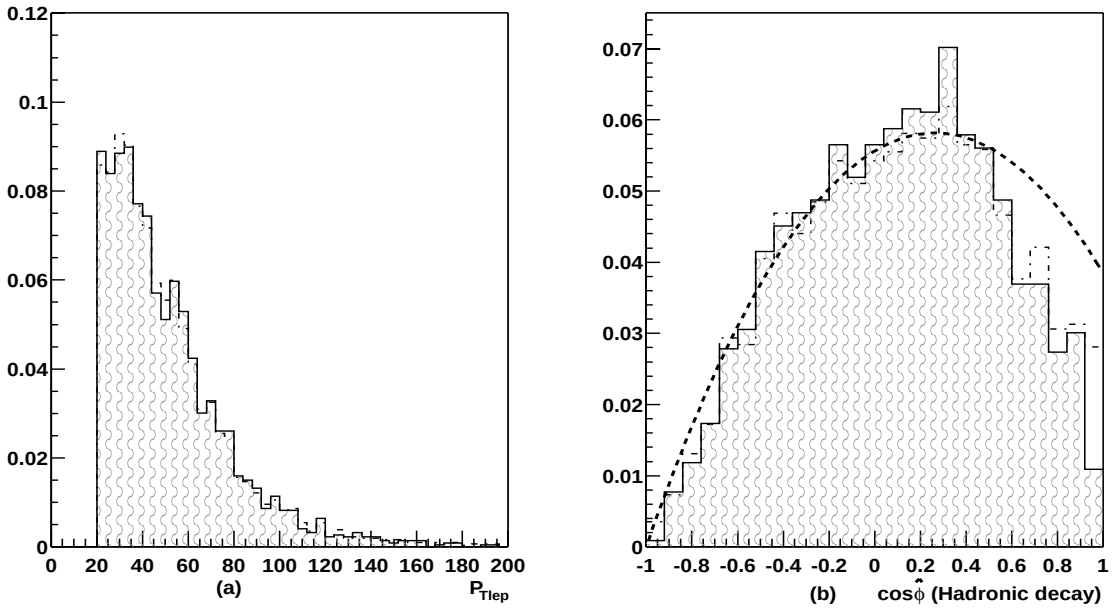

Figure 6.4: Comparison between reconstructed events with a total of only four jets all matched to partons (shaded histogram), and events with four matched jets, but having extra jets not matched (dot-dashed histogram). (a) p_T of electrons. (b) Angular distribution for the hadronic decay of the W, $\cos\hat{\phi}$, where $\hat{\phi}$ is the angle between the d quark and the b quark in the W rest frame. All the events passed the selections of Section 6.3. The matching required ΔR<0.15. The chopped line represents the uncorrected decay of the W in the $t\bar{t}$ matrix element.

to:

$$\delta < Acc(F_0 = 0.703) >= 0.0009 \quad . \tag{6.4}$$

Also, combining all the coefficients of Table 6.5 with their errors, we obtain the following acceptance for the case in which the background probability was applied

$$\begin{aligned} < Acc(F_0) > &= d_1 + d_2\, F_0 + d_3\, F_0^2 \\ d_1 &= 0.0526 \pm 0.0008 \\ d_2 &= 0.0147 \pm 0.0009 \\ d_3 &= 0.0005 \pm 0.0004 \end{aligned} \tag{6.5}$$

The line given by Eq. 6.5 is shown as a dotted line in Fig. 6.10. The band of uncertainty was calculated using all the errors and correlations from Eq. 3.48. The error on *Acc* for

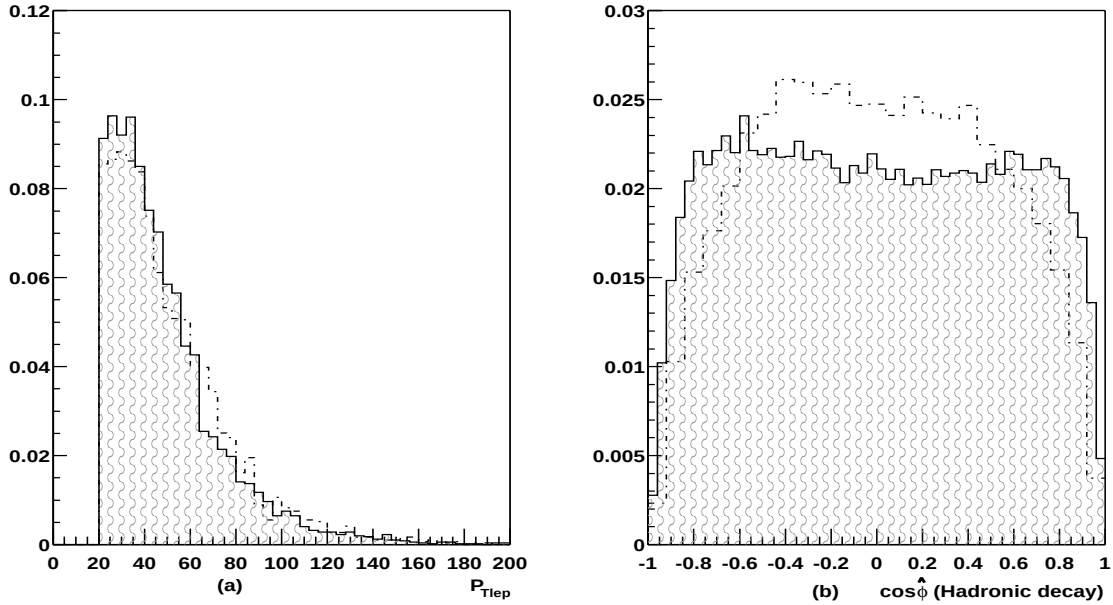

Figure 6.5: Comparison between reconstructed HERWIG $t\bar{t}$ events (shaded histogram) and reconstructed W+4 jets events processed via VECBOS/HERWIG (dash-dotted histogram). No jet matching was required, and all 12 combinations were included.

the SM is:

$$\delta < Acc(F_0 = 0.703) >= 0.0007 \quad . \tag{6.6}$$

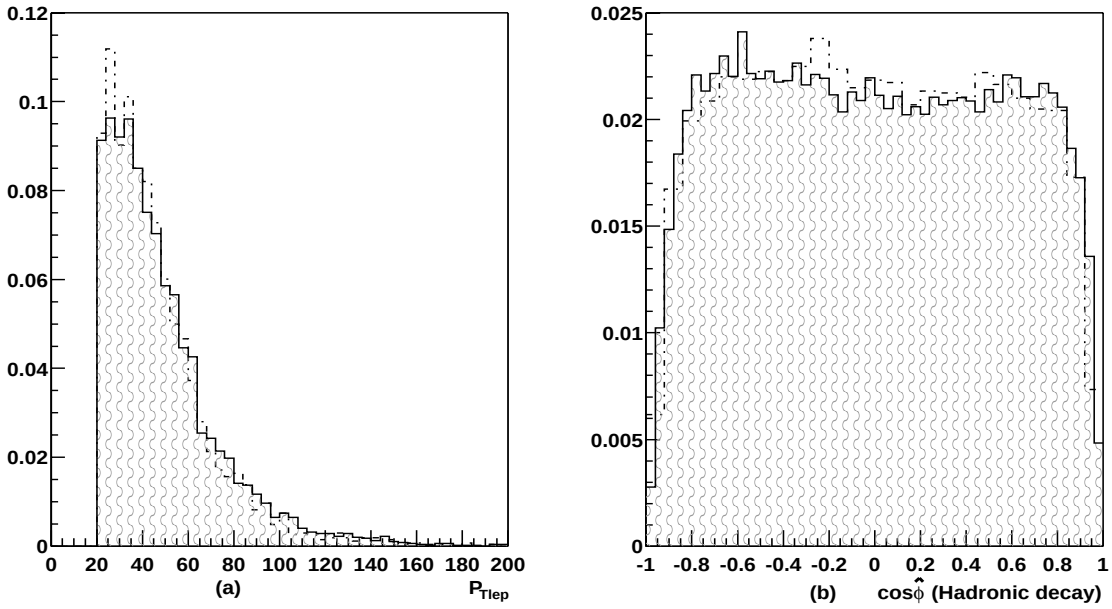

Figure 6.6: Comparison between reconstructed W+4 jets events generated with VECBOS/HERWIG (solid line) and with VECBOS/ISAJET (dot-dashed line). Not jet matching was required, and all 12 combinations were included.

Table 6.2: Acceptance corrections calculated by counting events (first method in Section 3.7.1). The events were selected according to Section 6.3, but without the requirement on background probability.

F_0	Generated events	Accepted events	Acceptance
0.50	22956	2060	0.0897±0.0019
0.55	34255	3033	0.0885±0.0015
0.71	29453	2732	0.0928±0.0017
0.83	24908	2475	0.0994±0.0019
0.91	31272	3093	0.0989±0.0017

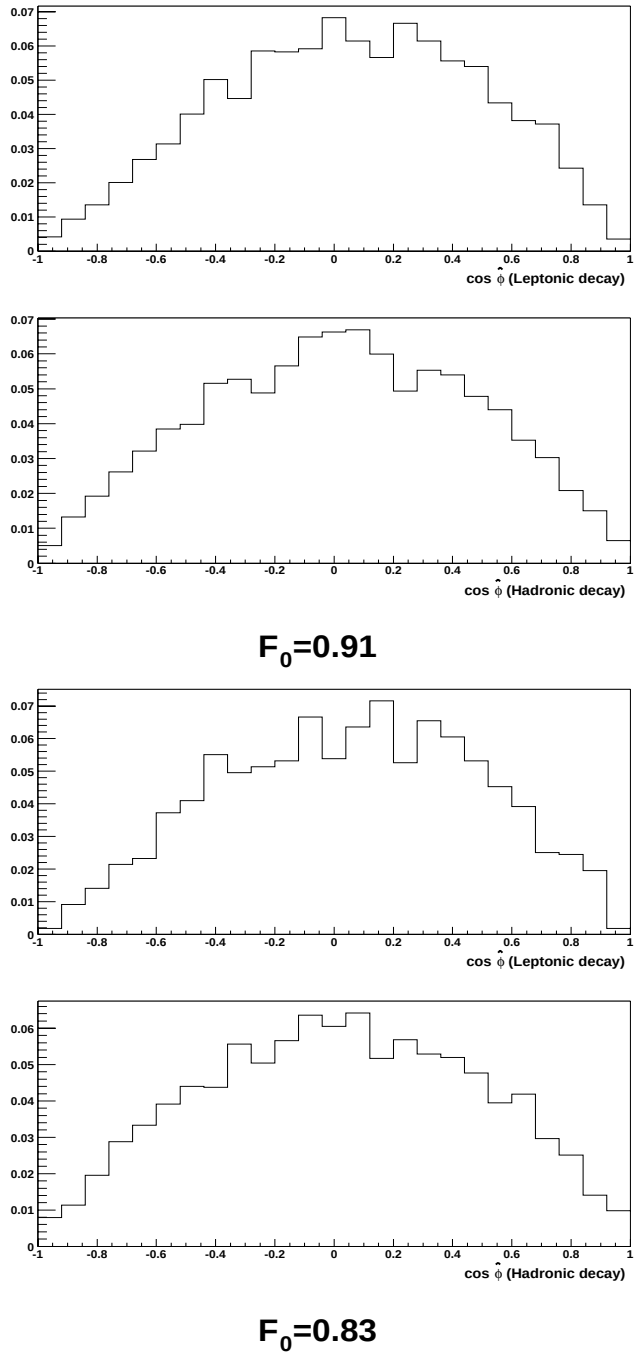

Figure 6.7: Angular distributions for leptonic and hadronic decay of the W for $t\bar{t}$ PYTHIA input samples with F_0=0.91 and F_0=0.83. Events were passed through full simulation and reconstruction and all selection criteria, including that on P_{VECBOS}.

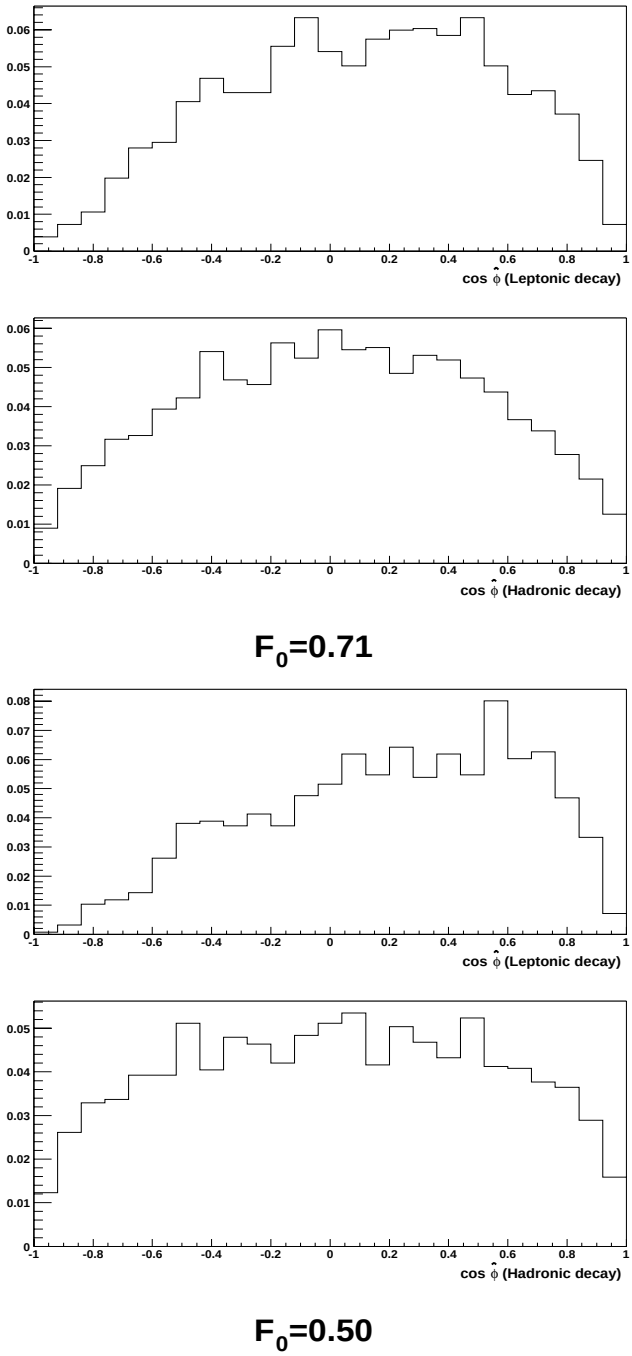

Figure 6.8: Angular distributions for leptonic and hadronic decay of the W for $t\bar{t}$ PYTHIA input samples F_0=0.71 and F_0=0.50. Events were passed through full simulation and reconstruction and all selection criteria, including that on P_{VECBOS}.

Table 6.3: Acceptance corrections calculated by counting events (first method in Section 3.7.1). The events were selected according to Section 6.3, including the requirement on the background probability.

F_0	Generated events	Accepted events	Acceptance
0.50	22956	1383	0.0602±0.0014
0.55	34255	1979	0.0578±0.0016
0.71	29453	1810	0.0615±0.0014
0.83	24908	1699	0.0682±0.0016
0.91	31272	2155	0.0689±0.0014

Table 6.4: Coefficients used to calculate the acceptance using Eq. 3.45 in Section 3.7.2. The events were selected according to Section 6.3, but without the requirement on background probability.

F_0	d_1	d_2	d_3	δd_1	δd_2	δd_3
0.50	0.0786	0.0221	0.0004	0.0019	0.0021	0.0011
0.55	0.0757	0.0228	0.0003	0.0016	0.0018	0.0009
0.71	0.0777	0.0200	0.0015	0.0020	0.0021	0.0011
0.83	0.0776	0.0248	0.0016	0.0024	0.0022	0.0012
0.91	0.0804	0.0205	-0.0001	0.0024	0.0020	0.0013

Table 6.5: Coefficients used to calculate the acceptance using Eq. 3.45 in Section 3.7.2. The events were selected according to Section 6.3, including the requirement on the background probability.

F_0	d_1	d_2	d_3	δd_1	δd_2	δd_3
0.50	0.0528	0.0145	0.0007	0.0016	0.0018	0.0009
0.55	0.0500	0.0142	0.0001	0.0013	0.0015	0.0008
0.71	0.0512	0.0134	0.0011	0.0016	0.0017	0.0008
0.83	0.0529	0.0172	0.0013	0.0020	0.0018	0.0011
0.91	0.0563	0.0143	-0.0005	0.0020	0.0017	0.0011

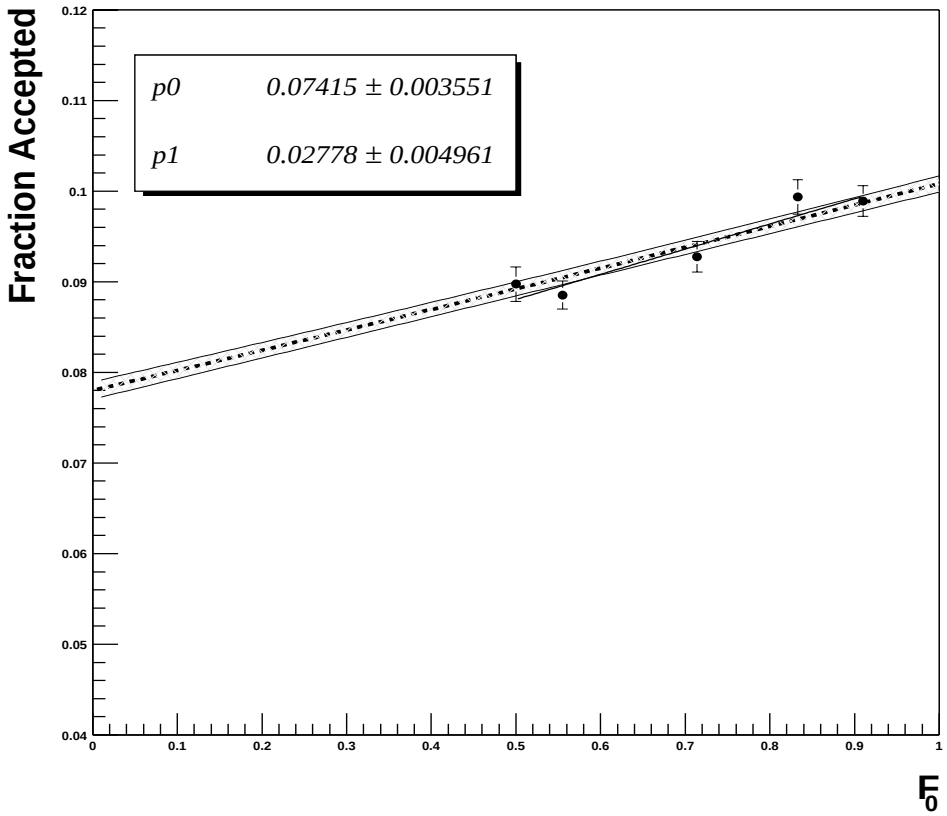

Figure 6.9: Fraction of fully reconstructed PYTHIA $t\bar{t}$ events accepted as a function of F_0. The points with error bars were obtained by counting events (see Section 3.7.1) that passed the selection of Section 6.3, except for the requirement on background probability. The straight line corresponds to a fit to the points. The dotted line and error band were calculated using the method of Section 3.7.2 and Eq. 6.3.

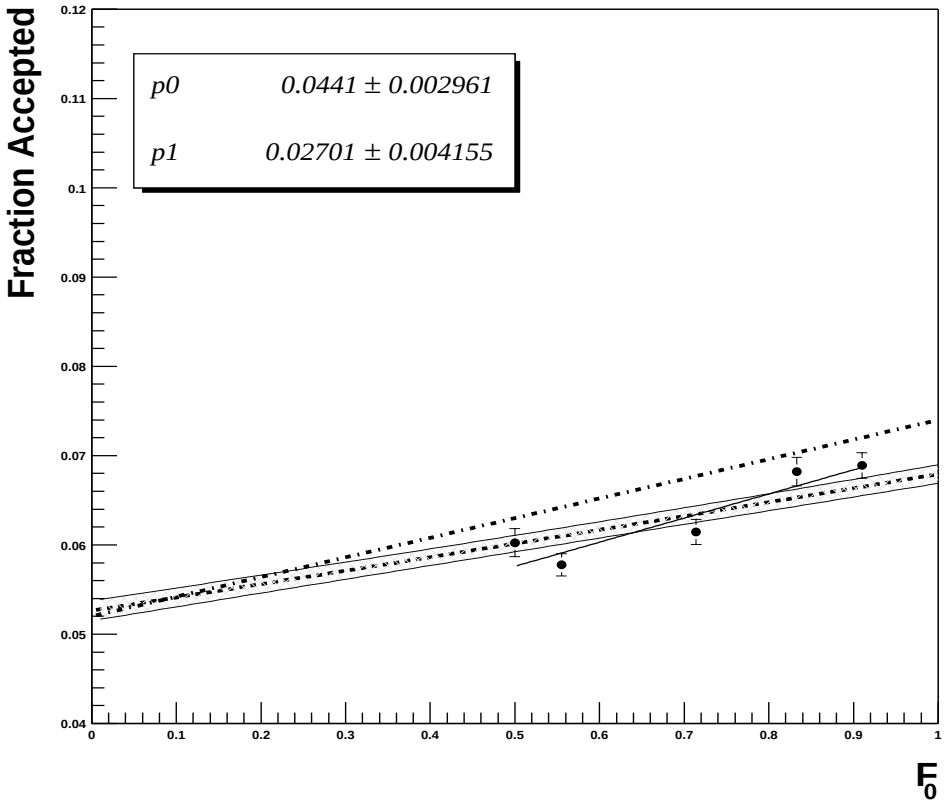

Figure 6.10: Same as Fig. 6.9, but after imposition of $P_{VECBOS} < 10^{-11}$. The dotted line corresponds to 0.052+0.022 F_0, the function that produces a slope of unity without an offset for cases without background.

6.6 Measurement of F_0, the Longitudinal Fraction of W Decays

We study the response of our method to different F_0 inputs, using fully simulated and reconstructed events that pass the selections criteria of Section 6.3. As in the case of smeared events, we use high-statistic samples to decouple the result from any bias due to low statistics, and we also investigate the effect of having background in the samples. A variety of ensemble tests are defined for the statistical samples of Run I. We again quote the most probable output value and the 1/2 68.27% interval as its uncertainty. The –ln(Likelihood) is fitted to a 5^{th} order polynomial as a function of F_0, and the smallest 68.27% interval is extracted from the exponentiation of this fit, that is from the probability distribution.

6.6.1 Studies using Signal

In this subsection we study only $t\bar{t}$ events. The likelihood is calculated for different values of F_0 using $\approx$ 2000-event PYTHIA samples, with the exception of samples for F_0=0.42 and 0.36 which contain 1000 and 800 events, respectively. We first use just the signal $P_{t\bar{t}}$ probability in the calculation, and require $P_{VECBOS} < 10^{-11}$. Figure 6.11 shows this result. (The square point uses 2000 events from HERWIG.) The deviation of the slope from unity can be attributed to the presence of poorly reconstructed events that are being forced to be fitted with just a $t\bar{t}$ signal probability. Once we admit a background probability in the calculation, we regain consistency with a slope of unity (Fig. 6.12). The signal background ratio in this case is about 88%, which indicates that 12% of signal is misidentified. We attribute the offset to the uncertainty on the acceptance. To investigate this further, we fluctuate the acceptance parameters d_1, d_2, and d_3 according to their respectives standard deviations in 100 experiments constructed with exactly the same signal events. The uncertainties obtained for each F_0 are shown in Table 6.6. Figure 6.13 is identical to Fig. 6.12, but also shows the result of the 100 experiment ensemble with the systematic error due to the acceptance at each point of F_0. We observe, however, that there is an acceptance function that produces a slope of unity without an offset for cases without background. This function (see Fig. 6.10) is 0.052+0.022 F_0, and it is within the errors of the acceptance parameters. Figure 6.14 shows the response using this function.

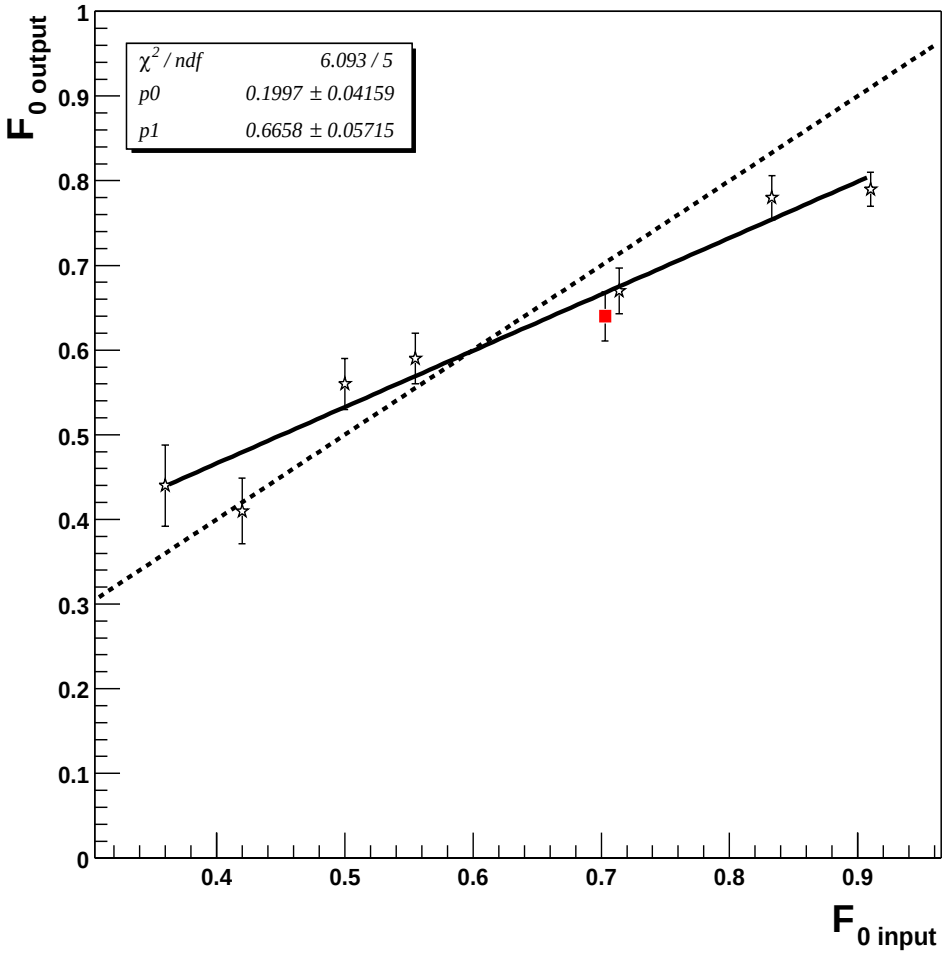

Figure 6.11: Response for only signal $t\bar{t}$ events, and only signal probability ($P_{t\bar{t}}$) used in the calculation. After the selection on P_{VECBOS}, there are ≈1400 events at each point, with exception of F_0=0.42 and 0.36, which use 700 and 400 events, respectively. The square point is based on the HERWIG sample (≈1100), and the stars are for the $t\bar{t}$ PYTHIA samples. The dotted line is a curve at 45 that passes through zero. The continuous line is a fit to the results from PYTHIA.

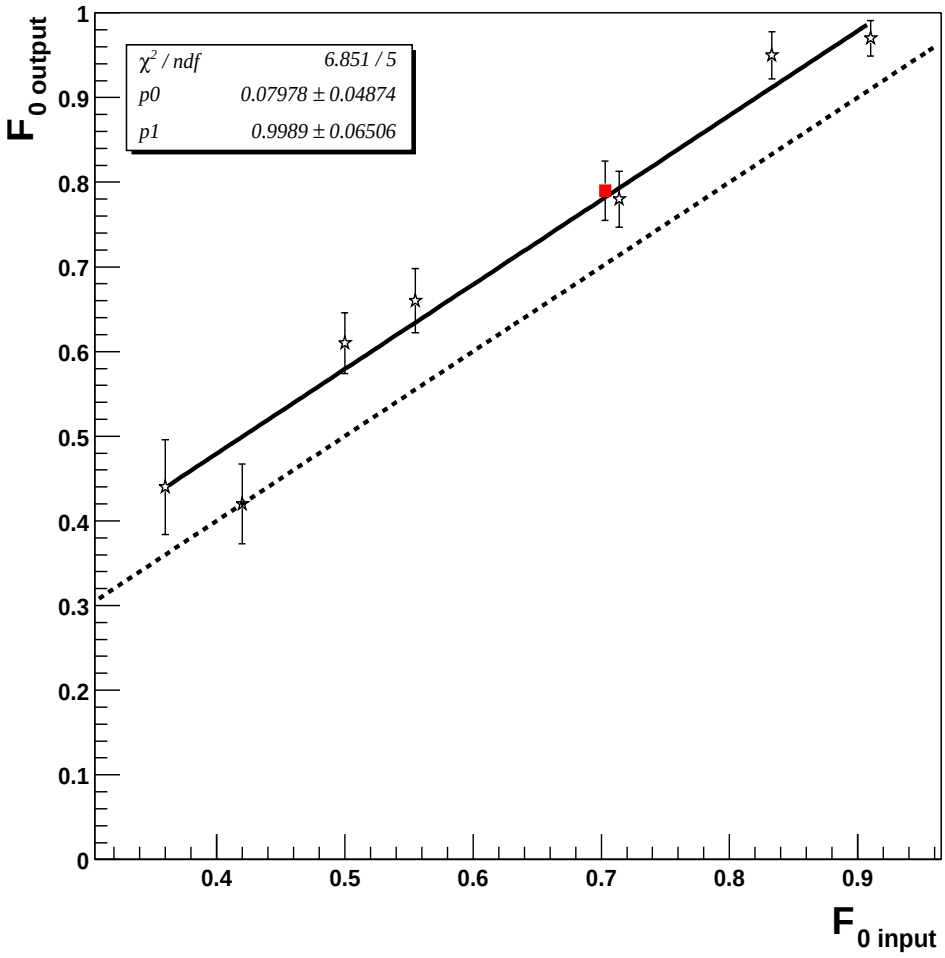

Figure 6.12: Same as Fig. 6.11, but allowing signal and background probabilities ($P_{t\bar{t}}$ + P_{VECBOS}) in the extraction of the output F_0.

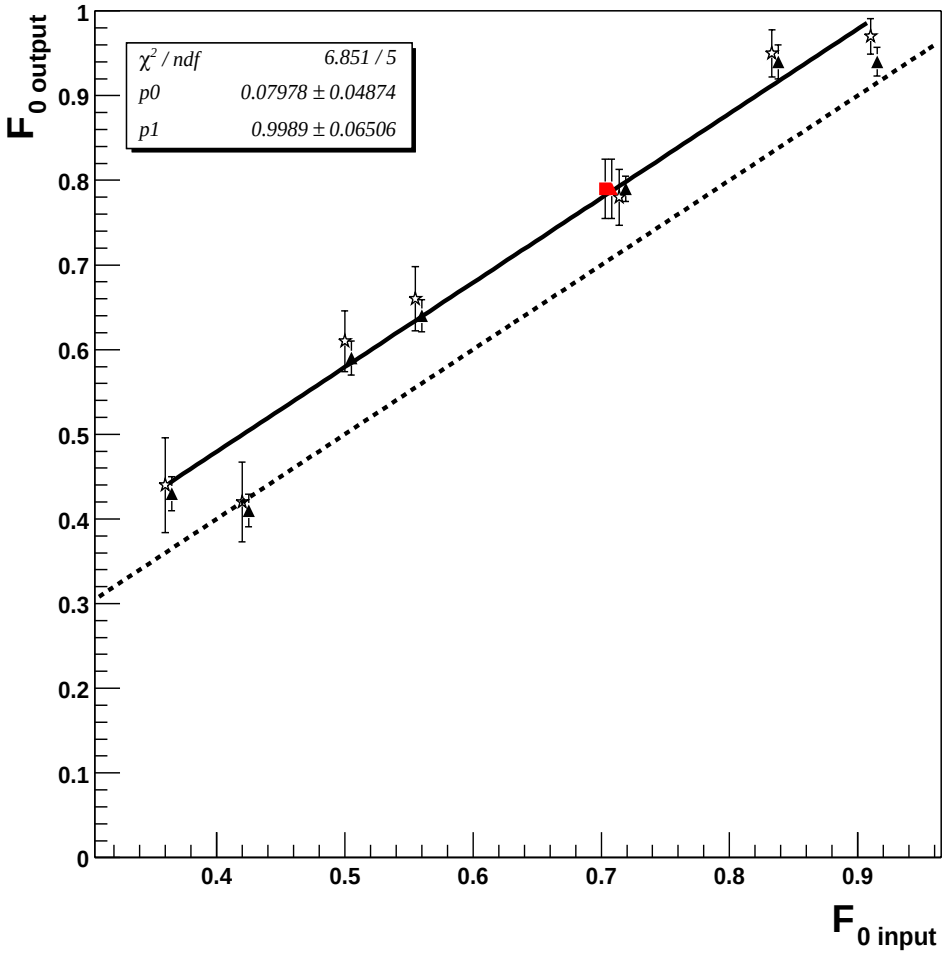

Figure 6.13: Same as Fig. 6.12, but with the triangles and their respective error bars showing the effect of modifying the acceptance parameters according to their respective standard deviations. (See Table 6.6). The triangle points are shifted somewhat for ease of comparison.

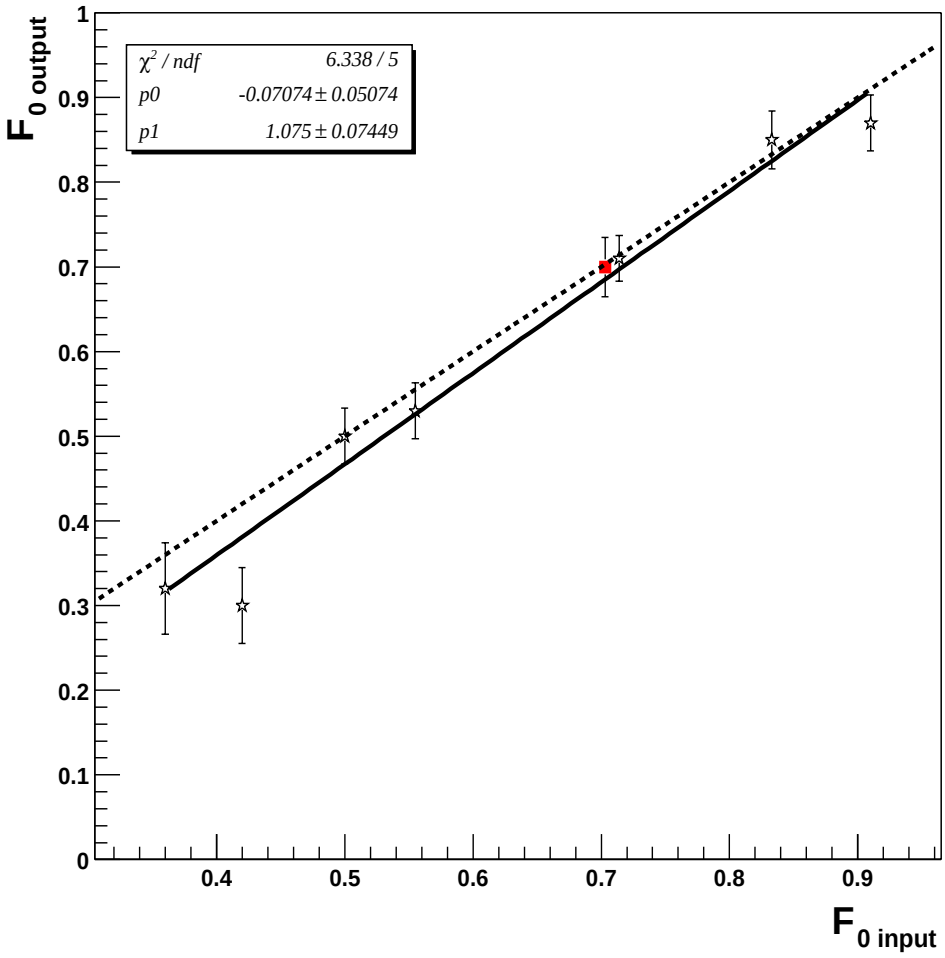

Figure 6.14: Same as Fig. 6.12, but using the specific acceptance correction $0.0519+0.022F_0$ (see text).

Table 6.6: Extracted value of F_0 as a function of the input value for MC samples of ≈1400 $t\bar{t}$ events (except 700 events for the F_0=0.42 sample and 400 with the F_0=0.36 sample). Uncertainty in acceptance was obtained using the same events and fluctuating the acceptance parameters in 100 experiments.

F_0 input	F_0 output	Statistical error	Error due to acceptance
0.36	0.42	0.056	0.020
0.42	0.44	0.047	0.019
0.50	0.61	0.034	0.020
0.55	0.67	0.035	0.019
0.71	0.79	0.031	0.015
0.83	0.93	0.031	0.020
0.91	0.97	0.028	0.017

6.6.2 Studies using Signal and Background

Here, we examine the VECBOS/ISAJET sample of 900 W+jets events, and, in particular, the effect of adding background in a high-statistics experiment. We use 1000 HERWIG SM $t\bar{t}$ events, and add the W+jets background until we use up the entire 900 events, at which point we decrease the number of $t\bar{t}$ signal events. The number of events in each combined sample is smaller, because the selection on P_{VECBOS} returns on average 70% of the $t\bar{t}$ events and 30% W+jets events. Figure 6.15 shows the result for extracted F_0 as a function of the signal fraction, and we see a bias towards smaller extracted values as signal/(signal+background) becomes smaller. From the "LB" analysis [69], we know that the Run I data sample corresponds to about 40% signal, at which the offset in Fig. 6.15 is ≈0.10±0.05. Comparing with a similar study using smeared level events in Section 5, we see that this effect appears to be more significant for fully simulated and reconstructed signal and background. Figure 6.16 compares the result for the two types of events. A complete understanding of this effect remains to be found, but there are many possibilities, such as like initial and final-state radiation, reconstruction issues, background, etc., that might be contributing to this bias.

We will examine the response of the method to different input F_0 values for a fixed ratio of signal and background. Before selecting on P_{VECBOS} we have a MC sample of 600 $t\bar{t}$ and 900 W+jets events at each input F_0. The number of events reflect the finding in previous top mass analyses, where there was ≈ 40% signal in the Run I data sample. Figure 6.17 shows the response as a function of input F_0. We perform two checks. First, we multiply the background acceptance by an arbitrary number, in this case 0.5, and

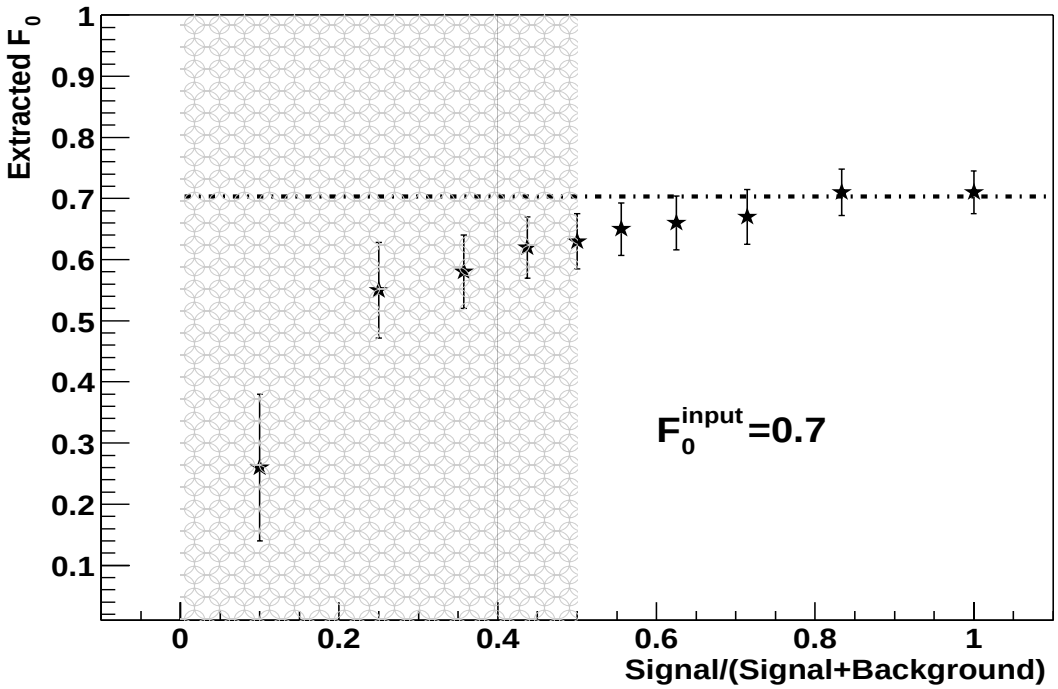

Figure 6.15: Extracted F_0 as a function of the ratio of signal/(signal+background), using a 1000 events HERWIG $t\bar{t}$ sample for F_0=0.7, and 900 VECBOS/ISAJET events as background. The number of events in each combined sample is smaller, because the selection on P_{VECBOS} returns on average 70% of the $t\bar{t}$ events and 30% W+jets events. In the shaded region, signal events are decreased as background remains at 900, while to the right of this region the number of background events increases and the signal is kept at 1000 events. The ratio of signal/(signal+background) events represents the number of events before applying the selection on P_{VECBOS}. The vertical line indicates the fraction of signal events (40%) that was obtained in the "LB" analysis [69] using Run I data.

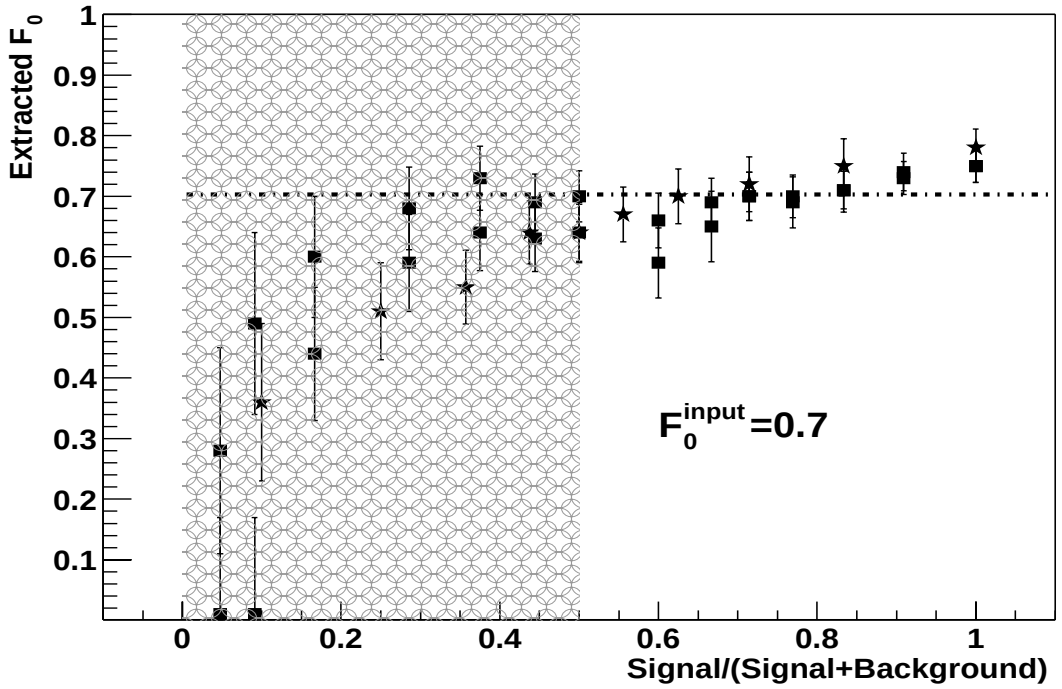

Figure 6.16: Same as Fig. 5.11 (stars), but now comparing with results using fully simulated and reconstructed PYTHIA $t\bar{t}$ and W+jets events (squares).

recalculate the response. Figure 6.18 shows that this change in the normalization does not affect the response of the method to the extraction of F_0. The other check is to see how the response is affected by a change in acceptance of the kind needed to account for the observed shift in F_0 (as in Fig. 6.14). Figure 6.19 shows the response using this corrected acceptance. We notice that the output values are shifted towards lower values of F_0, as expected from the difference between Figs. 6.14 and 6.12, but also the slope of the correlation increases somewhat (within uncertainty).

As a final test, we perform ensemble studies using the statistics of Run I for different F_0 samples. That is, 12 signal and 10 background events that pass the P_{VECBOS} selection criteria. Figures 6.20 to 6.26 indicate the number of ensembles and the most probable values and the distributions in uncertainty for input F_0=0.92, 0.83, 0.71, 0.55, 0.50, 0.42, and 0.36, respectively. The means and RMS uncertainties from these ensembles are plotted in Fig. 6.27. The fitted line yields somewhat different parameters, but consistent with the ones in Fig. 6.17. We will use the fit in Fig. 6.27 to correct the response (in fact, to correct the likelihood) in the data. We use this same correction on the likelihoods of all pseudo-experiments, and produce a corrected likelihood or probability, from which we extract the 68.27% interval in the physical region of F_0. We compare the percentage of the time that the input value of F_0 is within the defined 68.27% interval before and after applying the response correction. As expected, Figure 6.28 shows that there is better agreement with the 68.27% interval when the correction is applied. The distribution in the most probable F_0 and its uncertainty as well as the fraction of signal for the sample with F_0=0.7, after the correction for response, is shown in Fig. 6.29 for the 200 MC experiments. The extracted value of F_0 is 0.66$\pm$0.24 and the signal fraction is about 0.52, both consistent with expectation.

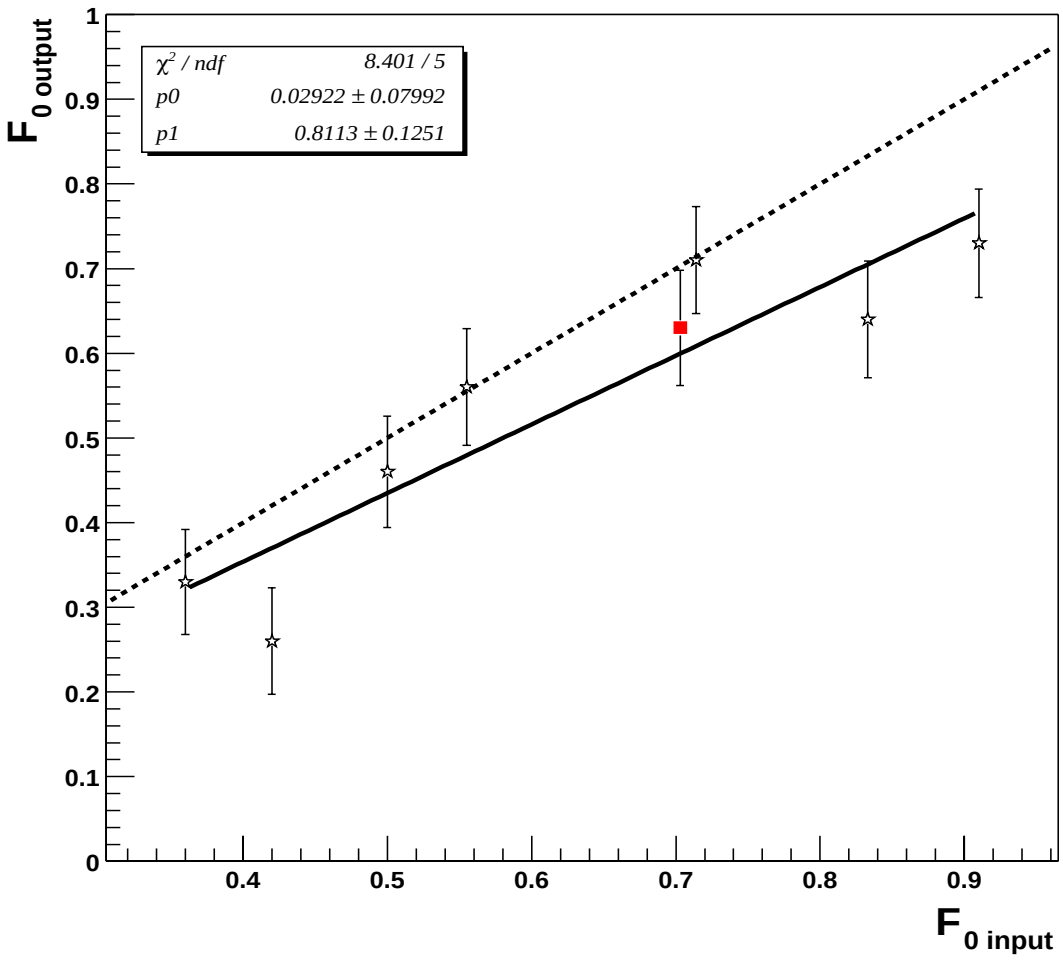

Figure 6.17: Result for extracted F_0 as a function of input F_0, for 600 PYTHIA $t\bar{t}$ events and 900 W+jets for the PYTHIA samples (stars), and for the HERWIG $t\bar{t}$ sample (square), after selecting on P_{VECBOS}. The linear fit is to the PYTHIA events.

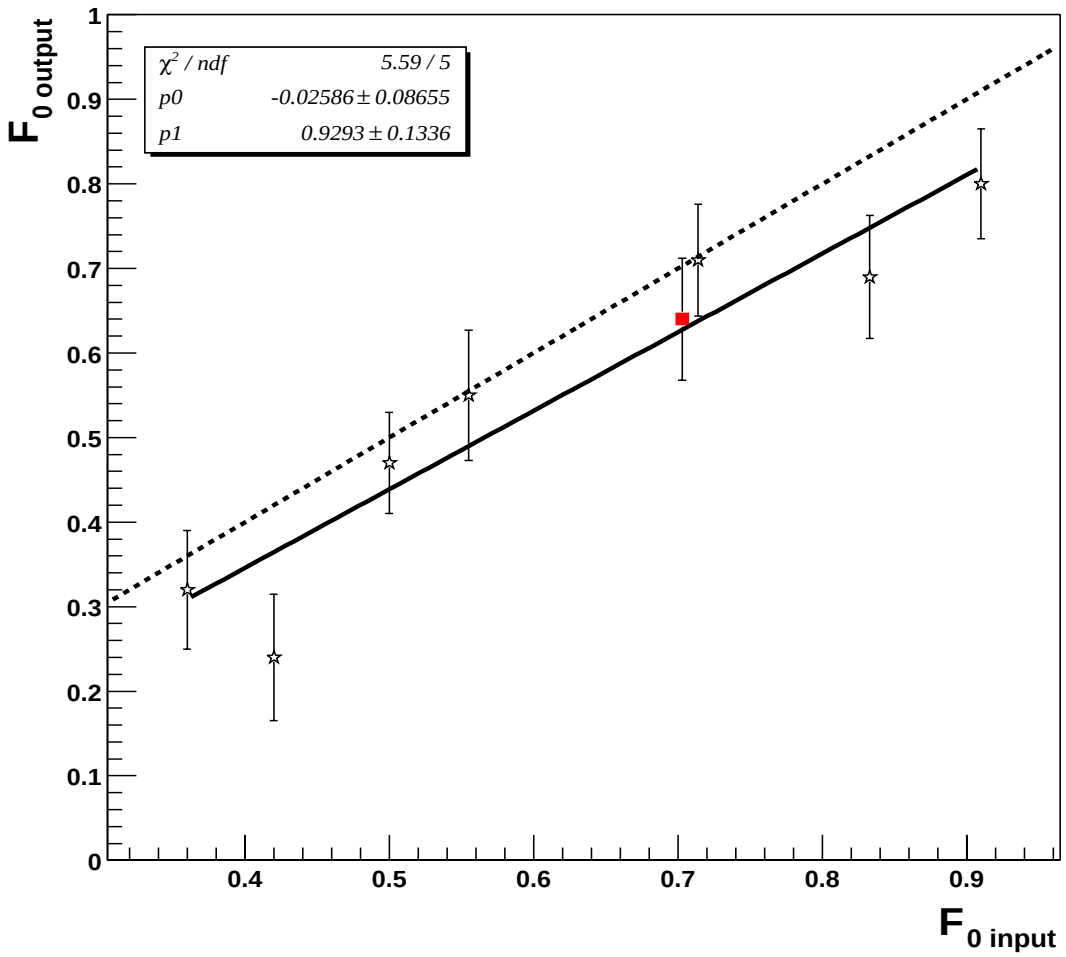

Figure 6.18: Same as Fig. 6.17, but with the acceptance multiplied by 0.5

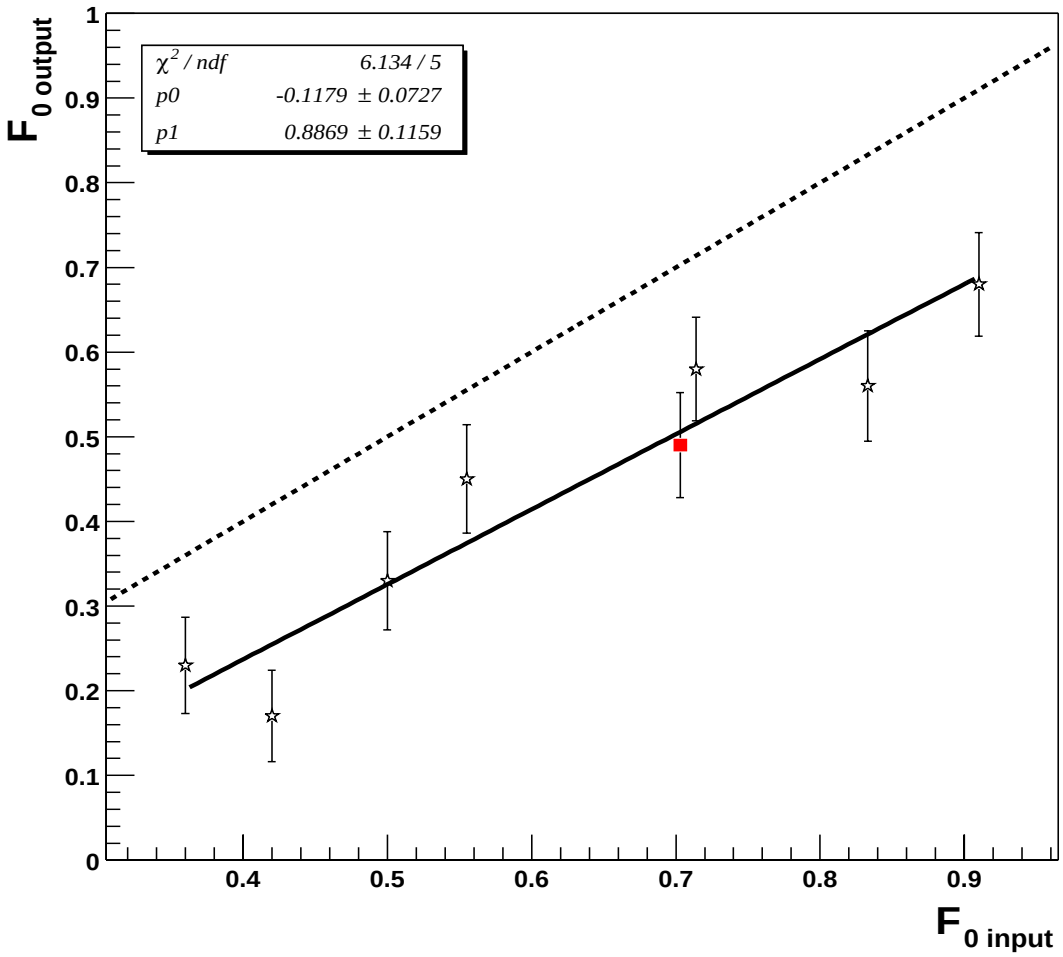

Figure 6.19: Same as Fig. 6.17, but using the acceptance that provides the response of Figure 6.14.

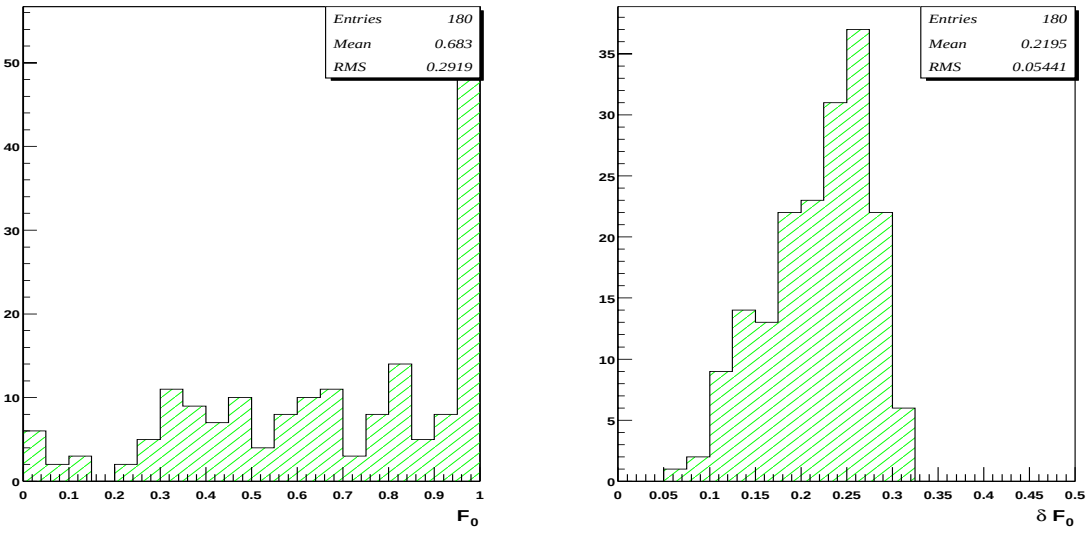

Figure 6.20: Ensemble result for most probable value of F_0 and its 68.27% interval in 200 experiments using 12 signal and 10 background events for F_0=0.91 after applying $P_{VECBOS} < 10^{-11}$.

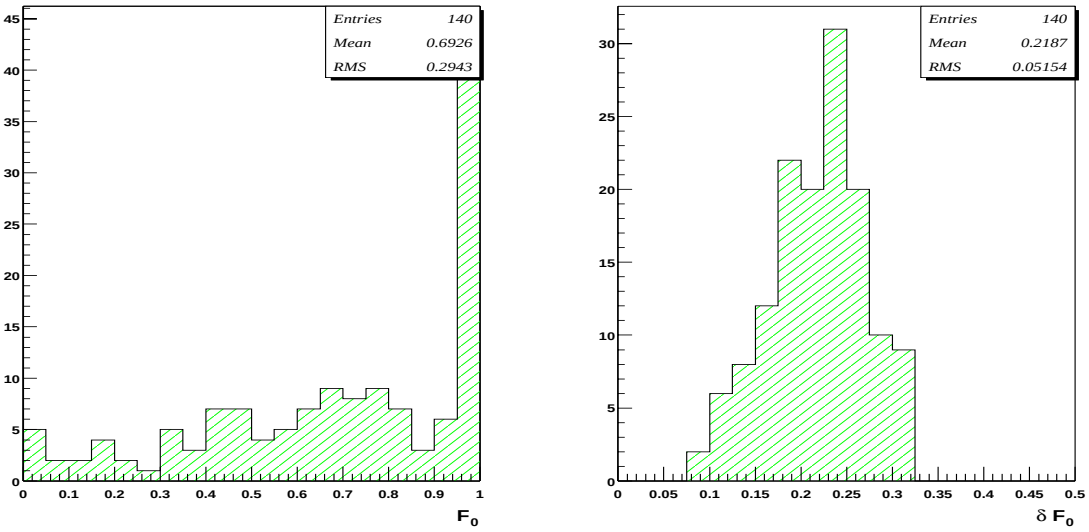

Figure 6.21: Same as Fig. 6.20, but for F_0=0.83.

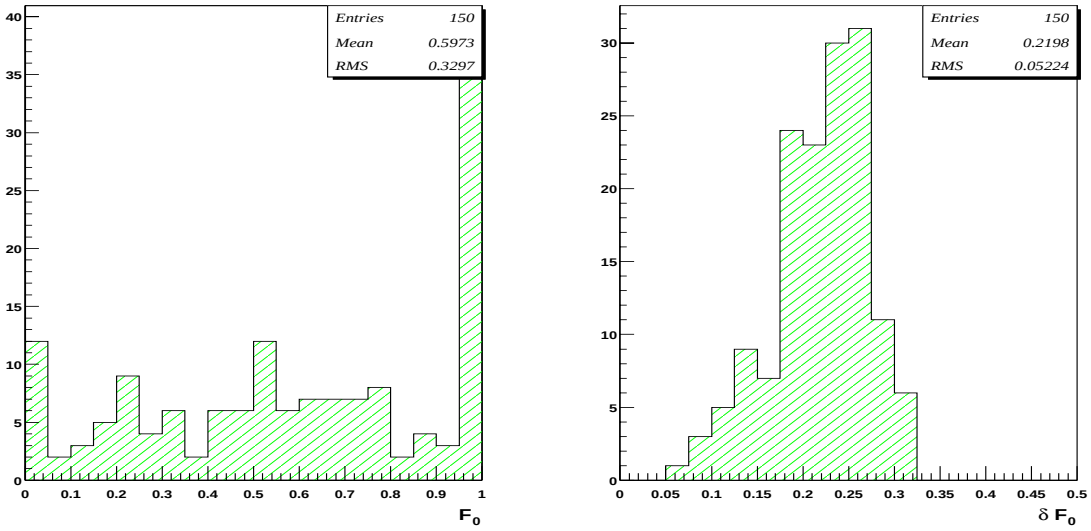

Figure 6.22: Same as Fig. 6.20, but for F_0=0.71.

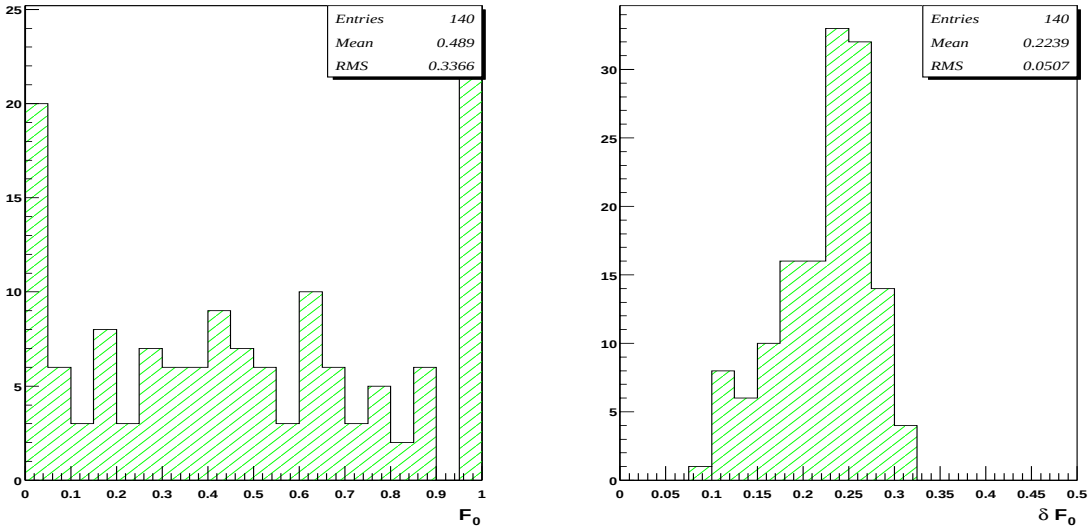

Figure 6.23: Same as Fig. 6.20, but for F_0=0.55.

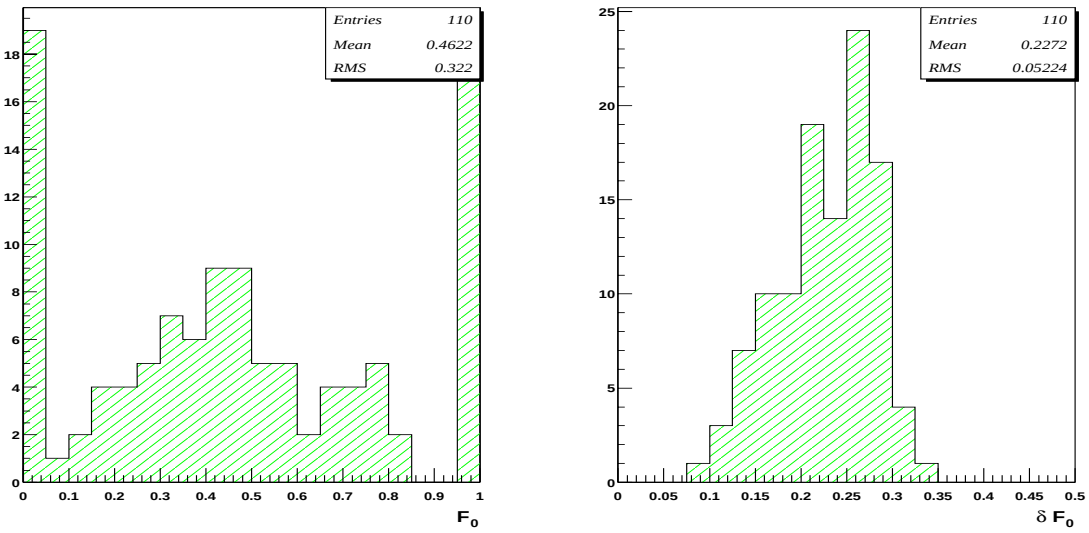

Figure 6.24: Same as Fig. 6.20, but for F_0=0.50.

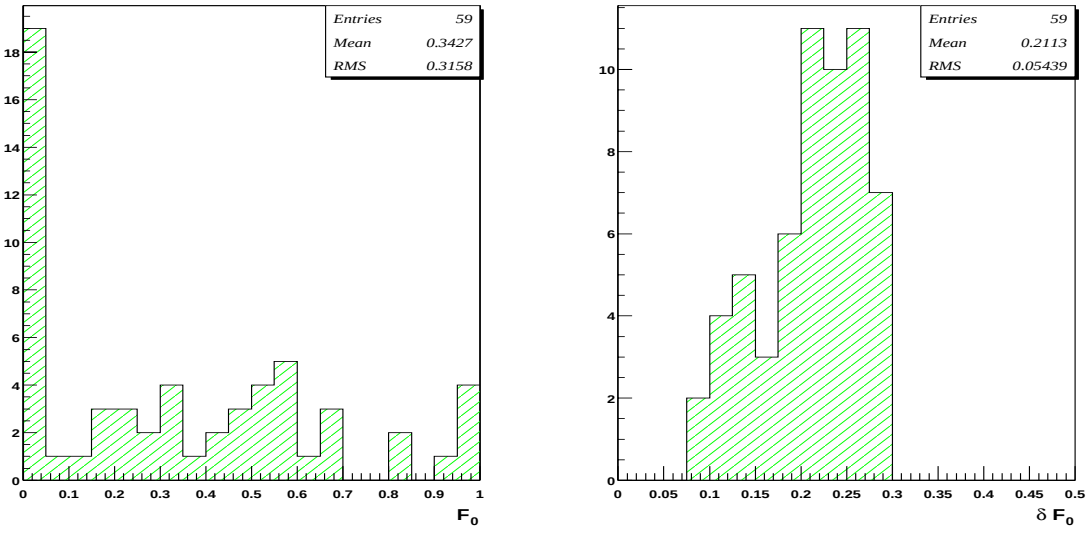

Figure 6.25: Same as Fig. 6.20, but for F_0=0.42.

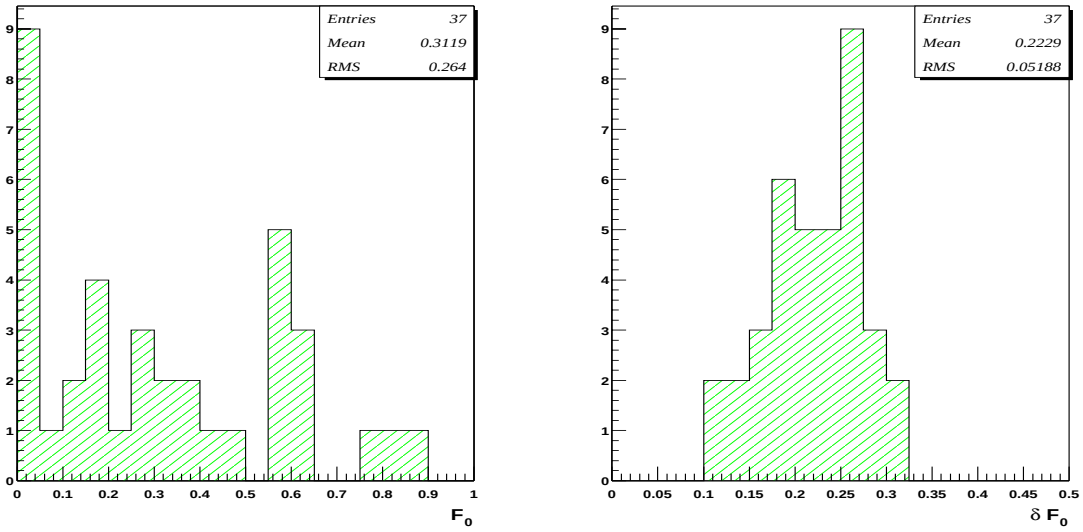

Figure 6.26: Same as Fig. 6.20, but for F_0=0.36.

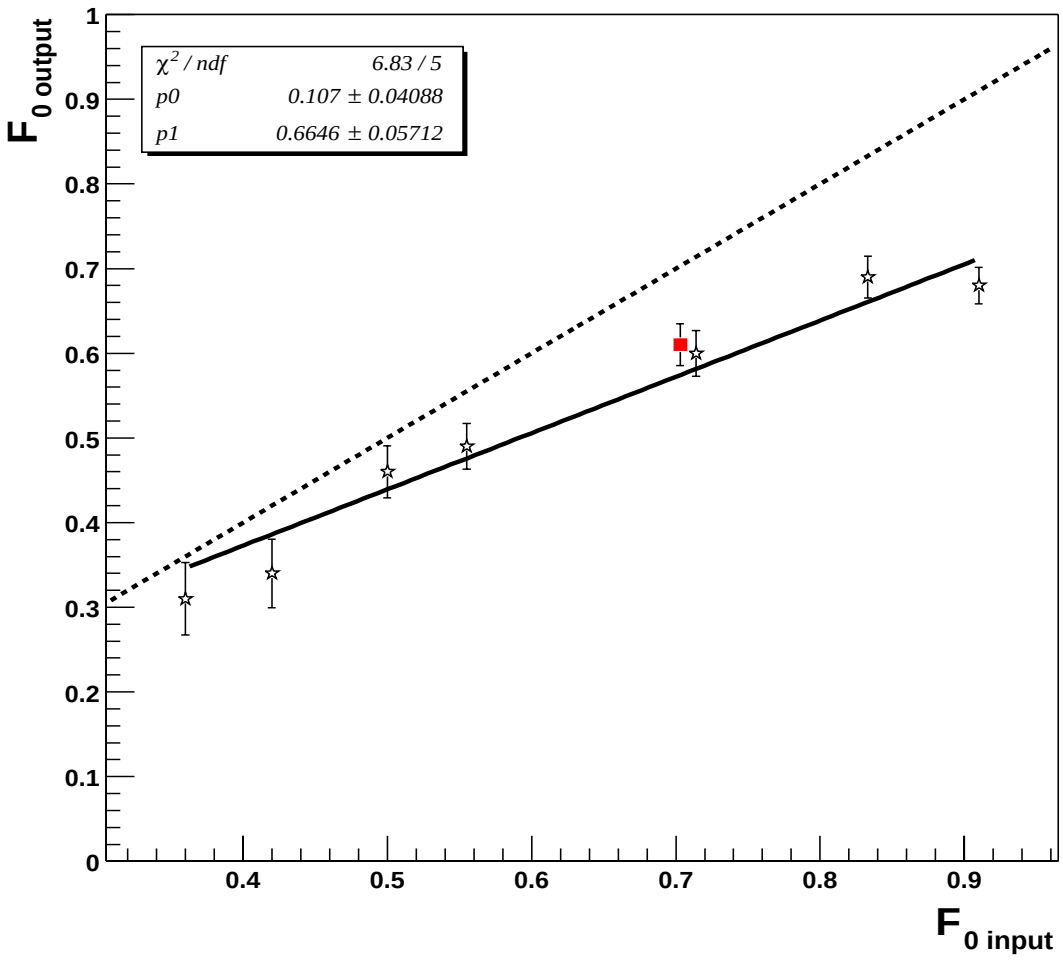

Figure 6.27: Result of F_0 extraction as a function of F_0 input, for ensembles of 12 $t\bar{t}$ signal events and 10 W+jets for the PYTHIA samples (stars) and HERWIG sample (square) after applying all selections.

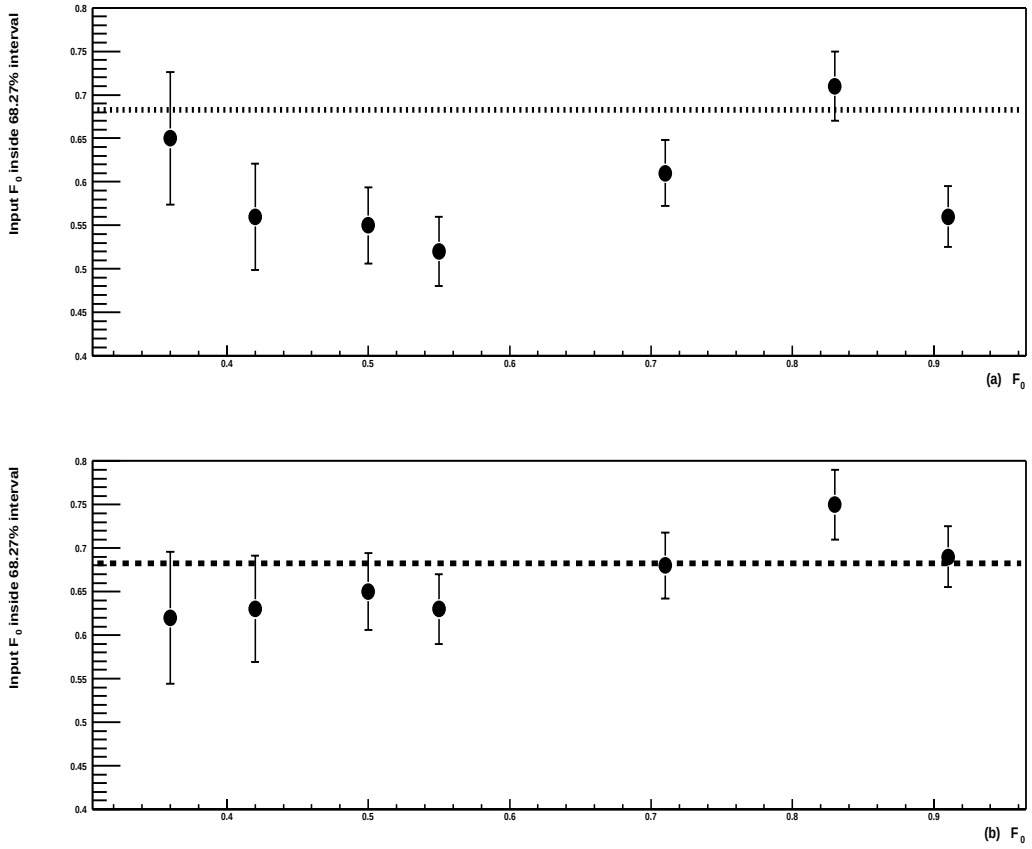

Figure 6.28: Percentage of the times that the input value of F_0 lies within the 68.27% interval before (a) and after (b) applying the response correction from Fig. 6.27.

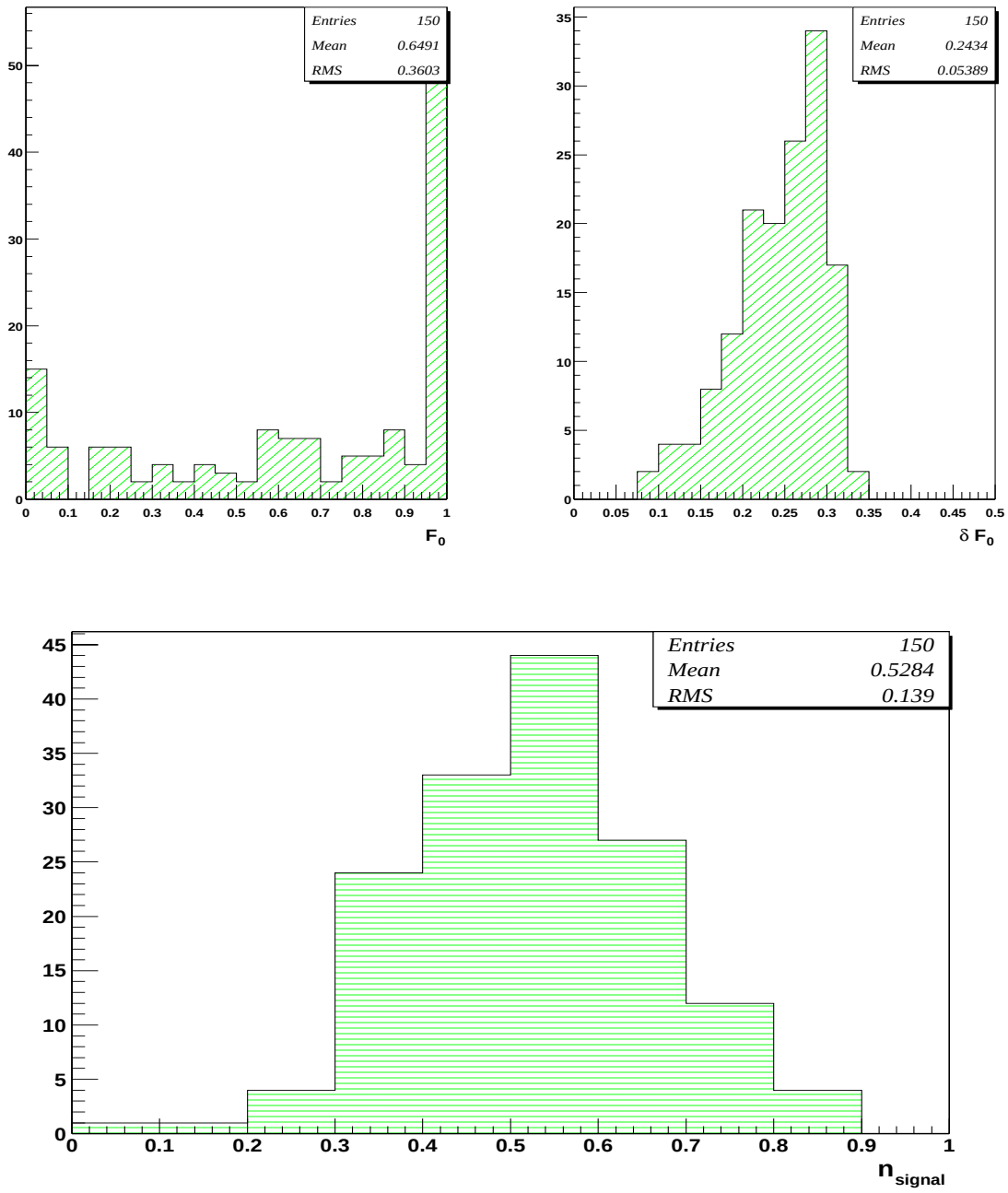

Figure 6.29: Ensemble results for the most probable value and its 68.27% interval in 200 experiments using 12 signal and 10 background for F_0=0.71, after applying $P_{VECBOS} < 10^{-11}$ and response corrections.

Chapter 7

Data

We apply the above analysis methods to data. We have 35 e+jets candidates and 36 μ+jets candidates in the Run I data sample. For events that contain a muon, the matrix element was integrated over the muon resolution (see Section 2.2.3), rather than assuming a δ-function in the integral of Section 3. This integration was done using Simpson quadrature with 49 points. All jets in the events use the η-correction from Section 2. After applying the requirement $P_{VECBOS} < 10^{-11}$, we retain 22 events. The result for F_0 is shown in Fig. 7.1. The most probable value is 0.506±0.273. After modifying the likelihood using the fit in Fig. 6.27 to account for the bias in response to input F_0, the likelihood of the Run I data sample changes to the one given in Fig. 7.2. We recalculate the 68.27% interval in the physical region of F_0, obtaining F_0=0.599±0.301.

We calculated the number of signal events in data according to Appendix H. The result yields a signal fraction or purity $r=\frac{n_s}{n_s+n_b}$=0.50±0.12. As can be seen in Appendix H, a correction factor of k=0.88 has to be applied to obtain the true number of $t\bar{t}$ events in the sample. This correction yields $n_s=n_{tot}\times r/k$ =12.54±3.01 $t\bar{t}$ events in the analysis (where n_{tot}=22 is the total number of events).

Figure 7.3(a) shows the probability for a background interpretation of signal and background, calculated for a large sample of combined MC events (solid histogram), and for the 71 individual $t\bar{t}$ candidates in the data (points). Only the 22 events to the left of the vertical line are chosen for the final analysis ($P_{VECBOS} < 10^{-11}$). The total number of MC events is normalized to the 71 4-jets $t\bar{t}$ candidates. The left-hatched (right-hatched) histogram shows the contribution from the $t\bar{t}$ (W+4 jets) MC events. The ratio of $t\bar{t}$ to W+4 jets in MC is normalized to the ratio S/B=12/10 observed in the data to the left of the vertical line.

A discriminant $D = P_{t\bar{t}}/(P_{t\bar{t}} + P_{VECBOS})$ was defined to compare the probability that an event corresponds to signal or background. Since the signal probability depends on M_t, D was calculated with the signal probability taken at its most likely value when scanned over the top-quark mass. Figure 7.3(b) shows a comparison of the discriminant calculated for data (points with errors bars) and for MC (solid histogram) events, with the MC normalizes as in Fig. 7.3a. The discriminant was not used to reject background, because (unlike the background probability) its value depends directly on the top mass, and therefore also on F_0, the parameter we are trying to determine.

To study the stability of the result with respect to the selection on background probability, we extracted F_0 with the values of cuttoff on P_{VECBOS}= (0.5, 1.0, 2.0, 3.0, and 4.0)$\times 10^{-11}$. The number of events that pass these selections are 19, 22, 31, 34, and 36, respectively. Figure 7.4 shows that a change in the cutoff by an order of magnitude, which changes the number of events used in the analysis by about a factor of two, leaves the extracted F_0 essentially unchanged. (Since the acceptance changes for different cuttoff values of P_{VECBOS}, we applied a recalculated acceptance correction at each of these points.)

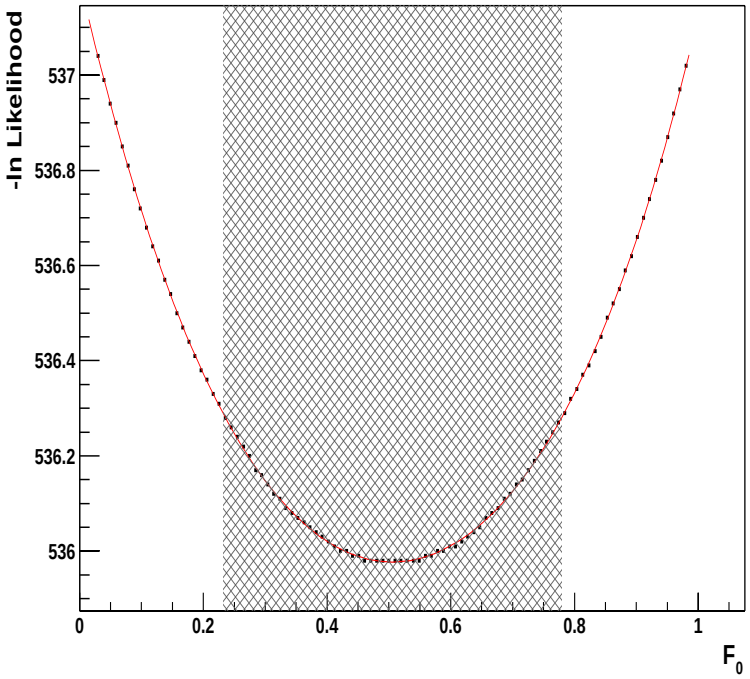

Figure 7.1: –ln(Likelihood) as a function of F_0 for data. The most probable value is F_0=0.506, and the 68.27% interval corresponds to an uncertainty of 0.273. Upon minimization, the 22 events in the Run I sample yield 12 signal and 10 background. No response correction was applied to this result.

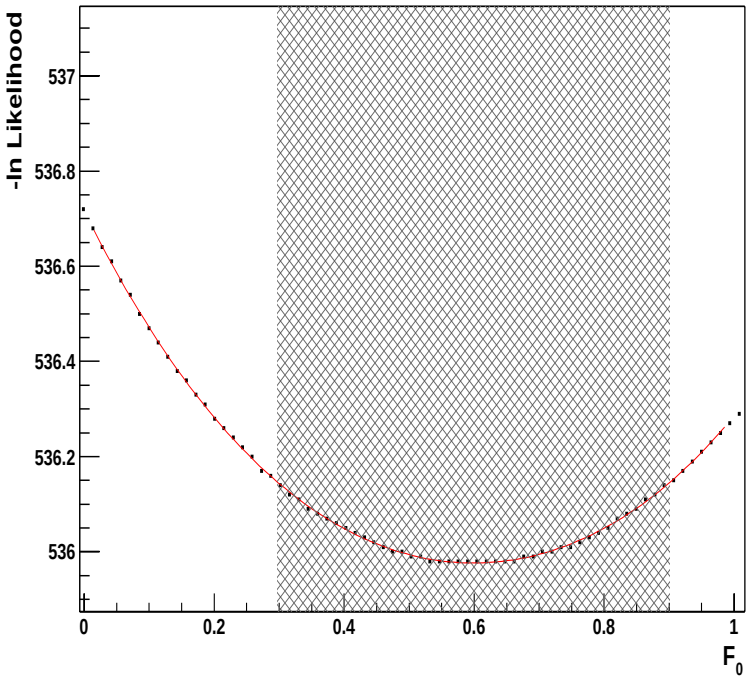

Figure 7.2: Same as Fig. 7.1 but after applying the response from Fig. 6.17. The most probable value is F_0=0.599, and the 68.27% interval is 0.301.

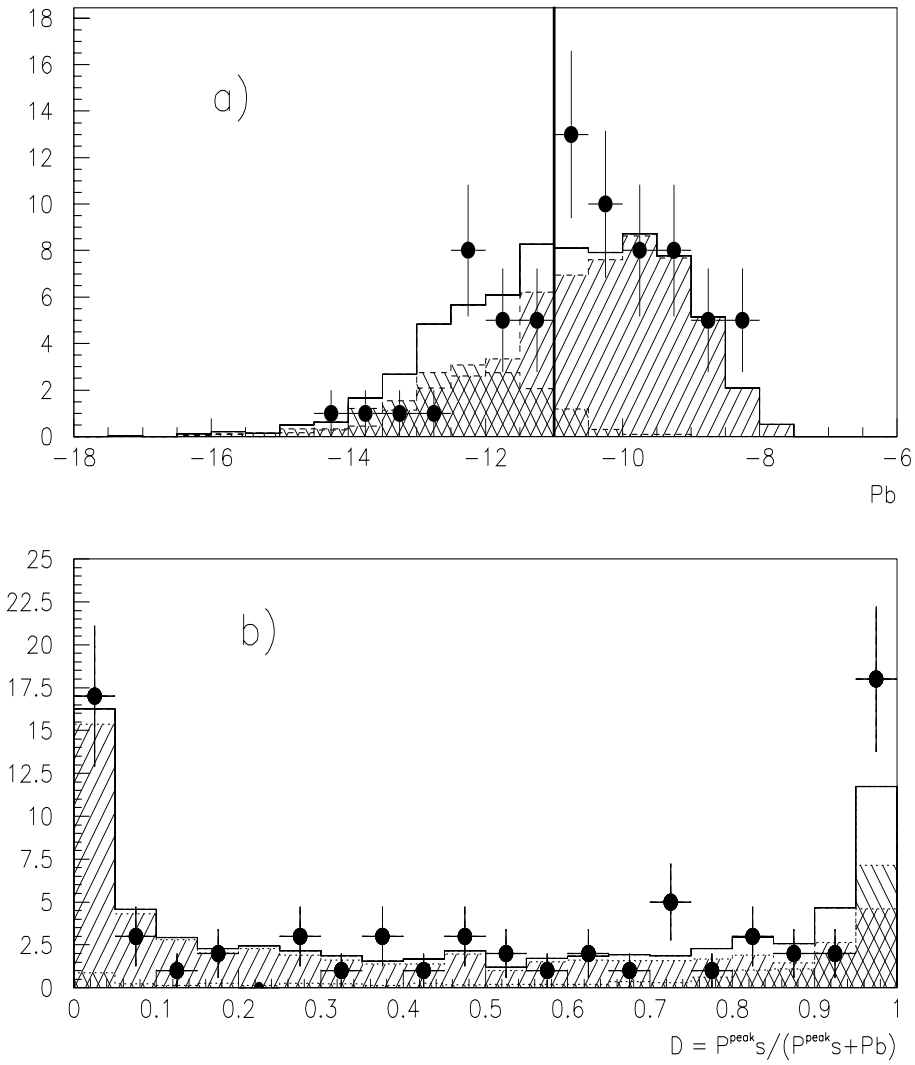

Figure 7.3: a) Distribution for probability of events being background, and b) discriminant $P_{t\bar{t}}/(P_{t\bar{t}} + P_{VECBOS})$, calculated for the 71 $t\bar{t}$ candidates (data points). The data are compared with the results expected from MC-simulated samples (solid histogram). Only events with $P_{VECBOS} < 10^{-11}$ are considered in the final analysis.

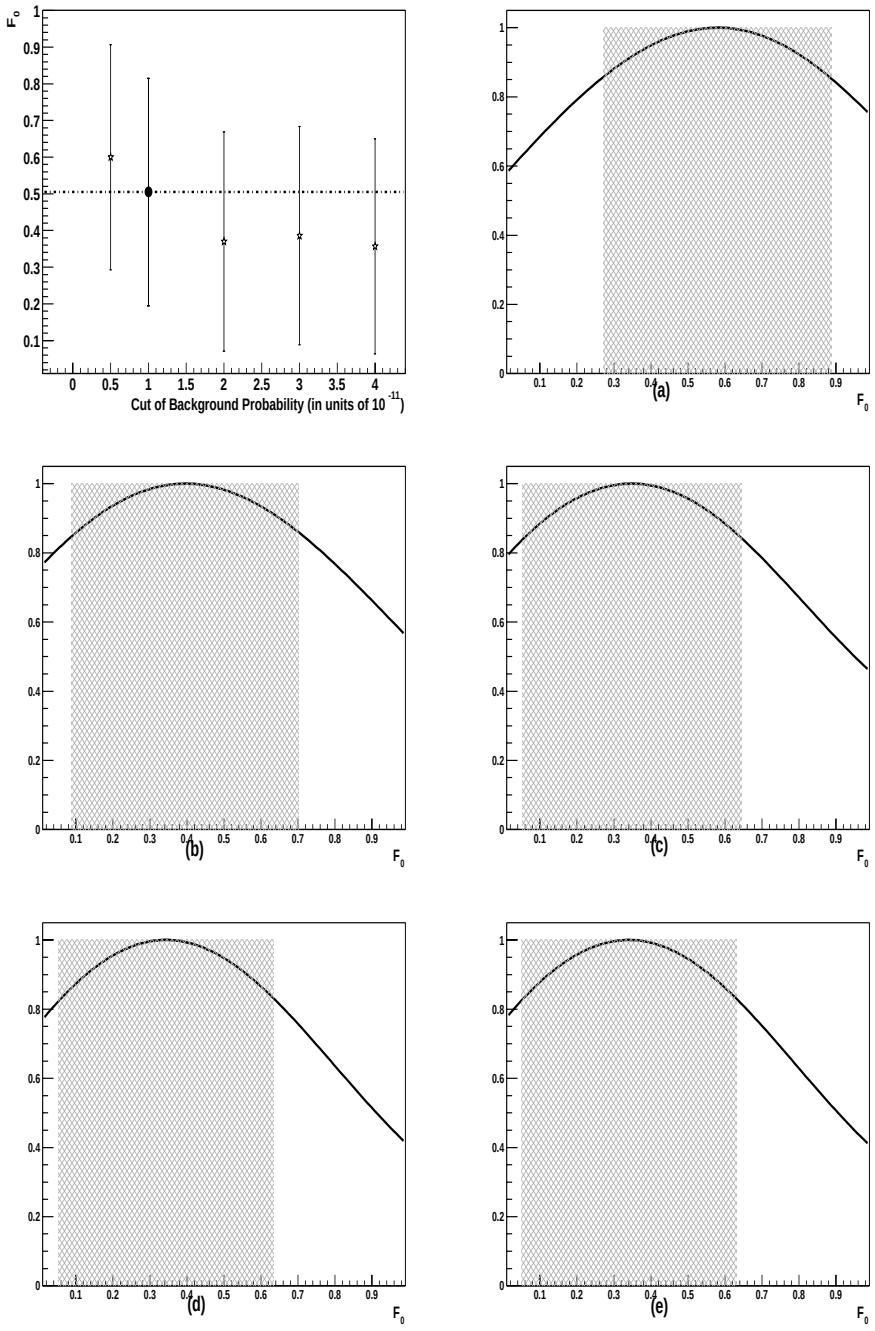

Figure 7.4: Uncorrected F_0 as a function of the cuttoff on background probability. The individual probability distributions, all of which have a different acceptance corrections, are shown in order of increasing value of the selection on P_{VECBOS} from (a) to (e).

Chapter 8

Systematic Uncertainties

Because the extracted F_0 is required to lie inside the physical region, its total uncertainty cannot be greater than 0.34, that is half 68.27% interval for the region between 0 and 1. We will calculate the total uncertainty based on the contributions discussed in the following sections. Adding all the separate components in quadrature, may in fact overestimate the total uncertainty, and perhaps bring it above the limit of 0.34 for the case of no information whatsoever on F_0. A fully Bayesian approach, integrating over all uninteresting parameters [78], would provide the best way of estimating the uncertainty, but this is not always possible.

Calculating errors using an external method and adding them in quadratures to the measurement of F_0 could overestimate the uncertainties in such a way that it might increase the limit beyond 0.34. Therefore, if possible, we should calculate the uncertainties internally so this limit can be attained.

8.1 Systematic Error due to Uncertainty on the Top Mass

In Run I of the TeVatron, the top-quark mass was measured to be M_t=174.6±5.4 GeV/c^2. To get a better understanding of the dependence of F_0 on M_t, we proceed in two ways. First, we generate events at different values of M_t, in particular, different HERWIG $t\bar{t}$ samples with M_t=170, 175, 180 GeV/c^2. As noted previously, F_0 has a weak dependence on mass: $F_0 = 1/(1 + 2(M_W^2/M_t^2))$. We calculate the probability for these samples for a top mass of 175 GeV/c^2. Figures 8.1a-c show the three –ln(Likelihood) as a function of F_0 using high-statistics samples, comparing their most probable values and

68.27% intervals in Fig. 8.1d. Second, we study the dependence of F_0 on the top-quark mass using a single $t\bar{t}$ MC same sample (HERWIG with F_0=0.703 and M_t=175 GeV/c^2), and analyze it using top masses M_t=170, 175, and 180 GeV/c^2. Figure 8.2 shows the three –ln(Likelihood) and a comparison of the results. It appears that the second approach shows a dependence on top mass opposite from the first one. The first method gives a difference of 0.11 on the most probable values of F_0 and the second method a difference of 0.08, for the extremes.

We compare Monte Carlo ensembles with similar Run I statistics (12 signal and 10 background events) to data and analyze both assuming different top-quark masses. Figure 8.3 shows a comparison of the mean of the most probable value for the ensemble with the mean for distribution of uncertainties given by the error bars, and the same results obtained analyzing the data using different input masses. From masses 170 and 180 GeV/c^2, the change in F_0 for data (stars) is about δF_0=0.1. Figure 8.4 shows the dependence of the extracted value of F_0 in data for a larger range of input top masses, with the shaded region indicating the uncertainty on the measured mass of the top quark. To see whether the dependence found in the data is reasonable, we compare the same MC pseudo-experiments analyzed with top masses of 180 GeV/c^2 and 170 GeV/c^2. The differences in F_0 obtained for each set of calculations yield the distributions shown in Fig. 8.5, which indicate RMS values of 0.10 and 0.13, consistent with half of the difference (0.1) found in data.

Because this systematic uncertainty will be among the largest on F_0, we calculate it via a Bayesian integration of the probability over the top mass (from 165 to 190 GeV/c^2, in steps of 2.5 GeV/c^2), using no other prior knowledge of the top-quark mass. Figure 8.6 shows the 2-dimensional probability density as a function of F_0 and M_t for the data, before applying the response correction from Fig. 6.27. To check that this correction can be applied before projecting M_t, we show in Fig. 8.7 the response to F_0 before and after integrating Monte Carlo samples over M_t. We therefore apply the same linearity correction from Fig. 6.27 before integrating over M_t. Figure 8.8 shows the probability from Fig. 8.6 after integrating over M_t, where we recalculate the 68.27% interval, which now reflects the statistical error convoluted with the uncertainty on the top mass, and we obtain,

$$F_0 = 0.557 \pm 0.306 \quad . \tag{8.1}$$

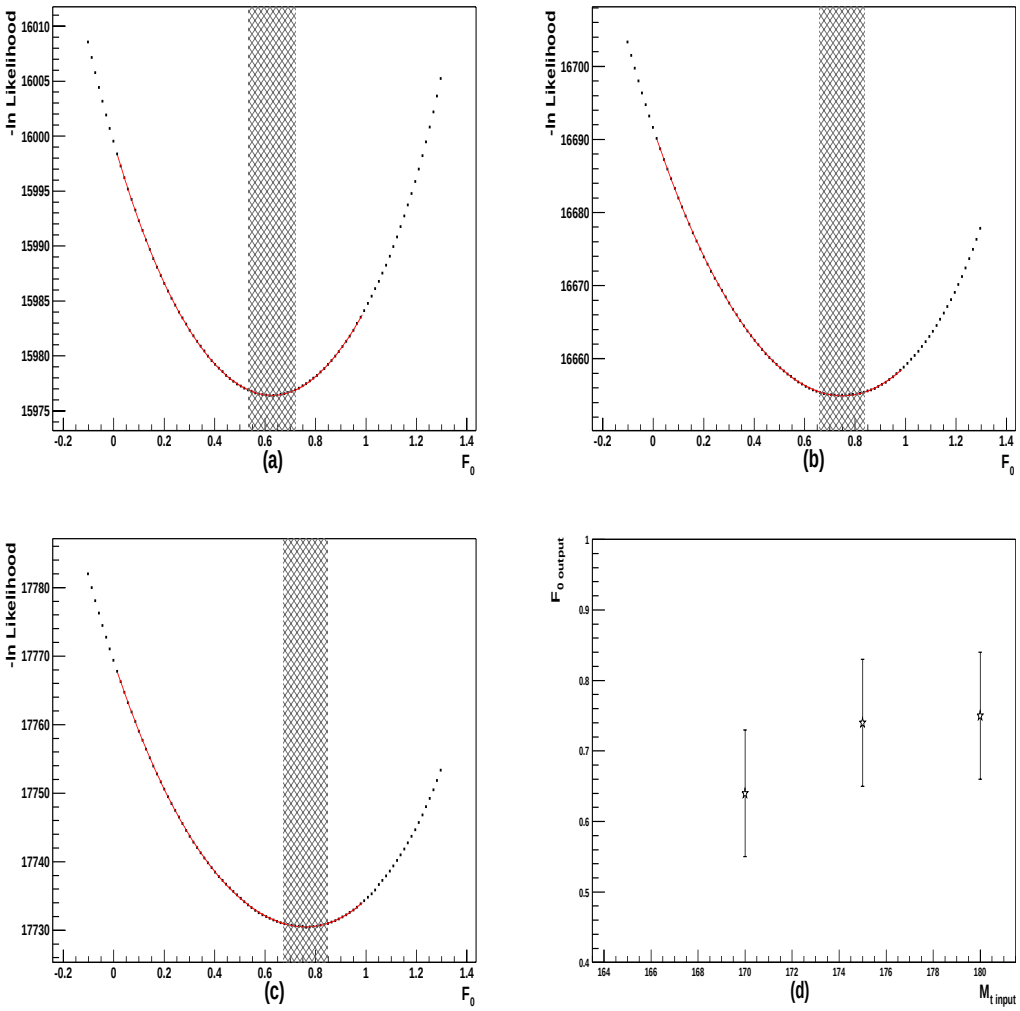

Figure 8.1: –ln(Likelihood) as a function of F_0 for 600 $t\bar{t}$ events and 900 W+jets events before selecting on P_{VECBOS}. Different HERWIG SM samples, with different top masses are analyzed assuming M_t=175 GeV/c^2. The number of events in each combined sample is smaller, because the selection on P_{VECBOS} returns on average 70% of the $t\bar{t}$ events and 30% W+jets events. (a) Sample with M_t=170 GeV/c^2, with extracted value F_0=0.63±0.09. (b) Sample with M_t=175 GeV/c^2, and extracted value F_0=0.74±0.09. (c) Sample with M_t=180 GeV/c^2, and extracted value F_0=0.76±0.09. (d) Most probable values and errors from a, b and c.

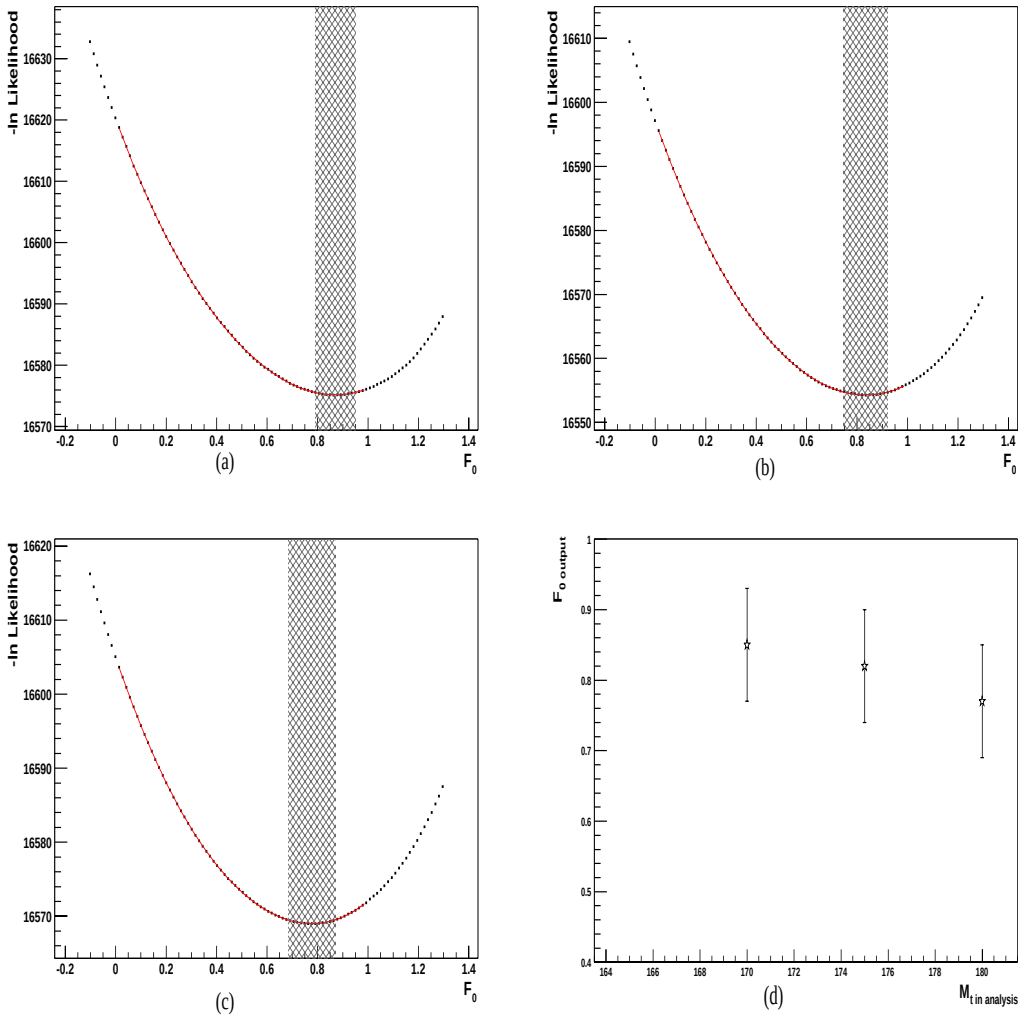

Figure 8.2: –ln(Likelihood) as a function of F_0 for 600 $t\bar{t}$ events and 900 W+jets events before selecting on P_{VECBOS}. The number of events in each combined sample is smaller, because the selection on P_{VECBOS} returns on average 70% of the $t\bar{t}$ events and 30% W+jets events. One HERWIG SM sample (M_t=175 GeV/c^2, F_0=0.703) is used, assuming different top masses in the probability calculation and acceptance correction. (a) Analyzed with M_t=170 GeV/c^2, with extracted value F_0=0.86±0.08. (b) Analyzed with M_t=175 GeV/c^2, and extracted value F_0=0.82±0.08. (c) Analyzed with M_t=180 GeV/c^2, and extracted value F_0=0.77±0.08. (d) Most probable values and their uncertainties.

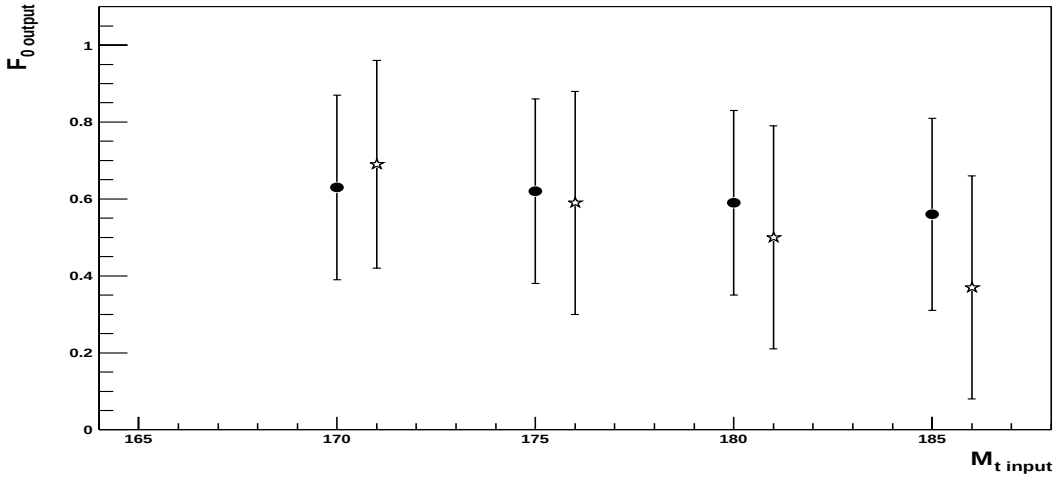

Figure 8.3: Extracted value of F_0, analyzing the experiments with different top-quark masses. Dots correspond to the mean value of the ensemble-distribution of most probable values of F_0 using 100 experiments of 12 $t\bar{t}$ and 10 W+jets Monte Carlo events. The Run I data sample points are indicated by stars.

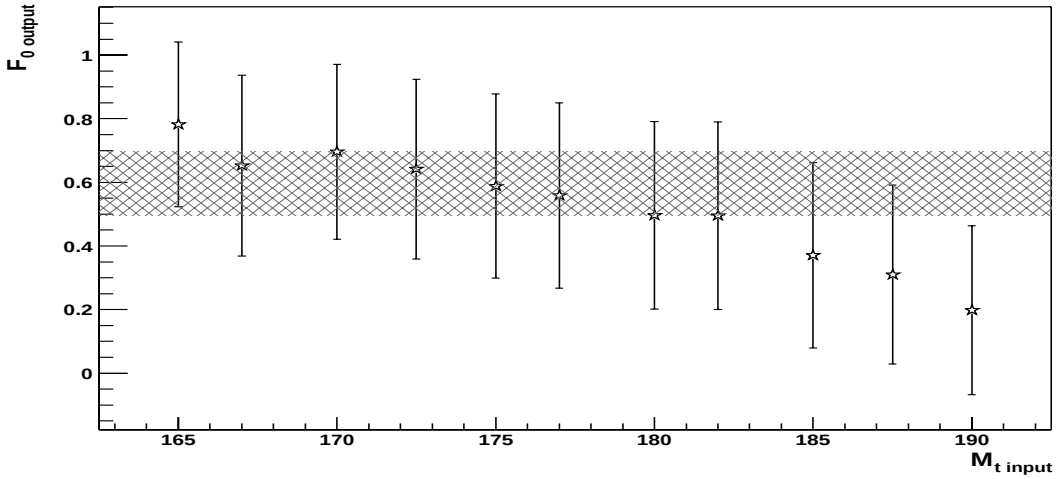

Figure 8.4: Run I data analyzed using different top masses. Shaded region indicates the measured mass of the top-quark and its uncertainty of 174.6±5.4 GeV/c^2.

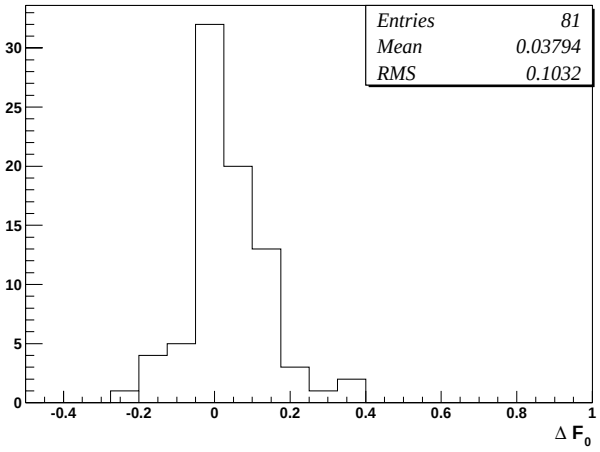

Figure 8.5: Difference between most probable value of F_0 in MC events for the same samples analyzed with different top-quark masses using M_t=180 GeV/c^2 and M_t=170 GeV/c^2. Each sample has 12 $t\bar{t}$ and 10 W+jets, events and they were generated for M_t=175 GeV/c^2.

Although it is not always possible, it is important that the value of any physical parameter we are trying to extract is constrained to have a physical value. This Bayesian approach offers the best way to estimate systematic uncertainties. Unfortunately, this is the only error that we are able to treat in this way in this analysis.

8.2 Systematic Error due to Uncertainty on Jet Energy Scale

We proceed in a manner that is similar to that used in previous DØ analyses. In order to determine the impact on F_0 of the $\pm$(2.5%+0.5GeV) uncertainty on jet energy scale (JES), all jet energies in the events are multiplied by the appropiate correction factor, and then F_0 is re-extracted. The corresponding results are shown in Fig. 8.9. The difference between the down-corrected and up-corrected values translates in an uncertainty of 0.014 in F_0.

Although there is an anti-correlation between the uncertainty on the top mass and the uncertainty on JES, because the JES has such a small effect, we decided to ignore the correlation, which somewhat over-estimates the systematic uncertainty.

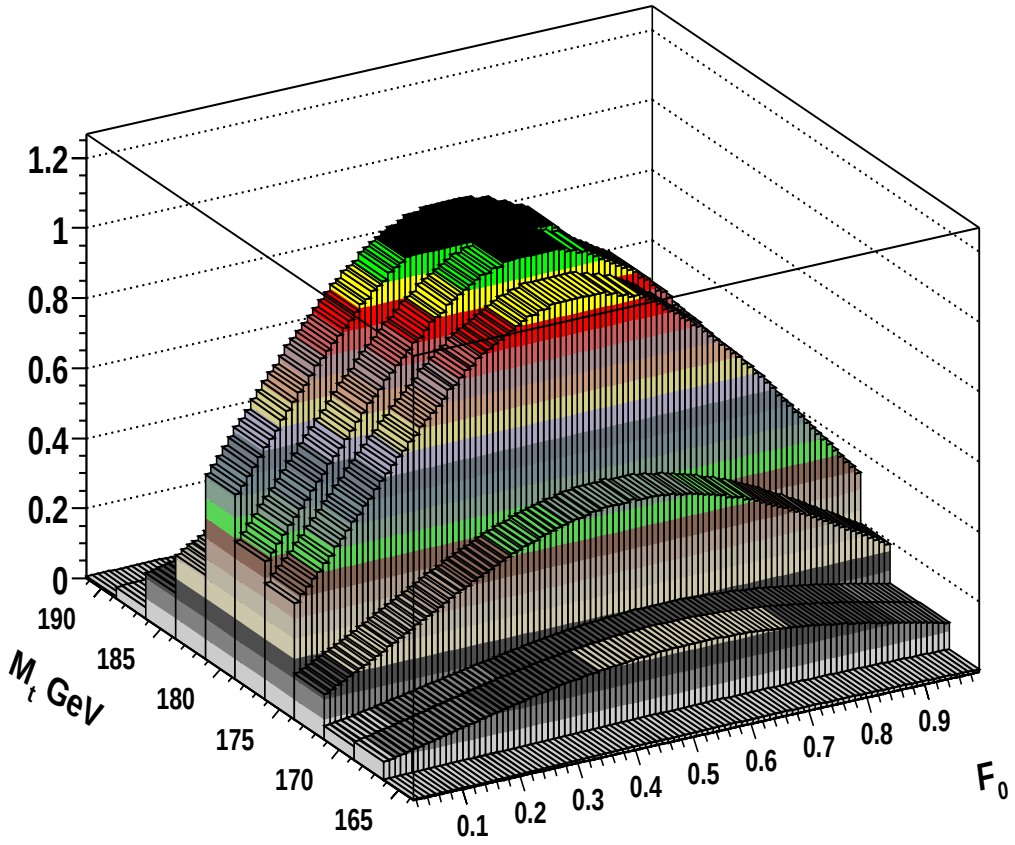

Figure 8.6: Probability density as a function of M_t and F_0 for Run I data before applying the response correction to F_0.

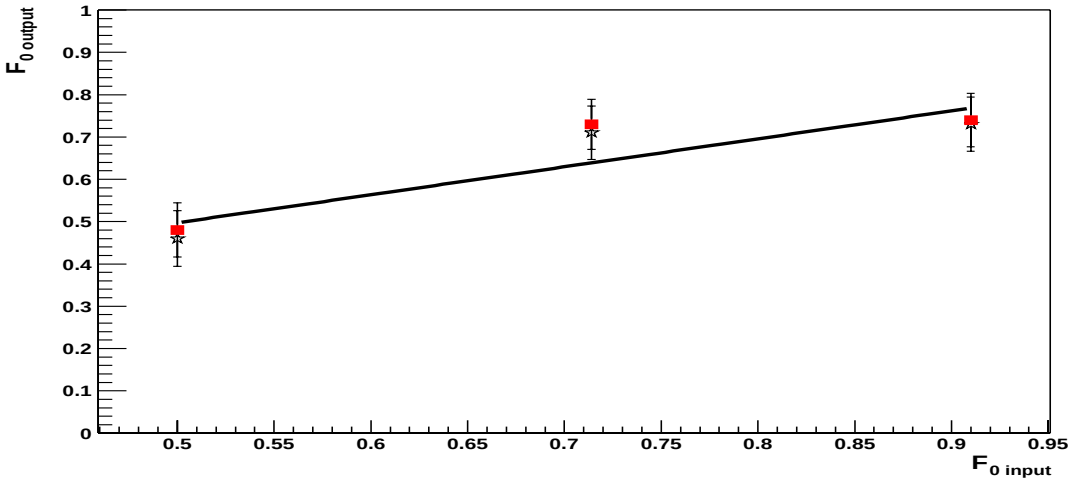

Figure 8.7: Response as a function of input F_0 after imposing $P_{VECBOS} < 10^{-11}$ in the analysis of 600 $t\bar{t}$ (F_0=0.70) events and 900 W+jets events. Square points correspond to the values extracted of F_0 after integrating over the top mass from 165 to 190 GeV/c^2. Star points have not been integrated over mass. We observe no difference between these two sets of results.

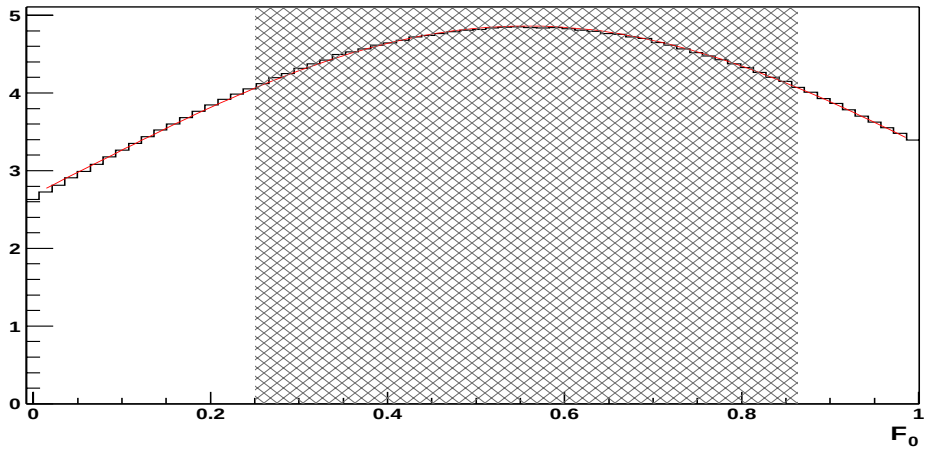

Figure 8.8: F_0 from the Run I data sample, after integrating over M_t from 165 to 190 GeV/c^2 in steps of 2.5 GeV/c^2. The 68.27% interval is 0.612 wide, half of which corresponds to the error on F_0 that convolutes the statistical and systematic uncertainties on the mass of the top quark.

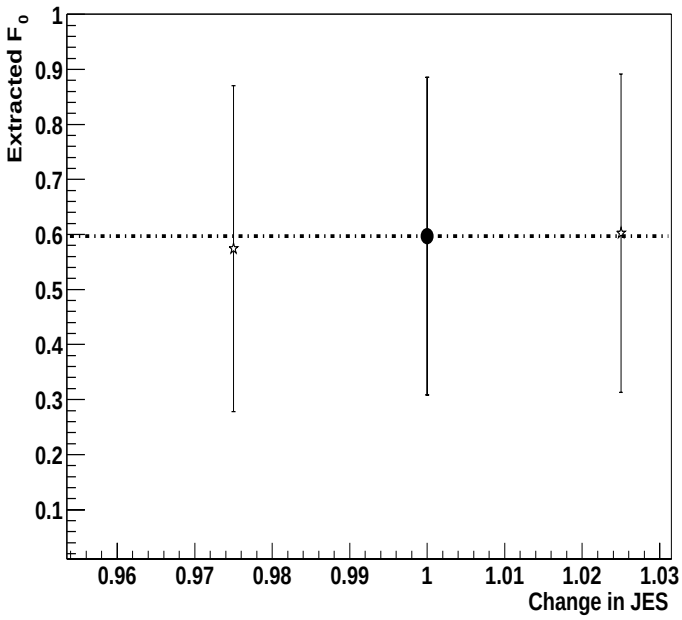

Figure 8.9: Run I data analyzed by changing the jet energies in the events according to the uncertainty on the jet energy scale. The points correspond to changing the jet energies by –(2.5%+0.5GeV), 0, and +(5.0%+0.5GeV). The systematic error assigned from this effect is defined by half the difference of the two extreme points, and equals 0.014.

8.3 Systematic Error due to Acceptance and Linearity of Response

Due to the limited amount of Monte Carlo events, the acceptance correction could not be calculated very precisely. This inaccuracy affects the linearity response for F_0. The corrections for acceptance and for response are correlated, and we must therefore account for these two uncertainties simultaneously. We proceed in the following way. We generate 10 different acceptance corrections by fluctuating the acceptance parameters independently according to the errors obtained in Section 6.5. We apply these acceptance corrections to 10 pseudo-experiments each containing on average 12 $t\bar{t}$ and 10 W+jets events, and find F_0 for each acceptance correction, in the same way as was done for the low statistics studies in Section 6.6.2. The number of events is fluctuated using a binomial distribution. Figure 8.10 shows the 10 linear corrections obtained from these ensembles that correspond to 10 acceptance corrections. As an aside, Figure 8.11 shows the result

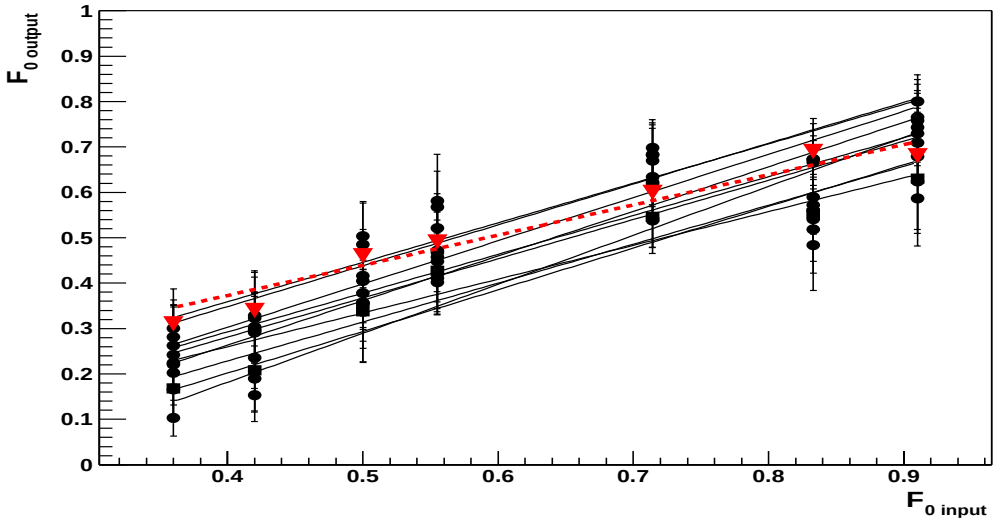

Figure 8.10: Response obtained using 10 acceptance corrections on the 10 MC experiments of 12 $t\bar{t}$ and 10 W+jets events in average. The number of events is fluctuated using a binomial distribution.

of applying 100 different acceptance corrections to the data of Run I by fluctuating the acceptance parameters within their uncertainties. To obtain a systematic uncertainty, we apply the set of 10 acceptance and response corrections to the data. We see in Fig. 8.12 that the net effect is very small, because these two corrections have opposite effect. Also, due to the fact that the statistical error is very large, we see no effect on the data. We assign a systematic error for the acceptance and response correction of 0.055, as extracted from the RMS of the distribution of most probable values.

8.4 Systematic Error due to $t\bar{t}$ Model

Since different Monte Carlo generators have different hadronization and radiation properties, we assign an error due to our poor understanding of these mechanisms. In particular, we extract F_0 for events generated with HERWIG and compare it with events that were generated with PYTHIA. We generated another sample of PYTHIA $t\bar{t}$ events with F_0=0.703, and passed it through DØ simulation and reconstruction. To estimate the systematic uncertainty arising from difference in generators, we do 100 experiments of 12 $t\bar{t}$ and 10 W+jets events obtained from the PYTHIA and HERWIG samples. Each

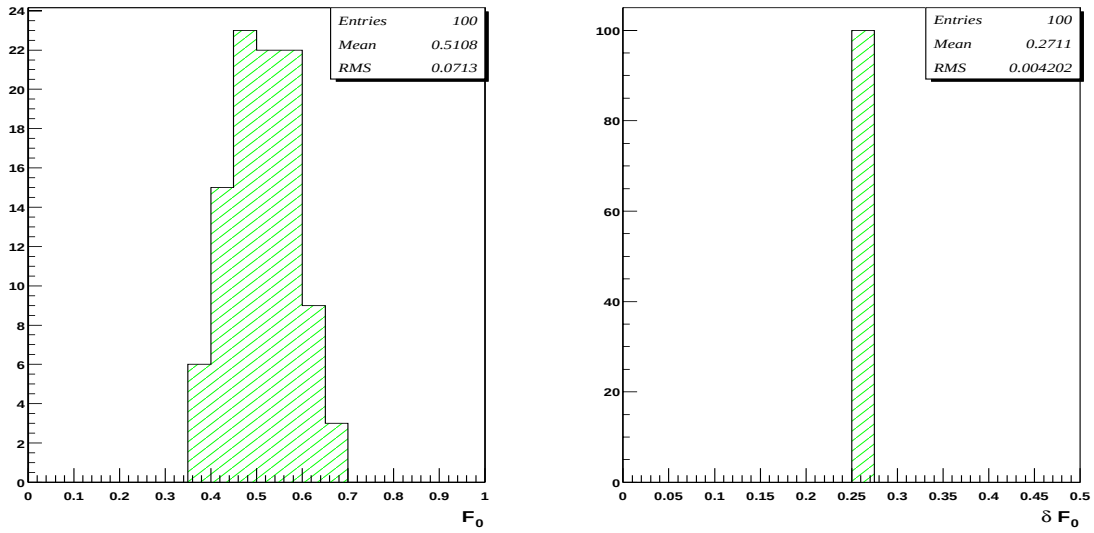

Figure 8.11: Run I data using a set of 100 acceptance corrections that were derived by fluctuating the acceptance parameters within their uncertainties (see Section 6.5.)

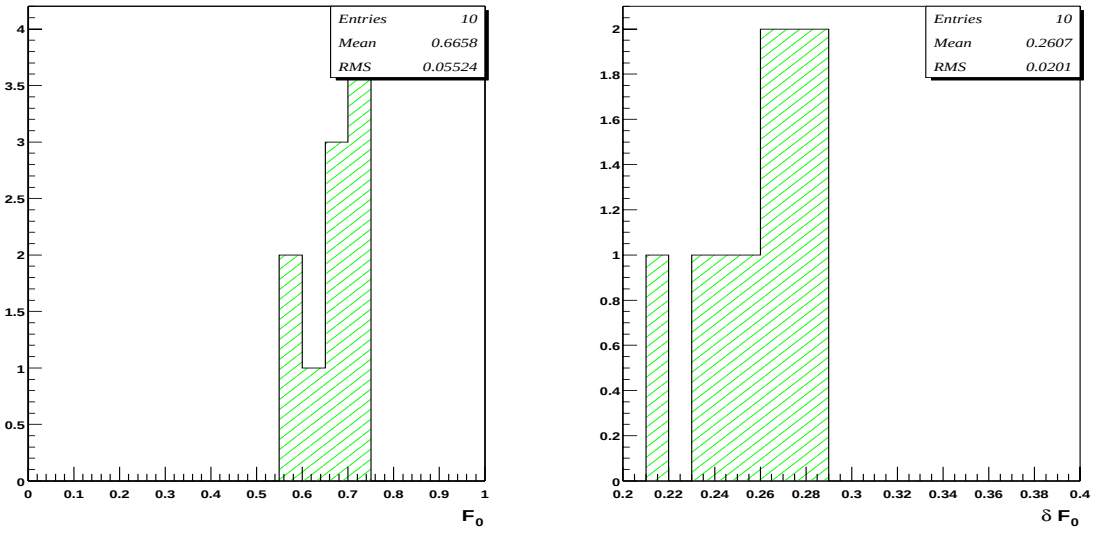

Figure 8.12: Run I data using a set of 10 acceptance-response corrections. We assign a systematic error of 0.055 to this effect.

sub-sample is corrected using the response in Fig. 6.27. We see from Fig. 8.13 and 8.14 that the difference on the mean of the most probable values of F_0 is 0.022, which is not significant, but we assign this value as a systematic uncertainty for modeling $t\bar{t}$ events.

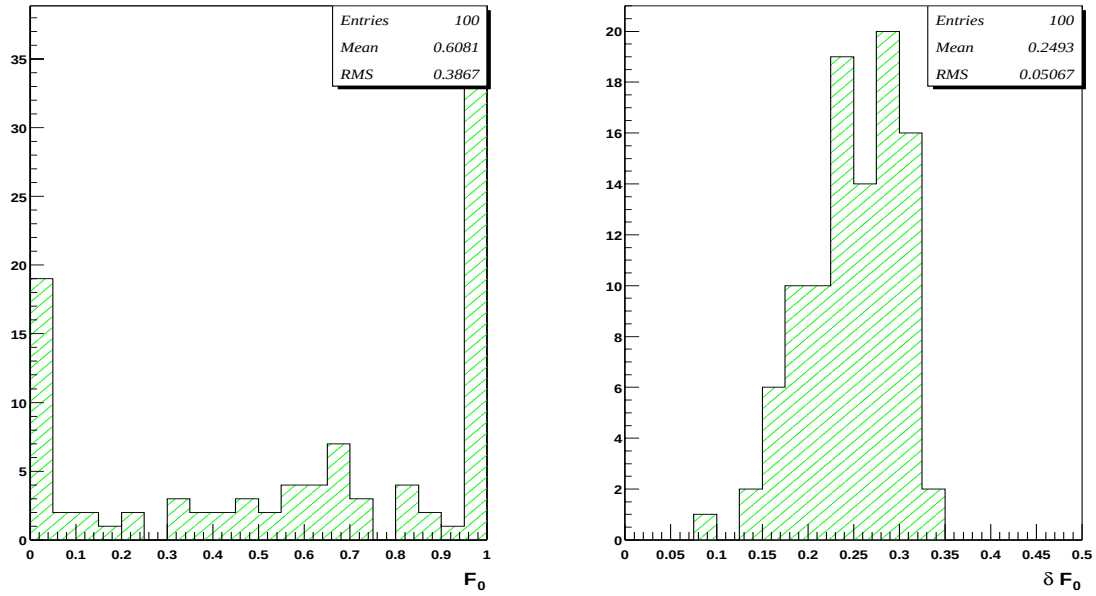

Figure 8.13: Ensembles of 12 $t\bar{t}$ HERWIG (F_0=0.703) and 10 W+jets events, after applying the selection on P_{VECBOS}. The mean value of the distribution of most probable values is 0.61±0.25.

8.5 Systematic Error due to PDFs

For the calculation of the probability, we choose CTEQ4M NLO QCD as our PDF for the light quarks inside the proton. Figure 8.15 shows the fractional momentum of the u quark. To estimate the systematic uncertainty in F_0 from this specific choice, we looked at other PDFs (see Fig. 8.15), and selected the one with the largest difference from CTEQ4M to estimate the uncertainty. Figure 8.16 shows the plots –ln(Likelihood) as a function of F_0 with the probabilities calculated using CTEQ4M (Fig. 8.16a) and CTEQ5L (Fig. 8.16b). The difference in F_0 relative to CTEQ4M is 0.008, and we quote this as the systematic error due to PDFs. (In fact, this may be an overestimate because CTEQ4M refers to NLO and CTEQ5L to LO QCD calculations, the latter being more

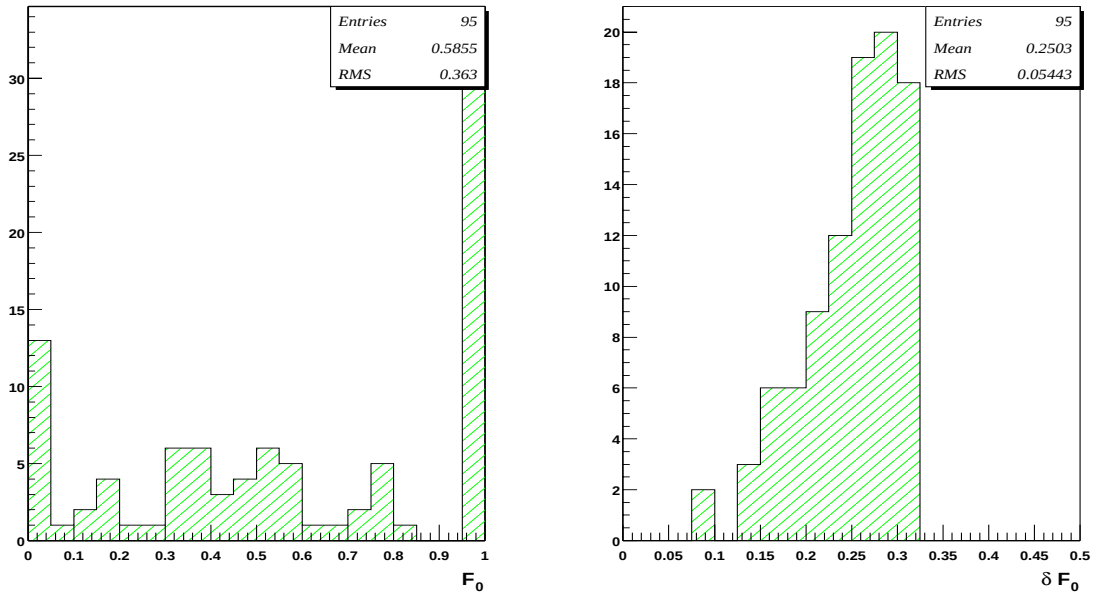

Figure 8.14: Ensemble of 12 $t\bar{t}$ PYTHIA (F_0=0.703) and 10 W+jets events, after applying selection on P_{VECBOS}. The mean value of the distribution of most probable values is 0.59±0.25.

appropiate for our leading-order matrix element.)

8.6 Systematic Error due to Multiple Interactions

At the luminosities of Run I, a single beam crossing can produce more than one $p\overline{p}$ interaction. The softer interactions accompanying the hard collision of interest do not have jets or a high-p_T object. But these interactions can increase the energy collected in the calorimeter cells, and can therefore affect jet calibration. The jet energy corrections take this into account. But since the Monte Carlo simulations we used in this analysis do not contain multiple interactions, we estimate the impact of this effect by generating $t\bar{t}$ PYTHIA events with multiple interactions switched on. These "dirtier" events were passed through DØ simulation and reconstruction programs, and analyzed as before. In Figures 8.17 and 8.18, we compare 95 samples of 12 $t\bar{t}$ events and W+jets events with multiple interactions to the previous cleaner PYTHIA events (see Section 8.4). There is no noticeable difference between the mean of the distributions, and we assign a systematic error due to this effect of 0.006, which corresponds to the difference in the

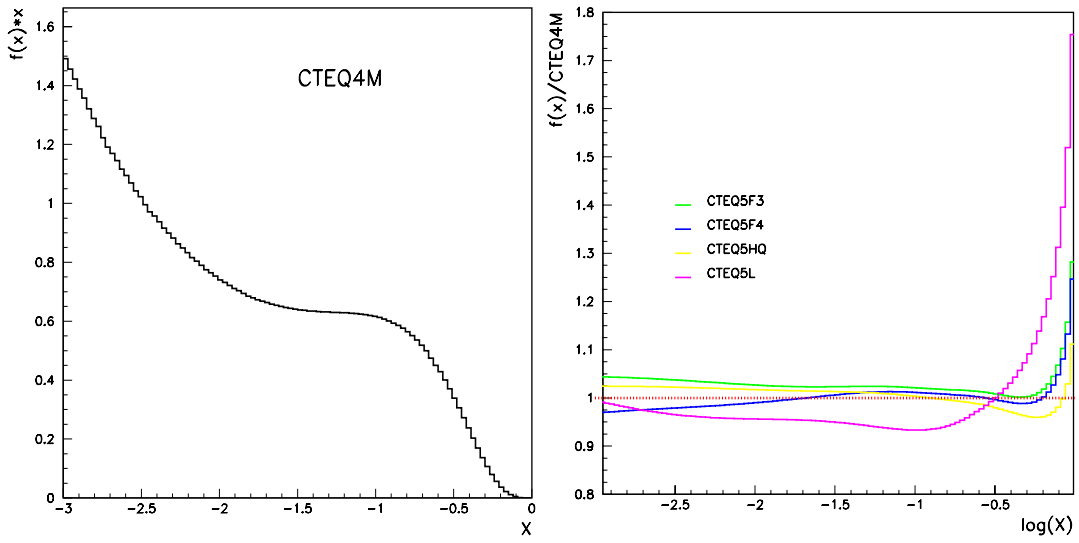

Figure 8.15: Left: CTEQ4M (NLO QCD) for the u quark inside the proton as a function of the fractional momentum of the quark. Right: Comparison between different PDFs, we select CTEQ5L (LO QCD) for estimating our systematic uncertainty.

mean values of F_0.

8.7 Systematic Error due to Multijet Background

We do not measure the ratio of W+jets to multijet (QCD) background, we assume that it is the same as quoted in the previous analysis of Ref. [32], that is, multijet/W+jets = 22±5%. The multijet background is reduced to 70% after the selection criteria on the reconstructed W boson based on the lepton and the missing transverse energy (see Section 6.3). And after the selection on P_{VECBOS}, only 22% multijet events remain. Therefore, we consider that the final background consists of 90% W+jets and 10% multijet (QCD).

There is no precise model to calculate the probability distributions for these type of events, and no reliable MC simulation for such rare multijet events. There is also no term we can use in Eq. 3.25 for a multijet contribution, and for this reason their impact is treated as a systematic uncertainty. In order to gauge the effect of such events on the measurement of F_0, we perform 100 experiments using 12 $t\bar{t}$ and 10 W+jets events, and another 100 experiments using 12 $t\bar{t}$ events and 9 W+jets events and one multijet event from data (all on average). The multijet events were obtained from the small

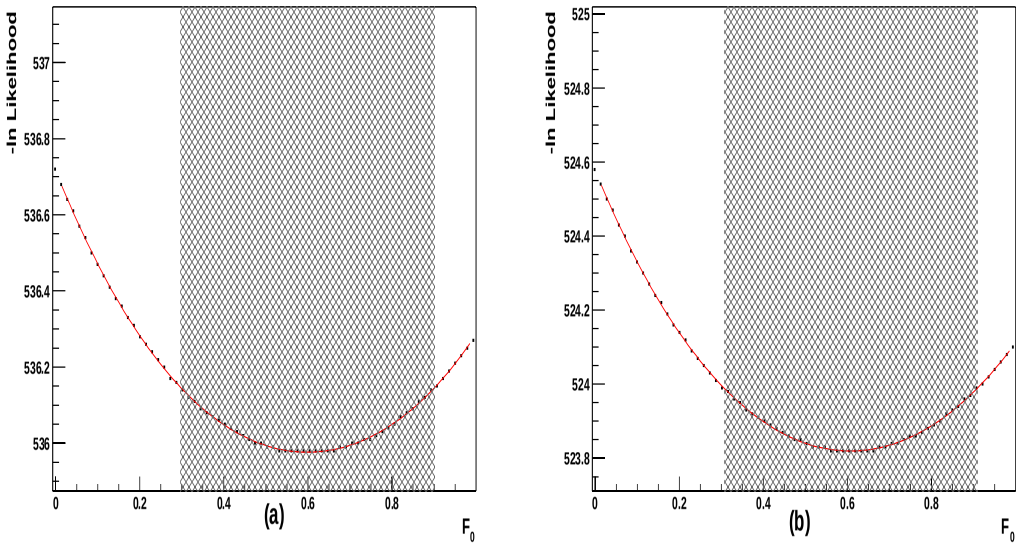

Figure 8.16: –ln(Likelihood) as a function of F_0 using Run I data. (a) The PDF used in this calculation is CTEQ4M. The value extracted is F_0=0.599±0.301. (b) The PDF used in this calculation is CTEQ5L. The extracted value is F_0=0.607±0.301.

original sample of 250 events. The result for F_0 from these two ensemble studies are shown in Figs. 8.19 and 8.20. The mean F_0 extracted not using multijet background is 0.598±0.039 and the F_0 extracted using this background is 0.622±0.038. These results are consistent, but we assign a possible systematic uncertainty on F_0 of 0.024 for the possible difference due to multijet background.

8.8 Systematic Error due to Spin Correlations

Because we are ignoring the known correlation between the top and antitop spins at production, and since we make use of both decays in the measurement of F_0, we will estimate the impact of this simplification. Although the theoretical limits on this effect are not well known, according to Ref [23], the effect of spin correlation on F_0 is likely small. HERWIG or PYTHIA do not include a term for $t\bar{t}$ spin correlations, we therefore use a generator based on Madgraph [76, 77] to examine this part of the matrix element. The angular distributions for the new events, with and without the correlation, are shown in Fig. 8.21. Fitting these to Eq. 1.13 (setting F_+=0) yields F_0=0.703 for events with

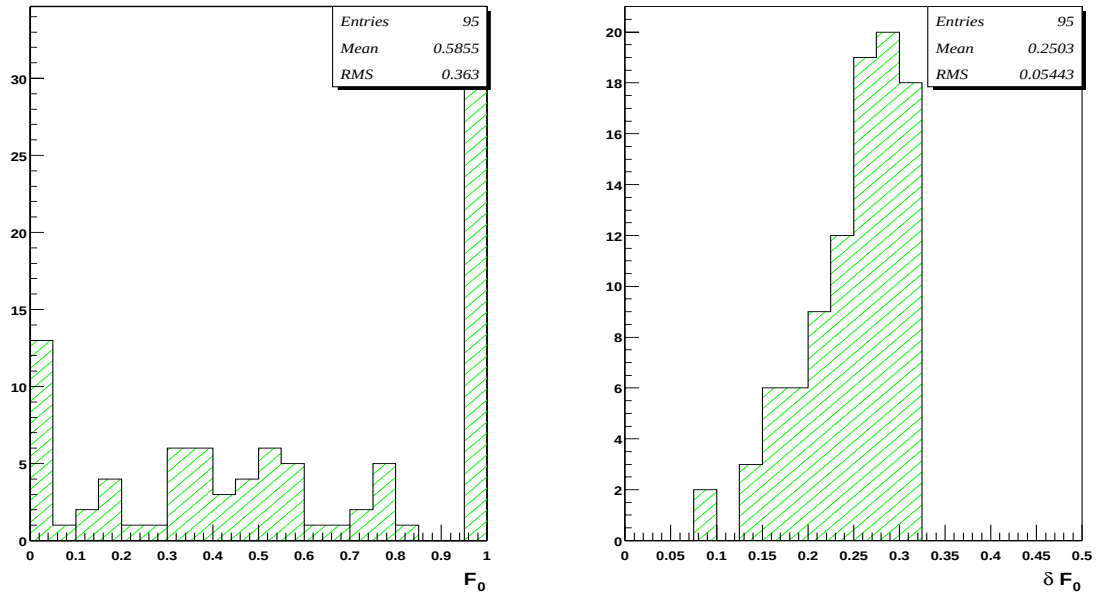

Figure 8.17: Ensembles of 95 pseudo-experiments of 12 $t\bar{t}$ PYTHIA events without multiple interactions and 10 W+jets VECBOS events (after selecting on P_{VECBOS} and correcting each experiment for response).

spin correlation and F_0=0.706 for events without correlations. We proceed as in Section 5, smearing the events using the transfer functions from Section 4, and applying the same selection criteria. We then calculate the signal probabilities for these parton-level events, using CTEQ5L because these PDFs were used to generate these events. The most probable value extracted using a sample of 3000 $t\bar{t}$ events without spin correlations is 0.718±0.017, and with spin correlations on is 0.721±0.017. Figures 8.21 and 8.22 show these likelihoods. To assess any systematic effect, we use 100 samples of 12 $t\bar{t}$ events with and without spin correlations. Figure 8.23 and 8.24 show the results for F_0. From the difference between the mean of these distributions, we assign a systematic uncertainty of 0.008 because of having ignored spin correlations.

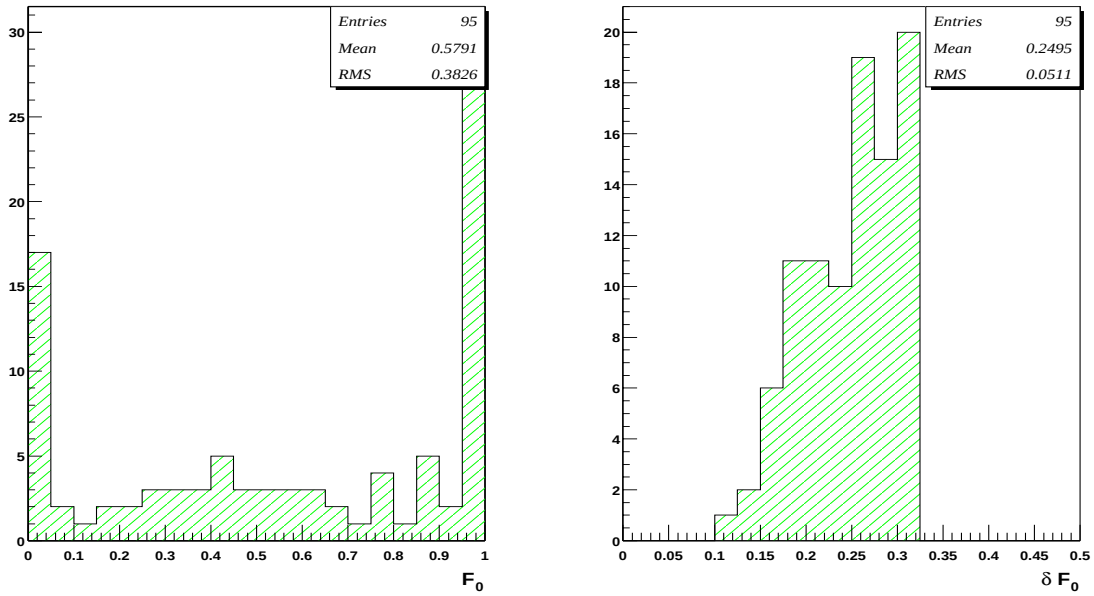

Figure 8.18: Ensemble of 95 pseudo-experiments of 12 $t\bar{t}$ PYTHIA events with multiple interactions and 10 W+jets VECBOS events (after selecting on P_{VECBOS} and correcting each experiment for response).

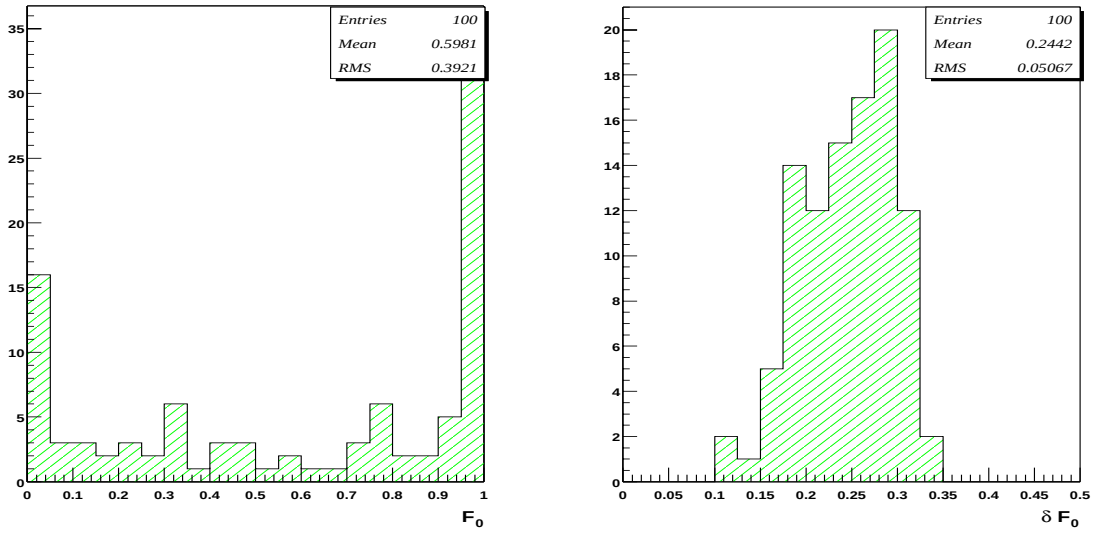

Figure 8.19: Ensemble of 100 pseudo-experiments of 12 $t\bar{t}$ HERWIG (F_0=0.703) and 10 W+jets events, after applying the selection on P_{VECBOS}, with correction for response from Fig. 6.27.

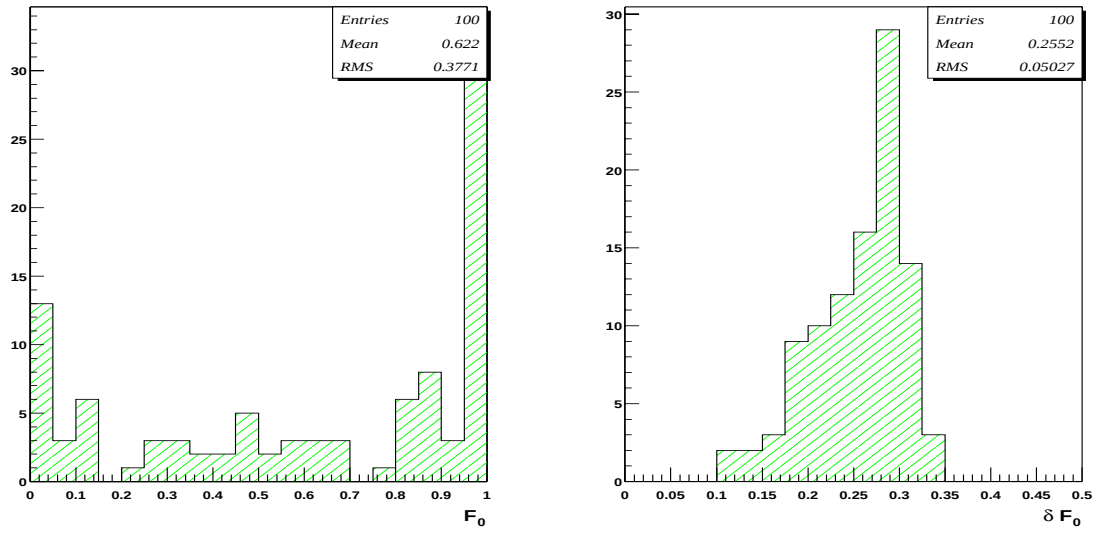

Figure 8.20: Ensemble of 100 pseudo-experiments of 12 $t\bar{t}$ HERWIG (F_0=0.703), 9 W+jets, and one multijet event, after applying the selection on P_{VECBOS}, with correction for response from Fig. 6.27.

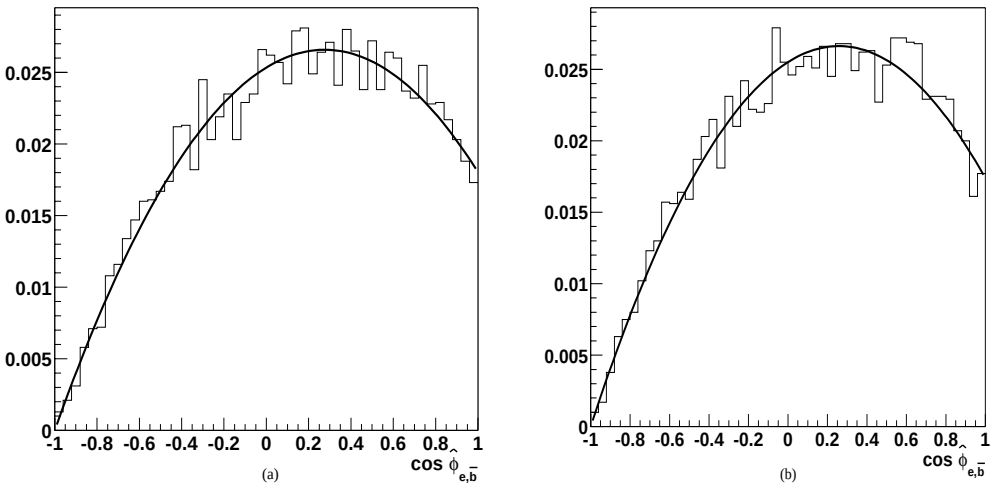

Figure 8.21: Arbitrarily normalized angular distributions $w_f(\cos\hat{\phi}_l)$ using parton-level information. (a) MC events do not contain $t\bar{t}$ correlations. (b) MC events contain $t\bar{t}$ correlations. The curves correspond to fits to the SM.

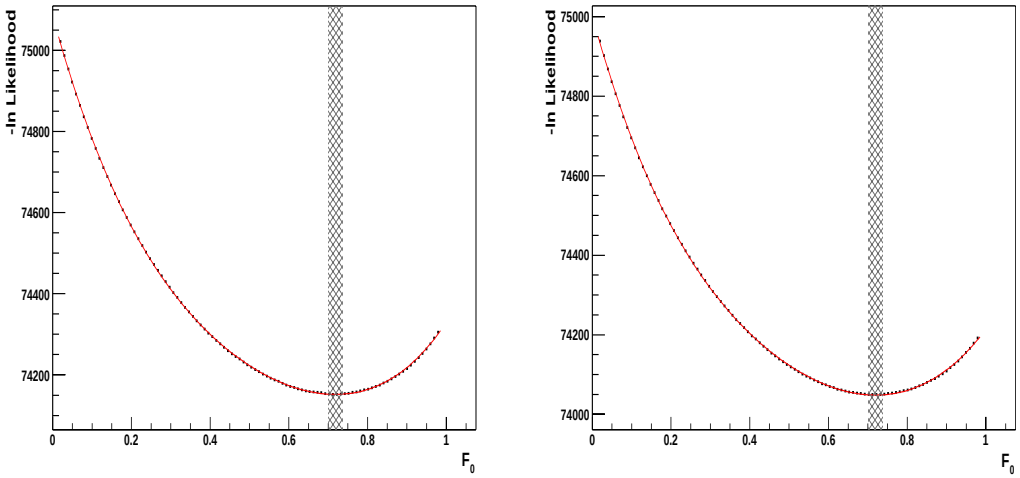

Figure 8.22: –ln(Likelihood) using $t\bar{t}$ events with spin correlations (right) and without (left). The extracted F_0 using 3000 smeared $t\bar{t}$ events with spin correlations is 0.721±0.0171, and without spin correlations is 0.718±0.0172.

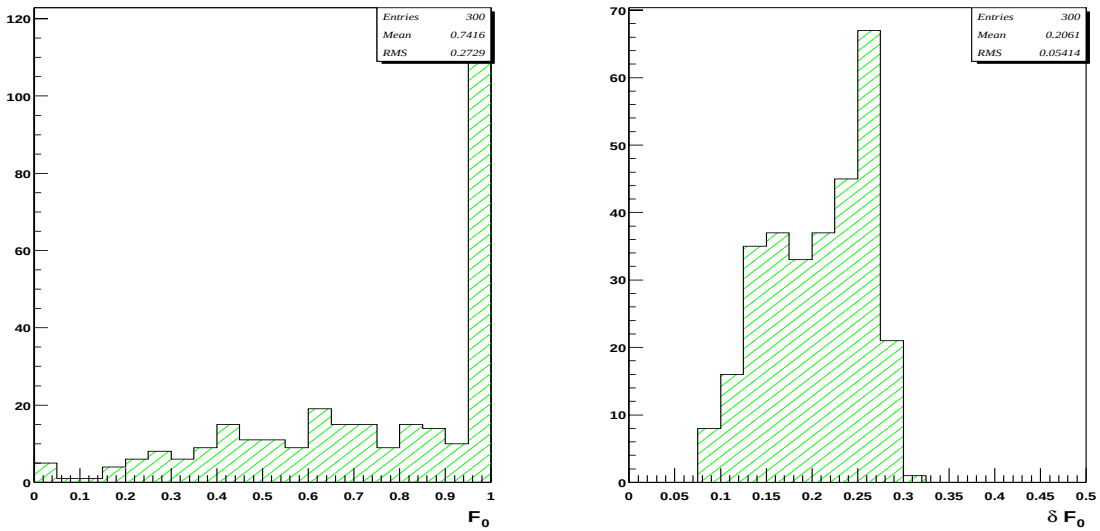

Figure 8.23: Ensemble of 12 $t\bar{t}$ events with F_0=0.703, without spin correlations. The extracted value of F_0 is 0.742±0.206.

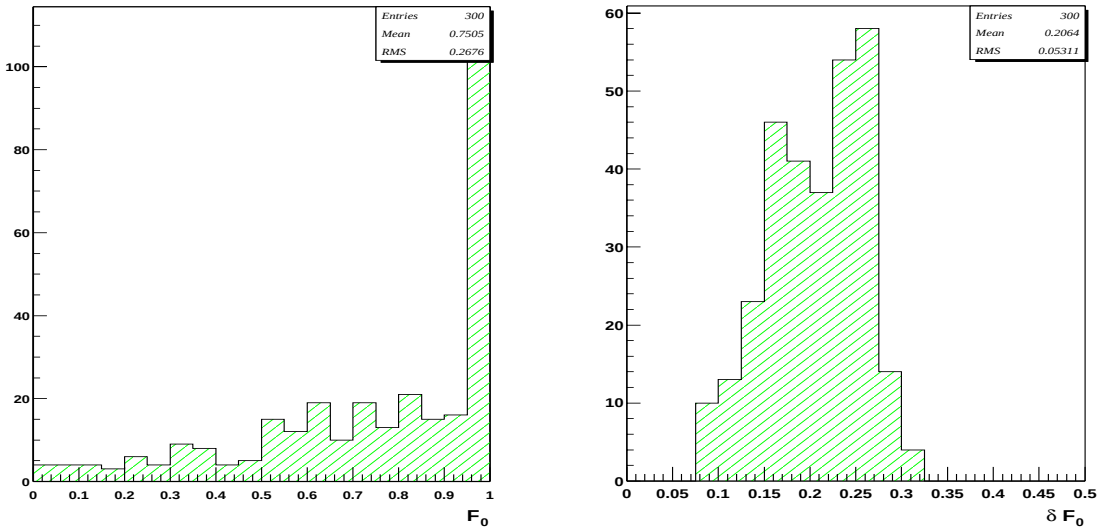

Figure 8.24: Ensemble of 12 $t\bar{t}$ events with F_0=0.703 and with spin correlations. The extracted value of F_0 is 0.750±0.206.

Chapter 9

Conclusions

Measurements of the mass of the top quark and its production cross section have indicated that these general parameters agree with expectactions of the SM. More detailed and interesting questions remain to be answered that may be especially sensitive to new physics. In particular, the top quark couples to a W boson and a b quark $\approx 100\%$ with a V–A coupling. The helicity of the W boson offers a way to learn about this coupling.

In this analysis, we used a matrix-element approach to measure the fraction of longitudinal helicity (F_0) in top decay. This method offers the possibility of increasing statistical accuracy by using both leptonic and hadronic W decays. And the extraction of F_0 is relatively unbiased, even for low-statistics data samples. The method makes simultaneous use of all information in an event, and the characteristics of each individual event are included in the calculation of event probabilities, thereby assumming that well measured events contribute more effectively than poorly measured events. It uses all possible jet combinations in the event, but each combination enters into the probability with a different weight. Apart from the unclustered energy, which refers to the energy deposited in the calorimeter from all sources except leptons and jets, the method utilizes all measured quantities to specify every event, which provides excellent discrimination between signal and background.

Applying this method to the Run I data we obtained

$$\boxed{F_0 = 0.56 \pm 0.31(\text{stat}) \pm 0.07(\text{syst})} \tag{9.1}$$

where the uncertainty from M_t is included in the statistical error. This result is consistent with the Standard Model prediction of F_0=0.70 for a top mass of 175 GeV/c^2. Our sample consisted on 22 candidates in lepton+jets final states, which contained 12±3 $t\bar{t}$

signal events.

A summary of the uncertainties is shown in Table 9.1. For the higher statistics anticipated in Run II of the TeVatron, it will be important to improve the calculation of the probabilities, and the method we have developed offers one of the best ways to measure the helicity properties of the W in the $t\bar{t}$ events.

Table 9.1: Uncertainties on the measurement of F_0.

Statistics + top mass uncertainty	0.306
Acceptance and linearity response	0.055
Jet energy scale	0.014
$t\bar{t}$ spin correlations	0.008
Parton distribution functions	0.008
$t\bar{t}$ model	0.020
Multiple interactions	0.006
Multijet background	0.024
Total	0.313

Appendix A

Definition of Likelihood

Let us assume that we have an event specified by a set of coordinates x_1 in a volume dx_1, another with coordinates x_2 in volume dx_2, a third one with coordinates x_3 in volume dx_3, etc, as shown in the following sketch [63]:

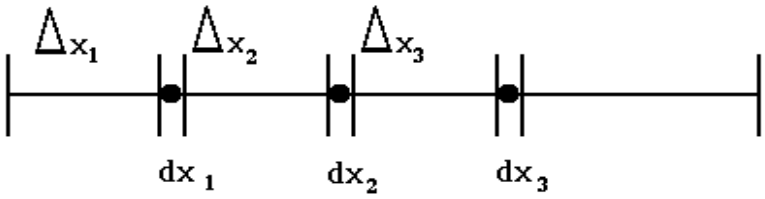

The coordinates x_i represent any relevant set of variables that are needed to specify an event in a unique way. The probability (up to a normalization constant) for obtaining any configuration of N observed events within the infinitesimal phase space volume elements dx_i, containing empty finite elements Δx_i, with $i = 1, 2, ..., N$, can be written as

$$\begin{aligned} P(x_1...x_N)dx_1...dx_N = & Prob\begin{pmatrix} 0 & \text{events} \\ \text{in} & \Delta x_1 \end{pmatrix} \times Prob\begin{pmatrix} 1 & \text{event} \\ \text{in} & dx_1 \end{pmatrix} \\ & \times Prob\begin{pmatrix} 0 & \text{events} \\ \text{in} & \Delta x_2 \end{pmatrix} \times Prob\begin{pmatrix} 1 & \text{event} \\ \text{in} & dx_3 \end{pmatrix} \quad .... \end{aligned} \tag{A.1}$$

Using Poisson statistics, the probabilities for having zero and one event, when the expected average is $\overline{n}$, are

$$P_{0,\overline{n}} = \mathrm{e}^{-\overline{n}} \quad \text{and} \quad P_{1,\overline{n}} = \overline{n}\mathrm{e}^{-\overline{n}} \quad . \tag{A.2}$$

If N is the number of observed events, and $\overline{P}(x)$ is the probability density for all coordinates (which we will not normalize to unity so as to keep to the most general formulation), then the average number of events expected in any volume Δx is

$$\overline{n} = N \int_{\Delta x} \overline{P}(x) dx \quad , \tag{A.3}$$

and the probability of having 0 events in the region Δx is

$$P_0(\Delta x) = \mathrm{e}^{-N \int_{\Delta x} \overline{P}(x) dx} \quad . \tag{A.4}$$

Similarly, the probability of having 1 event in the differential region dx around x is

$$P_1(x)dx = N\overline{P}(x)dx \quad \mathrm{e}^{-N\overline{P}(x)dx} \quad . \tag{A.5}$$

The total probability in Eq. A.1 is then given by the product off all such terms:

$$P(x_1 ... x_N)dx_1 ... dx_N = \mathrm{e}^{-N \int_V \overline{P}(x) dx} \prod_{i=1}^{N} N\overline{P}(x_i)dx_i \quad , \tag{A.6}$$

where V is the volume of our entire space.

Although a one dimensional sketch was used to motivate Eq. A.6, the result is clearly general. If $\overrightarrow{x}_i$ is a point in a k-dimensional volume (V), then the probability for having no events in the volume defined by V, but corrected for the infinitesimal elements ("holes") around the N points $\overrightarrow{x}_i$, is

$$\mathrm{e}^{-N \int_{V-holes} \overline{P}(\overrightarrow{x}_i) d^k \overrightarrow{x}_i} \quad , \tag{A.7}$$

and the probability for having one event in each of the N holes is

$$\prod_{i=1}^{N} N\overline{P}(\overrightarrow{x}_i) d^k \overrightarrow{x}_i \quad \mathrm{e}^{-N\overline{P}(\overrightarrow{x}_i) d^k \overrightarrow{x}_i} \quad . \tag{A.8}$$

The multiplication of Eqs. A.7 and A.8, yields Eq. A.6 for the case of many dimensions. To simplify the notation, the vectorial arrows will be dropped, but the x_i will always refer to a point in a multidimensional space.

$P(x_1 ... x_N)$ is the probability density for observing the N events characterized by $x_1, x_2, ..., x_N$, and it should always be at (or very near) its maximum value. If this were not the case, then a very different set of events would have been observed. In most

applications, the single-event probability density $\overline{P}(x)$ can be specified only as a function of some unknown set of parameters α. That set is then estimated by maximizing the likelihood function $P(x_1 ... x_N)$. Terms that do not depend on α (e.g. N^N) are usually not included in $P(x_1, ..., x_N)$, because they do not affect the values of the parameters α that maximize the likelihood. It can be shown that the best (unbiased) estimate of a given set of parameters is obtained through the maximization of the likelihood [64]:

$$L(\alpha) = \mathrm{e}^{-N \int \overline{P}(x;\alpha) dx} \prod_{i=1}^{N} \overline{P}(x_i;\alpha) \quad . \tag{A.9}$$

Appendix B

Examples

This Appendix gives examples of applications of our method of analysis, and provides some of the details for the calculations employed in this work.

B.1 Lifetime in Particle Decay

Consider the probability density $P_p(t)$ for decay of a particle as a function of time:

$$P_p(t) = C\mathrm{e}^{-\alpha t} \tag{B.1}$$

where α is the decay rate, and after normalizing $P_p(t)$ to unity, C equals $N\alpha$. Events can be generated according to this probability, using α=1. To extract the value of α in these events, we minimize -ln$L$. That is,

$$-\ln L = \sum_{i=1}^{N} \ln P_p(t_i) + \int P_p(t)dt \tag{B.2}$$

Using Eq. B.1 in Eq. B.2, the minimization of –ln$L$ yields:

$$\overline{\alpha} = \frac{N}{\sum_{i=1}^{N} t_i} \tag{B.3}$$

and its uncertainty,

$$\sigma = \frac{\overline{\alpha}}{\sqrt{N}} \tag{B.4}$$

Figure B.1 shows the distribution of the probability $P_p(t)$ for one experiment with N=1000 events with an input α=1. Figure B.2 shows the results for N_{exp}=1000 similar

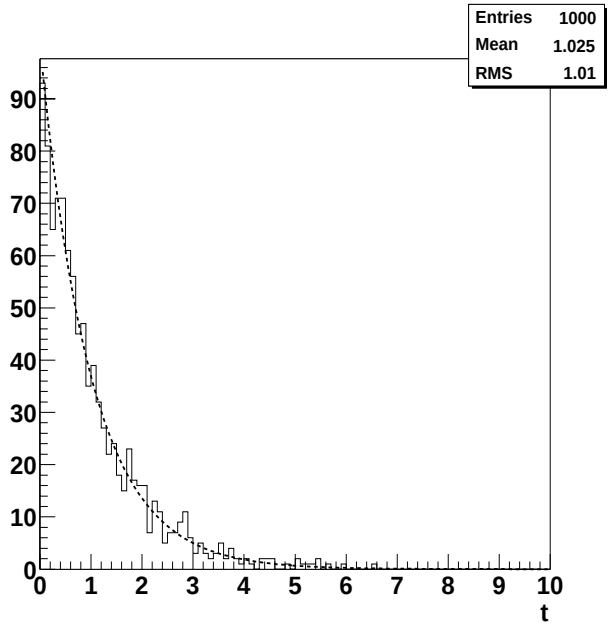

Figure B.1: Probability density $P_p(t)$ as a function of time for 1000 events.

independent experiments with N=1000 and α=1, from which we obtain a mean α=1.001 and σ=0.031.

B.2 Lifetime Taking into Account of Acceptance

Now consider the probability for the lifetime of a particle, taking into account that not all events are accepted. If we assume an acceptance of the form that reflects an inability to measure short decay time, e.g.,

$$A(t) = C_a(1 - \mathrm{e}^{-\beta t}), \tag{B.5}$$

then the probability distribution for the events is given by

$$P(t) = A(t)P_p(t) = D\mathrm{e}^{-\alpha t}(1 - \mathrm{e}^{-\beta t}). \tag{B.6}$$

where D refers to the convolution of all the constants in Eq. B.1 and B.5. Substituting

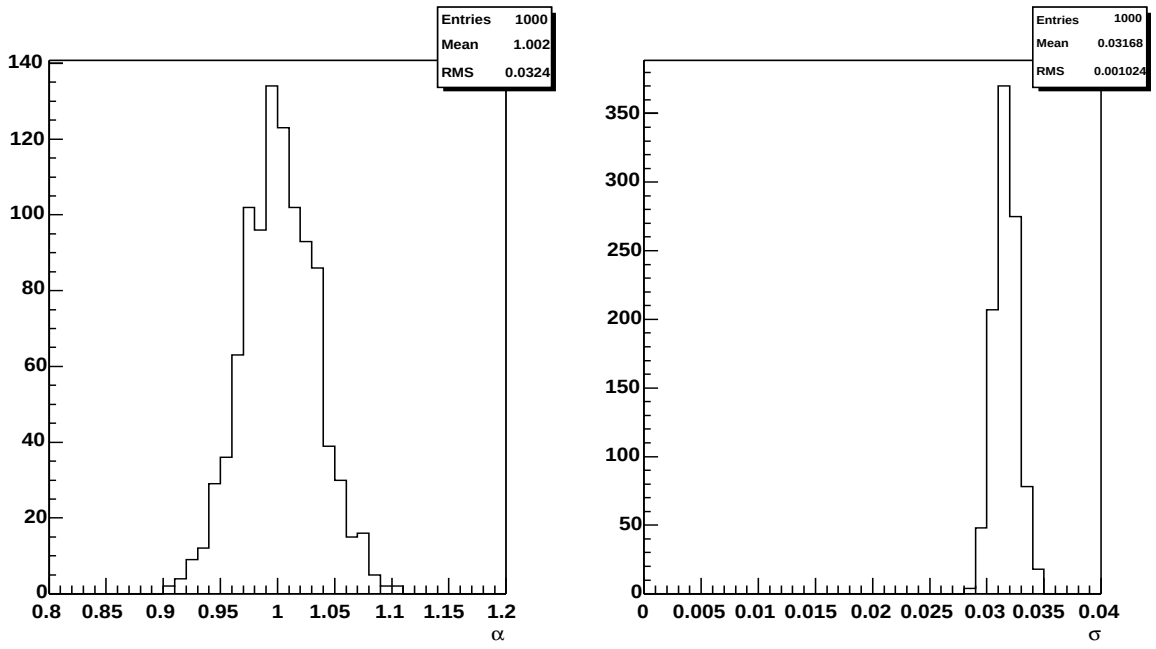

Figure B.2: Lifetime parameters calculated with 1000 experiments, each containing 1000 decays as in Fig. B.1.

Eq. B.6 in Eq. B.2 produces

$$-\ln L = -\sum_{i=1}^{N} \ln A(t_i) - \sum_{i=1}^{N} \ln P_p(t_i) + N \int A(t) P_p(t) dt \tag{B.7}$$

where the first term does not depend on the value of the physical parameters that we want to measure. Minimizing –ln$L$ with respect to α and D gives

$$D = \frac{N\alpha(\alpha+\beta)}{\beta}, \tag{B.8}$$

and

$$\alpha = \frac{2 - \beta t + \sqrt{4 + \beta^2 t^2}}{2t}. \tag{B.9}$$

Figure B.3 shows this probability distribution with α=1.0 and β=0.5, for 1000 events. Figure B.4 compares the results of 1000 experiments with events modified by the acceptance of Eq. B.5, using equations B.9 and B.3 to obtain α, with and without considering acceptance. We notice that there is a large underestimation of α if we do not include

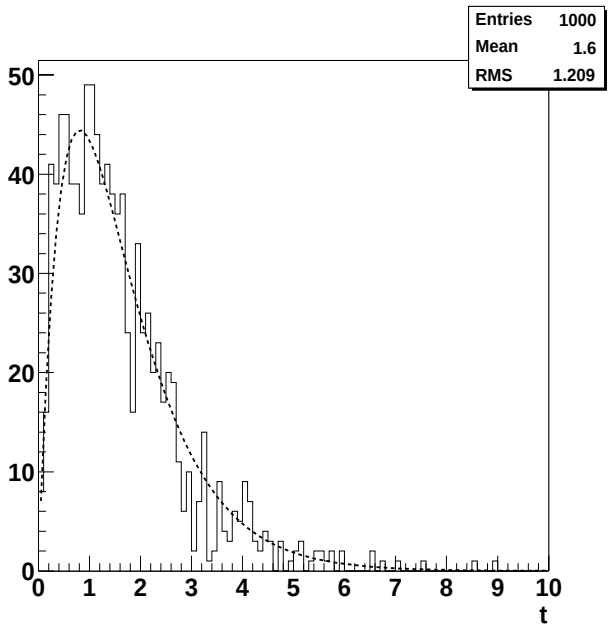

Figure B.3: Probability of decay modified by an assumed acceptance of the detector (Eq. B.5) as a function of time for 1000 events with α=1 and β=0.5.

the acceptance correction.

B.3 Acceptance Integral

The integrals from Eq. B.7 cannot always be calculated analytically, and in this section we compare different ways to perform this integration.

B.3.1 Analytical Solution

In our example, the exact solution for this integral is

$$\int A(t)P_p(t)dt = \frac{1}{\alpha} - \frac{1}{\alpha+\beta} \tag{B.10}$$

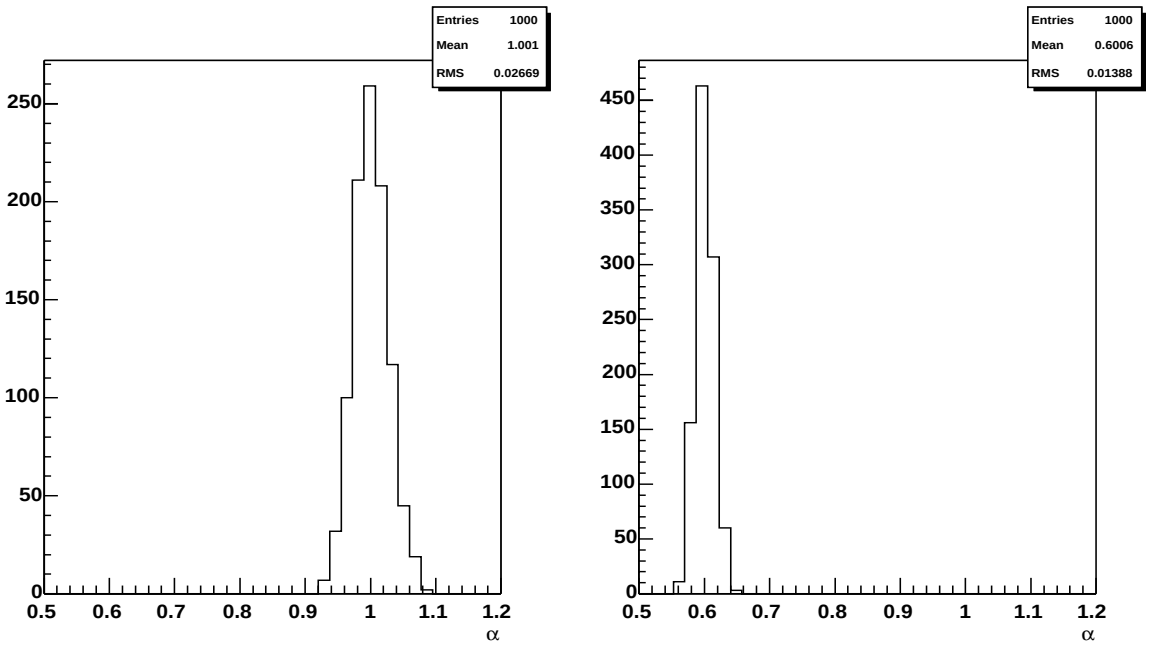

Figure B.4: Decay parameters calculated: (a) taking account of detector acceptance, and (b) ignoring acceptance of Eq. B.5. Each experiment contains 1000 events with α=1 and β=0.5.

B.3.2 Monte Carlo Method of Integration

In general, these multidimensional integrals can only be obtained using Monte Carlo techniques. The Monte Carlo integrals are given by the formula:

$$\int f(x)d[g(x)] = [\int d[g(x)]]\frac{1}{N}\sum_{i=1}^{N} f(x_i) \tag{B.11}$$

This method is very useful in cases where the acceptance function is not well known, in which case the value of $A(t)$ is 1 if the event is accepted, and 0 otherwise.

Using the Monte Carlo method of integration in our example gives

$$\int A(t)P_p(t)dt = \int_0^{\infty}(1-\mathrm{e}^{-\beta t})d(\frac{\mathrm{e}^{-\alpha t}}{-\alpha}) = \frac{1}{N\alpha}\sum_{i=1}^{N}(1-\mathrm{e}^{-\beta t_i}) \tag{B.12}$$

Method	α=1,β=0.5	α=1,β=2	α=2,β=1
Analytical	3333.33	6666.67	3333.33
Monte Carlo	3329.76	6670.53	3358.48
Numerical	3214	6655	3331

Table B.1: Lifetimes calculated exactly, with 10,000 Monte Carlo events, and numerical methods.

B.3.3 Numerical Integration

Another way to solve this integral is numerically. In our example, this gives:

$$\int A(t)P_p(t)dt = \int (1-\mathrm{e}^{-\beta t})\mathrm{e}^{\alpha t}\mathrm{e}^{2t}d(\frac{\mathrm{e}^{-2t}}{-2}) = \frac{1}{2N}\sum_{i=1}^{N}(1-\mathrm{e}^{-\beta t})\mathrm{e}^{(-\alpha+2)t} \qquad \text{(B.13)}$$

Table B.1 provides a comparison of the three methods for calculating Eq. B.7, for several α and β. The results are consistent with each other.

B.4 Lifetime Considering Detector Acceptance and Background

When background is included in the analysis, the probability density is a linear combination of signal and background probabilities, and can be written as:

$$P_p(t) = C_s\mathrm{e}^{-\alpha t} + C_b\mathrm{e}^{-\gamma t} \qquad \text{(B.14)}$$

We generate events using different values for the α and γ coefficients, and Fig B.5 shows the contributions of signal and background for different α and γ. Assuming γ is known, there are three free parameters in the minimization of –ln$L$: C_s, C_b and α. Thus the expression for –ln$L$ becomes:

$$-\ln L = -\sum_{i=1}^{N}\ln P_p(t_i) + C_s\int A(t)\mathrm{e}^{-\alpha t}dt + C_b\int A(t)\mathrm{e}^{-\gamma t}dt \quad . \qquad \text{(B.15)}$$

Using 1000 events generated with α=1 to represent signal, 1000 events with γ=3 to represent background, and the acceptance function in Eq. B.5 for β=0.5, we choose remove events with t <1, and minimize -ln$L$ with respect to C_s and C_b while scanning different values of α. The integral in Eq. B.15 is performed analytically from t >1 to t=50. The result of the minimization using MINUIT [75] for one experiment is given in

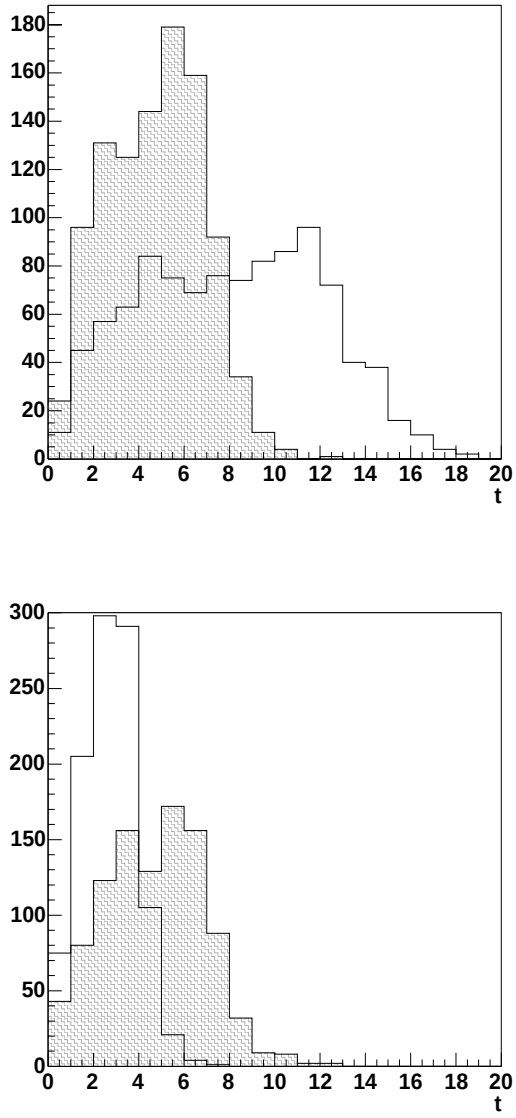

Figure B.5: Contribution from both signal (shaded histogram) and background (solid line) to observed lifetimes. (a) 1000 signal events with α=1, and 1000 background events with γ=0.5. (b) 1000 signal events with α=1, and 1000 background events with γ=2.

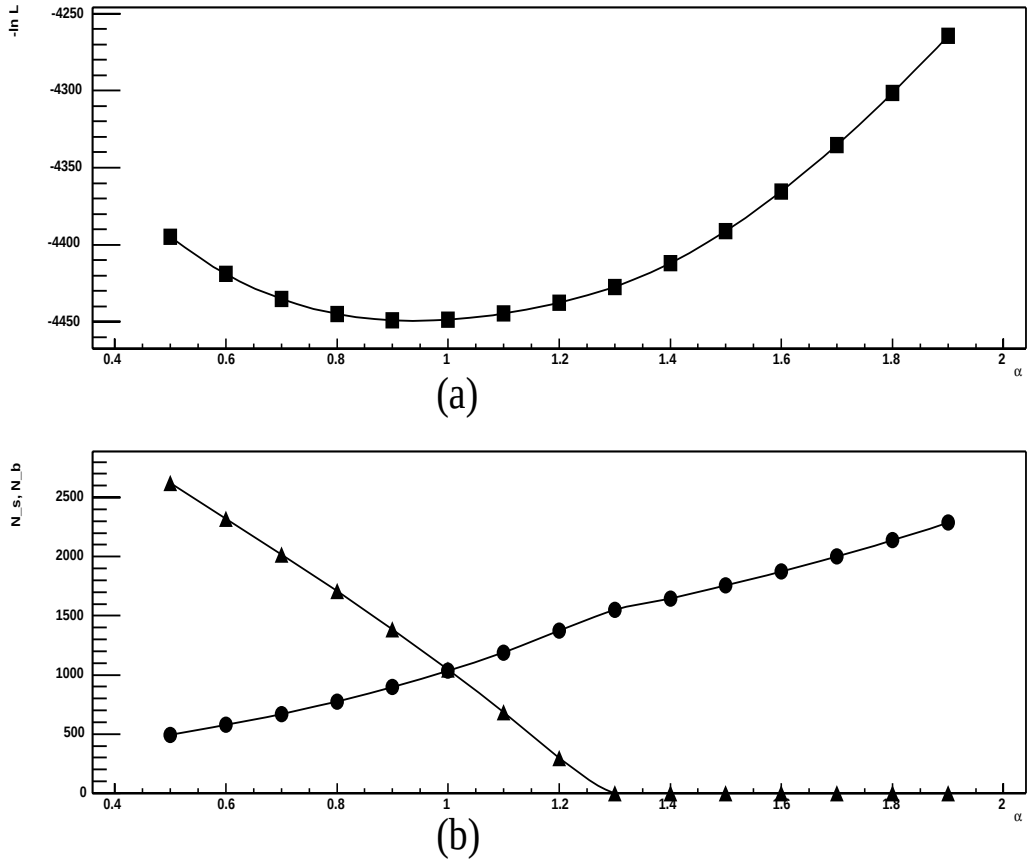

Figure B.6: (a) Minimization of the –ln$L$ with respect of C_s and C_b as a function of α. Events were required to have t>1. (b) N_s (circles) and N_b (triangles) as a function of α for an experiment with 1000 signal and 1000 background events.

Fig B.6, along with the values of N_s and N_b as a function of α. The values of N_s and N_b are derived from C_s and C_b using Eq. B.8. That is,

$$N_s = \frac{C_s \beta}{\alpha(\alpha + \beta)}, \tag{B.16}$$

and,

$$N_b = \frac{C_b \beta}{\gamma(\gamma + \beta)}, \tag{B.17}$$

We notice that the minimum of –ln$L$ coincides with the input values of α and the number of signal and background events.

Appendix C

General Lorentz Invariant Phase Space

Following the PDG, the N-particle Lorentz invariant phase space is written as [11]:

$$d\Phi_n(P; p_1, ..., p_N) = \delta^4(P - \sum_{i=1}^{N} p_i) \prod_{i=1}^{N} \frac{d^3\overrightarrow{p}_i}{(2\pi)^3 2E_i} \quad . \tag{C.1}$$

This comes from the following considerations. The volume in energy-momentum space is given by $d^4p = dEd^3\overrightarrow{p}$, with energy and momentum related by Lorentz-invariant $p^2 = E^2 - \overrightarrow{p}^2 = m^2$. For several particles, the volume element is just the product of the volume elements for each particle, with the constraints $p_i^2 = m_i^2$ and the conservation of total energy and momentum. That is,

$$\delta^4(P - \sum_{i=1}^{n} p_i) \prod_{i=1}^{n} \delta(p_i^2 - m_i^2) \frac{d^4p_i}{(2\pi)^3} \quad . \tag{C.2}$$

The $(2\pi)^3$ is a normalization constant. The above equation always appears inside an integral, and integrating with respect to dE_i, i.e., putting particles "on the mass shell", yields:

$$\int \delta(E_i^2 - \overrightarrow{p}_i^2 - m_i^2) dE_i = \frac{1}{2E_i} \quad , \tag{C.3}$$

and Eq. C.2 reduces to Eq. C.1. The integration of δ-functions is performed using

$$\int f(x)\delta[g(x)]dx = \frac{f(a)}{|g'(a)|} \quad , \text{ with } \quad g(a) = 0 \quad . \tag{C.4}$$

The phase space can be generated recursively. If $q = p_{j+1} + ... + p_n$, with $q^2 = M^2$

then

$$d\Phi_n(P;p_1,...,p_n) = (2\pi)^3 dM^2 \;\; d\Phi_{j+1}(P;p_1,...,p_j,q) \;\; d\Phi_{n-j}(q;p_{j+1},...,p_n) \qquad \text{(C.5)}$$

This recursive generation will be needed to calculate the phase space for single lepton $t\bar{t}$ events. It is obtained starting from Eq. C.2 and adding two δ-functions, one for the mass and another for the conservation of 4-momentum q (recall that the phase space factor is always inside an integral, and every δ-function effectively eliminates an integration).

$$\begin{aligned} d\Phi_n &= \delta^4(P - \sum_{i=1}^{n} p_i) \prod_{i=1}^{n} \delta(p_i^2 - m_i^2) \frac{d^4p_i}{(2\pi)^3} \\ &= \delta^4(q - \sum_{i=j+1}^{n} p_i)\, d^4q \quad \delta(q^2 - M^2) dM^2 \quad \delta^4(P - \sum_{i=1}^{n} p_i) \prod_{i=1}^{n} \delta(p_i^2 - m_i^2) \frac{d^4p_i}{(2\pi)^3} \end{aligned} \qquad \text{(C.6)}$$

integrating over $\delta(q^2 - M^2)dE_q$ and $\delta(p_i^2 - m_i^2)dE_i$, yields:

$$d\Phi_n = (2\pi)^3 dM^2 \left[\delta^4(P - \sum_{i=1}^{j} p_i - q) \frac{d^3\overrightarrow{q}}{(2\pi)^3 2E_q} \prod_{i=1}^{j} \frac{d^3\overrightarrow{p}_i}{(2\pi)^3 2E_i} \right] \left[\delta^4(q - \sum_{i=j+1}^{n} p_i) \prod_{i=j+1}^{n} \frac{d^3\overrightarrow{p}_i}{(2\pi)^3 2E_i} \right] \qquad \text{(C.7)}$$

which is just an expanded version of Eq. C.5.

Appendix D

Calculation of Phase Space for $t\bar{t}$ Events

For $\overline{q}_1 q_2 \to t\bar{t}$ events like the one in Fig. D.1, the Lorentz invariant phase space (see Eq. C.1) is characterized by the particle momenta ($\overrightarrow{p}_q$, $\overrightarrow{p}_e$, $\overrightarrow{p}_\nu$) and four-momenta:

$$d\Phi_6(q_1+q_2; p_1, p_2, p_3, p_4, p_e, p_\nu) = \delta^4(q_1+q_2-\sum_{i=1}^{6} p_i) \prod_{i=1}^{6} \frac{d^3\overrightarrow{p}_i}{(2\pi)^3 2E_i} \quad . \tag{D.1}$$

As discussed in Section 3.4, to integrate the probability, it is very convenient to change variables from the momenta to ($\overrightarrow{\Omega}_{jets}, \rho_1, M_1, m_1, M_2, m_2, \overrightarrow{p}_e$), where $\overrightarrow{\Omega}_{jets}$ are the jet solid angle, $\rho_i = |\overrightarrow{p}_{jet_i}|$ is the absolute momentum of the i-th jet, and (M, m) are the top and W masses. One way to perform the transformation of variables is by calculating the Jacobian of the transformation. A simpler way is to use the recursive character of the phase space, as described in Appendix C. The idea is to 1) group particles into a composite particle, 2) introduce a mass δ-function for the composite system, and 3) to integrate the δ-function over the variables of individual particles. The hadronic branch of the W gives:

$$\begin{aligned} \prod_{i=1}^{3} \frac{d^3\overrightarrow{p}_i}{(2\pi)^3 2E_i} &= \delta(p_{W_1}^2 - m_1^2) dm_1^2 \; \delta(p_{t_1}^2 - M_1^2) dM_1^2 \; \prod_{i=1}^{3} \frac{d^3\overrightarrow{p}_i}{(2\pi)^3 2E_i} \\ &= \frac{dm_1^2 \; dM_1^2 \; d\rho_1}{\left|\frac{\partial p_{W_1}^2}{\partial \rho_2}\right| \left|\frac{\partial p_{t_1}^2}{\partial \rho_3}\right|} \; \prod_{i=1}^{3} \frac{\rho_i^2 d\Omega_i}{(2\pi)^3 2E_i} \end{aligned} \tag{D.2}$$

in the last step the δ-functions were integrated with respect to ρ_2 and ρ_3, using Eq. C.4.

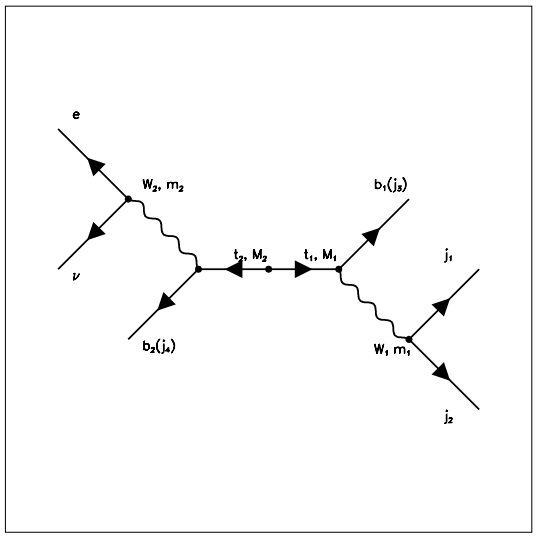

Figure D.1: Feyman diagram for the single-lepton $t\bar{t}$ event.

The value of the partial derivatives is

$$\begin{aligned}\frac{\partial p_{W_1}^2}{\partial \rho_2} &= \frac{\partial (p_1+p_2)^2}{\partial \rho_2} \\ &= \frac{\partial}{\partial \rho_2}(m_1^2+m_2^2+2E_1E_2-2\rho_1\rho_2 cos\theta_{12}) \\ &= 2E_1\frac{\rho_2}{E_2}-2\rho_1 cos\theta_{12}\end{aligned} \tag{D.3}$$

and

$$\begin{aligned}\frac{\partial p_{t_1}^2}{\partial \rho_3} &= \frac{\partial (p_1+p_2+p_3)^2}{\partial \rho_3} \\ &= \frac{\partial}{\partial \rho_3}(m_1^2+m_2^2+m_3^2+2\,p_1\cdot p_2+2E_1E_3-2\rho_1\rho_3 cos\theta_{13}+2E_2E_3-2\rho_2\rho_3 cos\theta_{23}) \\ &= 2E_1\frac{\rho_3}{E_3}-2\rho_1 cos\theta_{13}+2E_2\frac{\rho_3}{E_3}-2\rho_2 cos\theta_{23} \quad .\end{aligned} \tag{D.4}$$

For the lepton branch, the integration of the δ-function is performed over ρ_4 and the

neutrino longitudinal momentum p_ν^z. The derivatives are

$$\begin{aligned}\frac{\partial p_{W_2}^2}{\partial p_\nu^z} &= \frac{\partial (p_e + p_\nu)^2}{\partial p_\nu^z} \\ &= \frac{\partial}{\partial p_\nu^z}(m_e^2 + m_\nu^2 + 2E_eE_\nu - 2p_e^z p_\nu^z - 2\overrightarrow{p}_e^{\,t} \cdot \overrightarrow{p}_\nu^{\,t}) \\ &= 2E_e\frac{p_\nu^z}{E_\nu} - 2p_e^z\end{aligned} \tag{D.5}$$

and

$$\begin{aligned}\frac{\partial p_{t_2}^2}{\partial \rho_4} &= \frac{\partial (p_e + p_\nu + p_4)^2}{\partial \rho_4} \\ &= \frac{\partial}{\partial \rho_4}(m_e^2 + m_\nu^2 + m_4^2 + 2\,p_e \cdot p_\nu + 2E_eE_4 - 2\rho_e\rho_4 cos\theta_{e4} + 2E_\nu E_4 - 2\rho_\nu\rho_4 cos\theta_{\nu 4}) \\ &= 2E_e\frac{\rho_4}{E_4} - 2\rho_e cos\theta_{e4} + 2E_\nu\frac{\rho_4}{E_4} - 2\rho_\nu cos\theta_{\nu 4} \quad .\end{aligned} \tag{D.6}$$

Finally, two of the δ-functions in Eq. D.1 are integrated with respect to the neutrinos transverse momentum giving a value of unity. The other two δ-functions will be integrated later with respect to the initial parton's logitudinal momentum and energy. Combining everything, the phase space for $t\bar{t}$ events is

$$\begin{aligned}d\Phi_6 = \delta(E_{q_1} + E_{q_2} - \sum_{i=1}^{6} E_i)\ \ \delta(p_{q_1}^z + p_{q_2}^z - \sum_{i=1}^{6} p_i^z)\ \ \frac{d^3\overrightarrow{p}_e}{(2\pi)^3 2E_e}\frac{d\rho_1}{(2\pi)^3 2E_\nu}\prod_{i=1}^{4}\frac{\rho_i^2 d\Omega_i}{(2\pi)^3 2E_i} \\ \times \frac{dm_1^2}{|2E_1\frac{\rho_2}{E_2} - 2\rho_1 cos\theta_{12}|}\frac{dM_1^2}{|2E_1\frac{\rho_3}{E_3} - 2\rho_1 cos\theta_{13} + 2E_2\frac{\rho_3}{E_3} - 2\rho_2 cos\theta_{23}|} \\ \times \frac{dm_2^2}{|2E_e\frac{p_\nu^z}{E_\nu} - 2p_e^z|}\frac{dM_2^2}{|2E_e\frac{\rho_4}{E_4} - 2\rho_e cos\theta_{e4} + 2E_\nu\frac{\rho_4}{E_4} - 2\rho_\nu cos\theta_{\nu 4}|} \quad .\end{aligned} \tag{D.7}$$

Appendix E

Changing variables

The measured quantities in a single-lepton $t\bar{t}$ event are the three momenta of the four jets and of the charged lepton. As discussed in subsection 3.5, the probability has to be integrated over all neutrino momenta and jet energies. Due to the narrow widths of the top quark and of the W boson, it is better to perform the integration by changing variables to the two top and two W masses and to one of the jet energies (see Section 3.4).

The granularity of the DØ detector in (η, ϕ) is small compared to the rate of change of typical angular distributions, the jet and lepton directions are therefore measured with enough accuracy so that the integration is over these variables can be performed via a δ-functions. Also, the resolution for elcetrons is much better than for hadrons, and no integration is therefore needed over lepton energy.

E.1 The all-jets branch

In this branch, the variables are changed from $(|\overrightarrow{p}_1|, |\overrightarrow{p}_2|, |\overrightarrow{p}_3|)$ to $(|\overrightarrow{p}_1|, M, m)$, where M and m are the top and W masses, respectively. The W boson decays into $W \to (j_1, j_2)$ and the top quark into $t \to (W, j_3)$. Given the 3-momentum $\overrightarrow{p}_1$ of j_1 , the directional unit vectors $\hat{n}_2$ and $\hat{n}_3$ of jets (j_2, j_3), and the top and W masses we calculate $|\overrightarrow{p}_2|$ and

$|\overrightarrow{p}_3|$.

$$\begin{aligned} m^2 &= (p_1 + p_2)^2 \\ &= p_1^2 + p_2^2 + 2p_1p_2 \\ &= m_1^2 + m_2^2 + 2E_1E_2 - 2\,\overrightarrow{p}_1 \cdot \overrightarrow{p}_2 \\ &= m_1^2 + m_2^2 + 2E_1\sqrt{m_2^2 + x^2} - 2x(\overrightarrow{p}_1 \cdot \hat{n}_2) \end{aligned} \tag{E.1}$$

where x has been temporarily defined as $x = |\overrightarrow{p}_2|$. The above equation is quadratic in x and can be easily solved as follows

$$\frac{m^2 - m_1^2 - m_2^2}{2E_1} = \sqrt{m_2^2 + x^2} - x\frac{\overrightarrow{p}_1 \cdot \hat{n}_2}{E_1} \tag{E.2}$$

$$(a + bx)^2 = m_2^2 + x^2 \text{ ; with } a = \frac{m^2 - m_1^2 - m_2^2}{2E_1} \text{ and } b = \frac{\overrightarrow{p}_1 \cdot \hat{n}_2}{E_1} \tag{E.3}$$

$$(1 - b^2)x^2 - 2abx - (a^2 - m_2^2) = 0 \tag{E.4}$$

The two solutions to the above quadratic equation are

$$\begin{aligned} x &= \frac{ab \pm \sqrt{a^2b^2 + (1 - b^2)(a^2 - m_2^2)}}{1 - b^2} \\ &= \frac{ab \pm \sqrt{a^2 - (1 - b^2)m_2^2}}{1 - b^2} \\ &= \left(\frac{a}{1 - b}\right)\left(\frac{b \pm \sqrt{1 - (1 - b^2)(m_2/a)^2}}{b + 1}\right) \end{aligned} \tag{E.5}$$

Since $b \leq 1$, and $a \sim m$, the negative sign in the above equation always gives $x = |\overrightarrow{p}_2| < 1$, which is not allowed. Then $|\overrightarrow{p}_2|$ becomes

$$\boxed{\begin{aligned} |\overrightarrow{p}_2| &= \left(\frac{a}{1 - b}\right)\left(\frac{b + \sqrt{1 - (1 - b^2)(m_2/a)^2}}{b + 1}\right) \\ a &= \frac{m^2 - m_1^2 - m_2^2}{2E_1} \\ b &= \frac{\overrightarrow{p}_1 \cdot \hat{n}_2}{E_1} \end{aligned}} \tag{E.6}$$

For the decay $t \to (W, j_3)$, we replace $W \to t$, $j_1 \to W$ and $j_2 \to j_3$ in the previous equations. The result is

$$\boxed{\begin{aligned} |\overrightarrow{p}_3| &= \left(\frac{a}{1-b}\right)\left(\frac{b+\sqrt{1-(1-b^2)(m_3/a)^2}}{b+1}\right) \\ a &= \frac{M^2-m^2-m_3^2}{2E_w} \\ b &= \frac{\overrightarrow{p}_w \cdot \hat{n}_3}{E_w} \end{aligned}} \tag{E.7}$$

E.2 The lepton branch

In this branch, the variables are changed from $(|\overrightarrow{p}_4|, p_\nu^z)$ to (M, m), where again M and m are the top and W masses, respectively. The W boson decays $W \to (e, \nu)$, and the top quark into $t \to (W, j_4)$. The transverse momentum of the neutrino is calculated via conservation of total transverse momentum. Again, given the 3-momentum $\overrightarrow{p}_e$ of the lepton , the transverse momentum $\overrightarrow{p}_\nu^t$ of the neutrino, the directional unit vector $\hat{n}_4$ of jet j_4, and the top and W masses, we calculate $|\overrightarrow{p}_4|$ and p_ν^z. The set of coupled equations are:

$$\begin{aligned} m^2 &= (p_e + p_\nu)^2 \\ &= m_e^2 + m_\nu^2 + 2E_eE_\nu - 2\overrightarrow{p}_e \cdot \overrightarrow{p}_\nu \\ M^2 &= (p_w + p_4)^2 \\ &= m^2 + m_4^2 + 2E_wE_4 - 2\overrightarrow{p}_w \cdot \overrightarrow{p}_4 \\ \overrightarrow{p}_\nu^t &= -(\overrightarrow{T} + \overrightarrow{p}_4^t) \\ \overrightarrow{T} &= \overrightarrow{p}_e^t + \overrightarrow{p}_1^t + \overrightarrow{p}_2^t + \overrightarrow{p}_3^t - (\overrightarrow{q}_1^t + \overrightarrow{q}_2^t) \end{aligned} \tag{E.8}$$

where $\overrightarrow{T}$ has only transverse components, and $(\overrightarrow{q}_1, \overrightarrow{q}_2)$ are the incident parton momenta. It is convenient to normalize the energy E_e of the electron, and to define the

variables $x = |\overrightarrow{p}_4|/E_e$ and $y = p_\nu^z/E_e$

$$\begin{aligned}
\frac{m^2 - m_e^2 - m_\nu^2}{2E_e^2} &= \frac{E_\nu}{E_e} + \frac{\overrightarrow{p}_e^{\,t} \cdot \overrightarrow{T}}{E_e^2} + \left(\frac{\overrightarrow{p}_e^{\,t} \cdot \hat{n}_4^t}{E_e}\right) x - \frac{p_e^z}{E_e} y \\
\frac{M^2 - m^2 - m_4^2}{2E_e^2} &= \left(1 + \frac{E_\nu}{E_e}\right)\frac{E_4}{E_e} + \left(\frac{\overrightarrow{T} \cdot \hat{n}_4^t - \overrightarrow{p}_e \cdot \hat{n}_4}{E_e}\right) x + (\hat{n}_4^t)^2 x^2 - n_4^z xy \qquad \text{(E.9)} \\
E_\nu &= \sqrt{m_\nu^2 + (\overrightarrow{T} + \hat{n}_4^t E_e x)^2 + E_e^2 y^2} \\
E_4 &= \sqrt{m_4^2 + E_e^2 x^2}
\end{aligned}$$

The system of coupled equations that has to be solved corresponds therefore to:

$$\begin{cases} f_1(x,y) = e_\nu + a_1 x + a_2 y + a_3 = 0 \\ f_2(x,y) = (1+e_\nu)e_4 + a_4 x + a_5 x^2 + a_6 xy + a_7 = 0 \end{cases}$$

with

$$\begin{aligned}
e_\nu &= \sqrt{a_8 + 2(a_4 + a_1 + a_2 a_6)x + a_5 x^2 + y^2} \\
e_4 &= \sqrt{a_9 + x^2}
\end{aligned}$$

(E.10)

with

$$\boxed{\begin{aligned}
a_1 &= \frac{\overrightarrow{p}_e^{\,t} \cdot \hat{n}_4^t}{E_e} \\
a_2 &= -\frac{p_e^z}{E_e} \\
a_3 &= \frac{\overrightarrow{p}_e^{\,t} \cdot \overrightarrow{T}}{E_e^2} - \frac{m^2 - m_e^2 - m_\nu^2}{2E_e^2} \\
a_4 &= \frac{\overrightarrow{T} \cdot \hat{n}_4^t - \overrightarrow{p}_e \cdot \hat{n}_4}{E_e} \\
a_5 &= (\hat{n}_4^t)^2 = 1 - a_6^2 \\
a_6 &= -n_4^z \\
a_7 &= -\frac{M^2 - m^2 - m_4^2}{2E_e^2} \\
a_8 &= \frac{m_\nu^2 + \overrightarrow{T}^2}{E_e^2} \\
a_9 &= \frac{m_4^2}{E_e^2}
\end{aligned}} \tag{E.11}$$

E.2.1 Limits in x from W mass

For a fixed value of x, the equation $f_1(x, y) = 0$ is quadratic in y. The solution is

$$\begin{aligned}
e_\nu^2 &= (a_1 x + a_2 y + a_3)^2 \\
a_8 + 2(a_4 + a_1 + a_2 a_6)x + a_5 x^2 + y^2 &= (a_1 x + a_3)^2 + 2a_2(a_1 x + a_3)x + a_2^2 y^2
\end{aligned} \tag{E.12}$$

$$\begin{aligned}
& Ay^2 - 2By + C = 0 \\
& A = (1 - a_2^2) \\
& B = a_2(a_1 x + a_3) \\
& C = a_8 + 2(a_4 + a_1 + a_2 a_6)x + a_5 x^2 - (a_1 x + a_3)^2
\end{aligned} \tag{E.13}$$

Since y must be positive, $B^2 - AC \geq 0$, which set limits on the allowed values of x.

$$\begin{aligned} B^2 - AC &= a_2^2(a_1x + a_3)^2 - (1 - a_2^2)[a_8 + 2(a_4 + a_1 + a_2a_6)x + a_5x^2 - (a_1x + a_3)^2] \\ &= (a_1x + a_3)^2 - (1 - a_2^2)[a_8 + 2(a_4 + a_1 + a_2a_6)x + a_5x^2] \\ &= s_2x^2 + 2s_1x + s_0 \geq 0 \\ s_2 &= a_1^2 - Aa_5 \\ s_1 &= a_1a_3 - A(a_4 + a_1 + a_2a_6) \\ s_0 &= a_3^2 - Aa_8 \end{aligned} \tag{E.14}$$

Therefore, x must be inside the interval $[x_1, x_2]$ where

$$x_{1,2} = \frac{-s_1 \pm \sqrt{s_1^2 - s_2s_0}}{s_2} \tag{E.15}$$

E.2.2 Limits in x from the mass of the top quark

Following Ref. [29], we find from the lower limit on the top-quark mass

$$[m_4^2 + 2(ej_4)]\frac{m^2 + 2(ej_4)}{2(ej_4)} \leq M^2 \tag{E.16}$$

where $(ej_4) = E_eE_4 - \overrightarrow{p}_e \cdot \overrightarrow{p}_4$. Defining $z = (ej_4)/E_e^2$,the inequality transforms into

$$\begin{aligned} \left(\frac{m_4^2}{2E_e^2} + z\right)\left(\frac{m^2}{2E_e^2} + z\right) &\leq \frac{M^2}{2E_e^2}z \\ z^2 - \frac{M^2 - m^2 - m_4^2}{2E_e^2}z + \frac{m_4^2m^2}{4E_e^4} &\leq 0 \end{aligned} \tag{E.17}$$

The limits in z hen given by

$$\begin{aligned} z^2 + a_7z + \frac{m_4^2m^2}{4E_e^4} &= 0 \\ z_{1,2} &= \frac{-a_7 \pm \sqrt{a_7^2 - m_4^2m^2/E_e^4}}{2} \end{aligned} \tag{E.18}$$

Having calculated $z_{1,2}$,the limits on x e obtained

$$\begin{aligned} z &= \frac{(ej_4)}{E_e^2} \\ &= \frac{E_4}{E_e} - \frac{\overrightarrow{p}_e \cdot \hat{n}_4}{E_e} x \\ &= \sqrt{a_9 + x^2} - sx \\ s &= \frac{\overrightarrow{p}_e \cdot \hat{n}_4}{E_e} \\ &= a_1 + a_2 a_6 \leq 1 \end{aligned} \tag{E.19}$$

$$\begin{aligned} (z + sx)^2 &= a_9 + x^2 \\ (1 - s^2)x^2 - 2zsx + a_9 - z^2 &= 0 \\ x &= \frac{zs \pm \sqrt{z^2 s^2 - (1 - s^2)(a_9 - z^2)}}{1 - s^2} \\ &= \frac{zs \pm \sqrt{z^2 - (1 - s^2)a_9}}{1 - s^2} \\ &= \left(\frac{z}{1 - s}\right)\left(\frac{s \pm \sqrt{1 - (1 - s^2)a_9/z^2}}{1 + s}\right) \end{aligned} \tag{E.20}$$

In order for the argument of the square root to be positive, it follows that $z \geq \sqrt{(1 - s^2)a_9}$. Hence, the limits from the top mass are

$$\boxed{\begin{aligned} x_{1,2} &= \left(\frac{z_{1,2}}{1 - s}\right)\left(\frac{s \pm \sqrt{1 - (1 - s^2)a_9/z_{1,2}^2}}{1 + s}\right) \\ z_1 &= max\left(\sqrt{(1 - s^2)a_9}, \frac{-a_7 - \sqrt{a_7^2 - m_4^2 m^2/E_e^4}}{2}\right) \\ z_2 &= \frac{-a_7 - \sqrt{a_7^2 - m_4^2 m^2/E_e^4}}{2} \end{aligned}} \tag{E.21}$$

E.2.3 Constructing $P_8(x)$

Putting together the last sections, we obtain

$$\begin{aligned} s^2 &= (Ay - B)^2 \\ &= B^2 - AC \\ &= s_2 x^2 + s_1 x + s_0 \end{aligned} \tag{E.22}$$

where

$$\begin{aligned} A &= 1 - a_2^2 \\ B &= a_2(a_1 x + a_3) \\ s_2 &= a_1^2 - A a_5 \\ s_1 &= 2[a_1 a_3 - A(a_4 + a_1 + a_2 a_6)] \\ s_0 &= a_3^2 - A a_8 \end{aligned} \tag{E.23}$$

and, finally,

$$\begin{aligned} p &= a_1 x + (a_3 - A) \\ q &= q_2 x^2 + q_1 x + q_0 \end{aligned} \tag{E.24}$$

with

$$\begin{aligned} q_2 &= a_5 A + a_6 a_2 a_1 \\ q_1 &= a_4 A + a_6 a_3 a_2 \\ q_0 &= a_7 A \end{aligned} \tag{E.25}$$

Appendix F

Histogramming Different Quantities

To compare theory with data or with Monte-Carlo events, it is often useful to examine a variety of physical quantities. When $P(x)$ is suitably normalized, the total number of observed events will be given by:

$$N = \int Acc(x)P(x)dx \quad . \tag{F.1}$$

To examine the dependence of the yield on any quantity m_x, requires a calculation of the differential distribution dN/dm_x. This can be done by changing the set of variables $x = (x_1, x_2, ..., x_n)$ to the set $(m_x, x_2, ..., x_n)$, using the Jacobian $J\frac{(x_1,x_2...x_n)}{(m_x,x_2...x_n)}$, as follows:

$$\begin{aligned} N &= \int Acc(x)P(x)dx \\ &= \int dm_x dx_2 ... dx_n J(\frac{x_1, x_2, ..., x_n}{m_x, x_2, ..., x_n}) Acc(x)P(x) \end{aligned} \tag{F.2}$$

with the Jacobian specified by:

$$J(\frac{m_x, x_2, ..., x_n}{x_1, x_2, ..., x_n}) = \begin{vmatrix} \frac{\partial m_x}{\partial x_1} & \frac{\partial m_x}{\partial x_2} & \cdots & \frac{\partial m_x}{\partial x_n} \\ \frac{\partial x_2}{\partial x_1} & \frac{\partial x_2}{\partial x_2} & \cdots & \frac{\partial x_2}{\partial x_n} \\ \vdots & \vdots & \cdots & \vdots \\ \frac{\partial \dot{x}_n}{\partial x_1} & \frac{\partial \dot{x}_n}{\partial x_2} & \cdots & \frac{\partial \dot{x}_n}{\partial x_n} \end{vmatrix} \tag{F.3}$$

and dN/dm_x can be written as:

$$\frac{dN}{dm_x} = \int dx_2...dx_n J(\frac{x_1, x_2, ..., x_n}{m_x, x_2, ..., x_n}) Acc(x) P(x) \tag{F.4}$$

This integral can be evaluated using Eq 3.9 (summing over all permutations), by changing the order of integration:

$$\begin{aligned}
\frac{dN}{dm_x} &= \int dx_2...dx_n J(\frac{x_1, x_2, ..., x_n}{m_x, x_2, ..., x_n}) Acc(x) P(x) \\
&= \int dx_2...dx_n J(\frac{x_1, x_2, ..., x_n}{m_x, x_2, ..., x_n}) Acc(x) \sum_{perm.} \int d^n\sigma(y) dq_1 dq_2 f(q_1) f(q_2) W(y, x) \\
&= \sum_{perm.} \int d^n\sigma(y) dq_1 dq_2 f(q_1) f(q_2) \int dx_2...dx_n J(\frac{x_1, x_2, ..., x_n}{m_x, x_2, ..., x_n}) Acc(x) W(y, x) \\
&= \sum_{perm.} \int d^n\sigma(y) dq_1 dq_2 f(q_1) f(q_2)\, Q(y)
\end{aligned} \tag{F.5}$$

with

$$Q(y) = \int dx_2...dx_n J(\frac{x_1, x_2, ..., x_n}{m_x, x_2, ..., x_n}) Acc(x) W(y, x) \tag{F.6}$$

The integration over electron momenta and jet angles in $Q(y)$ can be performed using the δ-functions in $W(y, x)$ of Eq. 3.12:

$$\begin{aligned}
Q(y) &= \int dE_2^x...dE_4^x J(\frac{E_1^x E_2^x ... E_4^x}{m_x E_2^x ... E_4^x}) Acc(x) \prod_{i=1}^{4} W_{jet}(E_i^y, E_i^x) \\
\frac{dN}{dm_x} &= \sum_{perm.} \int d^n\sigma(y) dq_1 dq_2 f(q_1) f(q_2)\, Q(y)
\end{aligned} \tag{F.7}$$

The acceptance $Acc(x)$ is usually not a simple analytic function, and therefore some of the integrals have to be performed using Monte Carlo. This is done by generating events in the y variables, running them through detector simulation/reconstruction, and then counting only the events that are accepted. This procedure effectively integrates

over y and over the acceptance. We can therefore write:

$$\boxed{\frac{dN}{dm_x} = \frac{V}{N_{gen}} \sum_{acc} \frac{d^n\sigma(y)}{d^n\sigma_{MC}(y)} \frac{f(q_1)}{f_{MC}(q_1)} \frac{f(q_2)}{f_{MC}(q_2)} \times \sum_{perm.} \int dE_2^x ... dE_4^x J(\frac{E_1^x E_2^x ... E_4^x}{m_x E_2^x ... E_4^x}) \prod_{i=1}^{4} Acc(E_i^x) W_{jet}(E_i^y, E_i^x)} \tag{F.8}$$

where $V = \int d^n\sigma_{MC}(y) dq_1 dq_2 f_{MC}(q_1) f_{MC}(q_2)$ (see Section 3.5.)

To avoid edge effects in the integration, the cuttoff on jet energy should be lower in the MC than in the final analysis.

Appendix G

Statistical Issues in Analysis

Because the parameter F_0 is restricted to physical values, the probability density can be quite asymmetric in F_0, especially for poor statistics. We simulate this effect below using a simple example, and study different ways to extract a measurement and a well-defined uncertainty.

G.1 Signal

We generate signal events according to a shape similar to the expected probability density in x=cos$\hat{\phi}$:

$$P_s(F_0, x) = \frac{3}{4}F_0(1-x^2) + \frac{3}{8}(1-F_0)(1-x)^2 \tag{G.1}$$

with F_0=0.703. This function represents the signal, and is shown by the solid line in Fig. G.1. For a set of N such events, and no background, we calculate the likelihood or product probability distribution:

$$L(F_0) = \prod_{i=1}^{N} P_s^i(F_0) \quad . \tag{G.2}$$

Figure G.2 shows the results for four such experiments, each containing 100 signal events, from which we extract values of F_0 for an input F_0=0.7. For each experiment, we obtain a likelihood that is fitted with a 5^{th} order polynomial, which defines the probability function. The shaded region corresponds to 68.27% of the probability, centered on the

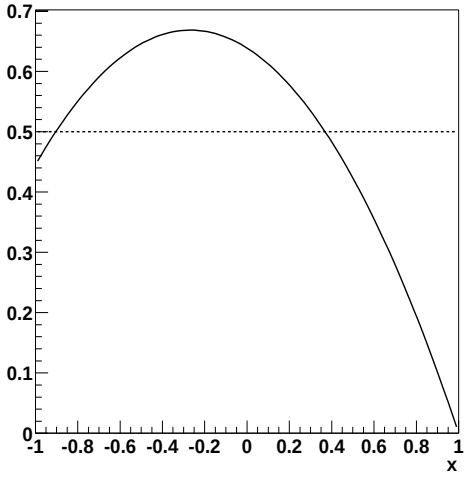

Figure G.1: Signal is represented by the solid line, and background by the dotted line, each normalized to 1.0.

most probable value. At this level of statistics, the mean and most probable value of the probability distribution essentially coincide, as do the RMS values and half of the 68.27% interval about the peak. (See the summary in Table G.1.)

As we mentioned before, the probability is restricted to the physical region, and our fits are therefore also restricted to $0 < F_0 < 1$. This restriction causes the output values to peak near 0 and 1, an effect more noticeable for low statistics. From Run I, we expect about 10 $t\bar{t}$ events. Figure G.3 shows distributions in the most probable value and its 68.27% interval, as well as the mean and its RMS, for 1000 experiments of 10 events each. In this ideal case, ignoring jet-resolution, detector acceptance, or background, the mean statistical error is about 0.2. We also notice that since the probability is constrained, the error extracted from it will also be constrained to the physical region. The error cannot be greater than ≈ 0.34. We choose to quote the most probable value for the extracted F_0 because it is closer to the input value.

For a more realistic simulation, we include two separate angular distributions, one to account for the leptonic decay and the other to account for the hadronic decay. That

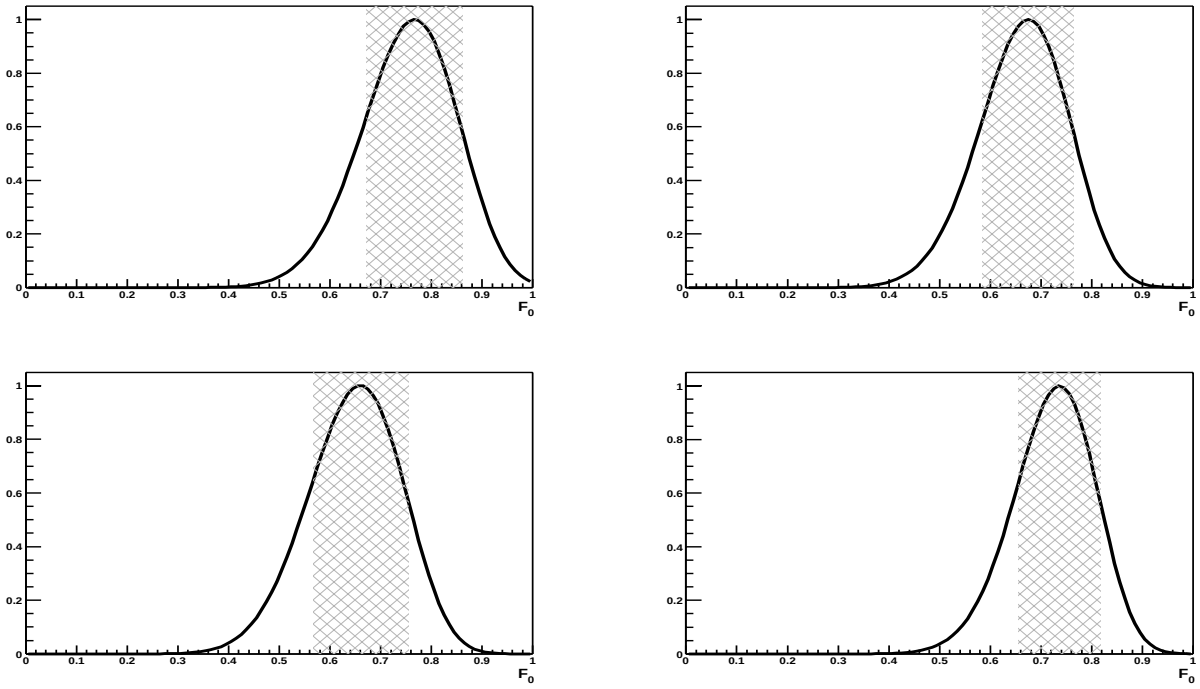

Figure G.2: Probability density as a function of F_0 for four experiments, each with 100 signal events. Shaded region indicates the 68.27% probability interval centered on the most probable value.

Experiment #	Mean	Most Probable Value	RMS	δ F_0 from 68.27%
1	0.753	0.767	0.094	0.095
2	0.663	0.675	0.089	0.089
3	0.646	0.660	0.092	0.093
4	0.722	0.736	0.081	0.081

Table G.1: Values of F_0 and their statistical uncertainties for the experiments of Fig. G.2. The extracted parameters based either on the mean or most probable values of F_0 agree fully.

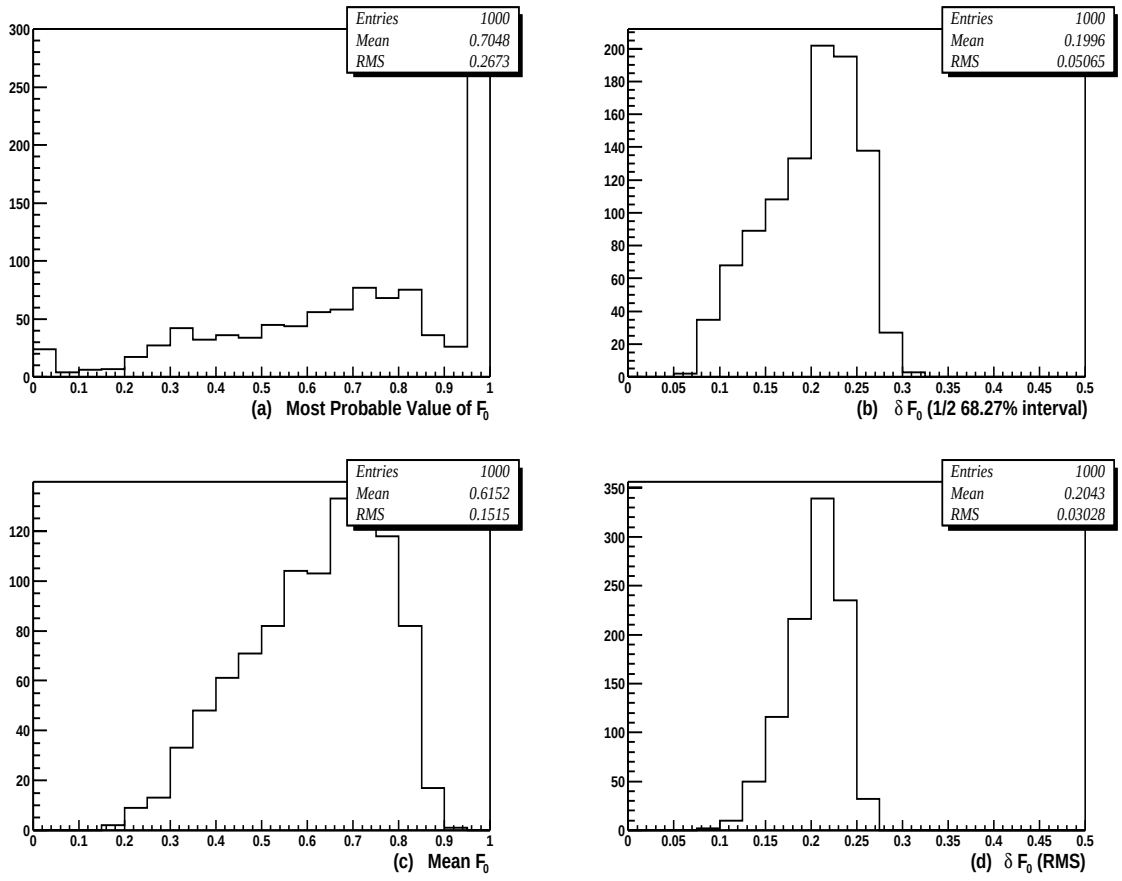

Figure G.3: Ensemble studies using 1000 experiments with 10 events in each. (a) Most probable value of F_0, and (b) its 68.27% interval, (c) mean F_0, and (d) and RMS.

is,

$$P_s(F_0,x) = [\frac{3}{4}F_0(1-x^2) + \frac{3}{8}(1-F_0)(1-x)^2] \times [\frac{3}{4}F_0(1-y^2) + \frac{3}{8}(1-F_0)(1+y^2)] \tag{G.3}$$

where the symmetrized function on the right represents the hadronic decay. In this case, we expect an increase of sensitivity by almost a factor of $\sqrt{2}$ due to the fact that we have almost twice as many events when we add the information from the second decay branch. Figure G.4 shows the most probable values and errors for an ensemble of 1000 experiments of 10 events using the probability from Eq. G.1 and G.3. Figure G.5 shows similar results using 60 events in each experiment. There is an improvement in the statistical error of almost a factor of 1.2, as was expected. Figure G.6 shows how the means (circles) and the most probable values (stars) change as a function of the number of events in each of 1000 experiments. Figure G.6b shows the fraction of times that the input value was recovered in the interval defined by 68.27% of the probability. We note that the results converge rapidly to the expected values (0.703 and 0.6827) as the number of events increases. Figure G.7 shows how the RMS of the pull (defined as $\frac{\mathrm{Extracted}F_0 - F_{0\mathrm{input}}}{\mathrm{Uncertainty}}$) converges to 1 when the number of events increases. For low statistics, the pull is not well behaved.

G.2 Signal and Background

For background events, we choose the simple density P_b=0.5, as shown by the dotted line in Fig. G.1. The total probability is now

$$P = c_1 P_s + c_2 P_b \quad . \tag{G.4}$$

which after normalizing to 1, yields c_2=1-c_1.

For each set of N events, we calculate the likelihood

$$L(F_0) = \prod_{i=1}^{N} [c_1 P_s(F_0) + (1-c_1)P_b] \tag{G.5}$$

where c_1 corresponds to the fraction of signal events. Because c_1 and F_0 are correlated,

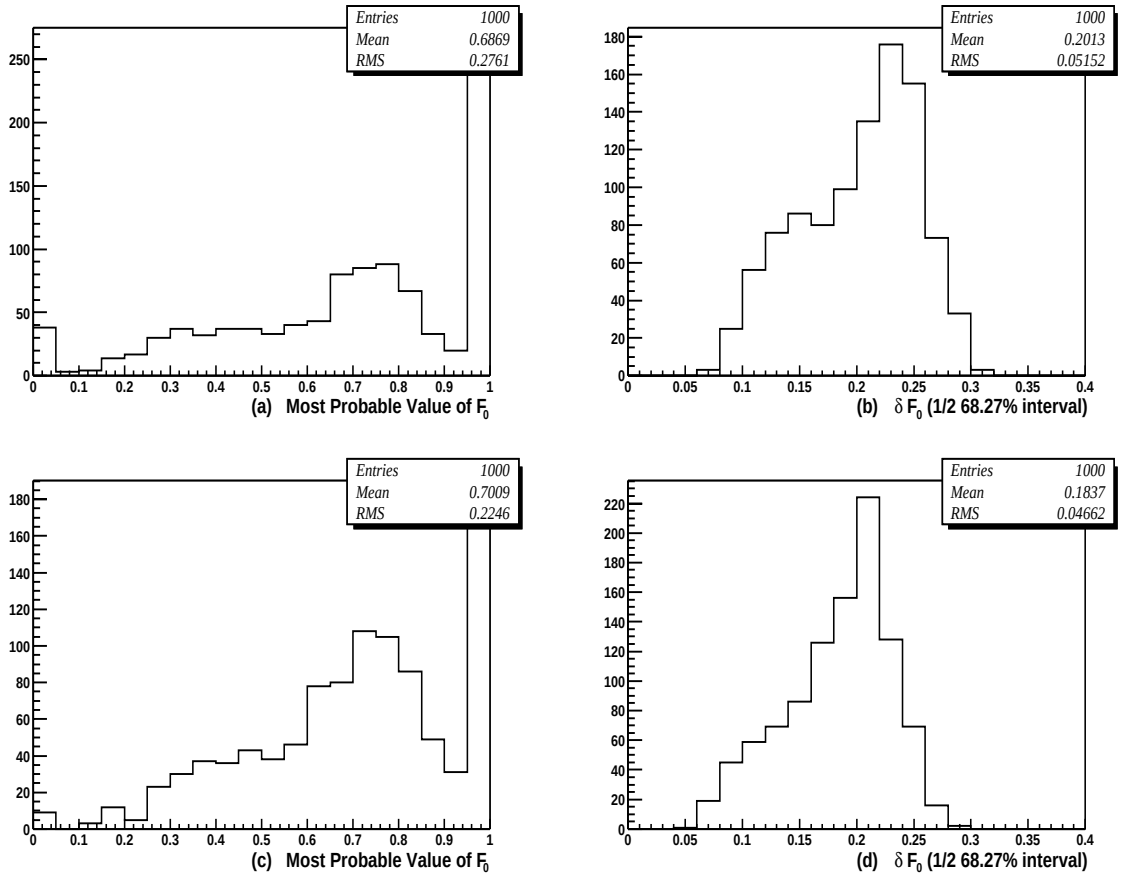

Figure G.4: Ensemble studies using 1000 experiments with 10 events in each. (a) Most probable value of F_0, and (b) its 68.27% interval, for events that were generated and analyzed using the probability of Eq. G.1. (c) and (d) show similar results but for events that were generated and analyzed using the probability of Eq. G.3.

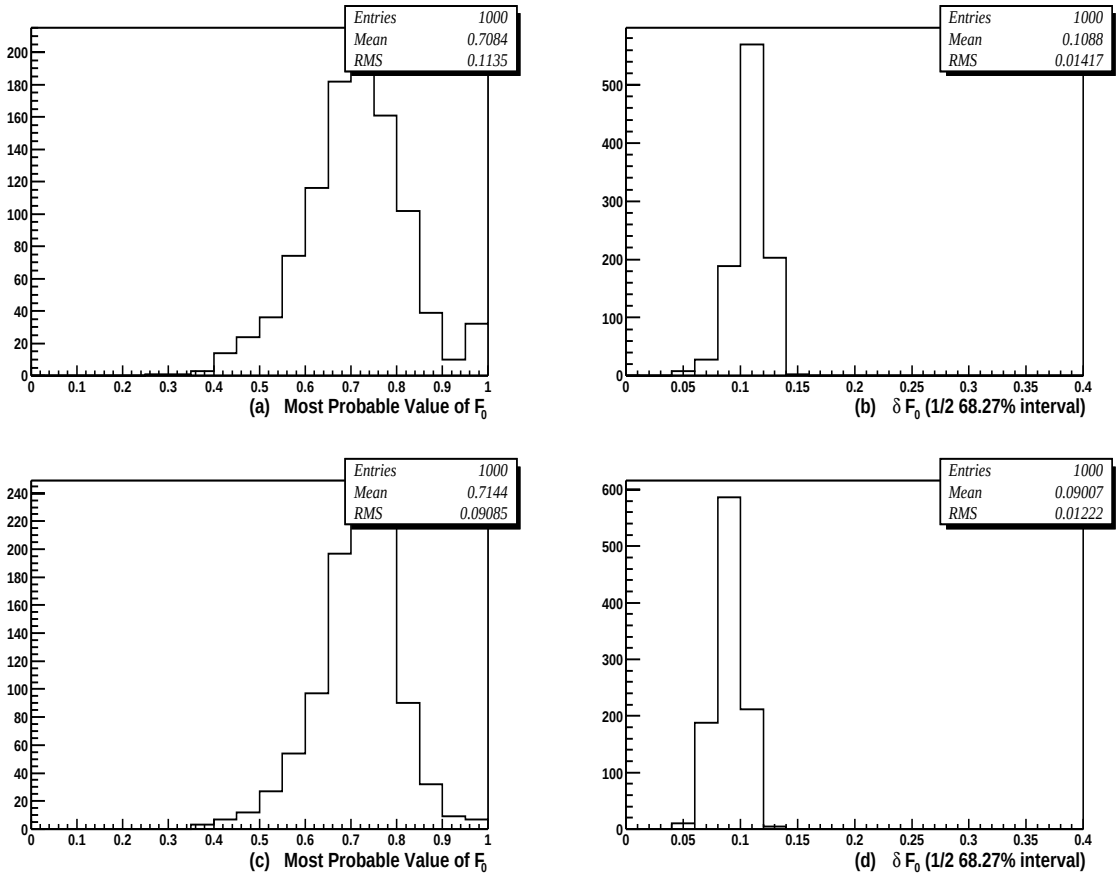

Figure G.5: Ensemble studies using 1000 experiments with 60 events in each. (a) Most probable value of F_0, and (b) its 68.27% interval, for events that were generated and analyzed using the probability of Eq. G.1. (c) and (d) show similar results but for events that were generated and analyzed using the probability of Eq. G.3.

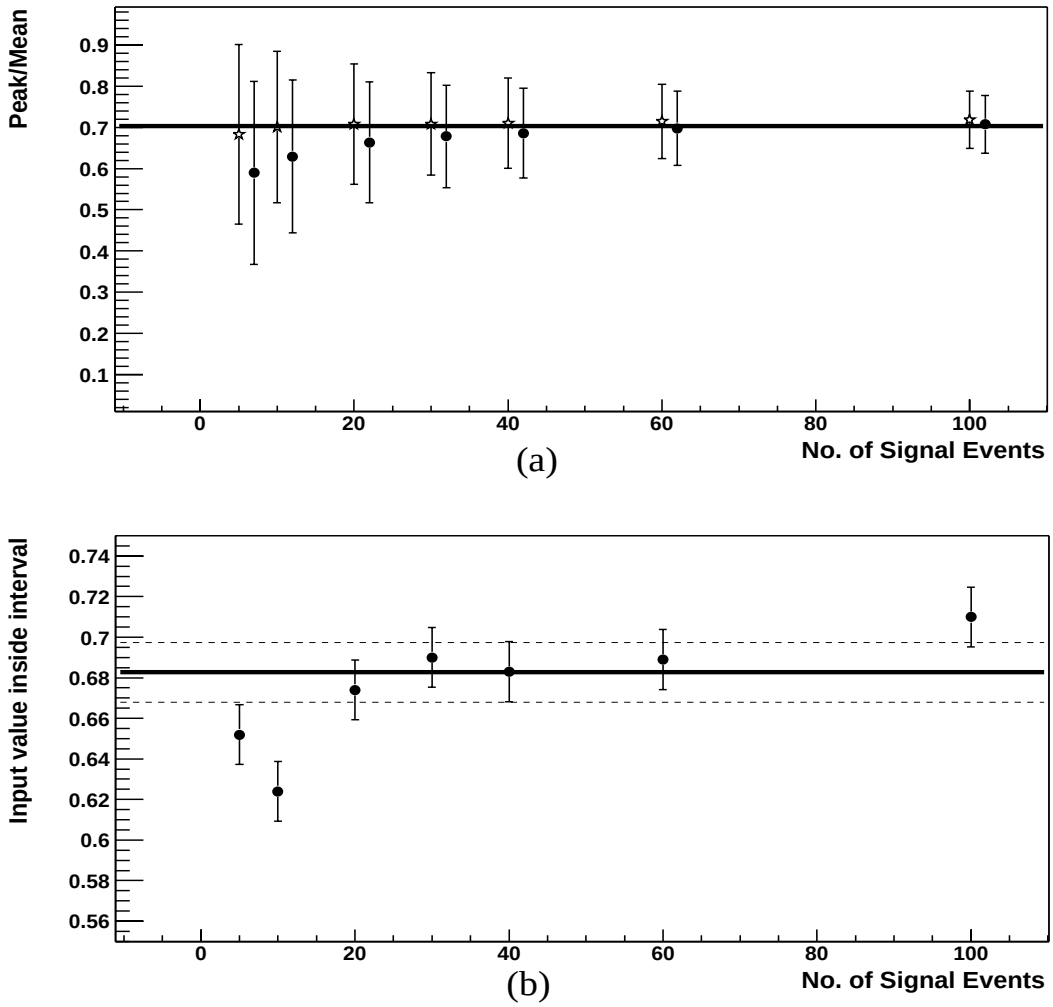

Figure G.6: Extracted parameters as a function of the number of signal events (and no background) in each of 1000 experiments. (a) Means (circles) and most probable values (stars) are plotted with error bars representing the RMS and the 68.27% interval about the peak-values, respectively. (b) Fraction of time that the input F_0 is within the interval defined by 68.27% of the area about the most probable value. The horizontal lines correspond to 68.27% and to ± 1 standard deviation.

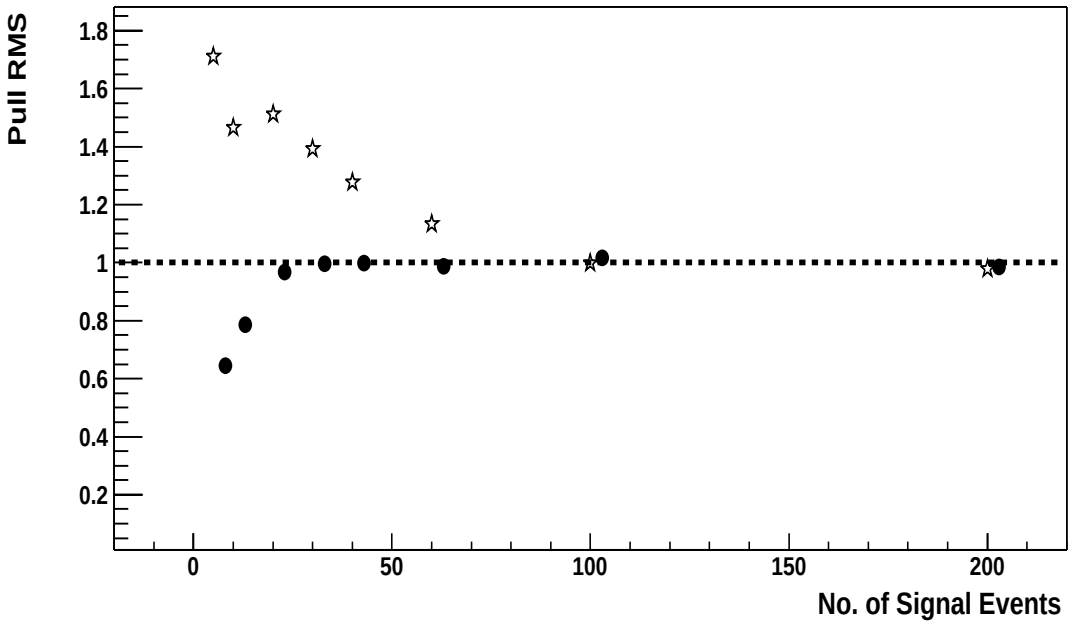

Figure G.7: RMS of pull distribution. Stars use most probable values and 68.27% interval of the probabilities to calculate the distribution. Circles use mean and RMS to calculate the pull distribution. We note that at low statistics the pull is not a reliable parameter.

we examine their interdependence in $L(F_0)$. We proceed minimizing –ln$L$ relative to c_1 for different values of F_0.

Figure G.8 shows the two-dimensional probability density for four experiments using a total of 500 events. The signal/(signal+background) in the samples is fluctuated about a mean of to 0.4. The rectangular region contains 68.27% of the area about the maximum probability. In Fig. G.10, we analyze the same four experiments, minimizing c_1 for each value of F_0. Figure G.10 shows the results for F_0 as the signal fraction increases.

Figure G.10(a) shows how the means (circles) and the most probable values (stars) change as a function of the signal fraction of the sample in each of 1000 experiments based on F_0=0.703 as input and using a total of 500 events per experiment. Figure G.10(b) shows the fraction of times that the input value was recovered in the interval defined by 68.27% of the probability as a function of the signal fraction in the sample.

We repeat the same analysis using a total of 30 events per experiment, and again a signal/(signal+background) ratio close to 0.4. In Fig. G.11, we show the two-dimensional probability for these 4 experiments. Figure G.12 shows the probability distributions for these four experiments after we minimize c_1 for events with F_0=0.7. Figures G.13 presents the results as a function of the signal/(signal+background) for these statistics after minimizing c_1.

Figure G.14 shows the fraction of the times that a given F_0 falls inside the 68.27% interval. Each point contains the result for 1000 experiments of 200 signal and 300 background events.

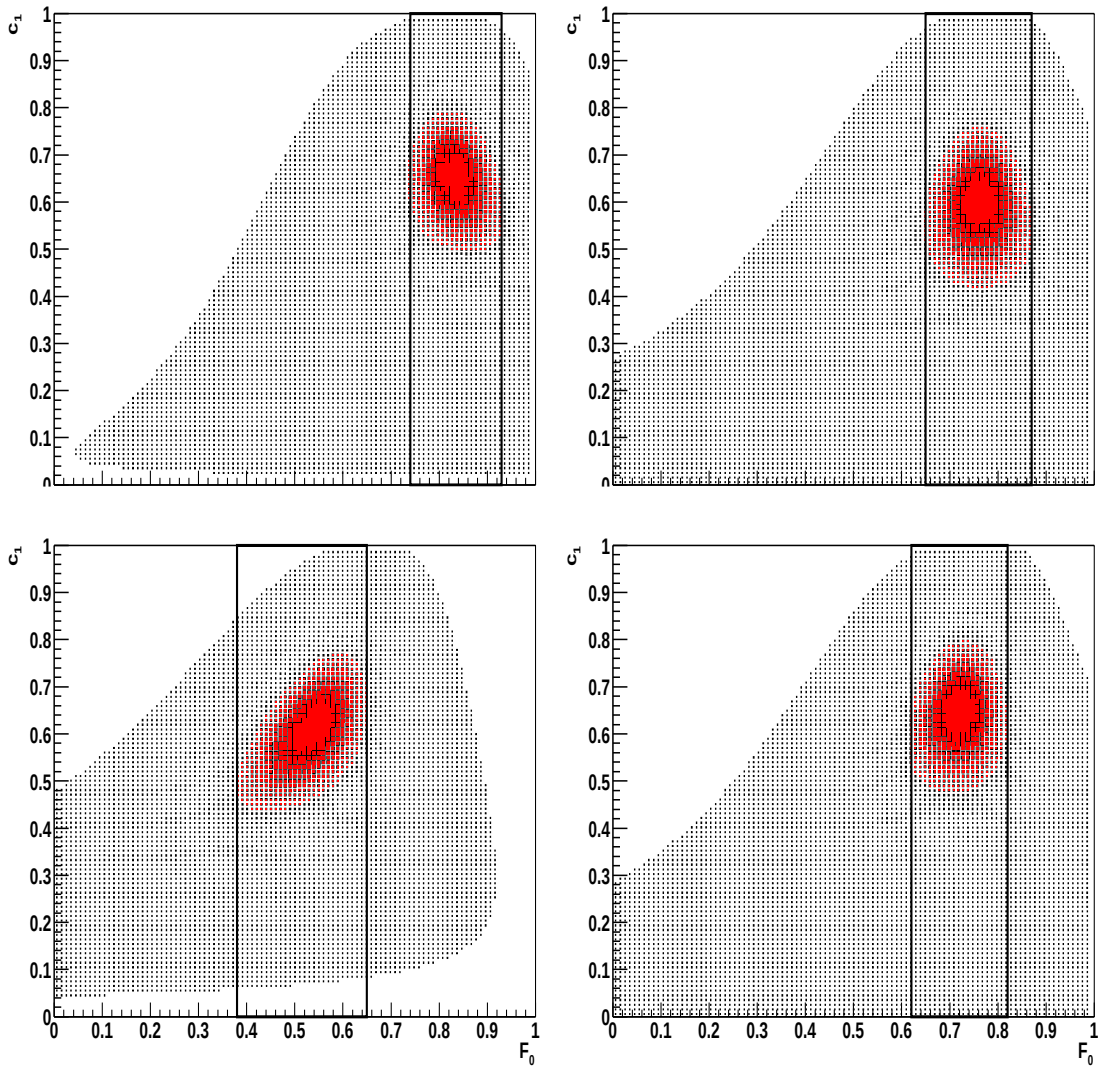

Figure G.8: Probability density as a function of c_1 and F_0 for 500 events with and input F_0=0.703 and a signal/(signal+background) fluctuating binomially about 0.4. Shadow inside box indicates the 68.27% of the total probability area in two-dimensional space.

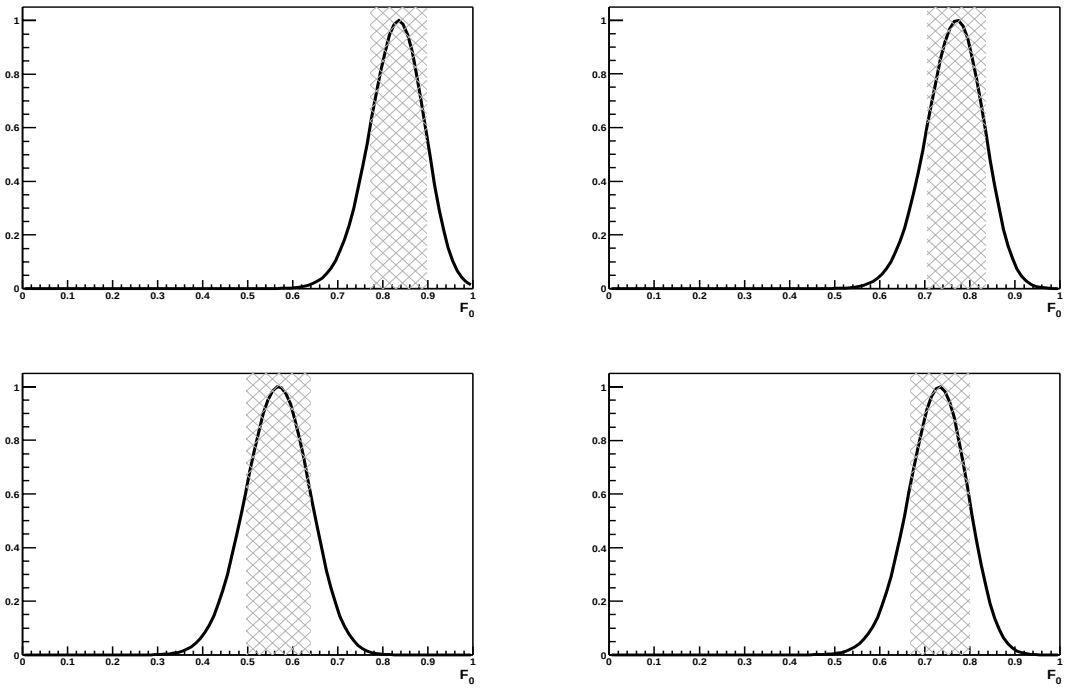

Figure G.9: Probability density as a function of F_0 for the same four experiments as in Fig. G.8. The projection onto F_0 was obtained by minimizing $-\ln L$ with respect to c_1. Each experiment has 500 events with an input F_0=0.703 and signal/(signal+background) fluctuating binomially about 0.4. Shadow region indicates 68.27% of probability around the most probable value.

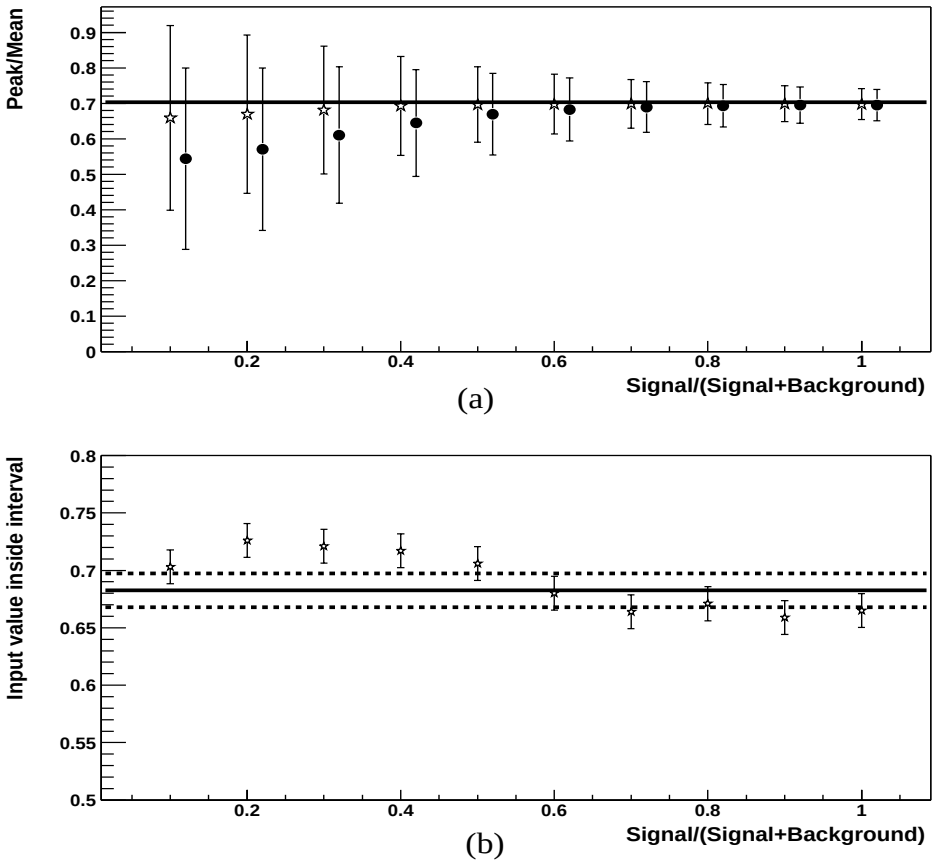

Figure G.10: Extracted parameters as a function of signal/(signal+background), using 500 events in each of 1000 experiments. We minimize -ln$L$ with respect to c_1 for each F_0. (a) Means (circles) most probable values (stars) are plotted with error bars representing the RMS and the 68.27% interval about the peak-values, respectively. (b) Fraction of time that the input F_0 (0.703) is within the interval defined by 68.27% of the area about the most probable value. The horizontal lines correspond to 68.27% and to ± 1 sigma.

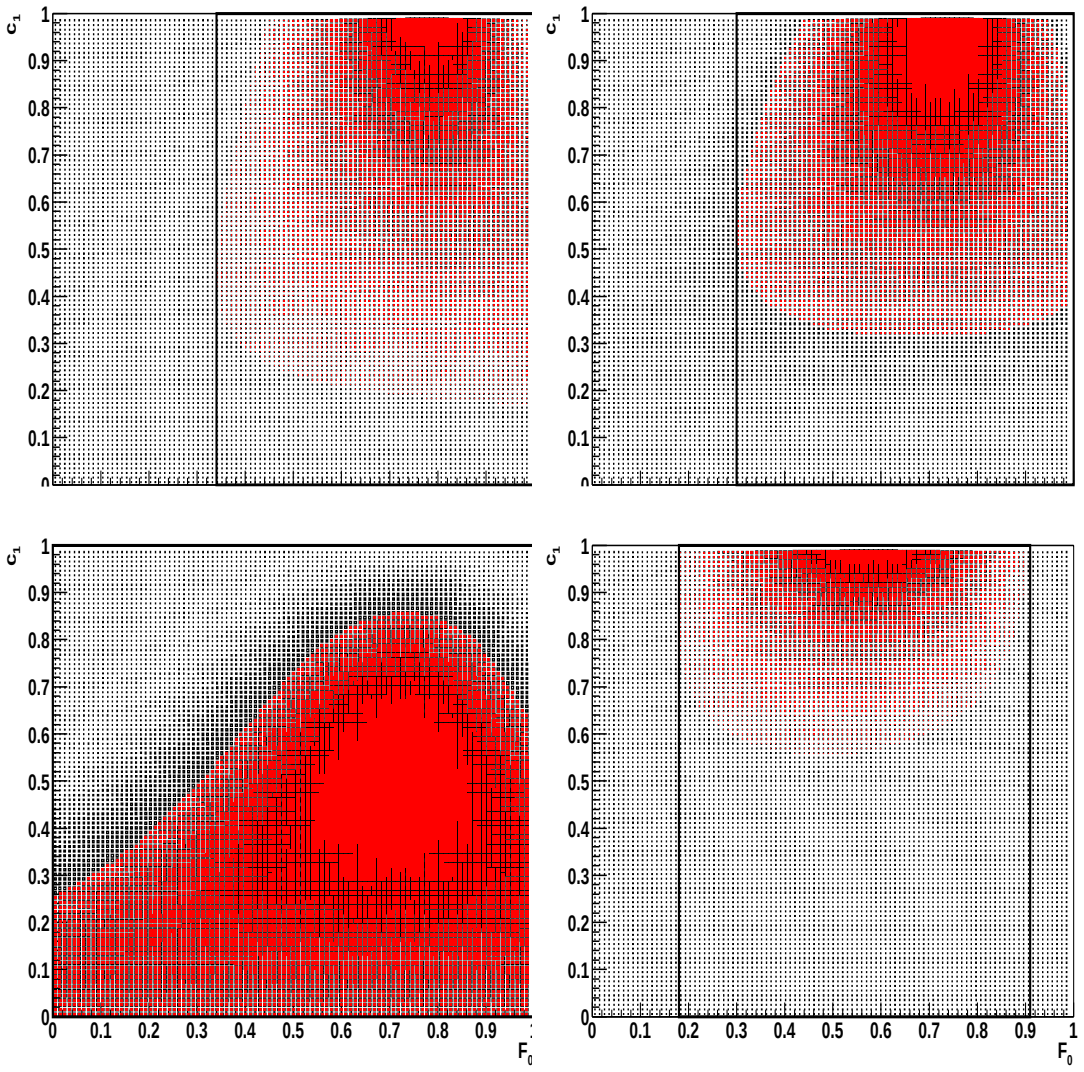

Figure G.11: Probability distribution as a function of c_1 and F_0 for 30 events with an input F_0=0.7 and fluctuating signal/(signal+background) about 0.4. Shadow inside box indicates the 68.27% of the total probability area in two-dimensional space.

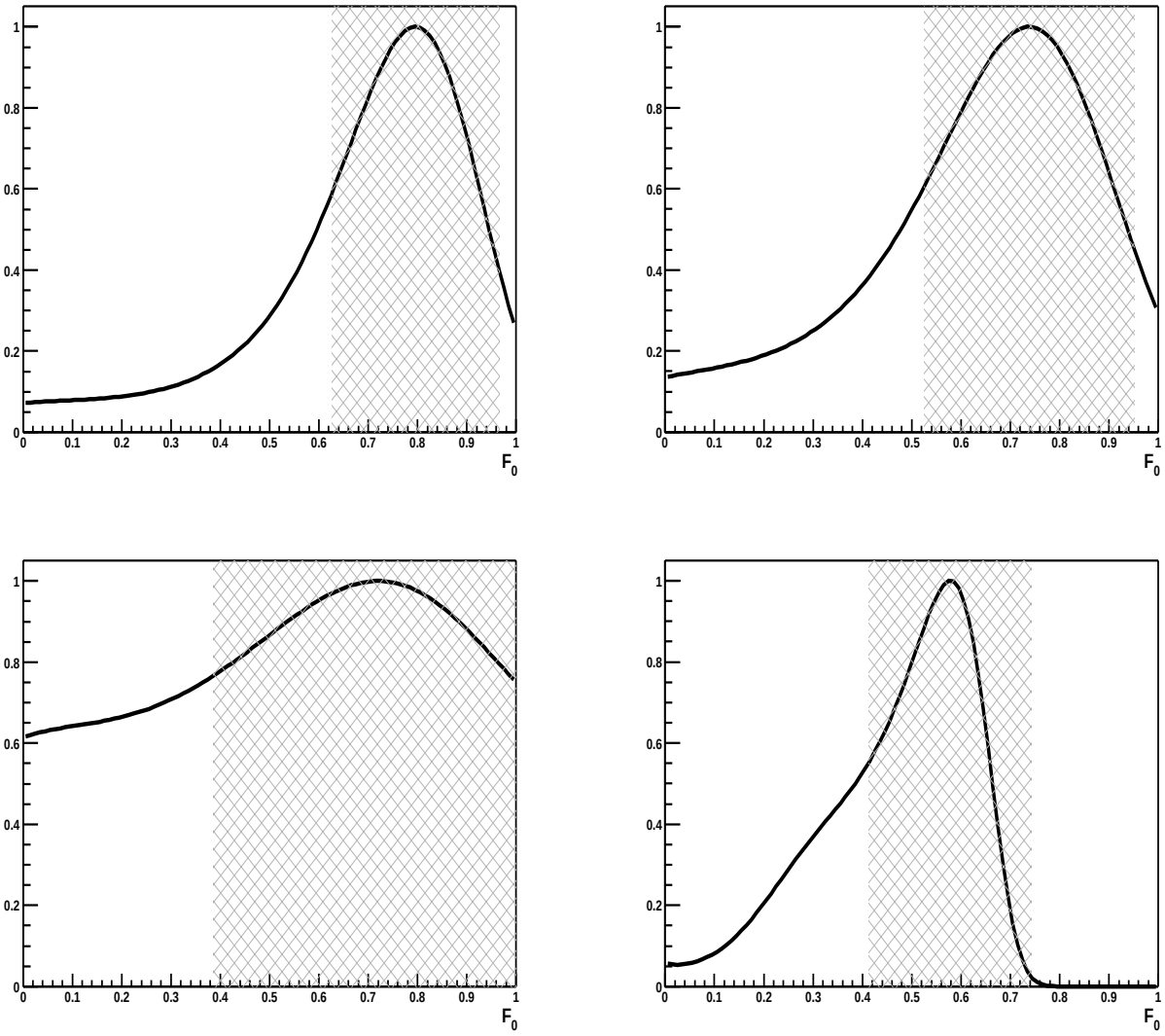

Figure G.12: Probability as a function of F_0 for the same four experiments as in Fig. G.11. The projection onto F_0 was obtained by minimizing c_1 at each F_0. Each experiments has 30 events with signal/(signal+background) fluctuating in 0.4 and input F_0=0.7. Shadow region indicates 68.27% of probability around the most probable value.

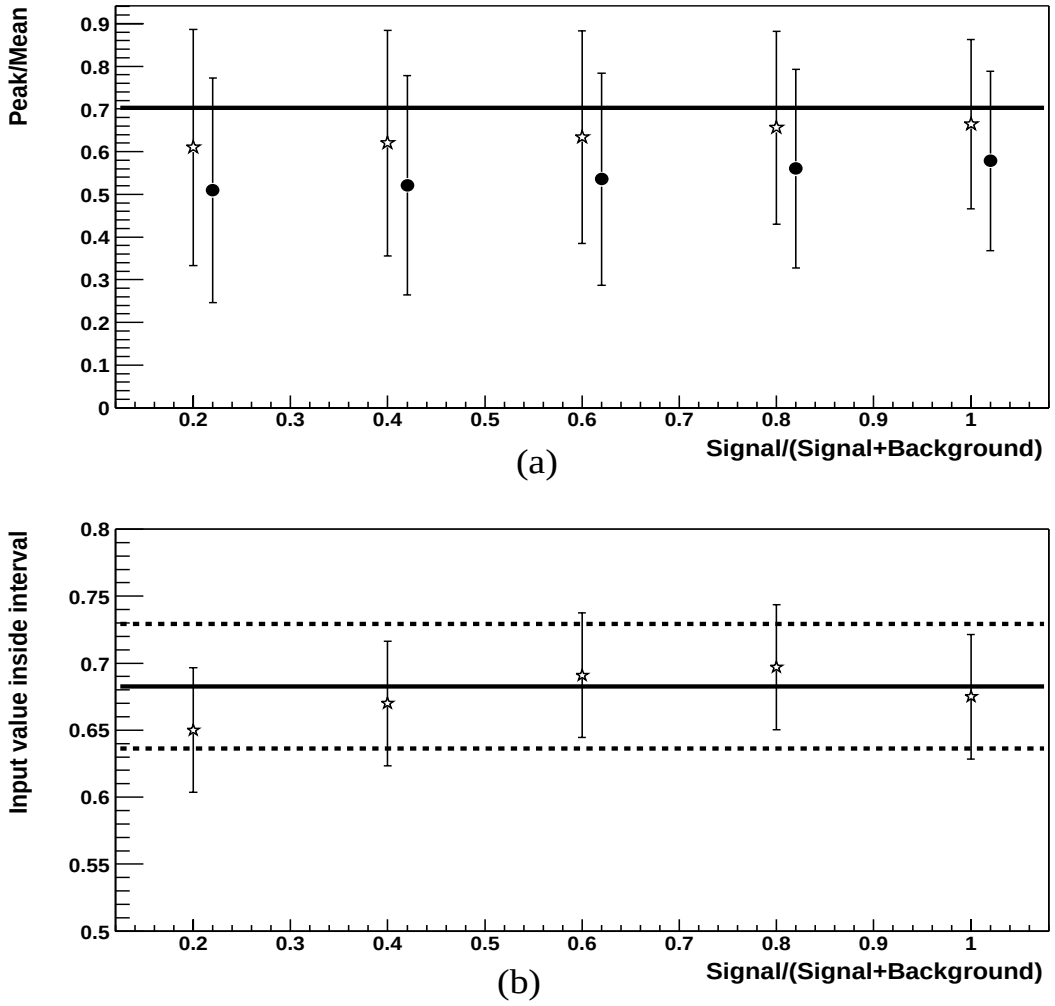

Figure G.13: Results as a function of the signal/(signal+background) ratio, using a total of 30 events and minimizing –ln(L) with respect to c_1. Each point contains the result for 1000 experiments with input F_0=0.703. (a) Means (circles) most probable values (stars) are plotted with error bars representing the RMS and the 68.27% interval about the peak-values, respectively. (b) Fraction of time that the input F_0 (0.703) is within the interval defined by 68.27% of the area about the most probable value. The horizontal lines correspond to 68.27% and to ± 1 standard deviation.

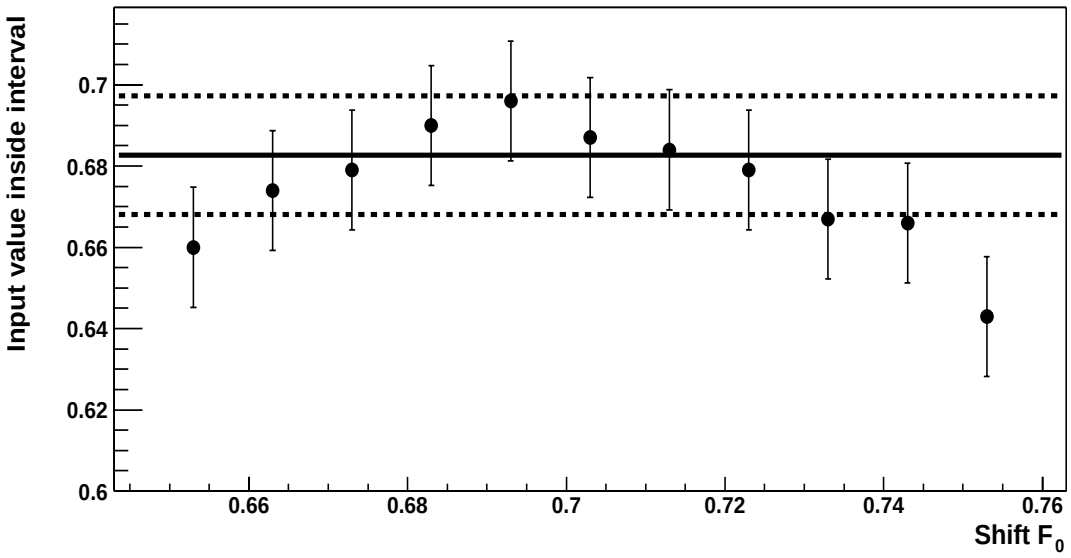

Figure G.14: Fraction of the time that a given F_0 falls inside the 68.27% interval. The horizontal lines correspond to 68.27% and to ± 1 standard deviation. Each point contains the result for 1000 experiments of 200 signal (F_0=0.703) and 300 background events.

Appendix H

Calculation of error on $r = n_s/(n_s + n_b)$

This was caclulated for the analysis of the top mass [61] but is also valid for the extraction of F_0.

For experiments of $n_s + n_b$ events, the likelihood $L(r, M_t)$ is a function of the top mass M_t and the ratio $r = n_s/(n_s + n_b)$, where n_s is the number of $t\bar{t}$ events and n_b is the number of background events. For a given experiment the average value of r ($< r >$) and its error (σ_r) can be calculated as:

$$< r >= \frac{\int_0^1 dr \int dM_t \; r \; L(r, M_t)}{\int_0^1 dr \int dM_t \; L(r, M_t)} \tag{H.1}$$

$$\sigma_r^2 = \frac{\int_0^1 dr \int dM_t \; (r - < r >)^2 \; L(r, M_t)}{\int_0^1 dr \int dM_t \; L(r, M_t)} \tag{H.2}$$

The integrals were calculated numerically replacing the double integrals by double sums:

$$\int dx \int dy \; f(x, y) \rightarrow \sum_i \sum_j \; f(x_i, y_j) \tag{H.3}$$

For the grid in r, 100 equally spaced points where taken between $0.1 \leq r \leq 0.99$. The grid for the top mass was taken every 2 GeV/c^2 in the following intervals: a) 120 GeV/c^2 to 180 GeV/c^2 for M_t = 160 GeV/c^2, b) 140 GeV/c^2 to 200 GeV/c^2 for M_t = 175 GeV/c^2, and c) 160 GeV/c^2 to 220 GeV/c^2 for M_t = 190 GeV/c^2. The integrals were also calculated using Simpson integration, and within errors the results are the same.

The results are shown in Fig. H.1 for experiments with $< n_s >$=24, $< n_b >$=40, and

$n_s + n_b = 64$. Plots H.1.a1 and H.1.a2 correspond to the distribution in $n_s/(n_s + n_b)$ and its pull for M_t= 190 GeV/c^2. Plots H.1.b1 and H.1.b2 are for M_t= 175 GeV/c^2, and plots H.1.c1 and H.1.c2 correspond to M_t= 160 GeV/c^2. The expected and measured ratios are summarized in Table H.1.

Table H.1: Summary of results for $n_s/(n_s + n_b)$.

Top mass	Signal efficiency	Bgd. efficiency	Expected ratio	Measured ratio	Ratio of ratios
190 GeV/c^2	0.807	0.295	0.62	0.52	0.84
175 GeV/c^2	0.695	0.295	0.58	0.51	0.88
160 GeV/c^2	0.583	0.295	0.54	0.49	0.91

We can see that: a) the pull of the RMS is very close to unity, and b) the ratio is still lower than expected (by $\approx 12\%$). As discussed before, this is most likely due to events with ISR and/or merged/split jets for which the $t\bar{t}$ probability is not calculated properly and therefore the events end up in the background.

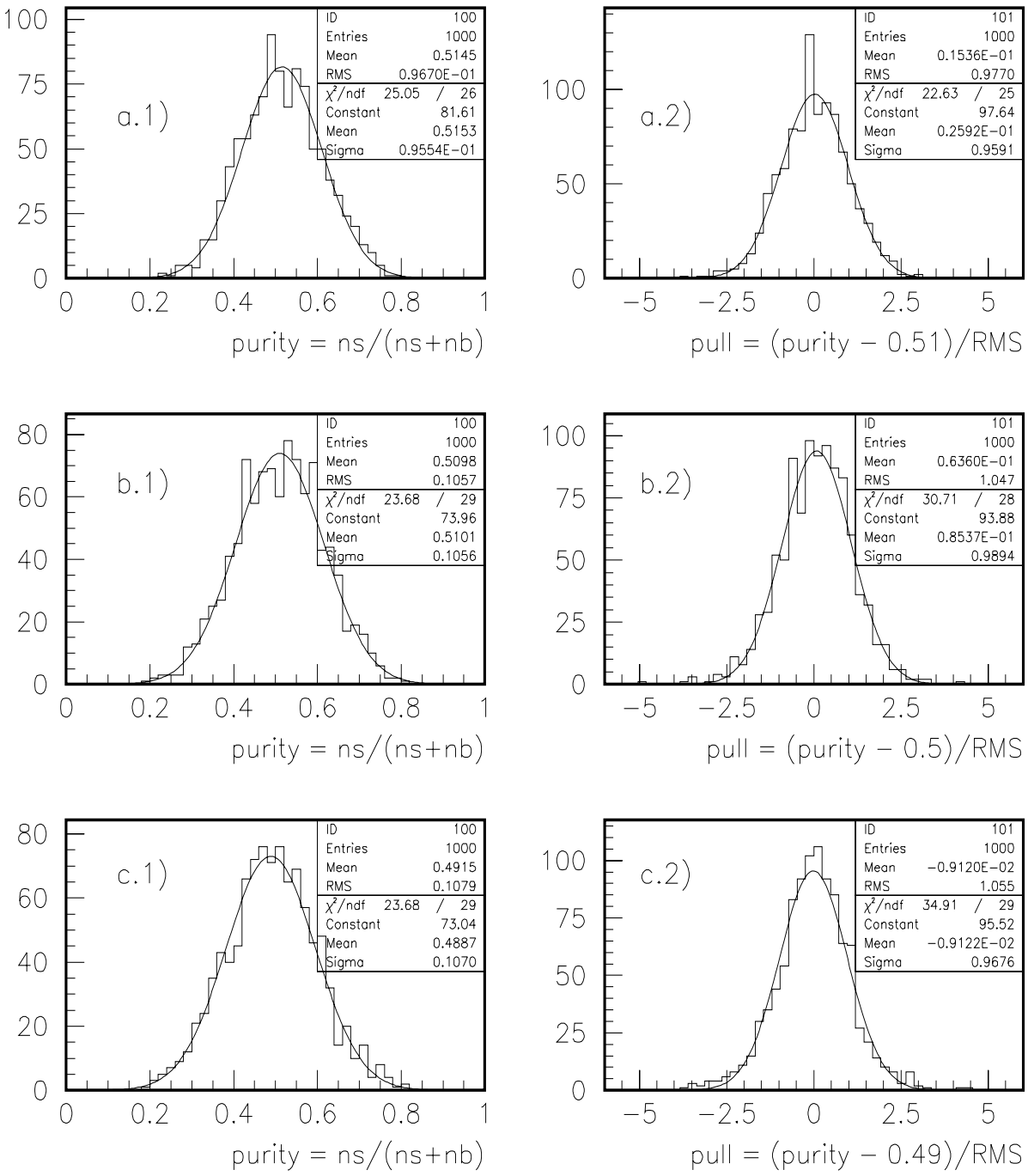

Figure H.1: Plots for experiments with $< n_s >$=24, $< n_b >$=40, and $n_s + n_b$=64. The plots on the left show the distribution in $n_s/(n_s + n_b)$ for M_t= 190 GeV/c^2 (a.1), 175 GeV/c^2 (b.1) and 160 GeV/c^2 (c.1). The plots on the right show the pulls for the same three top masses.

Bibliography

[1] F. Halzen, A. Martin, *Quarks and Leptons*, John Wiley & Sons, (1984)

[2] G. L. Kane, *Modern Elementary Particle Physics: The Fundamental Particles and Forces*, Addison-Wesley (1993)

[3] C. Quigg, *Gauge Field Theories*, Cambridge University Press (1983)

[4] G. 't Hooft, *Renormalizable Lagrangians for Massive Yang-Mills Fields*, Nucl. Phys. B35:167-188 (1971)

[5] G. Altarelli, *Status of the Standard Model and Beyond*, 38th Rencontres de Moriond on Electroweak Interactions and Unified Theories, hep-ph/030605 (2003)

[6] R. P. Feynman, *QED. The Strange Theory of Light and Matter*, Princeton (1985)

[7] M. Gell-Mann, *A Schematic Model of Baryons and Mesons*, Phys. Lett. 8:214-215 (1964)

[8] D. Gross, F. Wilczek, *Asymptotically Free Gauge Theories*, Phys. Rev. Lett. 30, 1343 (1973)

[9] M. Green, *String and Superstrings*, Phys. Scripta T15:7-18 (1987)

[10] L. Randall, R. Sundrum, *An Alternative to Compactification*, Phys. Rev. Lett. 83:4690-4693, (1999)

[11] Particle Data Group. *http://pdg.lbl.gov* (2002)

[12] M. Kamionkowski, *Cosmology and Dark Matter*, Nucl. Phys. Proc. Suppl. 117:335-352 (2003)

[13] M. Koshiba, *The Neutrino Oscillations as Observed by Kamiokandes and by Super-Kamiokande*, Prepared for International School of Subnuclear Physics: 36th Course: From the Planck Length to the Hubble Radius, (1998)

[14] J. Goldstone, A. Salam, S. Weinberg, *Broken Symmetries*, Phys. Rev. 127:965-970 (1962)

[15] P. Higgs, *Broken Symmetries and the Masses of Gauge Bosons*, Phys. Rev. Lett. 13:508-509, (1964)

[16] H. Haber, G. L. Kane, S. Dawson, *The Higgs Hunter's Guide*, Perseus Publishing (2000)

[17] A. Sirlin, *Thirty Years of Precision Electroweak Physics*, J. Phys. G29:213-224, (2003)

[18] R. K. Ellis, W. J. Stirling, B. R. Webber, *QCD and Collider Physics*, Cambridge Monographs on Particle Physics, Nuclear Physics and Cosmology (1996)

[19] S. Willenbrock, *Studying the Top Quark*, Rev. Mod. Phys.72:1141-1148, (2000)

[20] I. Bigi *et al*, *Production and Decay of Ultraheavy Quarks*, Phys. Lett. B181, 157 (1986)

[21] S.Abachi *et al*, DØ Collaboration. *Observation of the Top Quark*, Phys. Rev. Lett. 74: 2632 (1995) ; F.Abe *et al*, CDF Collaboration, *Observation of Top Quark Production in $p\overline{p}$ Collisions*, Phys. Rev. Lett. 74: 2626-2631 (1995)

[22] G. L. Kane, G. A. Ladinsky, *Using the Top Quark for Testing Standard-Model Polarization and CP Violation Predictions*, Phys. Rev. D 45, 124 (1992)

[23] T. Tait, C.-P. Yuan, *Single Top Quark Production as a Window to Physics Beyond the Standard Model*, Phys. Rev. D 63:014018, (2001)

[24] S. Abachi *et al.*, DØ Collaboration. *The DØ Detector*, Nucl. Instr. Meth. A338, 185 (1994)

[25] Tevatron Electroweak Working Group, *http://tevewwg.fnal.gov/top/*

[26] V. Abazov *et al*, DØ Collaboration. *$t\bar{t}$ Production Cross Section in $p\bar{p}$ Collisions at $\sqrt{s}$=1.8 TeV*, Phys. Rev. D 67, 012004 (2003)

[27] T. Affolder *et al*, CDF Collaboration. *Measurement of the $t\bar{t}$ Production Cross Section in $p\bar{p}$ Collisions at $\sqrt{s}$=1.8 TeV*, Phys. Rev. D 64, 032002 (2001)

[28] M. Fischer, S. Groote, J. G. Korner, M. C. Mauser, *Complete Angular Analysis of Polarized Top Decay at $O(\alpha_s)$*, Phys. Rev. D 65:054036, (2002)

[29] R. H. Dalitz, G. R. Goldstein, *Decay and Polarization of the Top Quark*, Phys. Rev. D 45, 1531 (1992)), and reference therein; K. Kondo et al., J. Phys. Soc. Jap. **62**, 1177 (1993

[30] T. Affolder *et al*, CDF Collaboration, *Measurement of the Helicity of W Bosons in Top Quarks Decays*, Phys. Rev. Lett. 84: 216-221 (2000)

[31] D. Amidei, R. Brock, *Future Electroweak Physics at the Fermilab Tevatron. Report of the TeV 2000 Study Group*, Fermilab-PUB-96/082. DØ note number 2589, CDF note number 3177, (1996)

[32] B. Abbott *et al*, DØ Collaboration, *Direct Measurement of the Top Quark Mass by the DØ Collaboration*, Phys. Rev. D 58, 052001 (1998)

[33] G. Mahlon, S. Parke, *Angular Correlations in Top Quark Pair Production and Decay at Hadron Colliders*, Phys. Rev. D 53, 4886 (1996)

[34] G. Mahlon, S. Parke, *Maximizing Spin Correlations in Top Quark Pair Production at the Tevatron*, Phys. Lett. B 411, 133 (1997)

[35] F. Abe *et al*, CDF Collaboration, *The CDF Detector: An Overview*, Nucl. Instrum. Meth. A271:387-403 (1988)

[36] Fermilab, *Design Report Tevatron 1 project*, FNAL internal note, (1984); FNAL. *A Report of the Design of the Fermi National Accelerator Laboratory*, FNAL internal note, (1979)

[37] DØ Collaboration, *DØ Upgrade: The Detector and its Physics*, DØ note number 2447 (1995)

[38] A.R. Clark *et al*, *DØ Vertex Drift Chamber Construction and Test Results*, Nucl. Instrum. Meth. A315:193-196 (1992)

[39] R. Fernow, *Introduction to Experimental Particle Physics*, Cambridge University Press (1986)

[40] F. Sauli, *Principles of Operation of Multiwire Proportional and Drift Chambers*. In T. Ferbel, editor, *Experimental Techniques in High Energy Physics*, Addison-Wesley (1987)

[41] B. Mansoulie *et al*, *The DØ Transition Radiation Detector*, Nucl. Instrum. Meth. A265:157-166 (1988)

[42] J. F. Detoeuf *et al*, *Status of the Transition Radiation Detector for the DØ Experiment*, Nucl. Instrum. Meth. A279:310-316 (1989)

[43] T. Behnke, *The Central Drift Chamber for the DØ Experiment: Design, Construction and Test*, SUNY, Stony Brook). FERMILAB-THESIS-1989-47, Ph.D. Thesis, (1989)

[44] J. Bantly, *The DØ Detector Forward Drift Chamber Performance and Physics Capability in the 1990 FNAL Test Beam Run.*, FERMILAB-THESIS-1992-43, Ph.D. Thesis, (1992)

[45] R. Angstadt *et al*, *A working, VME Based, 106-MHZ FADC Data Acquisition System For the Tracking Detectors at DØ*, IEEE Trans. Nucl. Sci. 39:1297-1301 (1992)

[46] C. Fabjan, *Calorimetry in High-Energy Physics*. In T. Ferbel, editor, *Experimental Techniques in High Energy Physics*, Addison-Wesley (1987)

[47] A. Spadafora *et al*, *Test Beam Results from the DØ Liquid Argon End Calorimeter Electromagnetic Module.*, Nucl.Instrum.Meth.A315:279-284, (1992); S. Chopra, R. Raja, *Estimation of the QCD background to W-eμ+jets*. DØ note number 2098, (1994)

[48] C. Brown *et al*, *DØ Muon System with Proportional Drift Tube Chambers*, Nucl. Instrum. Meth. A279:331-338 (1989)

[49] J. Bantly *et al*, *The Level 0 Trigger for the DØ Detector*, IEEE Trans. Nucl. Sci. 41:1274-1279 (1994)

[50] M. Abolins *et al*, *The Fast Trigger for the DØ Experiment*, Nucl. Instrum. Meth. A289:543-560, (1990)

[51] D. Culllen-Vidal *et al*, *DØ Level-2/Data Acquisition; the New Generation*, DØ note number 1121 (1992)

[52] S. Youssef, Comp. Phys. Comm.: 45:423-426, (1991)

[53] M. Narain, *Electron Identification in the DØ Detector*, DØ note number 1548 (1991)

[54] C. Gerber *et al*, *Muon Momentum Determination*, DØ note number 2140(1994)

[55] S. Abachi *et al*, *Top Quark Search with the DØ 1992-1993 Data Sample*, Phys. Rev. D 52, 4877-4919 (1995)

[56] A. Milder, *Dijet Angular Distributions at 1800 GeV Using the DØ Detector*, Ph.D Thesis (1993); R. Astur, *A Study of the Ability of the DØ Detector to Measure the Single Jet Inclusive Cross Section*, Ph.D Thesis (1992)

[57] DØ Jet energy scale group, *Jet Energy Scale (CAFIX 5.1)*, DØ note number 3139 (1996)

[58] B. Abbott, *et al*, *Determination of the Absolute Jet Energy Scale in the DØ Calorimeters*, Nucl. Instrum. Meth. A424 352-394, DØ notes numbers 3287 and 3288, (1999)

[59] F. Hsieh *et al*, *Jet Energy Scale Uncertainty for Top Cross Section PRL*, DØ note number 3200 (1997)

[60] B. Abbott *et al*, DØ Collaboration., *Measurement of the top quark mass using dilepton events*, Phys. Rev. Lett. 80, 2063 (1998)

[61] F. Canelli, J. Estrada, T. Ferbel, G. Gutierrez, *Maximizing the Use of Kinematic Information. An Application to single-lepton Events*, DØ note number 3975 (1999)

[62] V. Abazov *et al*, DØ Collaboration, *New Measurement of the Mass of the Top Quark in lepton+jets $t\bar{t}$ Events*, PRL in preparation (2003)

[63] J. Estrada,*Maximizing Use of Kinematic Information for the Extraction of the Mass of the Top Quark in Single-Lepton $\bar{t}t$ Events*, Ph.D. Thesis (2001)

[64] A. G. Frodesen and H. Tofte, *Probability and Statistics in Particle Physics*, Oxford University Press (1978)

[65] F.A. Berends, H. Kuijf, B. Tausk and W.T. Giele, *On The Production of a W and Jets at Hadron Colliders* Nucl. Phys. B 357, 32 (1991)

[66] T. Sjostrand *et al*, *PYTHIA 5.7 and Jetset 7.4. Physics and Manual*, hep-ph/9508391. (1998).

[67] G. Corcella, I.G. Knowles, G. Marchesini, S. Moretti, K. Odagiri, P. Richardson, M.H. Seymour and B.R. Webber, *HERWIG 6.4*, JHEP 01 (2001) 010 [hep-ph/0011363] and hep-ph/0107071 (2000)

[68] H.Baer, F.E.Paige, S.D.Protopescu, X.Tata, *ISAJET 7.40: A Monte Carlo Event Generator for P P, Anti P P, and e+ e- reactions*, hep-ph/9810440 (1998)

[69] S.Snyder, *Measurement of the Top Quark Mass at DØ*, University of New York at Stony Brook, Ph.D. Thesis (1995).

[70] R.Brun, F. Rademakers, *ROOT: An Object Oriented Data Analysis Framework*, Nucl. Instrum. Meth. A389:81-86 (1997)

[71] R.Brun, M.Hansroul, P.Palazzi, B.Peuchot, *HBOOK User Guide: Version 2.0*, CERN-DD/75-11 (1975)

[72] H. L. Lai, J. Botts, J. Huston, J. G. Morfin, J. F. Owens, J. W. Qiu, W. K. Tung, H. Weerts, *Global QCD Analysis and the CTEQ Parton Distribution*, Phys. Rev. D 51:4763-4782 (1995)

[73] A.Jonckheere, *DØGEANT User's Guide*, DØ note number 969 (1990)

[74] S.Wimpenny, *Studies of the MuSmear Correction Factors for the Run1b/c Single Top Analysis*, DØ note number 3281 and 3282 (1997)

[75] F. James, *MINUIT Minimization Package Reference Manual*, CERN Program Library Number D506 (1994)

[76] T. Stelzer and W.F. Long, *Automatic Generation of Tree Level Helicity Amplitudes*, Comput. Phys. Commun. 81:357-371, (1994)

[77] A. Juste, private communication.

[78] P. C. Bhat, H. B. Prosper, S. S. Snyder, *Bayesian Analysis of Multisource Data*, Phys. Lett. B407:73-78, (1997)